Analysing the Effect of Reynolds Number and Aspect Ratio on the Wing Performance with Bio-inspired Passive Flow Control Devices

A Thesis

Submitted in Partial Fulfillment of the Requirements for the Award of the Degree of

DOCTOR OF PHILOSOPHY

By

Anand Verma

Department of Mechanical Engineering

Indian Institute of Technology Guwahati

Guwahati-781039, Assam, India

February - 2025

Dedicated to my Parents

Mr. Surendra Nath

and

Mrs. Chandra Kala

Department of Mechanical Engineering
Indian Institute of Technology Guwahati
Guwahati-781039, Assam, India

DECLARATION

I hereby certify that the work compiled in this dissertation entitled **'Analysing the Effect of Reynolds Number and Aspect Ratio on the Wing Performance with Bio-inspired Passive Flow Control Devices'** is the outcome of the research work, performed by myself, else stated, under the guidance of **Professor Vinayak Kulkarni** in the Department of Mechanical Engineering, Indian Institute of Technology Guwahati, Assam, India.

Any part of this work has not earlier been submitted for the award of any degree, diploma, associate-fellowship, fellowship or its equivalent to any university or institution.

Anand Verma

Date: February 14, 2025

Anand Verma
Registration No. 186103004
Department of Mechanical Engineering
Indian Institute of Technology Guwahati
Guwahati-781039, Assam, India

Department of Mechanical Engineering
Indian Institute of Technology Guwahati
Guwahati-781039, Assam, India

CERTIFICATE

It is certified that the work contained in the thesis entitled **'Analysing the Effect of Reynolds Number and Aspect Ratio on the Wing Performance with Bio-inspired Passive Flow Control Devices'** by **Mr. Anand Verma**, a student, in the Department of Mechanical Engineering, Indian Institute of Technology Guwahati, Assam, India, for the award of the degree of the Doctor of Philosophy, has been carried out under our supervision and, that this work has not been submitted elsewhere for the degree.

Date: February 14, 2025

Dr. Vinayak Kulkarni
Professor
Department of Mechanical Engineering
Indian Institute of Technology Guwahati
Guwahati-781039, Assam, India

ACNOWLEDGEMENTS

I would like to express my heartfelt appreciation to all those who have contributed to the completion of this thesis. First and foremost, I would like to offer my deepest gratitude to my supervisor, **Prof. Vinayak Kulkarni**, for his invaluable guidance, encouragement, unwavering support, and insightful feedback throughout the research process. Their expertise and insightful feedback have been crucial in shaping the direction and quality of this research. Without his genuine dedication and help, I would not have been able to give my best efforts during the present research work. I am also thankful to my doctoral committee members, **Prof. Niranjan Sahoo**, **Dr. P. K. Mondal, Dr. Deepak Sharma,** and **Dr. Rishikesh Kulkarni,** for their thoughtful reviews and constructive suggestions, which have greatly contributed to the refinement of this work. Further, I would also like to share my heartfelt gratitude to **Prof. U. K. Saha** for sharing his deep knowledge and techniques regarding article preparation and presentation.

My appreciation extends to **Prof. K. S. R. Krishna Murthy**, HOD, Mechanical Engineering Department, for providing extensive research facilities and financial assistance. Additionally, I am also grateful to the **MHRD**, Government of India, for providing me a scholarship for the period of my PhD research, which enabled me to fulfil my financial needs. My sincere thanks also go to the Aeronautical Research and Development Board (**AR&DB**), a funding agency under **DRDO**, for their crucial financial support, which played a pivotal role in facilitating and advancing the investigations conducted in this thesis.

I am deeply thankful to my seniors, fellow lab-mates and friends, namely **Dr. Sumit Agarwal**, **Dr. Soumya Ranjan Nanda**, **Dr. Saibal Kanchan Barik, Dr. Anil Kumar Rout, Dr. Ojing Siram, Dr. Sangjukta Devi, Dr. Santosh Hotta, Dr. Shailendra Kumar, Dr. Ali Jraisheh, Dr. Umang Rathod, Dr. Shashank Kulkarni, Mr. Abhishek Kamal, Mr. Bastav Borah, Mr. Ravi Kumar, Ms. Kabita Naik, Ms. Amrita Pathak, Ms. Sima Nayak, Mr. Pankaj Kumar, Mr. Amit Kumar and Mr. Rishi Purohit** for their support, affection, and encouragements during the research journey. Without this group, my journey perhaps would have been less fun. Additionally, I would like to express my heartfelt gratitude to a special person in my life, **Ms. Rimpy Kalita**, for her unwavering support, encouragement, and understanding throughout this journey.

Last but not least, I am grateful to almighty God and my beloved family for their love and support; without their blessings, this achievement would not have been possible. Especially, I am solely indebted to my parents **Mr. Surendra Nath** and **Mrs. Chandra Kala**, my sisters, **Dr. Madhavi,** and **Ms. Shilpi Verma,** from whom I get moral and spiritual support at every step of my life.

Anand Verma
Indian Institute of Technology Guwahati
February 2025

ABSTRACT

Micro air vehicles (MAVs) are a special form of unmanned aircraft that are evolving rapidly every year due to their vast applications in civil and military sectors. Such vehicles have limited wing dimensions and power unit, due to which they operate under a low Reynolds number (*Re*) range of 10×10^3 to 100×10^3. Within this *Re* range, conventional airfoils experience a significant decline in performance as the *Re* decreases below 100×10^3. Apart from this, the wing design of such vehicles relies majorly on the use of wings with an aspect ratio (*AR*) lower than 2.0. These wings face a significant challenge of producing lower lift values at low *AoA* due to the presence of strong wingtip vortices. In this context, the present study is focused on investigating the aerodynamic characteristics of wings with an $AR \leq 2.0$, both in the presence and absence of bio-inspired passive flow control devices. The aim is to contribute to the advancement of MAV technology.

Two low-speed airfoils, S5010 and E214, have been chosen for the fabrication of rectangular wing models. The preliminary stage of investigation involves exploring the aerodynamic performance and wake field characteristics of these airfoil models within the *Re* range of $40 \times 10^3 \leq Re \leq 100 \times 10^3$. Subsequently, the effect of *Re* and *AR* on the aerodynamic performance of the wings associated with the S5010 and E214 sections is investigated in the next phase of the work. In this regard, the *AR* and *Re* have been chosen in the range of $2.0 \leq AR \leq 1.0$ and $60 \times 10^3 \leq Re \leq 150 \times 10^3$, respectively. The analysis exhibited that wings based on the E214 section demonstrate better aerodynamic performance compared to the S5010 airfoil for the tested *Re* and *AR* ranges. Consequently, in an effort to enhance the performance of the S5010 wing, bio-inspired passively acting devices have been implemented on the wing. These flow control devices are tested, targeting two different flow modes, specifically flow separation over the surface and flow of vortices through the wingtip.

In the first scenario, the self-actuating flaps, which are evolved by emulating the covert feathers on the upper wing of a bird, are tested for wings of $AR = 2.0$ and 1.0 to control flow separation over the surface. Focus has also been given for exploring flap effectiveness in various aspects, including flap span, chord length, and chord-wise placement within a *Re* range of 60×10^3 to 120×10^3. The flap does not impact pre-stall wing performance, but it significantly improves post-stall lift and drag characteristics over the clean wing. The optimal chord-wise position of the flap for

better performance enhancement is near the mid-chord for both models. Finally, the effectiveness of various bio-inspired wingtip devices is also examined to reduce the effect of wingtip vortices for wings of AR = 1.0 and 0.5 in the Re range from 80×10^3 to 150×10^3. The concept of slotted wingtips is inspired by structural features observed in primary feathers located at the tips of bird wings. Two different wingtip attachment shapes, viz., tapered and conical, have been chosen for this study and added in a planar manner to the wingtips to create tapered or conical slotted winglet configurations. The incorporation of tapered slotted winglets has proven to be beneficial for enhancing the performance of low AR wings. Overall, the present findings provide valuable insights for optimizing wing design and improving the aerodynamic efficiency of MAVs.

CONTENTS

Nomenclature

English Symbols

A	Wing surface area (m^2)
b	Wingspan (m)
c	Wing chord (m)
C_d	Drag coefficient for infinite wing
C_D	Drag coefficient for finite wing
c_f	Flap chord (m)
C_l	Lift coefficient for infinite wing
C_L	Lift coefficient for finite wing
C_{lmax}	Maximum lift coefficient for infinite wing
C_{Lmax}	Maximum lift coefficient for finite wing
C_l/C_d	Lift-to-Drag ratio for infinite wing
C_L/C_D	Lift-to-Drag ratio for finite wing
$C_{m,0.25c}$	Pitching moment coefficient about quarter-chord for infinite wing
$C_{M,0.25c}$	Pitching moment coefficient about quarter-chord for finite wing
d	Drag force on infinite wing (N)
D	Drag force on finite wing (N)
f_d	Dominant frequency (Hz)
fs	Vortex shedding frequency (Hz)
k	Induced drag factor
l	Lift force on infinite wing (N)
L	Lift force on finite wing (N)
m	Pitching moment on infinite wing (N-m)
M	Pitching moment on finite wing (N-m)
m/c	Maximum camber to chord ratio
N	Tunnel fan speed (rpm)
R^2	Coefficient of determination

Re	Reynolds number
S	Flap span (m)
St_s	Strouhal number
t/c	Maximum thickness to chord ratio
U_∞	Freestream velocity (m/s)

Greek Symbols

ρ	Air density (kg/m^3)
υ	Kinematic viscosity of air (m^2/s)
τ	Lift efficiency factor
Λ	Sweep angle (*deg*)

Abbreviations

2D	Two dimensional
3D	Three dimensional
AoA	Angle of attack (*deg*)
AR	Aspect ratio
CFD	Computational fluid dynamics
DAQ	Data acquisition
FDM	Fused deposition modeling
FFT	Fast Fourier transform
HWA	Hot wire anemometer
LE	Leading edge
LSB	Laminar separation bubble
MAV	Micro air vehicle
MSA	Mean square amplitude
PLA	Polylactic acid
TE	Trailing edge

List of Figures and Tables

List of Figures

List of Tables

CHAPTER 1

Introduction

Overview

This chapter presents an overview of micro air vehicles (MAVs) and discusses the relevant parameters that impact the aerodynamics of these vehicles. MAVs are unmanned aircraft that are rapidly advancing in various sectors. The benefits of MAVs include their ease of transportation, adaptability to challenging environments, and ability to perform tasks that are difficult for larger aircraft or humans. The design and development of fixed-wing MAVs place great importance on the aerodynamic efficiency of the wing. There are various parameters such as wing planforms, airfoil shape, aspect ratio, Reynolds number, and angle of attack that significantly influence their aerodynamics. Due to their limited wing dimensions and power input, MAVs operate within a low Reynolds number range. The selection of airfoils becomes a significant concern within this range, as conventional airfoils experience hysteresis effect and performance degradation at low Reynolds numbers. By addressing these factors, designers can enhance the aerodynamic efficiency of fixed-wing MAVs, leading to improved flight performance and maneuverability. The chapter also includes a brief introduction to flow control devices and concludes by providing a concise overview of the organization of the current thesis work.

1.1 Motivation

Low Reynolds number and low aspect ratio wings are essential parameters considered in the design phase of any advanced small-scale unmanned aircraft such MAVs. In general, unmanned air vehicles with a wingspan and weight of less than 500 mm and 500 g, respectively, are categorized as MAVs. Other dimensional specifications of the MAVs outlined by The Defence Advanced Research Projects Agency (DARPA) are that their size and weight limits should be around 150 mm and 100 grams, respectively [Mueller et al., (2007)]. These restrictions are intended to make the MAVs small and lightweight enough to be easily transported and deployed in various environments. The main advantage of such vehicles is their small size, which allows them to be conveyed by a single operator, achieves difficulty sighting, and makes them capable of performing tasks that are challenging or dangerous for larger aircraft or humans. Therefore, they are used in a variety of applications, including surveillance missions (video, infrared images of battlefields, etc.), border patrolling, disaster relief services, and improving communications in urban areas, etc.

The size and weight of the MAVs will depend on factors such as the desired flying characteristics, payload capacity, power source, and materials used in the construction. Based on their design and functionality, MAVs are broadly classified into three main categories as fixed wing, rotary wing, and flapping wing [Yan and Ebel, (2019)], as shown in **Fig. 1.1.** Fixed-wing MAVs have a rigid wing structure and they rely on forward motion to generate the lift. The rotary-wing MAVs use rotating blades to generate the lift and maneuver in all directions. Flapping-wing MAVs, on the other hand, use flapping motions similar to birds or insects to generate the lift. In comparison to other types, the fixed wing MAVs have higher flight speed and they can fly at higher altitudes with longer range and endurance [Hassanalian and Abdelkefi, (2017)].

For the efficient design and development of fixed-wing MAVs, various factors must be taken into account, viz. aerodynamics, maneuverability, propulsion system, power unit, and various accessories (cameras, sensors, etc.). Among these, the major area of serious concern is the aerodynamic efficiency of the wing because several parameters can affect it and those are wing planform, airfoil shape, wing loading, Reynolds number, angle of attack, etc. Such vehicles have limited wing dimensions and power input, due to which they operate under a low Reynolds number range. In general, the operational Reynolds number range for such vehicles is 10×10^3 to 100×10^3 [Mueller, (1999)]. The Reynolds number, which relates to the fluid flow around the wing,

affects the transition between laminar and turbulent flow and can significantly impact the performance characteristics of the wing. Therefore, it is important to carefully consider operating Reynolds number range during the design phase and hence for testing of fixed-wing MAVs to ensure optimal flight performance. This can implicity involve selecting airfoil and wing planform that are optimum for the desired flight conditions and carefully control the wing loading.

(a) Fixed wing MAV [CSIR-NAL, (2012)]

(b) Rotary wing MAV [Hassanalian, (2016)]

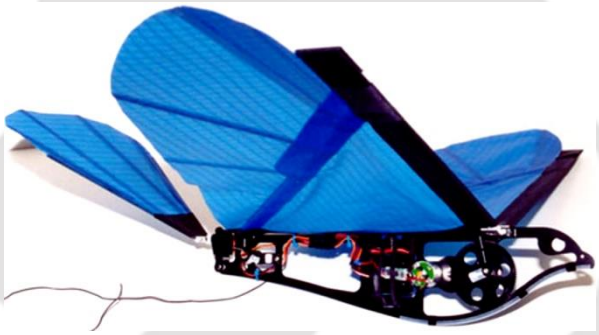

(c) Flapping wing MAV [Hassanalian, (2016)]

Fig. 1.1: Classification of MAV

Further, the fixed-wing MAV is designed as a flying wing that has distinct wing planforms and configurations. Some of the most common planforms that have been used for fixed-wing MAVs include rectangular, elliptical, dihedral delta, Zimmermann, and inverse Zimmermann. **Figure 1.2** exhibits various planforms of fixed-wing MAV for different aspect ratios. The wing planform controls the aspect ratio, sweep angle, and dihedral angle, all of which affect the stability and aerodynamics characteristics of the wing. Moreover, the airfoil shape is also an essential parameter in the wing design of this MAV that significantly affects its flight performance. The airfoil shape determines the lift and drag characteristics of the wing, which directly impacts the MAV's ability

to generate lift and fly at different speeds. Different airfoil shapes are optimized for different flight conditions, with some airfoils designed to provide high lift and low drag for slow flight, while others are optimized for high-speed flight with low drag. By selecting the appropriate airfoil shape, aerodynamic characteristics can be enhanced to achieve optimum flight performance. In conclusion, the aerodynamics of fixed-wing MAVs are significantly affected by several key factors such as airfoil shape, Reynolds number, aspect ratio, etc. By carefully considering these parameters, designers can optimize the aerodynamic behavior of fixed-wing MAVs to achieve the desired flight performance, including improved endurance, range, and maneuverability. Therefore, a detailed understanding of the effect of these parameters regarding the aerodynamic performance of MAVs is discussed in the following sections.

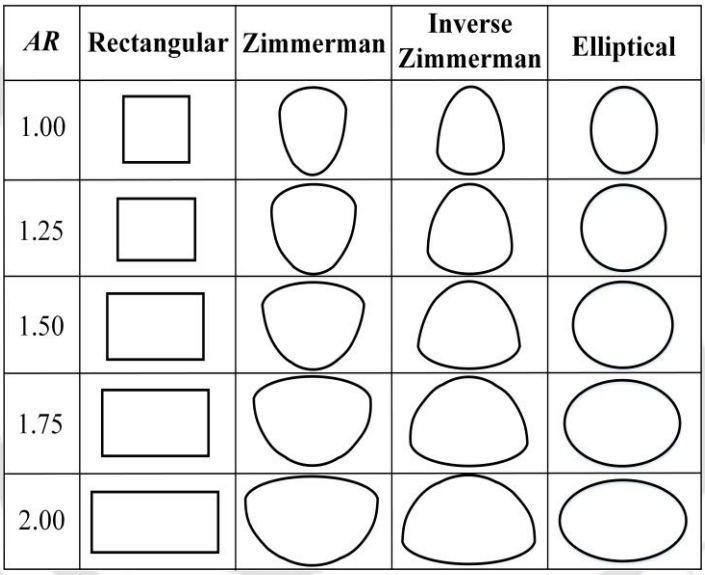

Fig. 1.2: Different wing planforms used for fixed-wing MAV study [Mueller et al., (2007)]

1.2 Aerodynamic Performance and Governing Parameters of Airfoil / Wing

Airfoils are a fundamental component of many fluid-dynamic systems, such as wings, blades, and turbines. These streamlined structures are designed to generate lift as it moves through the air or any fluid medium. Airfoils are classified using a specific nomenclature that describes their geometric features, such as maximum camber, camber location, thickness, and other attributes. Understanding these characteristics is essential in designing and optimizing airfoils to achieve the desired performance for their specific applications. Details description of geometric parameters and aerodynamic performance of airfoil/wing are discussed in the following sections.

1.2.1 Geometrical Parameters and Their Significance

Geometric parameters of an airfoil and wing describe its shape and dimensions, which play a crucial role in its aerodynamic properties. Various terminologies are used to express the geometrical characteristics of an airfoil, as shown in **Fig. 1.3.** These terminologies include terms such as chord length (*c*), maximum camber (*f*), camber location (X_f), thickness (*t*), trailing or leading edge shape, and angle of attack (*AoA*). The chord length is the distance between leading edge and trailing edge of the airfoil, measured in a straight line along the chord line. It is used to calculate the cross-sectional area of the airfoil, which is a critical parameter in determining the lift and drag. The front edge of an airfoil has a radius of curvature which is known as the leading edge radius. This is the radius of a circle that is centered on a line tangent to the leading edge camber and passes through the points where the upper and lower surfaces of the airfoil meet the leading edge. For subsonic airfoils, a common guideline for the leading edge radius is to use a value that is approximately 1% of chord length [Bertin and Cummings, (2009)].

The maximum thickness of an airfoil refers to the maximum distance between its upper and lower surfaces, measured perpendicular to its chord line. It is usually expressed as a percentage of the chord length and denoted as "*t/c*". The camber line, also known as the mean line, is a line that represents the locus of points halfway between the upper and lower surfaces of an airfoil, measured perpendicular to its chord line. At the same time, the maximum camber of an airfoil is the maximum distance between camber line and chord line. It is typically measured as a percentage of the chord length and represents the height of the airfoil's curved surface above the straight line connecting the leading and trailing edges of the airfoil. Further, if the airfoil has no camber; this means that the upper and lower airfoil surface is symmetric about its chord line, which is called as symmetric airfoil. The most common examples are flat plate and NACA 4-digit symmetric airfoil series such as NACA0012, NACA0018, etc. In general, symmetric airfoils are used in applications where a constant lift is required, such as vertical stabilizers, rudders, and control surfaces of aircraft. The flat plate is also commonly used in many applications, particularly in wind tunnel testing and basic aerodynamic studies.

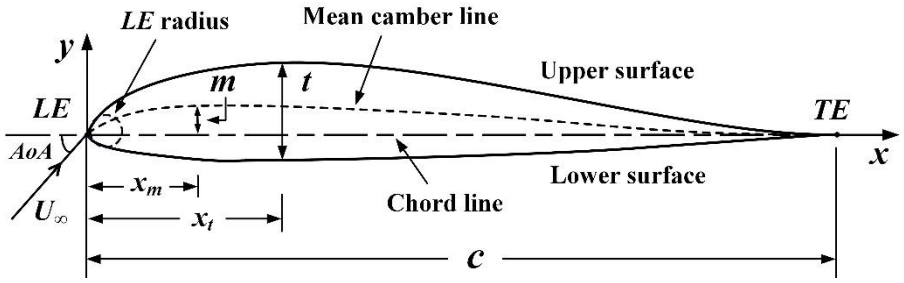

Fig. 1.3: Airfoil geometry and its terminologies [Ojha, (1995)]

To describe wing planform, various geometrical parameters are used and those are wingspan (b), root chord (c_r), tip chord (c_t), mean chord (c), aspect ratio (AR), taper ratio, sweep angle (Λ), etc., as revealed in **Fig. 1.4.** The wingspan is a distance between the left and right wingtips of a wing, while, the root or tip chord refers to the chord length at the root or tip of the wing, respectively. The mean chord is an average chord length along the wing, and the aspect ratio is the ratio of span to mean chord. A high aspect ratio wing has a span that is much longer than its chord length, while a low aspect ratio wing has a shorter span in proportion to its chord length. The specific values for high and low aspect ratios can vary depending on the context, but generally, a wing with an aspect ratio greater than 5.0 is considered high, while a wing with an aspect ratio less than 3.0 is considered low [Raymer, (2018)]. Another parameter is the taper ratio, which is the ratio of tip chord to root chord. A wing with a high taper ratio has a narrower root and wider tip, while one with a low taper ratio has a wider root and narrower tip (**Fig. 1.4d**). Finally, the sweep angle of a wing is defined as the angle between the wing's quarter chord line and a line perpendicular to the root chord. The quarter chord line is an imaginary line located at 25% of the chord from the leading edge of the wing. This angle is commonly measured in degrees and can vary from zero (no sweep) to 90 degrees (fully swept). Depending on the intended application and design goals, the actual sweep angle used in wing design can vary. For example, a high-speed jet fighter will typically have a greater sweep angle than a low-speed general aviation aircraft. In the case of a rectangular wing planform, where the wing has a constant chord length from root to tip, it means that the root chord is equal to the tip chord (**Fig. 1.4a**). This wing has no sweep angle, and the taper ratio of a rectangular planform is 1, as the chord length is constant. The rectangular wing is simple in design and is easy to manufacture, making it a common choice for low-speed and low-altitude applications [Corda, (2017)]. However, it may not be the most efficient wing planform at higher speeds due to the large amount of induced drag which it incurs.

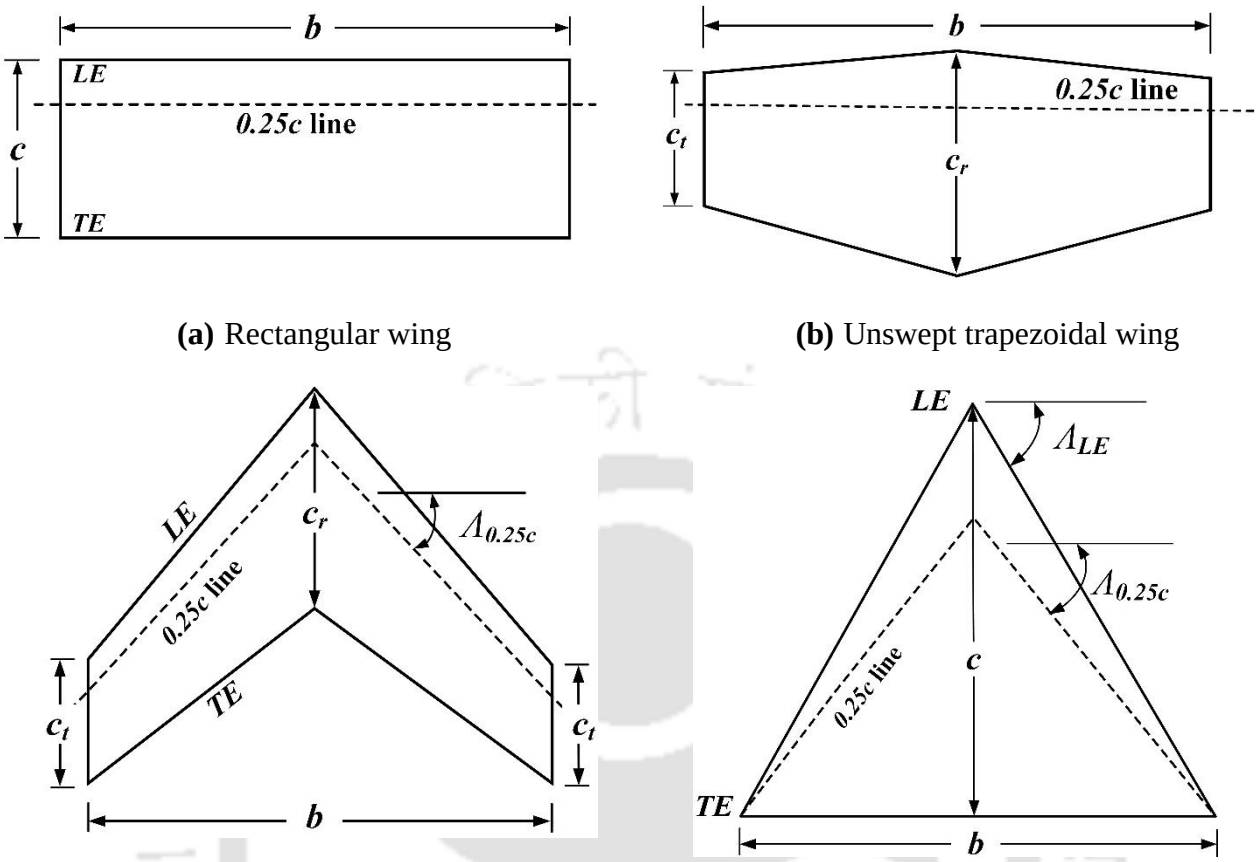

(a) Rectangular wing **(b)** Unswept trapezoidal wing

(c) Swept wing **(d)** Delta wing

Fig. 1.4: Wing geometry of different planforms

1.2.2 Aerodynamic Forces and Moments

When an airfoil is placed in a moving stream of air or it moves with a specific speed, it experiences aerodynamic forces and moments. These forces and moments have two basic sources: pressure and shear stress distribution over the airfoil surface. Pressure acts normally on the surface and is caused by the fluid particles colliding with the surface of the object. The pressure distribution depends on the shape and orientation of the object, as well as the velocity and density of the fluid. At the same time, shear stress acts tangential to the surface and is caused by the frictional forces between the fluid particles and the surface of the object. The shear stress distribution depends on the roughness of the surface and the viscosity of the fluid. Representation of pressure and shear stress distribution on the airfoil surface is shown by the schematic in **Fig. 1.5**. Further, the location where the resultant force (R) of this distributed aerodynamic load on the airfoil is assumed to act is often defined as the center of pressure (x_{cp}). The center of pressure is the imaginary point on the

airfoil where the aerodynamic forces can be considered to act, resulting in no pitching moment (**Fig. 1.5**). This point varies with the angle of attack and can move forward or backward along the chord of the airfoil. For the symmetric airfoil case, the center of pressure is located along the chord length at the quarter chord point from the leading edge [Anderson, (2011)].

The pressure and shear stress distributions should be integrated over the entire surface of the airfoil to obtain the forces and moments on the airfoil. This integration gives the lift, drag, and pitching moment acting on the airfoil. The lift force is perpendicular to the direction of the airflow and is generated by the pressure difference between the upper and lower surfaces of the airfoil or wing body. The drag force is generated by the air resistance to the motion of an airfoil through the airstream. It acts parallel to the direction of airflow and opposes the motion of the airfoil or wing body through the air. The distribution of these lift and drag forces over an airfoil produces a net moment, which is the pitching moment that causes the airfoil to rotate about its pitch axis. Illustration of lift, drag, and pitching moment on the aerodynamic surface is shown in **Fig. 1.6**. Positive pitching moment implies a nose-up moment, which means that the airfoil tends to rotate in an upward direction about its pitch axis. In contrast, a negative pitching moment implies a nose-down moment, which means that the airfoil tends to rotate in a downward direction about its pitch axis. Any airfoil has a point where the pitching moment remains almost constant even as the angle of attack changes; this point is known as an aerodynamic center (x_{ac}). The position of the aerodynamic center along the chord length can vary depending on the shape of the airfoil and the Reynolds number. However, for many airfoils at low to moderate Reynolds numbers, the aerodynamic center is located close to the quarter chord point (0.25c) behind the leading edge of the airfoil [Raymer, (2018)].

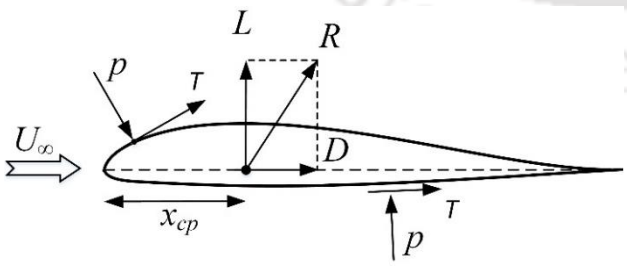

Fig. 1.5: Illustration of pressure, shear stress distribution, and resultant aerodynamic force with its components on the airfoil surface

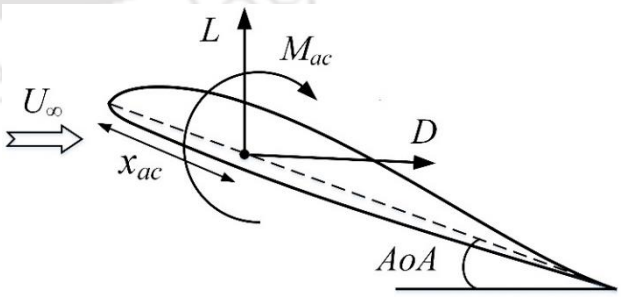

Fig. 1.6: Depiction of aerodynamic forces and moment acting at the aerodynamic centre of airfoil

These aerodynamic forces and moment depend on various factors such as freestream velocity (U_∞), density (ρ), surface area (A), kinematic viscosity of air (υ), angle of attack (AoA), airfoil shape, etc. In aerodynamics, it is common to express the lift, drag, and pitching moment in the non-dimensional form to facilitate performance comparison and analysis of different airfoils or wings. The dimensionless forms of these forces are known as the lift coefficient, drag coefficient, and pitching moment coefficient, respectively. To obtain these coefficients, the aerodynamic forces are divided by a reference quantity which is the product of the dynamic pressure of freestream flow and the reference area. At the same time, the pitching moment coefficient is obtained by dividing the pitching moment by the same reference quantity multiplied by a mean chord length. In general, lift, drag, and moment coefficients of an airfoil are denoted using lowercase subscripts such as C_l, C_d, and C_m, respectively. On the other hand, the aerodynamic coefficients of the wing are represented by uppercase subscripts like C_L, C_D, and C_M. The aerodynamic coefficients for the airfoil and wing are shown in **Eq. 1.1–1.3** and **Eq. 1.4–1.6**, respectively.

For airfoil or infinite wing,

$$C_l = \frac{l}{\frac{1}{2}\rho U_\infty^2 A} \tag{1.1}$$

$$C_d = \frac{d}{\frac{1}{2}\rho U_\infty^2 A} \tag{1.2}$$

$$C_m = \frac{m}{\frac{1}{2}\rho U_\infty^2 Ac} \tag{1.3}$$

For finite wing,

$$C_L = \frac{L}{\frac{1}{2}\rho U_\infty^2 A} \tag{1.4}$$

$$C_D = \frac{D}{\frac{1}{2}\rho U_\infty^2 A} \tag{1.5}$$

$$C_M = \frac{M}{\frac{1}{2}\rho U_\infty^2 Ac} \tag{1.6}$$

1.2.3 Significance of Understanding the Flow Field and its Effects

Flow field around an airfoil refers to the way in which air flows over and around the shape of the airfoil. This is an important area in the field of aerodynamics, as understanding the flow characteristics is critical to the design and performance of aircraft, wind turbines, and other devices that rely on the lift generated by the airfoil. The flow field around an airfoil can be analyzed using two main approaches: experimental testing and computational predictions. Airfoil testing is typically carried out in a wind tunnel. Wind tunnels are facilities that generate controlled airflows around the models of airfoils, allowing researchers to study the aerodynamic properties of the airfoil under various conditions. In addition to wind tunnel testing, computational fluid dynamics (CFD) simulations can also be used to obtain the flow over an airfoil. Such CFD simulations involve using mathematical modeling of the Navier-Stokes equations that govern fluid flow around the airfoil. In experimental aerodynamic studies of any airfoil, a constant chord wing is constructed with a span that covers the wall of the entire test section; such a wing is called an infinite wing. The flow around an infinite wing is referred to as a two-dimensional flow. The flow field around an airfoil has a significant impact on its aerodynamic performance, which is influenced by various parameters such as angle of attack, Reynolds number, surface roughness, etc.

When an airfoil is placed in a moving airstream, the flow of air over its surface can exhibit different behaviors (laminar, turbulent, separated flow) depending on the angle of attack. In general, at low Reynolds numbers and angles of attack, the airflow over the airfoil is laminar, with a relatively small separation bubble at the trailing edge. So it is also known as the "attached flow" regime, and it is the most efficient regime for generating lift and lesser skin friction drag [Bertin and Cummings, (2009)]. While in turbulent flow, the behavior of streamlines is a highly irregular and unpredictable pattern within the boundary layer. The fluid particles move in irregular, chaotic patterns, with mixing occurring between adjacent layers. This type of flow creates more drag but also delays the flow separation due to increased mixing between fluid layers compared to laminar case. Typically, the boundary layer characteristics such as laminar, transition or turbulent can be observed as sketched in **Fig. 1.7**.

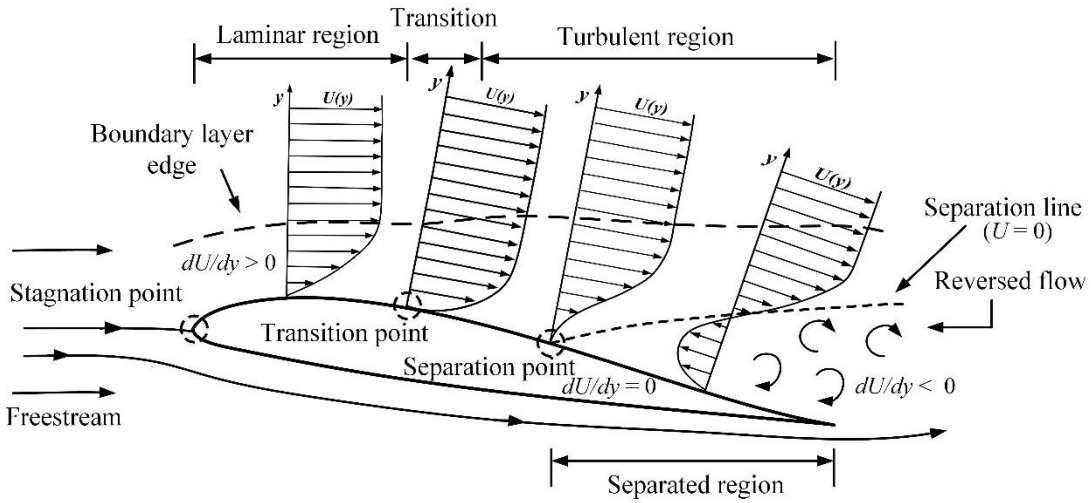

Fig. 1.7: Boundary layer characteristics over an airfoil [Gudmundsson, (2014a)]

When an airfoil experiences airflow, a thin decelerated layer of air closest to the surface of the airfoil is known as the boundary layer. In the upstream part of the airfoil, the boundary layer may be smooth and orderly, referred to as a laminar boundary layer. However, as the air continues to move over the surface, the boundary layer may become unstable and transit into a turbulent boundary layer, after which the flow may separate due to a strong adverse pressure gradient. The transition from laminar to turbulent flow is not an instantaneous process; it occurs gradually over a finite region as the flow moves along the airfoil surface. The point at which the boundary layer transition occurs is called the transition point, which depends on various factors, including surface roughness, Reynolds number, freestream turbulence, angle of attack, pressure gradient, etc. Further, adverse pressure gradient contributes a significant role to flow separation over an airfoil. An adverse pressure gradient is a situation where the pressure on the upper surface of an airfoil increases as the flow moves toward the trailing edge. This can cause the flow velocity to decrease, which in turn can lead to a thicker boundary layer. If the pressure gradient is strong enough, the flow may separate from the surface, resulting in the formation of a separation bubble or reverse flow, which it can further increase drag and decrease the lift.

The typical variation of lift coefficient (C_l) as a function of angle of attack (*AoA*) depending on the flow behavior over the airfoil is illustrated in **Fig. 1.8**. The lift generated by an airfoil at a zero angle of attack (*AoA* = 0) is a non-zero value, and the lift only decreases to zero when the airfoil is pitched to a negative *AoA*. The *AoA* at which the lift force becomes zero is referred to as the

zero-lift angle of attack ($AoA_{l=0}$). In the case of a symmetric airfoil, the zero-lift angle of attack is equal to zero degree. However, for airfoils with positive camber (camber above the chord line), the zero-lift angle of attack is a negative value. For low to moderate *AoA*, the lift coefficient varies linearly with rising angle of attack. This linear relationship between C_l and *AoA* is described by the lift slope ($C_{l\alpha}$), which represents the rate of change of lift coefficient with respect to the angle of attack. According to the thin airfoil theory for an incompressible flow, the theoretical lift-curve slope for any airfoil is 2π / radian [Anderson, (2011); Raymer, (2018)]. In the lower regime of *AoA*, the flow moves smoothly and remains attached to the majority of the surface, as sketched in the left side of **Fig. 1.8**. As the *AoA* is large, the flow tends to separate from the surface, resulting formation of recirculation or dead air zone close to trailing edge. When airfoil experiences separated flow, which usually occurs at high *AoA*, this results in a significant reduction in lift, and the lift curve becomes highly non-linear. This state of the airfoil is commonly referred to as a stall.

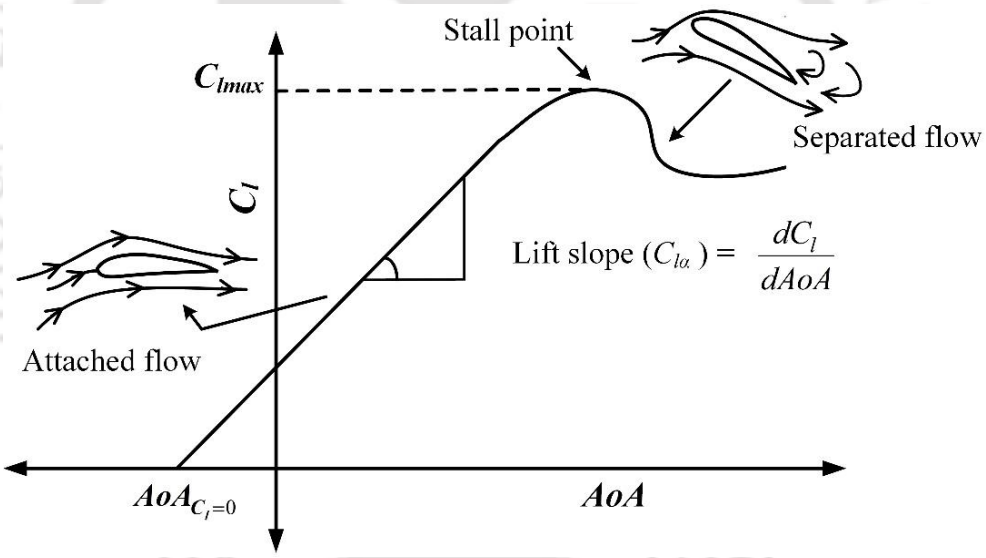

Fig. 1.8: Schematic of lift behavior with angle of attack [Anderson, (2011)]

The maximum lift coefficient (C_{lmax}), which is achieved just before the stall, is a crucial factor in the performance of an airfoil as it determines the minimum speed required to maintain lift and avoid a stall. The stalling speed of an airplane is directly related to the maximum lift coefficient of its airfoil, as a higher C_{lmax} allows the airplane to fly at a lower speed without stalling. Further, the drag coefficient (C_d) of an airfoil also increases significantly by the flow separation. The drag coefficient is a result of both skin friction drag and pressure drag (form drag). Skin friction drag is

caused by friction between the fluid and airfoil surface arising due to shear stress. At the same time, pressure drag is generated by pressure differences on opposite sides of the object due to flow separation. In a situation where the airfoil experiences a moderate adverse pressure gradient, it is not strong enough to cause flow separation. Consequently, the flow remains attached to the surface, and the drag is primarily due to skin friction drag. The contribution of pressure drag to the total drag is minimal in this case. However, when the angle of attack is high, the contribution of pressure drag becomes significant, especially during or after the stall point. As a result, the rate of increase in drag is greater at higher *AoA* than at lower angles.

The airflow characteristics around a wing are significantly different from those around an airfoil section. This is due to the three-dimensional nature of the airflow around a wing, which varies along the chord and span, as well as across the upper and lower surfaces of the wing. Both airfoils and finite wings generate lift through the creation of a pressure difference between the upper and lower surfaces of the object. However, the mechanisms behind this lift generation are slightly different. For a finite wing, the lift is generated through a combination of the pressure difference between the upper and lower surfaces of the wing and the vortices that form at the wingtips. The airflow over the upper surface of the wing is faster than over the lower surface, creating a pressure difference between the upper and lower surfaces similar to that of an airfoil. Due to this pressure difference, the high-pressure air beneath the wing flows towards the low-pressure air above the wing, which creates a circulation of air around both wingtips. This flow results in the formation of two counter-rotating vortices at the tips, commonly known as wingtip vortices which are like weak tornadoes and trail downstream of the wing. The schematic representation of flow behavior around the wing is revealed in **Fig. 1.9**. The size of such vortices depends on several factors such as including aspect ratio, angle of attack and Reynold number, etc. These vortices induce the downward component of flow velocity at the tips of the upper wing surface, called downwash. This induced downwash reduces the effective angle of attack of the wing and is responsible for a phenomenon known as induced drag. As a result of the reduction in the effective angle of attack, the finite wing produces a lower lift value and a lower lift curve slope than its airfoil section for the same Reynolds number. The theoretical lift slope ($C_{L\alpha}$) of any finite wing can be estimated using the Prandtl lifting line theory, as given by **Eq. 1.6.** Here τ is the lift efficiency factor, and the values of τ were calculated by Glauert, which vary between 0.05 and 0.25 [Anderson, (2011)].

$$C_{L\alpha} = \frac{C_{l\alpha}}{1+\left(\frac{57.3C_{l\alpha}}{\pi AR}\right)(1+\tau)} \quad \left(\frac{1}{deg}\right) \tag{1.6}$$

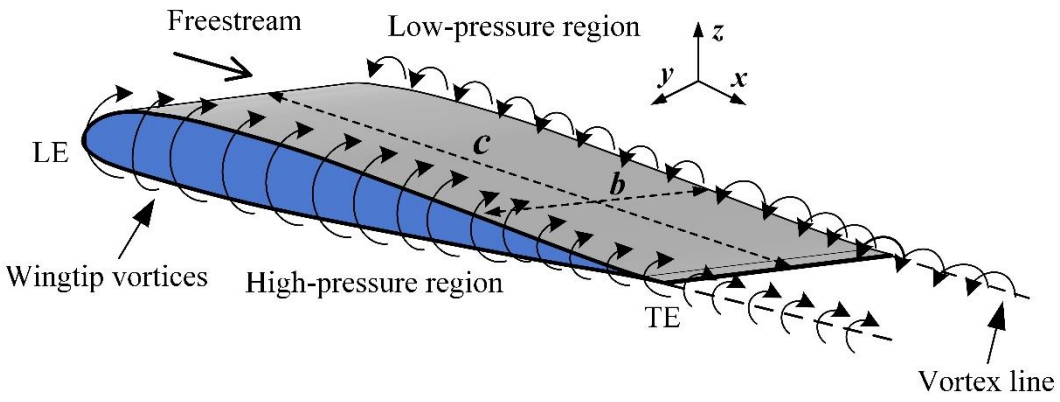

Fig. 1.9: Flow characteristics around a wing

In addition to the primary effect of reducing the lift coefficient, downwash also has a secondary effect of increasing the drag on the wing, specifically called as induced drag. Induced drag is a drag force that is generated by the lift itself and is proportional to the lift generated by the wing. Hence, the total drag for a finite wing can be broken down into three components: skin friction, pressure, and induced drag. The skin friction and pressure components are analogous to the drag experienced by an airfoil and are commonly referred to as profile drag. On the other hand, the induced drag is a result of the lift generation process and is unique to the finite wings. The total drag of the wing is shown by **Eq. 1.7,** where *AR* and *e* are the aspect ratio and Oswald efficiency factor of the wing planform, respectively. The Oswald efficiency factor is a parameter that quantifies how closely an aircraft's wing planform approaches an elliptical shape. An elliptical planform is the most aerodynamically efficient wing shape, resulting in minimum induced drag. Therefore, for elliptical planforms, *e* is equal to 1, while for other wing planforms, *e* is less than 1. For most subsonic aircraft, the Oswald efficiency factor ranges from 0.85 to 0.95, with higher values indicating a wing shape that more closely approximates an elliptical planform and therefore exhibits lower induced drag. To reduce the induced drag, designers often use winglets or other devices that reduce the size of the wingtip vortices, which in turn reduces the downwash and the

associated induced drag. The winglets help to improve the distribution of lift across the wing and reduce the drag, leading to increased efficiency and better fuel economy. In conclusion, the flow field has a significant impact on the aerodynamic performance of both airfoils and finite wings. Properly controlling and manipulating the flow can result in improved aerodynamic and flight performance.

$$C_D = C_d + \frac{C_L^2}{\pi e A R} \tag{1.7}$$

1.3 Effect of Reynolds Number on the Airfoil Performance

The Reynolds number is a dimensionless parameter that compares the magnitude of inertial force to viscous force in a fluid flow. At low Reynolds numbers, the flow around an airfoil is primarily laminar, characterized by smooth and orderly streamlines. The laminar boundary layer, adhering closely to the surface, experiences higher skin friction drag, which hampers the airfoil's performance. Laminar flow is more prone to separation, limits the maximum achievable lift and potentially causes early stalls. As the Reynolds number increases, the ratio of inertial to viscous forces grows, indicating a transition toward turbulent flow. Turbulent flow is characterized by chaotic eddies and mixing, resulting in better energy distribution along the airfoil surface and delayed boundary layer separation. This improves lift generation, and enhances overall performance. Higher Reynolds numbers offer several advantages for airfoil performance. They enable the airfoil to operate at higher angles of attack before experiencing stall, allowing for increased lift coefficients and better maneuverability. The turbulent boundary layer adheres more robustly to the airfoil surface, resulting in reduced skin friction drag and improved efficiency.

A brief survey of the Reynolds number's influence on the boundary layer behavior of airfoils was presented by Mueller, (1999). This study focused on a specific range of Reynolds numbers, ranging from 10×10^3 to 200×10^3, to investigate the flow regime characteristics. In general, when the Reynolds number falls within the range of 10×10^3 to 200×10^3, the boundary layer typically remains in laminar state, and the transition to turbulent flow becomes quite challenging. This particular flow regime is commonly observed when studying the flight of insects such as the housefly and dragonfly. Further, in the case of hand-launched sailplanes and gliders, which fly in

the range between 10×10^3 to 30×10^3, the flow within the boundary layer is completely laminar and it experiences no reattachment after separation. The Reynolds number from 30×10^3 to 70×10^3 is of major relevance to small-scaled aircraft manufacturers. Within this range, the selection of an appropriate airfoil section becomes crucial due to several factors.

One important consideration is the behavior of relatively thick airfoils (with a thickness-to-chord ratio of 10% or higher), which can exhibit significant hysteresis effects resulting from laminar separation with transitioning to turbulent flow. Additionally, at Reynolds numbers below 50×10^3, the free shear layer, after laminar separation, typically fails to transit to turbulent flow. However, thin airfoil sections (with a thickness-to-chord ratio of less than 10%) at the higher end of this Reynolds number regime can demonstrate reasonable performance characteristics. At a higher Reynolds number ($70 \times 10^3 \leq Re \leq 200 \times 10^3$), flow is laminar over an airfoil which improves its performance, but the presence of separation bubble still remains a hurdle for further performance improvement of some airfoils. For MAV designers, the Reynolds number range most commonly encountered is between 10×10^3 and 100×10^3. Several key challenges also arise in this regime. Firstly, the laminar boundary layer is highly susceptible to separation. Secondly, long laminar separation bubbles tend to form, which causes complications in the flow dynamics. Thirdly, the presence of thick boundary layer leads to increased drag and reduced maximum lift coefficients. Additionally, low Reynolds number flows exhibit sensitivity to free-stream turbulence and surface conditions. These factors collectively contribute to the nonlinear variation of airfoil performance. Moreover, the selection of airfoils is also major issue within this Reynolds number range, because, as the Reynolds number decreases below 100×10^3, the performance of conventional airfoils deteriorates rapidly in terms of their maximum lift coefficient and lift-to-drag ratio, as shown in **Fig. 1.10**. However, the performance of the simple flat plate section for changing Reynolds numbers below 100×10^3 shows higher stability than conventional airfoils, but the lift to drag ratio value is much lower than that of the airfoil. Beyond this range, for $Re > 200 \times 10^3$, the performance of the airfoil improves considerably as the size of the laminar bubble diminishes. Thus objects flying with velocities corresponding to Reynolds number below 200×10^3 encounter numerous problems, such as the formation of laminar separation bubble, bursting of the separation bubble, flow transition, hysteresis in performance parameters, vortex shedding in the wake, etc. Further, these features would have a large dependence on the Reynolds number in this flow regime. Hence,

airfoil selection and understanding of its aerodynamics within this Reynolds number range ($Re < 200 \times 10^3$) are crucial for addressing the specific challenges encountered by the flying objects.

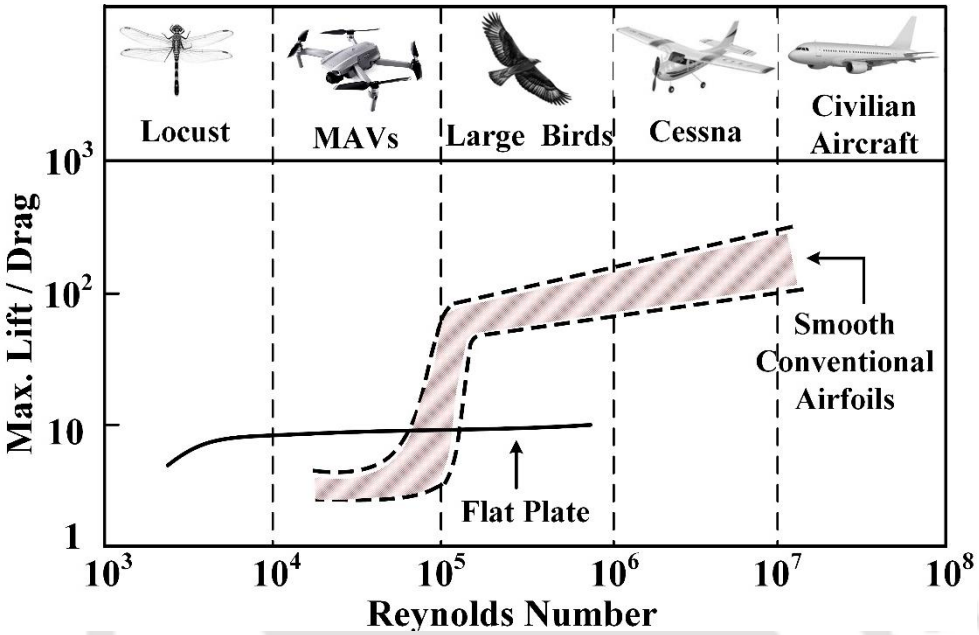

Fig. 1.10: Influence of Reynolds number on the maximum lift-to-drag ratio of an airfoil and depiction of Reynolds number ranges for various flying objects [Mueller, (1999)]

1.4 Effect of Aspect Ratio on the Wing Performance

The aspect ratio of a wing is a fundamental geometric parameter that significantly affects its performance characteristics. It plays a vital role in determining lift generation, drag, maneuverability, stall behavior, and structural loading. The understanding of how aspect ratio affects the wing performance is of utmost importance in the development of both low and high-scaled air vehicles. The choice between a low or high aspect ratio wing depends on specific design requirements. Some design scenarios favour a low-aspect-ratio wing, while others benefit from a high-aspect-ratio wing. For example, in general aviation, the aspect ratio typically falls within the range of 5 to 9, and high subsonic transport aircraft have aspect ratios ranging from 8 to 12 [Sadraey, (2013)]. On the other hand, supersonic fighter aircraft, optimized for high-speed performance, usually have lower aspect ratios between 2 and 4. An aspect ratio below 2.0 ($AR \leq 2.0$) is considered crucial for the efficient design of fixed-wing MAVs [Torres and Mueller, (2004)].

Higher aspect ratio wings have been shown to produce more lift compared to lower aspect ratio wings. This increased lift production is attributed to the larger wing surface area, allowing for more efficient utilization of the available airflow. As a result, higher aspect ratio wings are favoured in applications that require enhanced lift capabilities, such as gliders (sailplanes). Increasing the *AR* brings the aerodynamic features of a three-dimensional wing closer to those of a two-dimensional airfoil section. This is primarily due to the reduction of the influence of wing tip vortex. As the aspect ratio of a wing decreases, the strength of the wingtip vortices increases, which leads to an elevation in induced drag [Mizoguchi and Itoh, (2013)]. The increased strength of the wingtip vortices in low aspect ratio wings creates a stronger downwash, affecting the flow patterns over the wing surface. These altered flow patterns contribute to the generation of non-linear lift components. The non-linear lift generation becomes more significant as the aspect ratio decreases, resulting in a greater deviation from the linear lift predicted by potential theory. In summary, the aspect ratio of a wing has a significant impact on its performance characteristics. High aspect ratio wings generally offer increased lift production and reduced induced drag due to smoother flow patterns or weaker wingtip vortices. Usually, these are preferred in applications that require enhanced lift capabilities. On the other hand, lower aspect ratio wings experience stronger wingtip vortices, resulting in increased induced drag and more pronounced non-linear lift generation.

1.5 Overview of Flow Separation Control Devices

Flow separation control devices play a crucial role in improving the aerodynamic performance of airfoils. These devices are specifically designed to address the issue of flow separation, which occurs when the airflow over an airfoil detaches from its surface. Flow separation can have detrimental effects on the lift and drag characteristics of an airfoil, leading to reduced efficiency and stability. By implementing flow separation control devices, designers can effectively manage the airflow and prevent or delay separation. These devices come in two main categories: active and passive. Active flow separation control devices employ external mechanisms, such as jets, synthetic jets, blowing or suction, plasma actuators, etc., to actively manipulate the flow and maintain attached airflow over the airfoil surface [Baljit et al., (2017); Kim et al., (2007); Rizzetta and Visbal, (2012)]. These devices require an energy source and control system to generate the necessary flow modifications, providing real-time adjustments to optimize aerodynamic performance. On the other hand, passive flow separation control devices utilize geometric

modifications, surface textures or vortex generators, etc., to passively influence the airflow. These modifications alter the flow patterns around the airfoil, promoting better boundary layer attachment and reducing the likelihood of flow separation. Various passive methods were used to improve the performance of airfoils or wings in previous studies. These methods include the use of gurney flaps, self-actuating flaps, creating a cavity on the suction surface, and other similar techniques [Cravero, (2017); Lam and Leung, (2018); Meyer et al., (2007)]. Unlike active devices, passive devices do not require external energy sources or control systems, making them simpler and more cost-effective to implement. Although both active and passive approaches have their advantages and can be utilized based on design requirements and constraints. However, the implementation of an active strategy in small-scaled aircraft creates difficulty for the designer due to constraints of wing size, power unit as well as weight. Therefore, the current study is dedicated to explore a passive approach for addressing flow separation in low aspect ratio wings in the *Re* range of MAVs. This approach involves the utilization of self-adjusting flaps and wing-tip attachments specifically designed to improve aerodynamic performance.

1.6 Summary

Special form of unmanned aircraft, MAVs, are evolving rapidly every year due to their vast applications in civil and military sectors. Apart from these, such vehicles offer advantages in terms of transportation ease, versatility in challenging environments, and the ability to perform tasks that are difficult for larger aircraft or humans. But the aerodynamic efficiency of the wing is an important aspect in the design and development of fixed-wing MAVs. Various factors such as wing planforms, airfoil shape, aspect ratio, Reynolds number, and angle of attack significantly influence the aerodynamics of these vehicles. Since MAVs have limited wing dimensions and power input, due to which they operate within a low Reynolds number range ($10 \times 10^3 - 100 \times 10^3$). Within this Reynolds number range, the selection of airfoils is also a major issue. Because conventional airfoils experience a significant decline in performance as the Reynolds number decreases below 100×10^3. Additionally, it encounters numerous problems, such as the formation of a laminar separation bubble, bursting of the separation bubble, flow transition, hysteresis in performance parameters, etc., which affects the airfoil performance. Furthermore, understanding the effects of Reynolds number and aspect ratio is crucial for maintaining stable flight and efficient operation. By addressing these factors, designers can enhance the aerodynamic efficiency of fixed-wing MAVs, leading to improved flight performance and maneuverability.

1.7 Organisation of the Thesis

The thesis is structured into eight chapters to address the objectives of the present study effectively. **Chapter 1** presents a brief overview of MAVs and discusses the relevant parameters that affect the aerodynamics of these vehicles. These parameters include airfoil shape, wing planform, Reynolds number, aspect ratio, etc. Finally, the chapter introduces flow separation control techniques specifically for fixed wing aircraft. **Chapter 2** focuses on the comprehensive review of existing literature relevant to the present study. This chapter has three major sections; the first section provides a general overview of how the performance characteristics of airfoils are affected by variations in Reynolds number. The remaining two sections include an analysis regarding the performance of the low aspect ratio wing in the low Reynolds number regime and an exploration of passive flow separation control techniques. The chapter concludes with a literature summary and a clear presentation of the thesis objectives. **Chapter 3** describes the experimental setup and methodology used to achieve the research objectives. **Chapter 4** includes an investigation to explore the performance and vortex-shedding characteristics of S5010 and E214 airfoils for various Reynolds numbers. **Chapter 5** focuses on studying the effect of aspect ratio and Reynolds number on the performance of low aspect ratio wings based on airfoils viz. S5010 and E214. **Chapter 6** explores the feasibility of a self-adaptive movable flap for low aspect ratio wings and explores flap effectiveness in various aspects, including flap span, chord length, and chord-wise placement. **Chapter 7** deals with understanding the effect of different types of wingtip attachments on the performance of low-aspect-ratio wings. **Chapter 8** concludes the present study and outlines future investigations related to optimizing the aerodynamic design and performance of fixed-wing MAVs.

CHAPTER 2

Literature Review

Overview

The current chapter focuses on the comprehensive review of existing literature relevant to parameters that affect the aerodynamics of MAVs. This chapter has three major sub-sections; the first sub-section provides a general overview of the impact of Reynolds number variations on the performance of airfoils. The remaining two sub-sections include an analysis regarding the performance of the low aspect ratio wings in the low Reynolds number regime and an exploration of bio-inspired passive flow control techniques. The discussion of flow control techniques covers the research domain of self-actuating flaps and wingtip attachment devices, which draw inspiration from natural systems. Finally, the summary of identified literature gaps and the objective of the thesis are briefly outlined.

2.1 Review of Reynolds Number Effects on Airfoil Performance

A thorough literature review has been conducted to gain insights into the influence of Reynolds number (*Re*) on airfoil performance. This review focuses on the aerodynamic features which are encountered at different *Re* ranges, particularly in the context of MAVs. Numerous studies were undertaken in this research domain, and a selection of these studies is presented below.

Schmitz, (1967) investigated the aerodynamic behavior of three airfoils or cross sections viz. thin flat plate (*t/c*: 2.9%), cambered plate (*t/c*: 2.9%, *m/c*: 5.8%), and N60 (*t/c*: 12.41%, *m/c*: 4%) at $2 \times 10^4 \leq Re \leq 2 \times 10^5$. The results showed that the C_{lmax} of N60 airfoil decreases rapidly with decreasing *Re* below 100×10^3, whereas flat and curved plates were less affected by changing *Re*. Hence, thin flat and camber plates showed better aerodynamic performance as compared to N60 airfoil for *Re* below 100×10^3.

McMasters and Henderson, (1979) presented a survey of airfoil performance as a function of *Re* based on existing experimental data for conventional airfoils at various *Re*s. The findings of this study showed that as the *Re* decreases below 100×10^3, the performance of smooth airfoils, characterized by their C_{lmax} and $(C_l/C_d)_{max}$ ratio, deteriorates rapidly. Conversely, the performance of a simple flat plate section demonstrated greater stability within this *Re* range, although exhibiting lower values of C_{lmax} and $(C_l/C_d)_{max}$ compared to the airfoil operating at the same *Re*.

Carmichael, (1981) provided a brief description of the variation in flow phenomena of an airfoil with the influence of *Re*. Especially for $Re < 50 \times 10^3$, the flow near the surface experienced insufficient inertia or momentum to counteract adverse pressure gradients beyond a certain limit. As a result, the flow direction reversed and separated from the surface without reattachment prior to the trailing edge, leading to a significant decrease in lift and a substantial increase in drag. For $Re > 50 \times 10^3$, the separated laminar boundary layer underwent transition to turbulent and reattached as a turbulent boundary layer before reaching the trailing edge. This phenomenon took place within a specific region known as a laminar separation bubble (LSB), which holds significant significance within the *Re* range of 50×10^3 to 4000×10^3.

Mueller and Batill, (1982) conducted experimental investigations on a NACA 663-018 airfoil to explore the boundary layer phenomena, including laminar flow, transition to turbulent, and reattachment close to the leading edge for *Re* from 40×10^3 to 400×10^3. Further investigations

were carried out involving the implementation of distributed surface roughness near the leading edge of the airfoil. The study employed a low-speed wind tunnel, incorporating smoke visualization techniques to observe and analyse the flow structures. The experimental findings revealed that as the *Re* decreased, the length of the LSB increased, particularly showing a stronger dependence on the angle of attack *(AoA)* at $Re < 250 \times 10^3$. The laminar separation bubble exhibited a similar effect to that of surface roughness at high *AoA*. It played a facilitating role in transitioning the boundary layer and maintaining attachment of the flow at higher *AoA*. While the lift characteristics exhibited little disparity between the two scenarios (smooth and rough), the drag data revealed higher values for the airfoil with surface roughness.

Mueller, (1985a) explored the behavior of Lissaman 7769 and Miley M06-13-128 airfoils for *Re* range from 70×10^3 to 600×10^3. They observed hysteresis effects in the lift and drag measurements at high *AoA* for $Re < 300 \times 10^3$. As per their conclusion, the presence of hysteresis can be attributed to several factors, including the development of flow separation, reattachment of the separated flow, and transition between laminar and turbulent boundary layers. But these flow features are influenced by factors such as airfoil shape, *Re*, and surface roughness. It was noted that the size of hysteresis loop decreases with increasing *Re*.

O'Meara and Mueller, (1987) did experiments for NACA 66_3-018 to investigate the behavior of LSBs at different low *Re* ($50 \times 10^3 \leq Re \leq 200 \times 10^3$). They observed that as the chord *Re* is increased, the separation bubble becomes shorter in thickness due to early transition, and the separation angle decreases. This reduction in the separation angle indicated an improved ability of the airfoil to delay or mitigate flow separation. In addition to the *Re* and freestream disturbance, it was noted that the change in *AoA* also had an effect on the separation bubble characteristics. When the *AoA* was increased from 8° to 10°, it resulted in the forward movement of the laminar separation point. However, this change did not have a significant impact on separation bubble length. In contrast, with a further increase in *AoA* (*AoA>10°*), the separation bubble moved forward once again and exhibited an increase in length. At a particular *AoA*, the separation point remained unchanged over the entire range of *Re*.

Selig et al., (1996a) conducted experiments to measure the performance of 34 airfoils. The purpose of this study was to establish a comprehensive database that could be used in design studies related to low-speed vehicle applications. For symmetric airfoils at $Re = 40 \times 10^3 - 100 \times 10^3$; they

observed that the lift slope value is initially less than the theoretical slope of 2π, which then increases, and eventually returns to more expected linear behavior before reaching the stall point. The peculiar lift characteristics observed in symmetrical airfoils at low *Re* can be attributed to the behavior of LSBs on the upper and lower surfaces and their varying sizes with changes in *AoA*. As the *AoA* increased, the pressure gradient on the upper surface became steeper, resulting in the enlargement of the upper surface bubble. This larger bubble increased the displacement thickness, effectively introducing negative camber. On the other hand, the pressure gradient on the lower surface became more favourable, causing the shrinkage of the lower surface bubble. As a result, the displacement thickness decreased on the lower surface, introducing more negative camber. This negative camber, in addition to the non-cambered airfoil, reduced the lift compared to what would have been expected without considering the effects of LSBs. The lift curve exhibited hysteresis loops, which were influenced by the size of the LSB. These findings showed that certain airfoils displayed both counter clockwise and clockwise hysteresis loops at specific *Re*. Additionally, the occurrence of either type of loop first depended on the particular characteristics of the airfoil.

Mueller, (1999) presented the boundary layer behavior of airfoil for flow regime from $10 \times 10^3 \leq Re \leq 200 \times 10^3$. This study was an extension and modification of Carmichael's previous work (1981). Within the *Re* range of 10×10^3 to 30×10^3, the boundary layer remained entirely laminar, and triggering a transition to turbulent proved to be quite challenging. For *Re* of $30 \times 10^3 \leq Re \leq 70 \times 10^3$, the selection of an airfoil section was crucial, particularly for the thick airfoils (with thickness ratios of 10% and above). These airfoils can experience significant hysteresis effects attributed to the occurrence of laminar separation and the subsequent transition to turbulent flow. Additionally, the LSBs were observed on the upper surface of most airfoils for $Re \geq 50 \times 10^3$. On the other hand, thinner airfoil sections ($t/c < 10\%$) at the upper end of this range were inclined to demonstrate more satisfactory performance. In the range of *Re* above 70×10^3 and below 200×10^3, there was a possibility of achieving extensive laminar flow, resulting in improved airfoil performance. However, some airfoils faced challenges due to the presence of a LSB within this range. There was a notable improvement in airfoil performance for $Re > 200 \times 10^3$.

Burgmann et al., (2006) employed particle image velocimetry (PIV) to examine the spanwise structure and dynamics of vortices within a LSB of SD7003 airfoil at the *Re* range of $20 \times 10^3 \leq$

Re ≤ 60 × 10^3. During the investigation, it was found that the downstream region of the separation bubble exhibited the development of large vortex rolls in a quasi-periodic manner. These vortex rolls had a convex shape and extended spanwise for approximately 10 – 20% of the airfoil chord. Furthermore, the spanwise pattern of these vortices was observed to be irregular. The behavior of the local separation bubble involved different intricate phenomena. The progression of events appeared to initiate with an initial instability, characterized by the vortices within the laminar separation region. This instability gave rise to the formation of a distinctive convex patterns. As the process unfolded, the vortices grew in strength and size, eventually culminating in the abrupt burst of the vortex and influencing the flow field of the upstream side.

Hu and Yang, (2008) examined the transient characteristics of LSB on a NASA low-speed GA (W)-1 airfoil at *Re* of 70 × 10^3 using PIV. The analysis of surface pressure and PIV measurements provided clear evidence of LSB on the airfoil surface. When the *AoA* exceeded 8°, the upper surface of the airfoil experienced an increasingly adverse pressure gradient, resulting in the separation of the laminar boundary layer. This separated laminar boundary layer then quickly transitioned to turbulence, characterized by the formation of unsteady Kelvin-Helmholtz vortex patterns. As the turbulence transition occurred, the separated shear layer was reattached to the airfoil surface, forming a turbulent boundary layer. This reattachment took place at *AoA* < 12°, creating a laminar bubble on the airfoil. As the transition from laminar to turbulent flow occurred, there was a marked rise in the Reynolds stress within the flow region. Once the separation bubble formed, the rate of increase in lift coefficient decreased significantly, while the drag coefficient increased more rapidly with higher *AoA*. Ultimately, the separation bubble did suddenly burst, causing the occurrence of an airfoil stall when the adverse pressure gradient exceeded a certain limit at typically *AoA* above 12°.

Gerakopulos et al., (2010) investigated the variation of lift slope curve as a function of boundary layer characteristics and *AoA* in the *Re* range of 80 × 10^3 to 200 × 10^3 for NACA0018 airfoil. The analysis revealed the presence of two separate regions within the lift curves, which were distinguished by the movement of the separation bubble near the leading edge of the airfoil with increasing *AoA*. The Region I exhibited a rapid and linear increase in lift coefficients at lower *AoA*, while Region II displayed a gradual and linear rise at higher angles before the stall point. In both regions, a linear variation in the C_l with *AoA* was detected. However, Region I exhibited a lift slope

that was four times greater than that of Region II. When the *Re* was increased during investigations, Region I extended to higher *AoA*, while the expansion of Region II remained unchanged but its position shifted towards a higher *AoA*. The slope of Region I was reduced with increasing *Re*, whereas the slope of Region II remained unaffected by *Re*. The findings also revealed a proportional relationship between the advancement of the separation (S), transition (T), and reattachment (R) locations towards the leading edge and the rate of change in the lift curve slope as the *AoA* increased within each region. The lift curve in Region I exhibited a higher slope, indicating a more rapid progression of the S, T, and R positions to the leading edge. In Region II, the lift curve revealed a lower slope value, signifying a slower progression of the S, T, and R points.

Bai et al., (2016) performed unsteady numerical simulations and a PIV flow visualization in a water tunnel to explore the flow structure variation with *AoA* of symmetric airfoil SD8020 at *Re* = 40×10^3. They explained the comprehensive overview of time-averaged structures of two distinct types of LSBs, specifically the long laminar separation bubble (LLSB) and the trailing-edge laminar separation bubble (TLSB). The LLSB exhibited a "bump" shape on the top surface of the airfoil, while TLSB appeared as a "stick" attached to the trailing edge. As the *AoA* increased, the LLSB exhibited a movement of the separation point upstream, accompanied by a reduction in the size and length of the bubble. As the *AoA* increased, the TLSB demonstrated a similar upstream movement of the separation point, but the bubble expanded in size and length. The alteration between these two types of LSBs actually generated the nonlinear effects of the lift coefficient at low *AoA* with low *Re*, resulting in sudden changes in the corresponding profiles of the airfoil.

Winslow et al., (2018) conducted computational investigations on numerous airfoils to analyse the performance and flow field for the *Re* range between 10×10^3 and 100×10^3. The airfoils analysed in the study included NACA0009, NACA0012, Clark-Y, flat plate section (*t/c* = 1,3 and 5%), and cambered plates (*m/c* = 3, 6, and 9%). When the *Re* decreased, there was a noticeable rise in drag observed for airfoil NACA0012, primarily due to the occurrence of premature flow separation and the inability of the flow to reattach. Consequently, this led to a narrowing of the drag bucket, and a significant drop in the lift. As the thickness of flat plate reduced from *t/c* = 5% to *t/c* = 1%, both lift and drag coefficients were improved. In addition, the study demonstrated that increasing camber from *m/c* = 3% to 9 % of flat plate (*t/c* = 1%), led to a rise in both the lift and

the lift-to-drag ratio compared to flat plate section of the same thickness. This investigation also included the camber effect on NACA series airfoils (NACA 0003, 2403, 4403, 6403) over the *Re* range of $20 \times 10^3 \leq Re \leq 100 \times 10^3$, found a similar camber effect on the airfoil performance as seen for a flat plate. Further, they examined the distinction of boundary layer characteristics for thin flat plates and thicker airfoils at $Re < 50 \times 10^3$. Especially, the NACA0012 airfoil was more prone to trailing edge separation. In contrast, the flat plate experienced leading edge separation, allowing for more effective reattachment in the downstream region. The attachment of the upper boundary layer helped to maintain lower surface pressure, resulting in the flat plate generating a greater lift compared to the NACA 0012 airfoil at lower *Re*.

Xia et al., (2021) presented a comprehensive review of the influence of *Re* on airfoil performance based on previous studies. They concluded that airfoil performance decreases rapidly with decreasing *Re* and observed non-linear lift variation in the lift curve at lower *AoA*. Hysteresis was common in the measurements of aerodynamic coefficient for most conventional airfoils at low *Re*. Based on the directions, the hysteresis loop was categorized as clockwise and counterclockwise. The stall hysteresis, characterized by a clockwise loop, was typically observed when the airfoil reached its maximum lift coefficient. This phenomenon occurred when the lift coefficient suddenly decreased as the *AoA* was increased beyond a certain point and the LSBs fully detached from the airfoil surface. Conversely, when the *AoA* was reduced, the reattachment of the LSBs did not occur immediately. Instead, it required a decrease in the *AoA* before the lift coefficient experienced a sudden increase. A counterclockwise hysteresis, known as pre-stall hysteresis, was observed within the mid-lift range. Initially, as the *AoA* was increased, a long bubble was formed which grew larger and eventually merged with the wake. This led to a stable lift coefficient. With further increases in the angle of attack, the bubble transitioned into shorter bubbles and moved towards the trailing edge, resulting in a significant increase in the lift coefficient. As the *AoA* was continued to increase, the bubble moved closer to the leading edge and was shortened even more, causing a further increase in the lift coefficient. However, when the *AoA* was decreased, the short bubble remained attached until a smaller angle of attack was reached. At this point, the lift coefficient sharply reduced, forming a counterclockwise hysteresis loop.

2.2 Review of the Influence of Aspect Ratio on the Wing Performance

Extensive research has been carried out to investigate the effect of aspect ratio (*AR*) on wing performance at low *Re* ranges. Some of the studies done in this research area is presented below.

Marchman et al., (1985) performed a wind tunnel test to investigate the effect of *AR* on the wing performance in the *Re* range from 50×10^3 to 500×10^3. The Wortmann FX63-127 airfoil section was selected for the experiments, and models with different *AR*s, including 4, 6, 8, and 10, were tested to assess their aerodynamic characteristics. As the *Re* or *AR* was increased, the slope of the lift curve and maximum lift coefficients showed an upward trend. With the reduction in *AR*, the drag coefficient also reduced. Furthermore, the size of the hysteresis loop decreased with an increase in *AR*.

E. V. Laitone, (1997) measured aerodynamic forces acting on the wing of section NACA0012 and compared them with thin flat plates as well as a cambered plate (t/c = 1.3%, m/c = 5%) for *Re* below 70×10^3. The analysis of these measurements revealed that the performance of the NACA0012 airfoil experiences more significant variation with changing *Re* below 50×10^3 or increase in free stream turbulence level. At the same time, the cambered flat plate exhibited minimal variations in aerodynamic performance with *Re* or turbulence level. For the $Re < 70 \times 10^3$, the thin cambered flat plate wing showed a higher C_L/C_D ratio and C_L at all *AoA* than the other tested wing models.

Pelletier and Mueller, (2000) presented an analysis of aerodynamic performance of low *AR* flat and cambered plate wings (t/c = 1.93%, $0.5 \leq AR \leq 3.0$) for *Re* range from 60×10^3 to 200×10^3. The models used in the study had two different configurations: one with a 5-to-1 elliptical leading edge and a 3° tapered trailing edge, and the other with a 5-to-1 elliptical leading edge and trailing edge. The rounded arc shape with 4% camber was configured for a cambered plate wing, and this model offered higher performance than the flat wing. However, the trailing edge geometry and free stream turbulence showed negligible effects on the wing performance. When the *AR* was reduced, a decrease in the slope of the lift curve and an increase in the stall angle were observed. The effect of changing *AR* was not strongly observed on the drag coefficient at $Re = 80 \times 10^3$. As the *Re* is increased, wing performance in terms of C_{Lmax}, and $(C_L/C_D)_{max}$ were improved. No hysteresis was noticed in the measurement of forces and moment.

Torres and Mueller, (2001) explored the aerodynamic behavior of different wing planforms (rectangular, Zimmermann, inverse Zimmermann & elliptical) in the range of *Re* from 70×10^3 to 140×10^3. All models employed had flat plate sections without any camber (*t/c* = 1.96 %, *m/c* = 0%), and *AR*s of planforms were 0.5, 1.0, and 2.0. Both the leading and trailing edges of each model had a 5 to 1 elliptical curvature. The findings demonstrated that as the *AR* was decreased, the C_L-curve exhibited a more non-linear variation in lift, and the corresponding stall point increased. Furthermore, the value of the lift slope improved as *Re* was increased. For $AR \leq 1.0$, rectangular and inverse Zimmermann planforms offered better aerodynamic performance than the other two planforms at $Re = 100 \times 10^3$.

Torres and Mueller, (2004) extended their previous work (Torres and Mueller, 2001) with the same test models to explore the influence of distinct wing planforms and *AR* on the wing performance at *Re* between 70×10^3 and 200×10^3. Herein, the *AR* of each planform was varied from 0.5 to 2.0 with an increment of 0.25. The lift-curve demonstrated a more pronounced non-linear variation, especially for $AR \leq 1.25$. Also, such low *AR* wings showed higher C_{Lmax} and corresponding stall angle values than $AR \geq 1.25$. Among all wing planforms examined, the inverse Zimmermann configuration was identified as the most efficient compared to others for $AR \leq 1.0$ and high *AoA*. However, for high *AR*, the elliptical wing planforms were found to exhibit more advantageous characteristics. Hysteresis was not observed in any of the measurements conducted in this study. The absence of hysteresis was attributed to the low thickness-to-chord ratio of the wings investigated.

Cosyn and Vierendeels, (2006) conducted simulations to study the characterization of wingtip vortices and their influence on the performance of low *AR* wings at $Re = 100 \times 10^3$. These simulations focused on two different wing profiles, namely the flat plate (*t/c* = 1.96%) and S5010, with various *ARs* ranging from 0.5 to 2.0. The flat plate wing had a leading edge designed with a 5-to-1 elliptical curvature and a sharp trailing edge. They observed that as the *AR* was increased, the strength of tip vortices reduced, while the influence of bound vortices within the flow domain became more pronounced. At each corresponding *AR*, the lift curve exhibited nearly identical characteristics for both the flat plate and the profiled wing, with the exception of the stall point. The flat plate experienced an earlier stall compared to the profiled wing. Moreover, the drag curve

showed similar values at low *AoA* for both the S5010 wing and flat plate. However, at higher *AoA*, the S5010 wing demonstrated lower drag compared to the flat plate.

Okamoto and Azuma, (2011) investigated the impact of *Re* and aspect *AR* on the performance characteristics of different wing planforms, including rectangular, triangular, and elliptical shapes at *Re* order of 10×10^3. All the wing planforms had thin rectangular flat plates with flat leading and trailing edges. The *AR* of all models varied from 0.5 to 8.0. In this flow regime, the lift curve exhibited non-linear lift variation with *AoA* at low angles even for higher *AR* wing. The effect of *Re* on the wing performance was less significant for all the test models except triangular planforms of $AR \leq 2.0$. A reduction in the *AR* was observed to decrease the slope of the lift curve. Whereas the C_{Lmax} of $AR = 1.0$ was found to be 1.5 times higher than $AR \geq 2.0$ for rectangular and elliptical wing planforms. In the case of triangular planform, the C_{Lmax} of $AR = 2.0$ was higher than that of higher *AR* ($AR > 2.0$).

Ananda et al., (2012) presented the experimental investigations of Wortmann FX 63-137 rectangular wing ($AR = 4.0$), tapered and flat plate ($2.0 \leq AR \leq 5.0$) wings at *Re* range of $60 \times 10^3 \leq Re \leq 160 \times 10^3$. The results showed that there exist a critical *Re* ($Re = 90 \times 10^3$) at which the C_L and *L/D* ratio increased significantly for the profiled wing. At $Re < 90 \times 10^3$, the separated shear layer did not have enough energy to generate a laminar separation bubble, leading to the absence of turbulent flow transition and reattachment to the wing. Hysteresis was also detected in both pre and post-stall regions for the profiled wing at $Re = 90 \times 10^3$. In the case of taper and flat plate wings, no critical *Re was* found within the tested *Re* range. The flow did not reattach to the surface resulting in the absence of a separation bubble for these test conditions. Furthermore, no hysteresis was noticed in the aerodynamic measurement of taper and flat plate wings.

Anyoji et al., (2013) examined the aerodynamic properties of three different wing planforms, namely triangular, rectangular, and elliptical wings, with an *AR* of 4 in a low *Re* flow regime of 5×10^3 to 60×10^3. All wing models had flat plate sections with blunt leading edges, and the thickness-to-chord ratio was 3.0 %. The lift curve slope of elliptical and rectangular wings was found to be independent of *Re*. In contrast, for the delta wing, the lift slope decreased as *Re* decreased. When the aerodynamic performance of each planform was compared at a given *Re*, it was observed that the lift slope of the rectangular and elliptical wings was almost the same, and both were higher than that of the delta planform. However, the delta wing revealed a stall angle

twice as high as that of the elliptical and rectangular wings. The $(L/D)_{max}$ characteristics of the wing reduced with a decrease of *Re*, which was consistent across all wing planforms.

Mizoguchi and Itoh, (2013) explored the aerodynamic characteristics of two different leading edge geometry of flat plate wings for *Re* order of 10×10^3. Two wing configurations were considered in the study: one with a flat leading edge and the other with a blunt leading edge. The *AR* of the wings was varied from 0.5 to 6.0, while the thickness-to-chord ratio was maintained at 0.033 for all *AR*s except for *AR* 6.0. The effect of *AR* on the wing performance was found to be less pronounced for wings with $AR \geq 3.0$. However, for wings with $AR < 3.0$, the aerodynamic behavior was noticeably different compared to higher *AR* wings due to wingtip vortices. The effect of these vortices increased with a decrease in *AR*. For $AR \leq 1.0$, a significant increase in the stall angle and C_{Lmax} were observed. Additionally, hysteresis was also observed near the stall point, specifically in the case of $AR = 1.0$. This study also revealed that the performance characteristics of flat plate wings remained unaffected by changes in *Re* or variations in the leading edge shape within the *Re* range of 10×10^3 to 100×10^3.

Mizoguchi et al., (2014) demonstrated the influence of thickness ratio, freestream turbulence intensity, and *Re* on the performance and hysteresis behavior of rectangular flat plate wings with *AR* of 1.0. In this study, the wing models had flat leading and trailing edges. The thickness of the plate was varied between 1 mm and 9 mm, and the turbulence intensity of the tunnel ranged from 0.2% to 2.7%. While the *Re* was varied in the range of 10×10^3 to 150×10^3. At low *AoA*, the effect of thickness ratio on the C_L was found to be less significant. However, C_L showed dependency on the thickness ratio at high *AoA*. It was observed that the vortical lift component of the wing decreased with an increase in the thickness ratio. At the same time, the potential lift component remained unaffected by the thickness ratio, even at high *AoA*. Overall, the aerodynamic performance of the wing reduced as the thickness ratio was increased. However, as the thickness ratio was increased, the size of the hysteresis loop decreased. Furthermore, the influence of turbulence intensity on the wing performance was noticed to be negligible. However, the hysteresis region was enlarged with reducing in turbulent intensity. The influence of *Re* on the C_L was observed to be minimal for changing $Re \geq 25 \times 10^3$. The hysteresis region was found to increase with an increase of *Re*. Thus, the influence of turbulence intensity and *Re* on the hysteresis loop exhibited contrasting effects.

Ananda et al., (2015) conducted an experiment to examine the low *Re* aerodynamics for flat plate wings with low to moderate *AR and* varying taper ratio at *Re* ranging from 60×10^3 to 160×10^3. The tested wing configurations had *AR* of 2, 3, 4, and 5, along with varying taper ratios of 0.5, 0.75, and 1.0. The results revealed that the variation of C_{Lmax} with *AR* was observed to be minimum for *AR* > 2.0. The Oswald efficiency factor of the flat plate was found to be more sensitive with *AR;* it decreased with an increase in *AR*. Furthermore, the slope of lift curve increased as the *Re* was increased, while the taper ratio had minimal impact on it. No significant advantages were observed in terms of the use of tapered low-to-moderate *AR* wings at low *Re*. For the tested *Re,* no hysteresis was observed in the aerodynamic measurement of all models.

Mizoguchi et al., (2016) performed a study to understand the influence of *AR* on the stall and hysteresis behavior of low *AR* flat plate wing at *Re* of 52×10^3. The model had a flat shape of leading and trailing edges, and *AR* was varied from 0.5 to 1.5 with an increment of 0.1. When *AR* was decreased towards unity, both C_{Lmax} and associated stall angle increased significantly. The dependence of the *L/D* characteristics on the *AR* of the wing was more pronounced at low *AoA*, whereas this dependence diminished at high *AoA*. Hysteresis near the stall was also observed for the *AR* range between 0.7 and 1.2. Further, the size of the hysteresis region was found to be large for an *AR* close to 1.0.

Gutierrez-Castillo et al., (2021) performed experiments to investigate the lift curve slope of rectangular flat plate wings with various *AR* (*AR* = 1, 2, 4, 8) in low to moderate *Re* flow regime ($40\times 10^3 \leq Re \leq 200 \times 10^3$). The finding revealed that the lift slope increased with an increase in both *AR* and *Re*. However, the influence of *Re* was found to be minimal for low *AR* wings. They proposed a correlation for lift slope as a function of both *AR* and *Re,* which can predict lift slope with an uncertainty of less than 5%. This correlation consisted of two parts: the first part exhibited lift slope based on finite wing characteristics, which closely matched the predictions of Prandtl's lifting line theory. At the same time, the second part revealed dependency on *Re* only. This relationship predicted precise results, even beyond the range of *AR* values studied.

2.3 Review of the Passive Flow Control Devices and Their Applications

This section delves into the extensive literature on passive flow control methods, specifically drawing inspiration from the flight mechanics of birds. In particular, it focuses on two notable techniques: self-actuating flaps and wingtip slots. Self-actuating flaps, inspired by the natural movements of a bird's covert feathers during flight, offer a hopeful approach to manipulate the airflow around the wing surface. By employing flexible materials and strategic positioning, it is expected to adjust to a position that optimizes lift, reduces drag, and increases overall maneuverability. Wingtip slots, another fascinating aspect of avian-inspired flow control, involve the addition of specialized devices or structures at the tips of wings. These attachments, designed to mimic the features observed in birds, can significantly impact the aerodynamic behavior of the wing. There are many studies conducted in this research area, and the selection below presents a glimpse of these studies, showcasing their key findings and contributions to the field.

2.3.1 Survey of Self-Actuating Flap Based Studies

Bechert et al., (1997) conducted a comprehensive survey on the structure and characteristics of the skin of various animals, focusing on their influence on fluid flow. The study also explored various approaches inspired by animal surface structures that had been utilized to mitigate wall shear stresses and boundary layer separation. One example discussed in the study was the behavior of a bird's covert feathers, which exhibited effective flow control properties in situations such as landing or flying at high *AoA*. These covert feathers, located on the leading edge of the bird's wing, played a crucial role in regulating airflow and preventing boundary layer separation. In this study, a thin plastic sheet with a thickness of 0.35 mm, simulating the structure of a bird's covert feather, was tested on the glider airfoil HQ17 at *Re* of 1250×10^3. The flap, with a chord size of $0.12c$ and positioned slightly upstream from the airfoil trailing edge ($\geq 1\%$), was initially tested in its simple solid form. However, the results did not demonstrate any significant beneficial effect on the airfoil performance. As a result, the flap design was subsequently modified to incorporate a porous surface and a jagged trailing edge. This flap configuration exhibited improvement in C_{lmax} by 10% than the reference airfoil. When the flap size was increased to $0.22c$, an even greater enhancement of 18% in C_{lmax} was observed. However, further increasing the flap size beyond this point did not provide any additional advantage. Therefore, the optimal flap size for achieving the maximum C_{lmax} enhancement was determined to be $0.22c$ in this study.

Bramesfeld and Maughmer, (2002) performed experiments to explore the performance characteristics of airfoil S824 considering the presence of single and double flap configurations at *Re* of 1000×10^3. The flap used in the experiments was constructed from a Mylar sheet of thickness 0.35 mm, and its chord length was 0.09*c*. For a single flap configuration, the flap was positioned at 0.86*c* from the leading edge. While in the case of double flaps model, the flaps were located at 0.7*c* and 0.86*c*. Both the flap configurations exhibited almost the same improvement in lift curve, showing 18-20% higher C_{lmax} compared to clean airfoil. The deployment of the flap resulted in a pressure recovery at high *AoA*, causing the pressure at the trailing edge to be slightly higher than that of the clean airfoil. However, the flap device acted as a pressure dam by preventing the spread of adverse pressure effects on the upstream side of the flap and allowing for lower pressure in the upstream area. The lift enhancement was a result of the reduction in pressure in the front region of the flap. Further, the drag coefficient was found to be a higher for flapped wing than the reference wing in the pre-stall region.

Schatz et al., (2004) extended the flap study conducted by Bechert et al. (1997) using the same airfoil and flap configuration in the *Re* range of 1000×10^3 to 2000×10^3. They carried out 2D numerical studies for the airfoil HQ17 with two different flap configurations, namely fixed and freely movable flaps, to optimize the flap deflection angle. The optimum deflection angle of the flap was achieved when the separated shear layer just touched the flap edge. In the case of low deflection angles, the flap remained within the reverse flow regime, which resulted in a divided flow that was less effective for improving performance. Conversely, at higher flap angles, the flap acted as a spoiler, reducing lift generation and increasing drag. The static-flapped wing showed lower C_L than the un-flapped wing in the pre-stall region. Whereas for higher post-stall angles, it exhibited a higher C_L than the clean wing. On the other hand, the freely movable flap arrangement displayed a similar lift curve to that of the clean wing in the pre-stall angle, but at post-stall angles, it demonstrated a higher C_L than the un-flapped configuration.

Kernstine et al., (2008) tested various passive flap configurations for NACA 2412 airfoil to optimize the flap material, chord size, and chord-wise placement within the *Re* range of 100×10^3 to 500×10^3. The study revealed that the flap material should be flexible and follow the airfoil curvature, thereby preventing premature separation at low *AoA*. In the case of rigid flaps, premature separation in specific regions was observed at low *AoA*, which led to a reduction in lift.

Additionally, the thickness of the flap material played a significant role in determining the flap's effectiveness. Thicker flaps created a protrusion on the wing surface, which disrupted the flow and caused the flow to separate early, resulting in reduced lift. Moreover, the flap chord sizes ranging from 0.1*c* to 0.4*c* were found to produce beneficial effects. Flap locations near the leading edge were noted to be unproductive, showing a loss of lift even at high post-stall angles. However, the placement of the flap between mid-chord to trailing edge did not demonstrate loss in lift at high *AoA*.

Schlüter, (2010) carried out experiments in a water tunnel to investigate the effectiveness of a passive flap on various airfoils in a low *Re* flow regime of 30×10^3 to 40×10^3. This study focused on three airfoils: NACA0012, NACA4412, and SD8020. The flap was fabricated using carbon fiber material, which had a total weight of approximately 5 g. All flapped wing configurations exhibited the same lift curve as the corresponding base airfoil in the pre-stall region. However, in the post-stall region, higher lift and smoother stall behavior was observed for the flapped wings. The flap positioned at 0.6*c* with a size of 0.2*c* provided better improvement in performance than other locations, which was the same for all airfoils. Further, increasing the flap chord size from 0.2*c* to 0.4*c* did not offer any beneficial effect on lift compared to the smaller flap size. It was also noticed that the inclusion of an additional flap near the trailing edge did not yield significant advantages compared to the single flap configuration.

Wang and Schlüter, (2012) focused on the use of a self-activated flap for the rectangular finite wing of profile SD8020 to analyze the 3D flow effects on the flap dynamics for the *Re* range of 40×10^3 to 60×10^3. They tested numerous flaps with variations of flap span lengths (1*b*, 0.8*b*, 0.6*b*, and 0.4*b*) for different chord sizes (01*c*, 0.2*c* and 0.3*c*) and positions (0.5*c*, 0.6*c*, 0.7*c*, 0.8*c*, and 0.9*c*) It was observed that wingtip vortices influenced the movement of the flaps in the case of full-span flaps (1*b*), due to which it did not provide any positive effect on the performance. As the length of the flap span decreased, the effect of these tip vortices on the flap mechanism decreased. The best improvement in the lift was achieved when the flap span covered 80% of the wingspan. Additionally, the optimal flap size and location were determined to be 0.3*c* and 0.7*c* from the leading edge. For the same flap parameters and flow conditions, the performance gained by the flap was found to be higher in the analysis of an airfoil or infinite wing than that of a finite wing.

Altman and Allemand, (2016) examined the effectiveness of a self-deployable flap for three different profiled wings with varying *AR* ($3.0 < AR < 15.0$) at *Re* of 200×10^3. The study focused on the symmetric airfoil NACA0012, moderately cambered USA-28, and highly cambered E423 profiled wings. The response of each wing to the placement of this passive flap was found to depend on their individual pressure distribution**,** stall properties, and boundary layer characteristics. The study did not find a universally effective flap arrangement that applied to all wings. However, through careful investigation and analysis, the optimal flap configuration was identified for each specific wing. These optimal configurations demonstrated significant improvements in post-stall lift coefficients ranging from 5% to 30%. Additionally, it was observed that the flaps had a minimal effect on the drag characteristics of the wing. The effectiveness of the flaps was not significantly influenced by the *AR* within the tested range.

Arivoli and Singh, (2016) conducted a study to investigate the effectiveness of self-movable flaps in delaying flow separation on low *AR* wings with three different platforms (rectangular, Zimmermann, and Inverse Zimmermann) at *Re* of 100×10^3. All of the wing planforms were characterized by a flat plate section with a thickness-to-chord ratio of 0.024. The study investigated a range of flap chord sizes between $0.08c$ and $0.15c$ for chord-wise placement locations between $0.4c$ and $0.8c$. In most cases, the flapped wing configurations demonstrated larger stall angles and post-stall lift characteristics than the un-flapped wing. The optimal placement of the flap to improve performance varied depending on the specific wing planforms. For the Zimmermann and inverse Zimmermann planforms, flaps located at the maximum wingspan of the respective planform showed optimum performance. On the other hand, the flap close to the trailing edge was the optimal location for the rectangular wing. In addition, the single-flapped configuration did not affect drag characteristics in the case of the rectangular and inverted Zimmermann wing planforms. However, a substantial increase in drag behavior was noticed for the single and double-flapped arrangements of the Zimmermann planform as compared to the clean wing.

Hao et al., (2022) performed an experimental investigation of passive flaps on the NPU-WA-180 airfoil to investigate the effect of flap gap height, flap angle, and their position. In this, wooden flaps were tested with different flap gaps ranging from 0 mm to 1.5 mm and fixed flap angles of 7° to 14°. The flapped wing configuration exhibited a lower lift value than the baseline before the stall point. After the stall point, the flap enhanced the post-stall lift and reduced the drag coefficient

significantly. Flaps placed with a small gap on the airfoil surface presented a better improvement in performance than those placed with higher gap. When the flap angle was decreased for the same flap gap and location, the range of improving stall features of the airfoil was found to be enhanced. On the other hand, decrement was noted for both the rate of increase in C_{Lmax} and reduction in C_D. In this study, two optimum locations were observed based on different perspectives. The flap placed at 0.6c showed a better delay in stall point, whereas C_{Lmax} was higher when the flap was located at 0.7*c*.

2.3.2 Survey of Wing Performance with Slotted Wingtip

Smith et al., (2001) demonstrated the effect of multiple winglet attachments on the performance of rectangular NACA0012 profiled wing in the *Re* between 166×10^3 and 300×10^3. The flat plate section was employed in the construction of winglets. Five winglets were mounted at the tip with two different arrangements: winglet at 0° dihedrals with respect to the wing or each winglet kept at some dihedral angle. Both configurations exhibited better lift slopes than the baseline, but the dihedral configuration was more efficient. However, drag was also higher for a wing with winglets, so the *L/D* ratio sometimes appeared lower than the base wing. In order to address this issue, the winglets were positioned with an optimal dihedral angle and subjected to a geometric twist. This configuration exhibited significant enhancement in the *L/D* ratio than other arrangements.

Coiro et al., (2008) performed numerical and experimental investigations to examine the influence of single and multiple winglet arrangements on the wing performance. The elliptical wing planform with profiled NFL-1015 was tested in this study. The configuration with five winglets demonstrated a notable improvement in the *L/D* by 10% and a reduction in drag by 8% than a base wing. Furthermore, the Oswald efficiency factor of the wing was found to be higher for both single and multiple winglet arrangements than a base wing. Based on the comparison, it was observed that the single winglet configuration was more advantageous compared to the multiple winglet configuration.

Céron-Muñoz et al., (2013) performed an experiment to evaluate the effectiveness of wingtip blowing and multiple fixed winglet arrangement on the induced drag reduction at *Re* of 350×10^3. The multiple winglet configuration involved attaching three small sails with a E387 profile to the wingtip. The sail had a root chord of 50 mm and a tip chord of 23 mm. In this study, the cant angle

of each tip sail was varied from -45° to 60° to create other winglet configurations. The results showed that the multiple winglet arrangement showed less induced drag than the base wing, but this reduction in drag was less than that from tip blowing. Furthermore, it was noticed to improve the lift slope, and the corresponding estimated effective *AR* increased by 55% compared to the baseline configuration. The $(L/D)_{max}$ ratio was found to improve up to 20% for the tip configuration of 45/45/-15. However, the multi-winglet configuration demonstrated higher C_D compared to the baseline configuration for $AoA > 16°$. This was attributed to the occurrence of separation on the suction side of the tip sails, resulting in increased drag.

Mitchell and Jacob, (2013) investigated rectangular wing performance with a variety of wingtip designs, namely rounded, feather, and long feather, in the low *Re* range from 19×10^3 to 38×10^3. Results indicated that the presence of winglets, regardless of their specific configurations, enhanced the C_L of the rectangular wings. The rounded tip generally exhibited a similar trend to the no-tip condition, implying that their interaction with the wingtip vortex was comparable. This similarity in performance was attributed to their similar effects on aerodynamics. Conversely, the long feather tip demonstrated relatively poor performance compared to the other configurations, suggesting that its narrow design limited its effectiveness in providing significant aerodynamic benefits. It was inferred that the performance of regular feather tip was between the rounded tip and the long tip in terms of overall aerodynamic effectiveness.

Fluck and Crawford, (2014) conducted a numerical study with the objective of optimizing the design parameters of slotted wingtips to achieve better aerodynamic performance. This investigation considered various design factors related to wingtip slot designs, such as dihedral, twist, and swept angle. The findings indicated that incorporating multiple vertically spread tip slots with sufficient dihedral to create a non-planar configuration had a positive impact on the overall aerodynamic performance. When the twist angle varied for each tip slot, there were cases where a slight increase in the $(L/D)_{max}$ ratio was observed. However, it was also suggested that a twist may provide additional advantages when combined with a dihedral. The swept angle did not directly contribute to drag reduction or lift enhancement. This served as a practical wing design consideration and allowed for the effective integration and placement of a greater number of tip slots in the wingtip configuration.

Lynch et al., (2018) computed the aerodynamic characteristics of wings with planer and non-planer wingtip device attachments at *Re* of 100 $\times 10^3$. These wingtip devices were simulated with various gap sizes, which ranged from 0 to 40 % of the chord length. The wing with planer wingtip slots of gap size 20% exhibited 7.25% higher C_L for the pre-stall region and 5.6% enhancement in C_{Lmax} compared to those without slot gap. The non-planer wingtip configurations generated less lift than the planer as well as extended wingtip in the pre-stall region. However, non-planner arrangements were observed to be efficient for induced drag reduction. The study also revealed that the effect of wingtip gap sizes was independent of whether the wingtip device was planar or non-planar. This independence allowed designers to decouple the wingtip parameters and adjust them individually to achieve the desired lift and drag characteristics.

Siddiqui et al., (2018) conducted a comparative analysis of the aerodynamic performance of a flat plate wing with different types of wingtip designs inspired by bird feathers at *Re* of 300×10^3. The study focused on investigating the effects of flexible and rigid wingtips, considering both flat and curved shapes. The rigid flat wingtip configuration demonstrated higher lift slope, $C_{Lmax,}$ and induced drag compared to the other wingtip configurations. However, despite the larger C_{Lmax}, the rigid flat tip exhibited a relatively small *L/D* ratio. In contrast, the rigid curved wingtip shape yielded the maximum *L/D* ratio among the tested configurations. Further, the *L/D* ratio was found to be higher for flexible curved than flexible flat wingtips.

Liu et al., (2021) presented a comprehensive review of the research status regarding the use of wingtip slots to enhance the aerodynamic performance of wings. They analysed various parameters that affect the aerodynamics of wingtip slots in steady-state conditions, namely structural and deformational parameters. Within the structural parameters, the shape of the winglets (triangular, rectangular, etc.), the planar contour of winglets (number of slots, length, and width of slots), and some pattern angles such as twist, sweep, and cant angles were termed to be significant contributors. These parameters determine the overall geometry and configuration of the wingtip slots. Additionally, the deformational parameters were chord-wise and spanwise flexibility.

2.4 Summary

Through a comprehensive literature review on various areas, including the effects of aspect ratio, low Reynolds number, and passive flow separation control devices, it is clear that there is substantial opportunity for additional research and investigation within this domain. The survey also focused on identifying gaps in the existing literature, which are analysed and summarized in the following points:

- Available literature reveals that various numerical and experimental investigations have been reported for understanding the performance of conventional and flat plate airfoils/wings at low to high *Re* flow. Those airfoils showed hysteresis in measuring lift and drag forces at the low *Re* range. In the presence of hysteresis, it becomes difficult to quantify the stall condition of airfoils. Furthermore, the aerodynamic performance of a symmetric airfoil becomes lower than a cambered airfoil for MAVs range of *Re*.
- It is observed that the aerodynamic performance of conventional airfoils declines rapidly when the *Re* decreases below 100×10^3 and improves if $Re > 1000 \times 10^3$. Therefore, low-speed vehicles with conventional airfoil wings require more power input to operate for low *Re* operations due to the higher amount of drag and limitations on maximum lift incurred.
- Apart from this, aerodynamic data of some high-performance airfoils based on wind tunnel testing also has also been reported in the literature, but they also have their limitations. This data is useful for understanding the effect of *Re* on the airfoil performance for $Re > 100 \times 10^3$. However, for $Re < 100 \times 10^3$, the lift and drag data of such airfoils are available only for particular *Re* below 100×10^3, which is insufficient to quantify performance in the low *Re* region.
- Mounting of self-deployed flaps is a feasible technique for improving the lift and stall characteristics of an infinite wing or airfoil under various *Re* regimes. Most investigations focused on the effect of parametric variation in flaps on the performance of conventional airfoils or large aspect ratio wings ($AR > 3.0$). However, there is a lack of information and understanding available regarding the application of this passive flap in low aspect ratio ($AR < 2.0$) wings.

2.5 Objectives of the Thesis

The core objective of the present research work involves **'Analysing the effect of Reynolds number and aspect ratio on the wing performance with bio-inspired passive flow control devices'**. In order to achieve this key objective, the work is categorized into a few milestones, which are listed as follows:

- Exploring the performance and wake characteristics of two low-speed airfoils, S5010 and E214, in a low Reynolds number regime.
- Understanding the effect of aspect ratio and Reynolds number on the performance of two different cross-sectional wing configurations.
- Examining the influence of self-adjustable bio-inspired flaps on low aspect ratio wings at various Reynolds numbers.
- Investigating the potential benefits and limitations of using bio-inspired wingtip devices to improve the performance of low aspect ratio wings.

CHAPTER 3

Experimental Facility and Methodology

Overview

This section comprehensively covers the descriptions of the experimental facility established in the Department of Mechanical Engineering, IIT Guwahati. It mainly focuses on instrumental facilities such as the wind tunnel, force balance, hot-wire anemometry setup, etc., which have been utilized to achieve the present research objectives. The entire process, from airfoil selection to wing model fabrication, is also detailed. Additionally, this chapter explains the complete experimental arrangement for aerodynamic analysis of the wing model, including measuring methodology. In order to ensure that instruments provide accurate, reliable, and consistent measurements, all the instruments are calibrated before conducting experiments, and calibration results are presented here. Finally, the chapter addresses the details of blockage effects and error analysis to ensure the accuracy and reliability of the data collected during the experiments.

3.1 Experimental Facility

The research has been conducted using a comprehensive experimental facility that includes a wind tunnel, force balance system, hot-wire anemometer, and other essential components. These specialized units are installed within the premises of the Department of Mechanical Engineering, IITG. The salient features of those are discussed in the following subsections.

3.1.1 Wind Tunnel

The wind tunnel is a facility designed to generate a controlled and consistent airflow of known value within a duct, enabling the examination of fluid flow phenomena. This facility serves as a valuable tool to investigate the performance and flow characteristics around the various models, including small-scaled aircraft, wind turbine prototypes, etc. In the present study, all experiments are conducted in an open-circuit subsonic wind tunnel to analyze the aerodynamics of different wing configurations. The dimensional layout of this tunnel is exhibited in **Fig. 3.1**, and its specifications are given in **Table 3.1**. This wind tunnel has square test section of size 0.6 m × 0.6 m and length is 2 m. The controlled uniform airflow within the tunnel is generated by an axial flow fan used for suction, which is powered by a 3-phase 30 HP induction motor. It is capable of generating freestream velocities in the range of 0.1 m/s to 50 m/s. Here, flow velocity is measured using a pitot static tube connected to an electronic manometer. This measurement has an accuracy of ± 0.3%. The electronic manometer is configured with a sampling frequency of 100 Hz, and in the current study, data acquisition has been carried out over a sampling duration of 30 s.

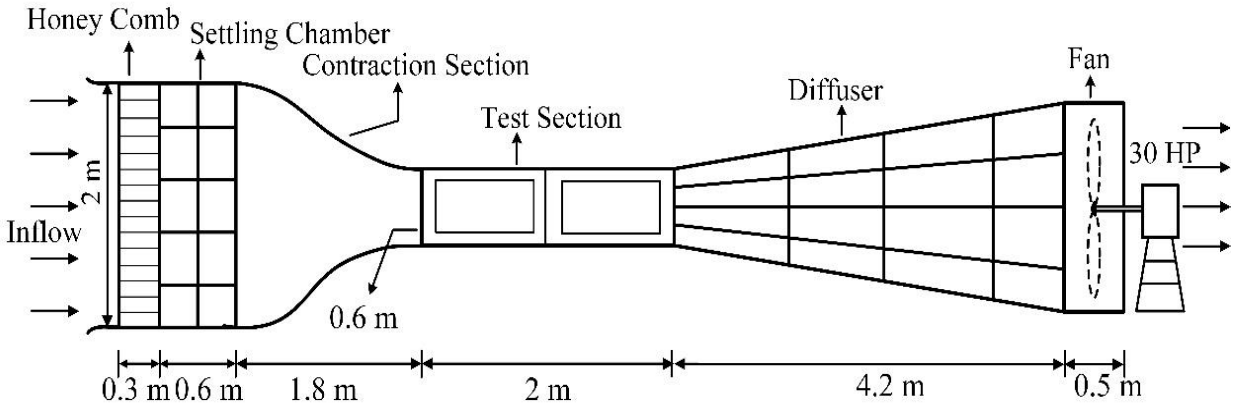

Fig. 3.1: Schematic of subsonic wind tunnel at IITG

Table 3.1: Wind tunnel specifications

Parameters	Details
Tunnel	Open loop suction type
Test section size	2 m × 0.6 m × 0.6 m
Wind speed regime	0.1-50 m/s
Fan rpm range	0-1450 rpm
Contraction ratio	9:1
Settling chamber size	1.8 m × 1.8 m
Overall tunnel length	9.4 m
Motor power	30 HP
Turbulent intensity	< 0.35%

For the purpose of the present study, the experimental investigations are carried out within a flow velocity range of 5-13 m/s. Consequently, this tunnel is calibrated for a wind speed range of 3-15 m/s, where the required velocity is obtained in the test section by changing the tunnel fan rpm. In this speed range, the maximum rotational speed of the tunnel fan could reach up to 480 rpm. The tunnel calibration curve for the current flow regime is given in **Fig. 3.2**, where correlation factor (R^2) = 0.9998. The R^2 value approaching unity is evidence of the linear relationship between the tunnel fan RPM (N) and the corresponding freestream velocity (U_∞).

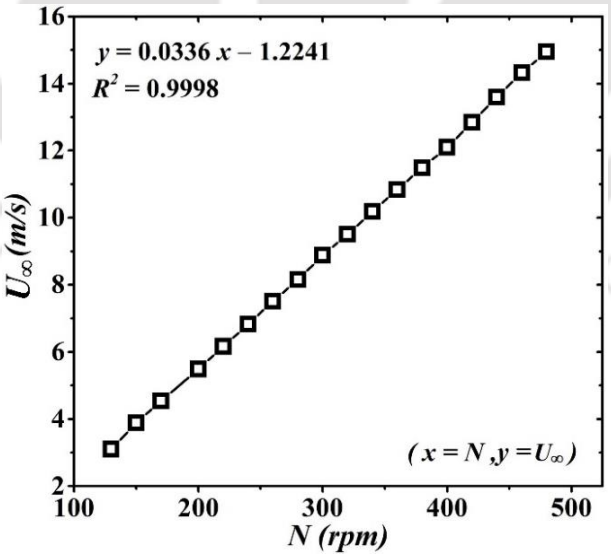

Fig. 3.2: Wind tunnel calibration curve

The freestream turbulence level within the test section is determined using a hot-wire anemometer system, and it is found to be less than 0.35% for the calibrated speed range. This level of turbulence

is typically adequate to ensure that all flow phenomena and the aerodynamic characterization of models are considered acceptable [Bruun, (1995)].

3.1.2 Force Balance System

The forces experienced by the model in moving air are critical parameters for evaluating the aerodynamic characteristics of the model. Here, aerodynamic forces and moment acting on the wing models are measured using three component strain gauge-based force balance [**Model:** WBAL-00103, **Make:** Sunshine Measurements]. This balance estimates lift, drag, and pitching moment with optimum load capacities of 1 kg, 0.4 kg, and 5.0 kg-cm, respectively. The complete force balance system is shown in **Fig. 3.3**. Here, the model is mounted to the top portion of the balance using the model support plate, which is connected to the vertical load-carrying bar. This plate is also linked to a vertical strut, enabling controlled rotation of the model support for adjusting the model's pitch, either upwards or downwards, as required during testing. The bottom portion of this load-carrying bar is fixed to a metric plate, and all the loads acting on the model are transmitted to this plate. These loads are then appropriately transferred through link elements to strain gauge sensors. Further, the balancing mechanism is connected to an electronic panel through an input/output 25-pin connector. This panel is used to convert the instantaneous voltage signal received from strain gauge sensors into respective forces and moments.

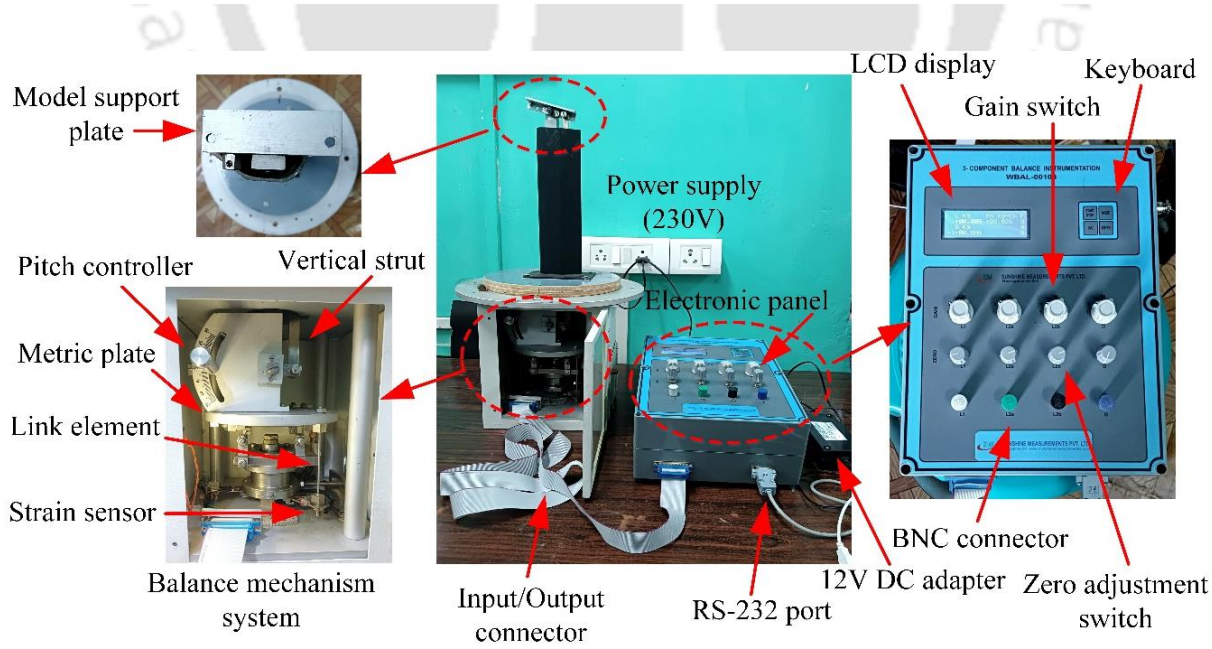

Fig. 3.3: Wind tunnel force balance system

The output data is stored in a computer that is connected to the balance using an RS232 cable. In the study, the gain value is selected as 400 for the amplifier to amplify the incoming voltage signal produced by the strain gauge. This gain adjustment is accomplished manually through the use of the gain switch located on the electronic board. Moreover, biases or disturbances can potentially manifest in the strain signal when the model is affixed to the balance, but these biases can be rectified by employing the zero adjustment switch. The pitch angle of a mounted model can be adjusted between – 10° and 30° to the flow direction using a pitch controller.

To perform the calibration of 3-component force balance, the calibration body is mounted to balance, as shown in **Fig. 3.4**. Three pans, denoted as P_1, P_2, and P_3, are affixed to a calibration body. Pans, P_1 and P_2, are connected to the calibration body via calibration arms, while P_3 is linked to the arm by means of a string that passes over a pulley. This balance is configured with a sampling frequency of 100 Hz. The data acquisition has been carried out over a sampling duration of 10 s, and the gain value is selected as 400 for the calibration. An average period of 10 sec. has been found to be adequate to reduce minor fluctuations in output caused by either the load pans not being fully stabilized or small fluctuations in the electronics.

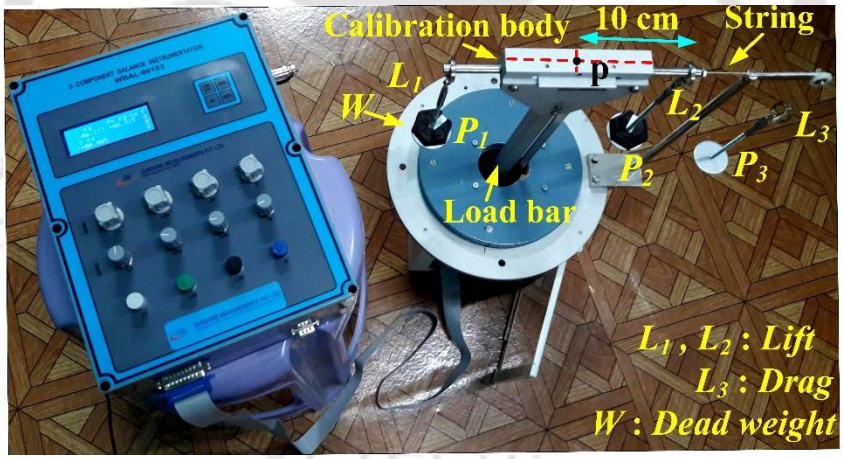

Fig. 3.4: Calibration setup for force balance

Following the initial balance configuration, known loads, namely, L_1, L_2, and L_3, are applied to their respective pans, and the output load and moment are recorded in the microcontroller-based display panel. The loads, L_1 and L_2, represent the vertical loads acting on the object and are associated with lift and moment. The theoretical moment is estimated using these loads at about the center of applications of loads, which is denoted by point 'p'. Conversely, L_3 pulls the object

horizontally by means of a string and is specifically related to the drag force. In the present study, this balance is calibrated to measure loads ranging from 5-500 gm for lift measurements and 5-250 gm for drag force. For lift and pitching moment, the maximum calibration error measured is less than 4%, and for drag force, it is found to be less than 2%.

3.1.3 Hot-wire Anemometry Setup

The primary function of a hot-wire anemometer (HWA) is to monitor velocity fluctuations in the flow field, making it useful for investing turbulence, boundary layers, and other dynamic fluid flow phenomena. This instrument is based on the principle of convective heat transfer through a heated fine wire placed in a fluid flow. Any changes in fluid flow behavior that directly affects the heat transfer rate from the heating wire is instantaneously detected by the HWA system. The convective heat loss from the wire surface is expressed as I^2R, where I and R are current through wire and resistance of wire [Bruun, (1995); Russo, (2011)]. Based on this feature, HWA can be operated in two different modes, depending on whether the current through the wire is kept constant or the resistance of a wire is kept constant. For constant temperature mode, the resistance is kept constant, and the current flowing through the wire is allowed to change with the corresponding flow velocity.

In the present study, a constant temperature anemometer (CTA) setup has been employed to investigate and analyze the flow field mapping. The working concept of this hot-wire is that when the wind speed increases, it enhances the heat transfer between the fluid and the sensor [Russo, (2011)]. Consequently, the probe sensor tends to cool down, causing its resistance to decrease. To maintain a consistent resistance, the amplifier sends more current into the wire to keep the wire's resistance constant. This increase in current results in a higher potential difference across the resistor. Here, the output voltage across the probe is the amplifier output voltage or the voltage necessary to maintain the desired current through the wire. The single wire/channel CTA probe is tested for the estimation of flow field mapping in this research. The probe wire is made of platinum-coated tungsten with a length of 3 mm and a diameter of 10 μm. This thin wire is aligned and welded to the two stainless steel prongs using the microscope and welding assembly unit [**Model:** AMW-717, **Make:** Sunshine]. The probe is connected to the hot-wire system through a BNC socket. The HWA unit captures both instantaneous and fluctuation signals, which are acquired using a data acquisition (DAQ) system [**Model:** DAQ6363, **Make:** NI] with a maximum sampling frequency of 2 MHz. The complete hot-wire setup, including the acquisition system and PC, is shown in **Fig. 3.5**.

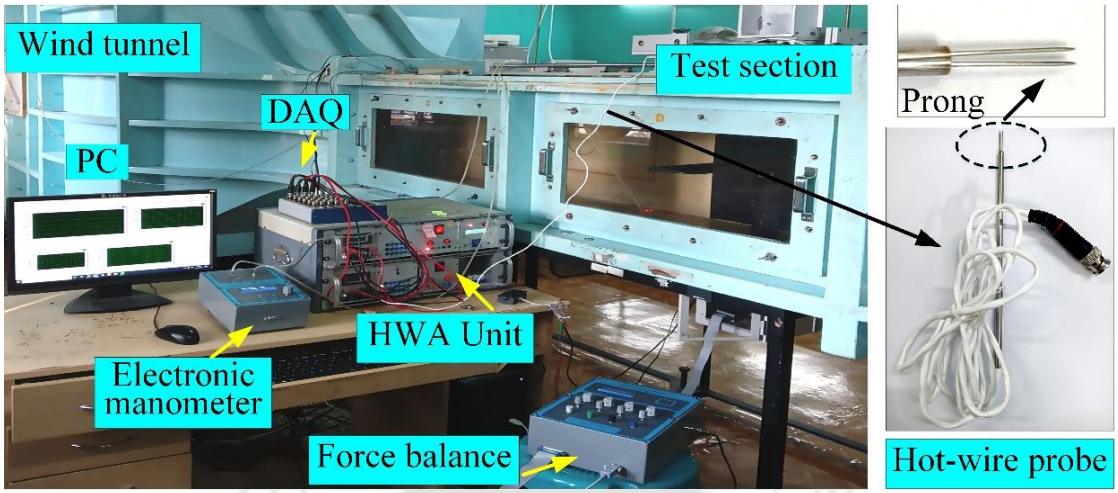

Fig. 3.5: Hot-wire anemometry setup

The simplified form of the analytical relationship between the electric power supplied to the probe sensor and the speed of the surrounding fluid flow is shown in **Eq. 3.1** [King, (1914)]. This equation represents the linear variation of dependent variable E^2 as a function of an independent variable $\sqrt{U_\infty}$, where E is the voltage across the hot-wire, U_∞ is free stream velocity, A and B are the calibration constants. The sensitivity (S) of hot-wire probe is also obtained by taking the derivative of **Eq. 3.1** with respect to freestream velocity, as given in **Eq. 3.2** [Lee and Ken Kauh, (1997); Wagner and Kent, (1988)].

$$E^2 = A + B\sqrt{U_\infty} \tag{3.1}$$

$$S = \frac{dE}{dU_\infty} = \frac{B}{4E\sqrt{U_\infty}} \tag{3.2}$$

The HWA calibration is achieved by measuring the tunnel's velocity using a Pitot-Static probe. The obtained velocity data is then employed to establish the relationship between the voltage changes in the HWA, with the expectation of achieving a correlation R^2 value close to unity. The probe sensor is positioned within the tunnel in such a way that its axis is normal to the freestream flow direction, allowing for uniform heat transfer. It was observed that well aligned single wire probe produces less deviation or uncertainty in the measurement of mean and fluctuation quantities [Yavuzkurt, (1984)]. For the current study, the anemometer is calibrated for the wind speed of 3-15 m/s by keeping a probe wire normal to the flow stream in the test section. The signals captured by the hot-wire are acquired in a DAQ system at a sampling rate of 10 kHz for a sampling time of

10 sec. Further, the post-processing of the acquired signal is accomplished using the NI-LabVIEW program. A typical hot-wire calibration curve for the current flow regime is shown in **Fig. 3.6.** The variation of mean voltage response of HWA corresponding to freestream velocity is exhibited in **Fig. 3.6a**. The polynomial equation of this curve is employed to estimate the sensitivity of the hot-wire probe at given velocity. For example, the value of *S* is found as 0.044 V/(m/s) at wind speed of 3.0 m/s. Furthermore, the hot-wire calibration curve is also expressed in terms of E^2 and $\sqrt{U_\infty}$, as presented in **Fig. 3.6b**. This curve exhibits correlation factor (R^2) close to unity, which suggests a linear relationship between these two variables. The calibration constants, denoted as A and B, are found to be 1.5139 and 0.6248, respectively, which are used to estimate the probe sensitivity, turbulence intensity and other essential flow field parameters.

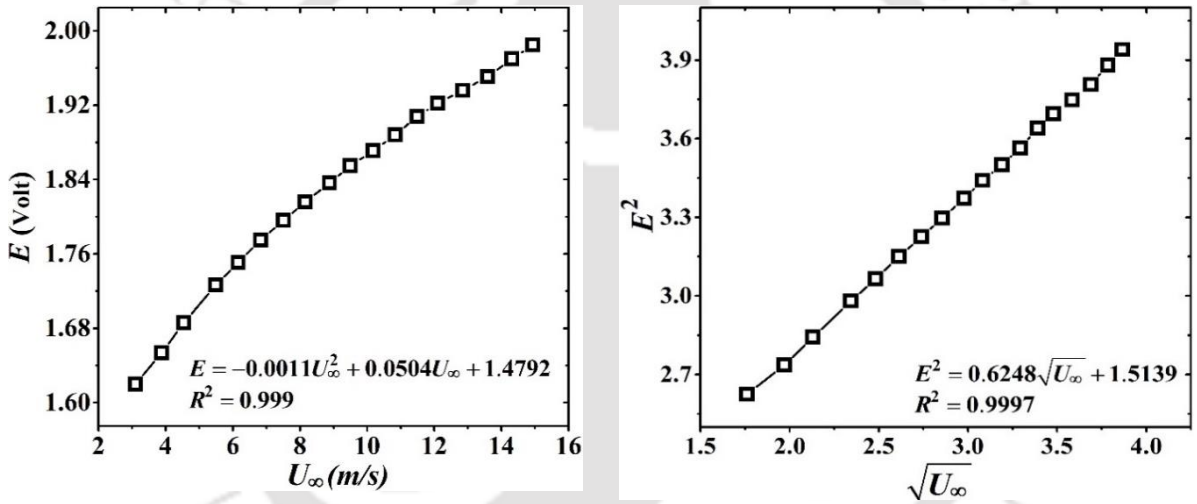

(a) Mean voltage variation as a function of Pitot-static probe velocity

(b) Mean voltage and velocity relationship by King's law

Fig. 3.6: Calibration curve for HWA

3.1.4 Wing Model Design and Fabrication Methodology

Two different airfoils, S5010 and E214, have been chosen for the fabrication of a rectangular wing model. These airfoils have their own advantages and are chosen based on the specific requirements of the MAV application. Both the airfoils are cambered, produce high lift at lower pitch angles, and belong to the category of low *Re* airfoil family [Selig et al., (1996b), (1989)]. The geometry of these airfoils is shown in **Fig. 3.7**. The S5010 profile has a maximum camber of 0.018*c* at 0.32*c*, and the maximum thickness is 0.098*c* at 0.276*c* [Selig et al., (1996b)]. However, the maximum

camber and its positioning for the E214 profile are 0.037*c* and 0.569c, respectively, while the maximum thickness is 0.111*c*, which is at 0.331*c* [Selig et al., (1989)]. Thus, the E214 airfoil is more cambered than the S5010 airfoil and is designed with a laminar separation bubble ramp to moderate pressure recovery on the upper surface. Apart from this, the aerodynamic data of these high-performance airfoils, based on wind tunnel testing, also have been reported in previous literature, but they also have their limitations. This data is useful for understanding the effect of *Re* on the airfoil performance for $Re > 100 \times 10^3$. However, for $Re < 100 \times 10^3$, the lift and drag data of such airfoils are available only for particular *Re* below 100×10^3, which is insufficient to quantify performance in the low *Re* regime. Therefore, the aerodynamic performance of both infinite and finite wing configurations, in association with these airfoils, is investigated for a wide range of *Re* in this study.

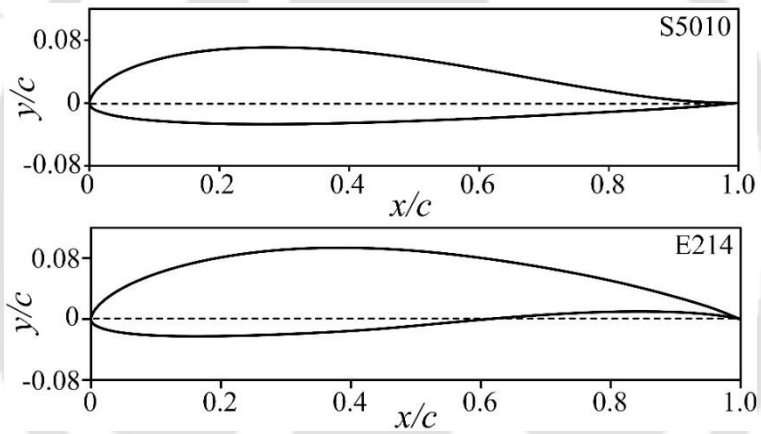

Fig. 3.7: S5010 and E214 profiles

All wing models are designed in rectangular planform, and hence, all wings have zero sweep angle and a tapered ratio of 1.0. This planform is simple in design, easy to manufacture, and cost-effective, making it a popular choice for aircraft applications operating at low speeds and low altitudes [Corda, (2017)]. However, this may not be an efficient wing planform at high speeds due to the large amount of induced drag produced, but it offers better stall characteristics than tapered and swept wing planforms. These models are fabricated from polylactic acid (PLA) material and are printed using a 3D printing machine employing fused deposition modeling (FDM) technology [**Model:** Pro2, **Make:** RAISE3D]. In FDM technology, a thermoplastic filament is heated and extruded layer by layer to create a three-dimensional object. For the printing process, it is essential to maintain a nozzle temperature between 210-235°C, while the bed temperature should be within the range of 60-70°C. The printing infill density is kept between 30% and 60%, which is found to

be sufficient to ensure the structural strength of the wing up to a wind speed of 15 m/s. Apart from this, some other important parameters that have been used to achieve better surface finish during the model printing process are given in **Table 3.2**. The entire process that has been followed for the wing model fabrication is shown through the flow chart in **Fig. 3.8**. In this study, computer-aided 3D models of the selected airfoils are created using modeling software such as SolidWorks and saved in the STL file format. Subsequently, the STL file is transferred to slicing software like ideaMaker, which plays a vital role in converting the 3D model into a machine language that the printer can easily interpret. This language is referred to as the G-code file. All the essential printing parameters, including layer height, infill density, print speed, and others, are configured within the slicing software to ensure precise and accurate 3D printing. Once this process is completed, the G-code file is used by the 3D printer to build the physical model layer by layer. After the printing process is finished, the wing model is subjected to surface finishing processes, which usually include steps such as sanding and painting, the aim of which is to achieve a smooth and refined surface texture.

Table 3.2: Description of 3D printing machine and key parameters used for the printing process

Parameters	Description
Filament diameter	1.75mm (PLA material)
Build volume (W×D×H)	305 × 305 × 300 mm (Single print)
Slicing software	ideaMaker
Supported file type	STL
Nozzle diameter	0.4 mm
Layer thickness	0.08 to 0.12mm (For better surface finish)
Infill pattern type	Grid (to optimize object weight, strength, and printing time)
Support infill type	Rectilinear
Shell width	1.6 mm
Infill density	30 to 60 % (Provides stiffness)
Infill speed	30 mm/sec to 60 mm/s (Usually low for better surface finish)
Heated bed temperature	60 °C
Extruder temperature	215 °C

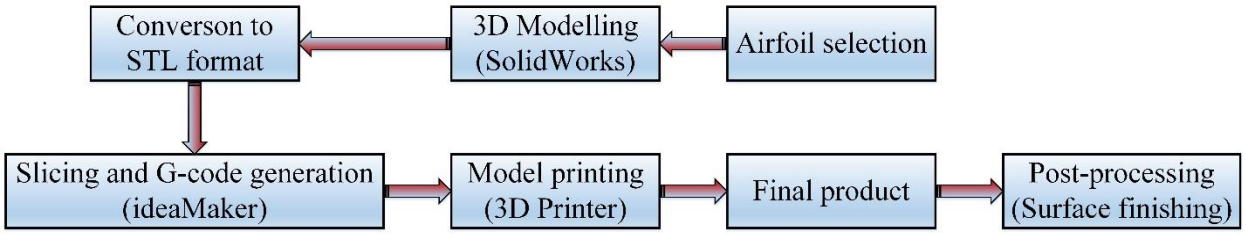

Fig. 3.8: Wing model fabrication procedure

3.2 Experimental Setup and Measurement Approach

The complete experimental arrangement for the aerodynamic measurements of various wing models is shown in **Fig. 3.9**. Here, the balance is attached to the bottom surface of the test section, and the wing model is fixed on the top portion of the balance. The balancing mechanism is connected to an electronic panel through a wire. This panel converts the instantaneous voltage signal received from strain gauge sensors into respective forces and moment. Further, the output data is stored in a computer that is connected to the balance using an RS232 cable. The balance measures force and moment data in kg and kg-cm, respectively. In order to obtain the aerodynamic force coefficients, the lift and drag forces are non-dimensionalized using freestream dynamic pressure ($1/2\rho U_\infty^2$) and wing surface area (A). Simultaneously, pitching moment data for each wing model is computed at the quarter chord ($0.25c$) station of the mean chord from the leading edge. It is also non-dimensionalized, employing freestream dynamic pressure, wing area, and mean-chord length. The pitch angle of the mounted model can be varied from –10° to 30° and the same is measured using a digital spirit level with an uncertainty of ±0.2°. For obtaining the frequency of shed vortices behind the airfoil, a hot-wire probe is placed in the wake region, and its movement is controlled by the 3D traverse mechanism, which is mounted at the top of the tunnel. This mechanism allows mobility of the probe in the working section along streamwise (z), vertical (y), and spanwise (x) directions with a resolution of 0.05mm. However, the non-dimensional location of the probe in the measurement region is denoted by x/c, y/c, and z/c for the respective directions. The origin of this coordinate system is assumed here to be located at intersection of the mid-plane of span and leading edge of the airfoil at a zero pitch angle. The data acquisition system is used to acquire the output from the hot wire setup. Further, the frequency response of shed vortices is obtained from power spectra of the velocity signal generated by the FFT approach with a maximum deviation of ± 4% for the current flow regimes.

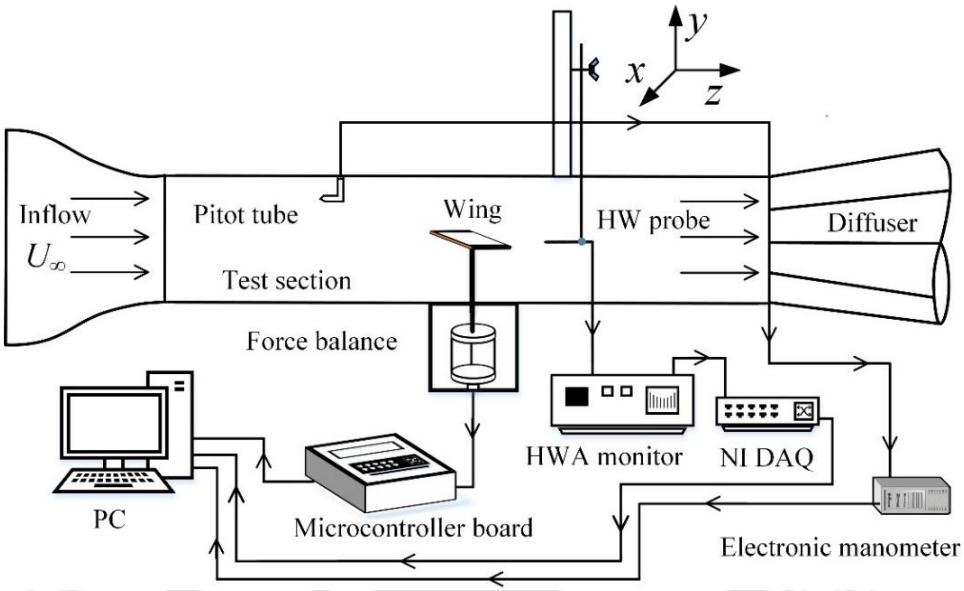

Fig. 3.9: Schematic of experimental setup

In wind tunnel testing, the airflow around an object may not behave the same way as it does in open-air conditions. This difference arises when there is limited space between the tested model and the tunnel walls, commonly referred to as the blockage effect [Barlow et al., (1999)]. The evaluation of the blockage effect caused by the wing model plays a crucial role in wind tunnel testing, which can significantly affect the accuracy of aerodynamic measurements. This effect is assessed through the blockage ratio, which is defined as the ratio of the wing's projected area to the cross-sectional area of the tunnel test section. In the current study, the maximum blockage ratio is found as 2.7% for *AR* = 2.0 at maximum tested *AoA* of 20°, while it is noted as 2.2% for *AR* = 0.5 at 26°. This value consistently decreases with decreasing *AoA* and *AR*, signifying a reduction in the blockage effect during wind tunnel testing. For the finite wing, the value of blockage ratio is observed to be lower even at higher *AoA*, indicating that the need for blockage correction is minimal or not necessary in these cases. It was also reported that when the blockage ratio is less than 5%, the influence of blockage becomes negligible [Barlow et al., (1999); Chen and Liou, (2011); Jeong et al., (2018)]. Furthermore, to estimate errors in the measurement of aerodynamic coefficients, the experiment is repeated multiple times for each *AoA* while keeping the same operational conditions [Moffat, (1988)]. This iterative process allows for the calculation of the standard deviation of the collected samples, followed by the determination of the standard error of the mean. The details of error or uncertainty present in the measurement are addressed in the subsequent chapters.

3.3 Summary

This chapter provides a comprehensive discussion of the details and functioning of the experimental facility installed at the premises of the Department of Mechanical Engineering, IITG. It covers various ground-based facilities, viz. wind tunnel, force balance, hot-wire anemometry setup, and others, which are considered for the current studies. The wind tunnel, specifically, is of the open-circuit subsonic type and maintains turbulence intensity below 0.35% for the present calibrated speed range. Aerodynamic forces and moment acting on the wing models are measured using a 3-component strain gauge-based force balance. Additionally, a constant temperature hot-wire anemometry setup is employed to investigate the turbulence level inside the test section and estimate the flow field mapping. In this study, two different airfoils, S5010 and E214, are chosen for the fabrication of wing models with various aspect ratios. These models are made out of PLA material and are printed using a 3D printing machine. Before conducting the experiments, all instruments have been successfully calibrated to ensure accurate and reliable data collection. Overall, this experimental facility is crucial for exploring the aerodynamic performance and flow field characteristics of different wing models in the current research.

CHAPTER 4

Wake Analysis of Low Reynolds Number Airfoils for Their Performance Assessment

Overview

Experimental investigations are carried out to explore the performance and vortex-shedding characteristics of S5010 and E214 airfoil-based wings to provide guidance for the design of MAVs and other low-speed vehicles. Force and wake shedding frequency measurements are carried out in a subsonic wind tunnel in the Reynolds number (Re) range of 40 × 10^3 - 100 × 10^3. The measurements with increasing Re show that the slope of the lift curve in the linear region increases by 14% for S5010, while this increment is 11% for E214. The peak lift coefficient of both airfoils reduces with reducing Re, which is seen as a sign of enhanced stability as compared to the conventional airfoil. For lower angles of attack (AoA), the influence of Re on drag coefficients is less significant, but at higher angles, the drag increases as the Re drops. Consequently, the maximum lift-to-drag ratio of airfoils improves with the flow Re. Unlike pre-stall mountings, the pitch-down propensity of the airfoil enhances in the post-stall region for high Re flows. No hysteresis is seen in the aerodynamic data of any sections in the present Re limit. Moreover, the frequency of shed vortices reduces with rising AoA at a given Re. In contrast, the Strouhal number almost remains constant with varying Re at a fixed AoA. For S5010 and E214 airfoils, the Strouhal number is noticed to vary between 0.68-0.36 and 0.58-0.36, respectively, for AoA variation of 12°-28°.

4.1 Introduction

Low Reynolds number (*Re*) aerodynamics plays a very significant role in the evolution of advanced small scale unmanned aircraft. These vehicles include micro unmanned air vehicle (μUAV), micro air vehicle (MAV), nano air vehicle (NAV), etc., which have various applications in both military and civilian sectors. Due to the limitation of wing dimensions, weight, and power input, such vehicles operate in a flow regime of *Re* below 200×10^3, whereas, the large-scale conventional flight vehicles operate at *Re* greater than 1000×10^3 [Mueller, (1999)]. In this low *Re* fluid flow, viscous effects are dominant as compared to inertial effects. Accordingly, the boundary layer flow characteristics such as laminar-turbulent transitions, separation point, and reattachment zone vary with the *Re*. Therefore, the aerodynamic behavior of low-speed air vehicles is prominently different from that of high-speed flight vehicles. The overview of flow characterization for flow over an airfoil in this *Re* range ($1 \times 10^3 – 200 \times 10^3$) was presented by Carmichael, (1981). In general, for the flow over an airfoil in the *Re* range from 1×10^3 to 10×10^3, the boundary layer remains laminar, and transitioning to turbulent flow is very difficult. The housefly and dragonfly are the insects which fly in this flow regime. Further, in case of hand-launched sailplanes and gliders, which fly in the range between 10×10^3 to 30×10^3, the flow within the boundary layer is completely laminar, and experiences no reattachment after separation. Moreover, the *Re* from 30×10^3 to 70×10^3 is of major relevance to MAV designers and small-scaled aircraft manufacturers. For the flow with higher *Re* ($70 \times 10^3 \leq Re \leq 200 \times 10^3$) as well flow is laminar over an airfoil which improves its performance, but the presence of separation bubble still remains a hurdle for further performance improvement of some airfoils. Beyond this range, for $Re > 200 \times 10^3$, the performance of the airfoil improves considerably as the size of the laminar bubble diminishes. Thus objects flying with velocities corresponding to *Re* below 200×10^3 encounter numerous problems such as formation of laminar separation bubble, bursting of the separation bubble, flow transition, hysteresis in performance parameters, vortex shedding in the wake etc. Further, these features would have large dependence of *Re* in this flow regime. Hence, many researchers have got motivation to work in this flow regime to understand the aerodynamics of the flying objects. Prominent finding, in this regard, are compiled herein.

Gerakopulos et al., (2010) investigated separation bubble characteristics for the NACA0018 airfoil for $80 \times 10^3 \leq Re \leq 200 \times 10^3$. According to their investigations, increasing the *AoA* at a given *Re*

leads the separation bubble to progress towards the leading edge, and to drop its the length. After certain angle, length rapidly increases and makes the bubble longer in size. The transition from short separation bubble to a long one is known as bubble bursting and usually it occurs at the stall *AoA*, resulting in a substantial loss in lift. Similar separation bubble attributes for various *AoA* were observed for DAE51 airfoil in the *Re* range of $39 \times 10^3 \leq Re \leq 118 \times 10^3$ [Park et al., (2020)]. Further, the strong effect of *Re* was seen on the boundary layer characteristics of airfoil. The separation bubble length in terms of displacement thickness drops as the *Re* rises, and the bubble persists at a larger *AoA* [Gerakopulos et al., (2010); O'Meara and Mueller, (1987); Park et al., (2020)]. As a result, the stall angle as well as the maximum lift coefficient rises with the *Re*. Similarly, a reduction in bubble length was observed for the E387 airfoil with increasing *Re* at a constant *AoA* or when the *AoA* is increased at a constant *Re* [McGhee and Walker, (1988)].

In earlier studies, a number of researchers had reported the critical *Re* for various airfoils at which their performance varies significantly. In this regard, Schmitz investigated the aerodynamic behavior of three airfoils or cross sections viz. flat plate (*t*: 2.9%), cambered plate (*t*: 2.9, 5.8% camber), and N60 (*t*: 12.41 %, 4% camber) at $20 \times 10^3 \leq Re \leq 200 \times 10^3$ [Schmitz, (1967)]. The results showed that the maximum lift coefficients of N60 airfoil decrease rapidly with decreasing *Re* below 100×10^3, whereas flat and curved plates were less affected by changing *Re*. Hence, thin flat and camber plates showed better aerodynamic performance as compared to N60 airfoil for $Re < 100 \times 10^3$. Similar observations are seen in the literature that conventional airfoils have better aerodynamic performance in the form of maximum lift coefficient and the sectional lift-to-drag ratio at $Re > 1000 \times 10^3$ [McMasters and Henderson, (1979); Mueller, (1999)]. However, their performance decreases rapidly with decreasing *Re* below 100×10^3. Some other studies conducted for the aerodynamic behavior of airfoils designed for $Re > 5 \times 10^5$, showed rapid performance drop with decrease in *Re* below 500×10^3 due to the presence of laminar separation bubbles [Lissaman, (1983); Mueller, (1985b)]. Therefore, it is essential to note that most of the conventional airfoils perform better for the $Re > 100 \times 10^3$; but their performance deteriorates sharply with decreasing *Re* below 100×10^3. Hence, the selection of airfoils becomes very significant for this flow regime because the thick camber, or symmetric airfoils are found to have major hysteresis problem during the measurement of lift and drag forces, mainly due to laminar boundary layer separation or bursting of laminar bubbles [Marchman et al., (1987), (1985); Mueller, (1985a)]. This issue is observed at high-*AoA*; therefore, aerodynamic hysteresis is seen to affect the stall condition of the

airfoil. Moreover, Mueller, (1985a) found that hysteresis loop size decreases with increasing *Re* for Lissaman 7769 and Miley M06-12-128 airfoils. However, this correlation between *Re* and hysteresis is not the same for all airfoils, since for the airfoils S1210 and FX 63-137, the size of the hysteresis loop grew with *Re* [Selig et al., (1996a)].

Further, the enhanced boundary layer thickness and the separated shear layer around the airfoil affect its aerodynamic performance and also create coherent structures in the wake region [Huang and Lee, (2000); Huang and Lin, (1995); Yarusevych et al., (2006)]. These structures are responsible for undesirable noise and structural vibrations. The characteristics of these structures depend significantly on the boundary layer behaviour, such as separation bubble size, reattachment location, and turbulent transition. Moreover, different types of vortex-shedding structures were observed in the wake region of airfoil, for both pre and post stall *AoA*. It was reported that the airfoil wake typically behaves like a bluff body wake at higher *AoA* [Huang and Lee, (2000); Huang and Lin, (1995)]. But for pre-stall region, its development is significantly different from that of bluff body wake [Oertel, (1990)]. Typically, the dimensionless parameter, such as the Strouhal number, is used to analyse the unsteady phenomenon in the wake. Here, the Strouhal number is related to an oscillation in unsteady flow caused by inertial forces relative to the change in velocity of fluid particles caused by the convective acceleration in the flow field [Katopodes, (2019)]. Huang and Lin recorded wide range of Strouhal numbers for different modes of vortex shedding in the wake region of NACA0012 airfoil, in *Re* regime of 25×10^3 to 120×10^3 [Huang and Lin, (1995)]. It was found that separated shear layer instabilities affect the evolution of vortex shedding in the airfoil wake. They detected periodic coherent structures in the wake only in case of laminar and turbulent boundary layer separations, without reattachment to the surface. However, the coherency of shed vortices diminished as the flow transitioned from laminar to turbulent, and as a result, no frequency peak appeared in the wake domain. In contrast, Yarusevych et al., (2009), (2006) observed organised wake structures, downstream of NACA0025 airfoil, for both types of flows, such as laminar flow separation without reattachment and with existence of separation bubbles. The results revealed that, as the *Re* rises and a separation bubble develops, the coherency of the wake pattern and the length scale of these vortices diminish. Similarly, *Re* and separation bubble dynamics were also studied for the wake structures of NACA0018 airfoil [Yarusevych and Boutilier, (2011)]. In some investigations, the Strouhal number was found to be almost constant with variation of *Re* for the wake of bluff bodies such as cylinder and plate at a position of 90°

[Lienhard, (1966); Roshko, (1954a)]. However, the Strouhal number deviation with *Re* is more significant for airfoil than bluff bodies. Further, the Strouhal number for the wake of symmetric airfoils was noted to be higher in comparison to flat plate and bluff body wake for the same flow regime [Roshko, (1954a); Yarusevych et al., (2009); Yarusevych and Boutilier, (2011)]. This signifies that more streamlined bodies encounter larger Strouhal number for a given flow conditions. Further, the influence of turbulence intensity on the wake shedding behaviour was also investigated for NACA0012 airfoil [Huang and Lee, (2000)]. This study demonstrated that vortex shedding frequency does not get affected by the freestream turbulence particularly at high *AoA* and *Re*.

In view of the available literature, most of the researchers have focused on exploring the coherent structure characteristics for the wake of symmetric airfoils such as NACA 0012 [Huang and Lee, (2000); Huang and Lin, (1995)], NACA0015 [Gerontakos and Lee, (2005)], NACA0018 [Yarusevych and Boutilier, (2011)], NACA0025 [Yarusevych et al., (2009), (2006)], experiencing wide range of *Re* flows. As a result, the majority of past studies address vortex shedding in the wake of symmetric airfoils or bluff bodies. Therefore, very little focus is given for vortex shedding characteristics in the wake region of thin-cambered airfoils. Hence, the explorations for vortex shedding characteristics of cambered airfoils is still an open area for the researchers. Further, various numerical and experimental investigations have been reported for understanding the performance of conventional and flat plate airfoils at low to high *Re* flows [Mueller and Batill, (1982); Wang et al., (2014); Winslow et al., (2018)]. Those airfoils showed hysteresis in the measurement of lift and drag forces at the low *Re* range. In the presence of hysteresis, it becomes difficult to quantify the stall condition of airfoils. Furthermore, the aerodynamic performance of such a symmetric airfoil becomes lower than a cambered airfoil for MAVs in the range of $Re \leq 100 \times 10^3$. Such effects on the airfoil performance were studied for the various airfoils (NACA0003, 2403, 4403, 6403) at $Re = 20 \times 10^3 - 100 \times 10^3$, and found that the lift coefficient increases with increase in the camber of the airfoil [Winslow et al., (2018)]. However, raising the camber increases drag also, but still the cambered airfoils perform better than symmetric ones in terms of lift-to-drag ratio and maximum lift coefficient. Similar increase in the camber effect on the performance of flat plate airfoils was also reported [Okamoto et al., (1996); Winslow et al., (2018)]. It was observed that the aerodynamic performance of conventional airfoils decline rapidly when the *Re* decreases below 100×10^3 and improves if $Re > 1000 \times 10^3$ [McMasters and

Henderson, (1979); Mueller, (1999)]. Therefore, low-speed vehicles with conventional airfoil wings require more power input to operate for low *Re* operations due to higher amount of drag and limitations on maximum lift incurred. Apart from this, aerodynamic data of some high-performance airfoils, based on wind tunnel testing, also have been reported in previous literature, but they also have their limitations. This data is useful for understanding the effect of *Re* on the airfoil performance for $Re > 100 \times 10^3$. However, for $Re < 100 \times 10^3$, the lift and drag data of such airfoils are available only for particular *Re* below 100×10^3, which is insufficient to quantify performance in the low *Re* region [Lyon et al., (1997); Selig et al., (1996b), (1989)]. In the view of all short comings in the open literature, the goal of the current study is to explore the aerodynamic behavior of low-speed cambered airfoils for various *Re* below 100×10^3. In this regard, wind tunnel experiments are planned with two low-speed airfoils, S5010 and E214, to understand the performance characteristics over the low *Re* range of $10 \times 10^3 < Re < 100 \times 10^3$. These studies are also extended to investigate the wake flow analysis for those airfoils at different angles of attack and freestream conditions. The details of the test model, experimental setup, and measurements are discussed in the following sections.

4.2 Test Models

Two airfoils, S5010 and E214, have been chosen for the fabrication of rectangular wing model. Both the airfoils are thin, cambered, produce high lift at lower pitch angles and belong to the category of low *Re* airfoil family. The chord length and span of the wings are 0.15 m and 0.6 m, respectively. The maximum thickness and cambered of airfoil S5010 are 0.098*c* at 0.276*c* and 0.018*c* at 0.32*c* [Selig et al., (1996b)]. For the wing of E214 profile, maximum thickness and cambered are 0.111*c* at 0.331*c* and 0.037*c* at 0.569*c*, respectively [Selig et al., (1989)]. Thus, the E214 profile is slightly thicker and cambered than the S5010. Since the span of the models covers the entire tunnel test section width, therefore flow through the wingtip can be neglected and flow may be termed as two dimensional (2D). These models are made out of PLA material, and are printed using a 3D printing machine. During experiments, these wing models are mounted on a force balance, which is located at the centre of the text section, as shown in **Fig. 4.1**. Here, the aerodynamic forces and moment acting on the wing are measured using a three component strain gauge balance. While, frequencies of wake coherent structure in the airfoil wake are measured using a hot wire anemometer. The frequency response of shed vortices is obtained from power spectra of the velocity signal generated by the FFT approach with a maximum deviation of ± 4%

for the current flow regimes. In this study, the blockage factor varies within the range of 0.87% to 8.55% for *AoA* range of 2° to 20°. As suggested by reported studies Siram et al., (2022); Van Treuren, (2015), when the blockage factor is below 10%, there is no need for blockage correction in the measurements. In such cases, the interference effects of the model on the airflow are considered to be minimal, and the impact on experimental results is deemed negligible. Furthermore, the maximum standard errors of the mean are found to be less than ±3% for lift and moment measurement, while for drag, it is lesser than ±1.5%. These estimated errors are represented by the error bars in the lift and drag curve for the two *Re* as 40×10^3 and 100×10^3, as shown in **Fig 4.2.**

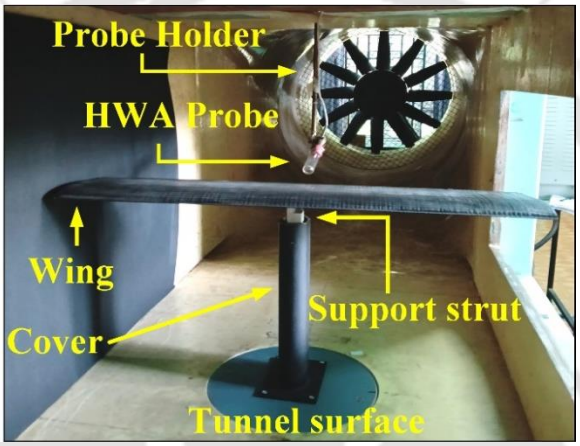

Fig. 4.1: Model mounted on balance in the test section

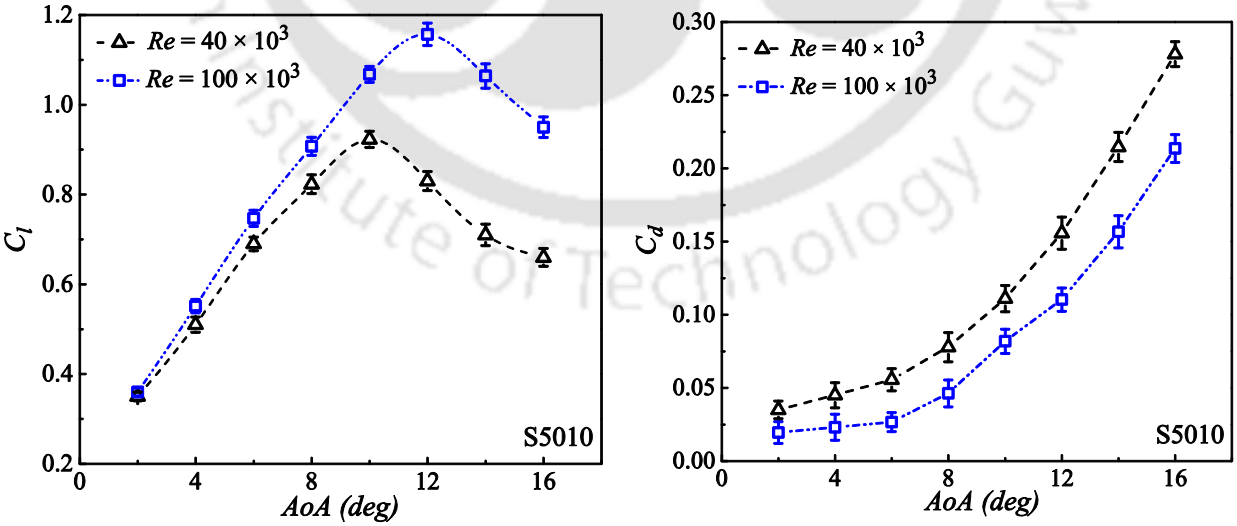

(a) Lift coefficient **(b)** Drag coefficient

Fig. 4.2: Error analysis in C_l and C_d

4.3 Results and Discussion

Experimental studies have been conducted to explore the aerodynamic performance and vortex shedding characteristics of the selected airfoils (S5010, E214) at chord-based *Re* ranging from 40 × 10^3 to 100 × 10^3. The results are therefore discussed in different sections. The first two sections reveal the analysis of performance (lift, drag, and pitching moment) and frequency of shed vortices in the airfoil wake region for the S5010 profile-based wing model. Next sections discuss aerodynamic behavior and wake region characteristics with respect to *Re* and *AoA* for the E214 wing model. It is known that aerodynamic hysteresis commonly observed in the force and moment measurements at a high *AoA* for the airfoil. Therefore, experiments are also conducted to study the aerodynamic force and moment data for the existing test models for both rising and falling *AoA* in order to examine the hysteresis, and the same is also addressed separately.

4.3.1 Performance Analysis of S5010 Airfoil

The experimental results of lift, drag and moment characteristics as a function of *AoA* for a wide range of *Re* are shown in **Figs. 4.3-4.7**. **Figure 4.3a** reveals the lift coefficient variation with pitch angle from 0° to 16° at *Re* of 40 × 10^3 to 100 × 10^3. The results show that C_L increases with an increased *AoA* up to 10°; after that, it starts to decline rapidly for *Re* = 40 × 10^3. The stall point is detected close to 10°. While, for *Re* = 60 × 10^3, C_L rises up to 11°, after which it starts declining with pitch angle. The current lift coefficient data of *Re* = 60 × 10^3 are compared to Selig's experimental lift results [Selig et al., (1996b)] and XFLR5 predictions, as shown in **Fig. 4.3b**. Here, the solid line indicates theoretical lift predictions for an airfoil section wing using classical thin airfoil theory [Anderson, (2011)]. Both experimental predictions show slightly higher lift values for the present cambered airfoil as compared to the symmetric airfoil lift values at a low *AoA*. In contrast, the XFLR5 lift predictions show higher values at each *AoA* from both experimental estimations but still follow a consistent trend of rising and falling of the lift curve with the incidence of stall. Beyond these minor discrepancies the present lift data shows satisfactory agreement with the reported values. In the case of *Re* = 80 – 100 × 10^3, C_l increases to an angle of 12°, and after that, dropping trends are observed in both cases. So, the stall point is marked as 12°, which is consistent for this *Re* range. Moreover, changing the *Re* has very little effect on the C_l for the pre-stall region but has some effect on the lift value in the post-stall region. At an angle below 8°, the effect of the *Re* is minimal on the lift characteristics. Whereas over 8°,

the lift coefficient increases with increasing *Re*. It is found that on reducing the *Re* from 100 × 10^3 to 40 × 10^3, the maximum lift coefficient (C_{lmax}) falls by approximately 20%, and the corresponding stall angle decreases from 12° to 10°. However, the variation of C_{lmax} with *Re* for the tested airfoil is low as compared to conventional symmetric airfoil NACA0012 for *Re* range from 10 × 10^3 to 100 × 10^3. It has been observed that for NACA0012 airfoil, the C_{lmax} decreases approximately up to 46% with a dropping *Re* from 100 × 10^3 to 10 × 10^3 [Winslow et al., (2018)]. Hence, the performance of airfoil S5010 changes less than that of a symmetrical airfoil with a change of *Re* below 100 × 10^3. This represents the stability of an airfoil with varying *Re* in this flow regime.

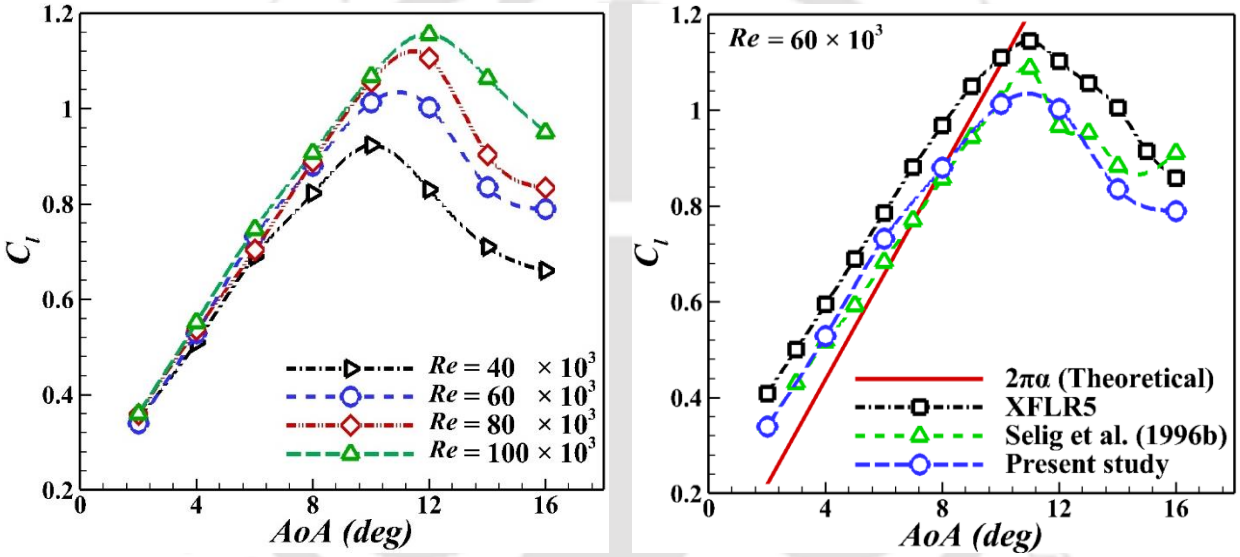

(a) Lift coefficient **(b)** Validation of lift coefficient

Fig. 4.3: Lift characteristics of S5010 airfoil at various *Re*

A significant influence of altering *Re* is found on the linear characteristics of the lift curve in the pre-stall region. The performance of the aircraft in terms of control and stability is influenced by the linear or non-linear lift characteristics at small *AoA* in the lift curve [Meng et al., (2018)]. The present investigations reveal that C_l varies almost linearly with *AoA* up to 8°, after that, non-linear variation is observed for *Re* = 40 × 10^3. While this linear region of C_l versus *AoA* is extended to 10° with larger slope in the case of *Re* = 100 × 10^3. So, high *Re* shows the more linear region in the lift curve for pre-stall angle as compared to low *Re* flows. In the present study, the lift slope values are computed in the linear region of the lift curve using the first derivative of the second-degree polynomial equation with respect to the *AoA*. This polynomial equation is derived from the

C_l-curve using the curve fitting procedure. Similar methods were used by Torres and Mueller to calculate the lift coefficient slope for flat plate wings [Torres and Mueller, (2004)]. According to the conventional thin airfoil theory, the lift coefficient of the airfoil varies linearly with an *AoA*, and the slope of the curve is equal to 2π /rad or 0.11 /*deg*. In the current study, the lift coefficient slope is computed for $2° \leq AoA \leq 6°$ at $Re = 40\times 10^3$, it is found as 0.085 /*deg*. While for $2° \leq AoA \leq 8°$ and the same *Re*, the lift slope value decreases by 0.08 /*deg*. In the case of $Re = 100 \times 10^3$, the lift slope is noticed as 0.097/*deg* for $2° \leq AoA \leq 6°$ and while it is noted as 0.091 /*deg* for $2° \leq AoA \leq 8°$. Based on the observation, the current lift slope value at $Re = 100 \times 10^3$ is closer to the theoretically predicted slope of 0.11/*deg* than lower *Re* at low *AoA*. Moreover, the lift slope value of the linear region increases by 14% for the change in magnitude of *Re* from 40×10^3 to 100×10^3. Similar behavior of lift slope as a function of *Re* was observed for NACA0012 and cambered plate (5%, camber) at *Re* from 20×10^3 to 70×10^3 [E. V Laitone, (1997)].

Prior studies have mentioned that the presence of non-linearities in the lift curve are due to the evolution of the laminar separation bubble (LSB) on the suction surface of the airfoil at different *AoA* [Bai et al., (2016); Hu and Yang, (2008); E. V Laitone, (1997)]. When a separation bubble does not form on the airfoil as usually occurs at small *AoA*, the lift curve remains nearly linear, and the slope of this curve is close to the predicted theoretical slope as 2π. The non-linear effect is found to increase with increasing *AoA*, when a separation bubble is formed on the airfoil. When the *AoA* approaches its critical point, the length of the separation bubble in terms of displacement thickness abruptly increases which in turn leads to formation of a larger separation bubble. The transition from a short bubble to a large one is known as bubble bursting, which is directly related to the stall of an airfoil and results in a sudden and significant reduction of peak lift. Moreover, Bai *et al*. claimed that the abrupt alteration between the long LSB and the trailing edge LSB resulted in a non-linearity in the lift curve of a symmetric airfoil at low *AoA* [Bai et al., (2016)]. In the current case, the separation bubble is expected to be absent or of small size till the *AoA* of 6° at $Re = 100 \times 10^3$, hence C_l varies linearly with *AoA*, and the lift slope value is found to be close to the theoretically predicted slope. After the setting of 6°, non-linearity is detected in the C_l-curve and its effect increases continuously with *AoA*, and after the stall point, the lift curve becomes highly non-linear. This signifies the gradual growth of separation bubble from 6° to 12°, after which the bubble bursts and consequently C_l drops dramatically.

Figure 4.4a shows the drag coefficient (C_d) variation as a function of *AoA* for the *Re* range of 40 × 10^3 to 100 × 10^3. The results depict that the C_d increases consistently with *AoA* from 2° to 16°, which is the same for the tested *Re* range. The C_d varies with almost the same value up to the *AoA* of 6°; however, the rate of increase of C_d becomes greater at *AoA* ≥ 8°, which is because of higher pressure drag at a high *AoA*. Here, plotted drag data in the C_d - *AoA* curve is the profile drag of the airfoil, which is the sum of pressure or form drag (due to flow separation) and skin friction (due to shear stress acting on the airfoil body, depending on the viscosity of fluid and *Re*) [Anderson, (2011)]. At a low *AoA*, the fluid flow is nearly attached to the airfoil surface, resulting in a low value of form drag. Therefore, the contribution of form drag to the total drag is lesser at low *AoA* than the skin friction drag. Due to this fact, the rate of increase in drag with *AoA* is slower at lower *AoA*. However, as the *AoA* increases, the flow begins to separate from the upper surface, leading to an increase in form drag. As a result, the drag coefficient is observed to increase significantly faster as *AoA* increases. Moreover, Hu and Yang analysed the evolution of separation bubble characteristics and revealed that when the laminar boundary layer was noticed to be strongly attached to the airfoil surface, usually at low *AoA*, then the drag coefficient value appears to be very small [Hu and Yang, (2008)]. In contrast, when a laminar separation bubble forms on the airfoil, the drag force increases rapidly with increasing *AoA*.

The influence of *Re* on the C_d is observed to be minimal at small *AoA*. However, for 6° ≤ *AoA* ≤ 16°, drag force decreases as *Re* is increased from 40 × 10^3 to 100 × 10^3, which indicates the early formation of a separation bubble at low *Re*. Previous studies showed that the laminar separation bubble reduces in length with the increase of *Re*, resulting in a lower value of form drag [Brendel and Mueller, (1988); Gerakopulos et al., (2010); O'Meara and Mueller, (1987)]. Therefore, the profile drag of the airfoil decreases as *Re* rises at moderate to high *AoA*. Moreover, lift to drag ratio (C_l / C_d) of the S5010 airfoil is estimated for *AoA* from 2° to 16° at *Re* range of 40 × 10^3 to 100 × 10^3, as presented in **Fig. 4.4b**. An efficient airfoil section provides high lift with minimal generation of drag, so the C_l / C_d measures the aerodynamic efficiency of airfoil. In the present observation, initially, the magnitude of C_l / C_d rises with a rising *AoA* up to a maximum of 6°, after which it continues to decline with angles that are the same for all *Re*. Further, the strong influence of *Re* is noted on the C_l / C_d characteristics of the airfoil. The maximum lift-to-drag ratio (C_l / C_d)$_{max}$ increases from 12 to 28 when *Re* is varied from 40 × 10^3 to 100 × 10^3.

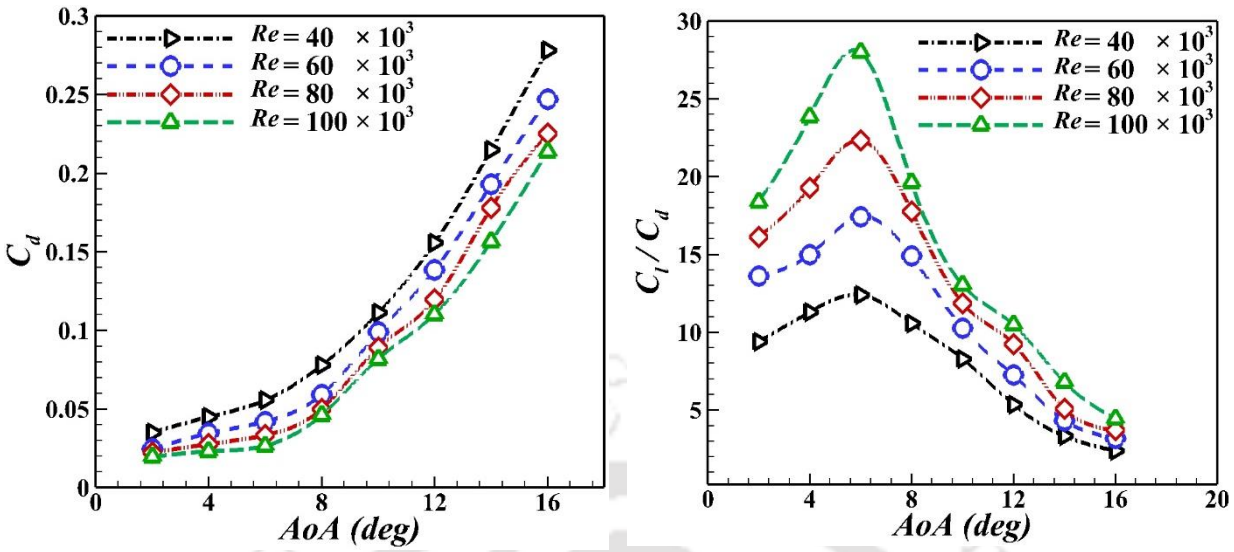

(a) Drag coefficient **(b)** Lift-to-drag ratio

Fig. 4.4: Drag and lift-to-drag ratio characteristics of S5010 airfoil at various *Re*

The variation of the pitching moment coefficient about a quarter chord ($C_{m,0.25c}$) with a *AoA* in the *Re* range of 40 × 10^3 to 100 × 10^3 is illustrated in **Fig. 4.5**. The moment coefficient decreases to a negative value with rising angles up to 10°, after this angle, an increasing trend is observed for *Re* = 40 × 10^3. Similarly, for *Re* = 60 × 10^3 – 100 × 10^3, the moment curve reduces up to 12°, then an increasing trend with *AoA* is detected. In this case, the negative pitching moment denotes that when the *AoA* rises, it tends to rotate the wing towards its equilibrium position to counteract the disturbance that arises due to *AoA*. Also, it is mentioned that the slope of the moment curve must be negative for static longitudinal stability of aircraft [Nelson, (1998)]. In the current study, the moment slope is obtained from the linear region of the moment curve and is found in negative values such as –0.0226 /*deg* and – 0.0236 /*deg* at *Re* = 40 × 10^3 and 100 × 10^3, respectively. According to Mizoguchi and Itoh, (2013), the significance of decreasing pitching moment towards negative values before stall angle reveals the spreading of the laminar separation bubble over the airfoil surface. Here, the pitching moment is caused by normal and axial forces generated by pressure and shear stress distribution over the airfoil surface. An increase in moment value is noted after a particular angle, which is caused by a reduction in lift. Moreover, the influence of the *Re* on the moment characteristics has less significance for the pre-stall region. While for the post-stall angle, the magnitude of the pitching moment declines with increasing *Re*; this indicates that the pitch-down tendency of the airfoil becomes higher for high *Re* in the post-stall region.

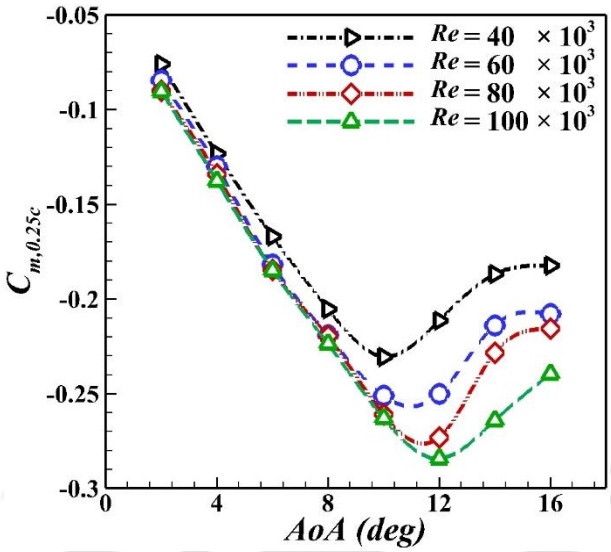

Fig. 4.5: Pitching moment characteristics of S5010 airfoil at various *Re*

4.3.2 Wake Vortex Shedding Analysis of S5010 Airfoil

In the above discussion, it has been observed that the lift characteristics of the S5010 airfoil decline after a *AoA* of 12° for most of the *Re* case. After *AoA* = 12°, the lift coefficient continues to decrease as the angle increases, which signifies that the flow is completely separated from the airfoil surface. These separated shear layers are expected to develop the unstable periodic coherent structures in the wake region of an airfoil. Therefore, characterization of the wake is accomplished for vortex shedding frequency and corresponding dimensionless parameter, Strouhal number in the post-stall region ($12° \leq AoA \leq 30°$) and *Re* range of $40 \times 10^3 \leq Re \leq 100 \times 10^3$. In order to measure frequency, the hot wire probe is placed in several positions in the downstream region of the airfoil, including streamwise (z/c), across the span (x/c), and orthogonal to the stream (y/c). The details of the tested wake domain are as follows; $1.5 \leq z/c \leq 2.5$ along the stream direction, while in the vertical direction, it is moved below the leading edge (LE) of airfoil up to $y/c = 0.3$, whereas above LE, it is varied up to $y/c = 0.25$. For the investigation along spanwise, the probe is shifted from quarter to mid-span length ($1.0 \leq x/c \leq 2.0$). The origin of the *x*, *y* and *z* coordinates system is at the LE of the wing model at zero *AoA*. Initially, to explore the frequency response with the position of the probe in the wake regime, the probe is varied in various locations along the streamwise direction as z/c = 1.6, 1.8, 2.0, 2.4 at given y/c = 0.15 (above LE), x/c = 1.2 (along span). The shedding frequency (f_s) is obtained from the output signal of hot wire through FFT spectral analysis for various streamwise locations corresponding to *AoA* = 12° and $Re = 60 \times 10^3$, as demonstrated in **Fig. 4.6**.

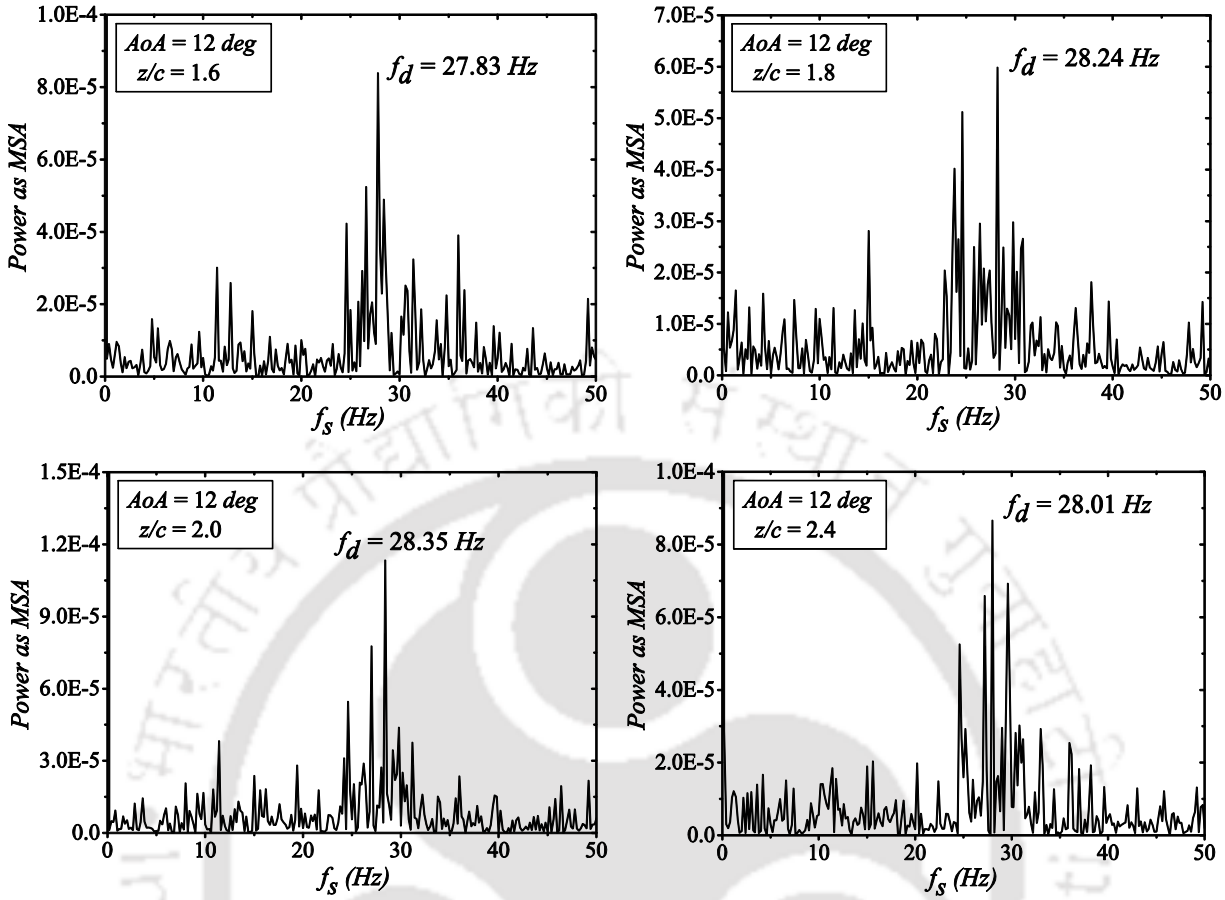

Fig. 4.6: Frequency response in the wake of an airfoil with the variation of probe locations along streamwise

The peak of power spectrum represents the dominant frequency (f_d) of shed vortices. Results reveal that no significant variation is observed in dominant frequency with varying probe locations along stream direction from z/c =1.6 to 2.4. However, the amplitude of each spectrum varies with different probe positions. After z/c = 3.0 or before z/c = 1.5, the hot wire signal becomes ire-regular, resulting in no dominant frequency peak detected in the power spectrum signal for S5010 airfoil in the currently tested *Re* and *AoA* ranges. Also similar tests are carried out for different probe positions normal to the free stream ($-0.3 \leq y/c \leq 0.25$) and for same pitch angle. No significant variation is found in the vortex shedding frequency for these conditions and set measurements coordinates. Such experiments are performed for several *AoA* ($12° \leq AoA \leq 30°$) at defined probe location of z/c = 1.8, y/c = 0.15, x/c = 1.2 in the wake at $Re = 60 \times 10^3$ to investigate the influence of *AoA* on the wake field. When the *AoA* is raised from 12° to 28°, the dominant frequency is seen to decline from 28.24 Hz to 14.62 Hz, as depicted in **Fig. 4.7**. This decline is likely due to the increased separation of the flow from the airfoil surface at higher *AoA*, which

leads to larger, slower-moving vortices and, consequently lower wake shedding frequencies. After *AoA* = 28°, the peak of f_d is found to be constant with angles. Further, a strong influence of *Re* has been observed on the shedding formation. **Figure 4.8** shows that when the *Re* increases from 40 × 10^3 to 100 × 10^3 at given *AoA* = 12°, the frequency peaks in the spectrum shift towards the right from 18.55 *Hz* to 43.58 *Hz*.

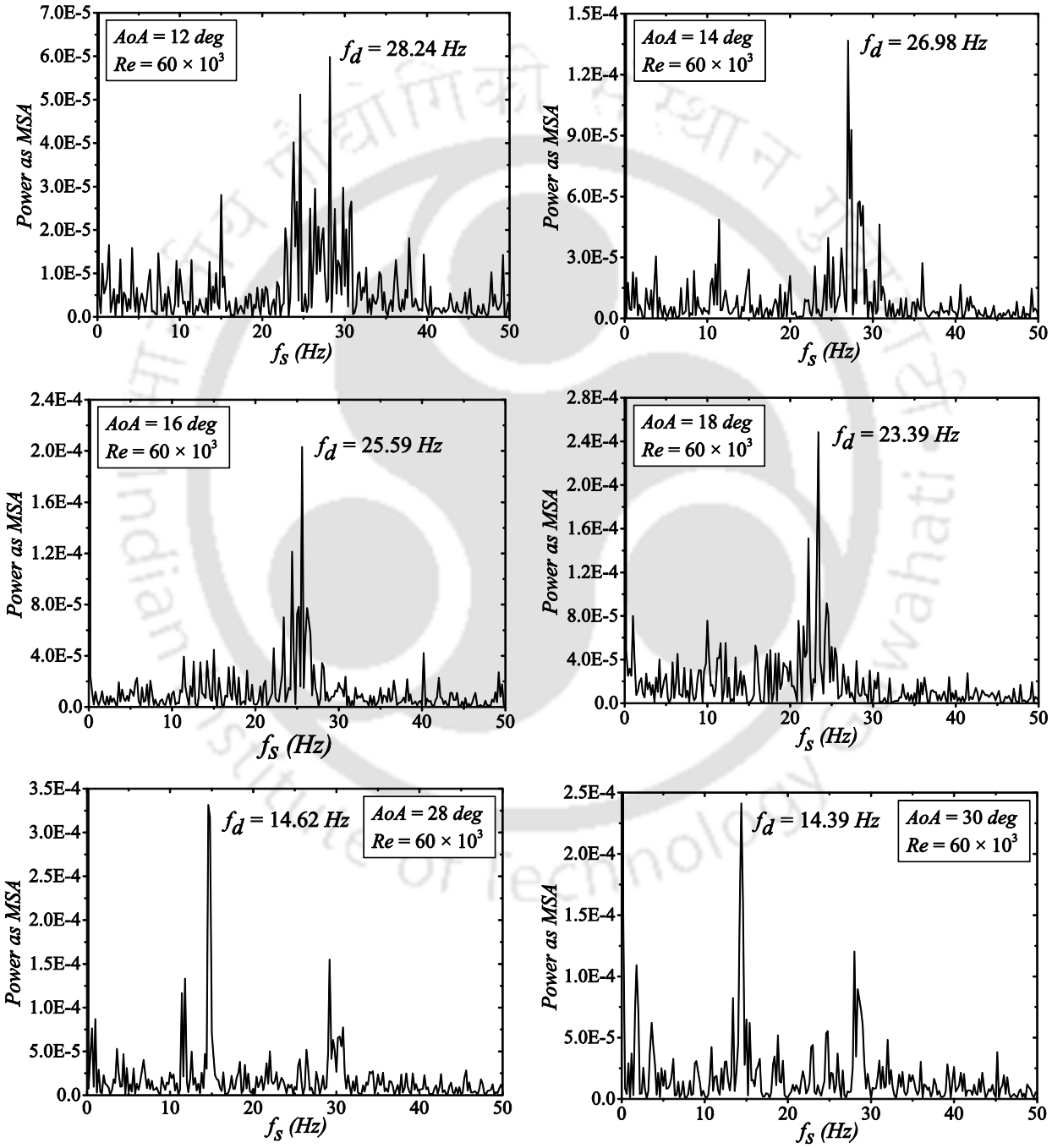

Fig. 4.7: Variation of vortex shedding frequency with the *AoA* at *Re* = 60 × 10^3

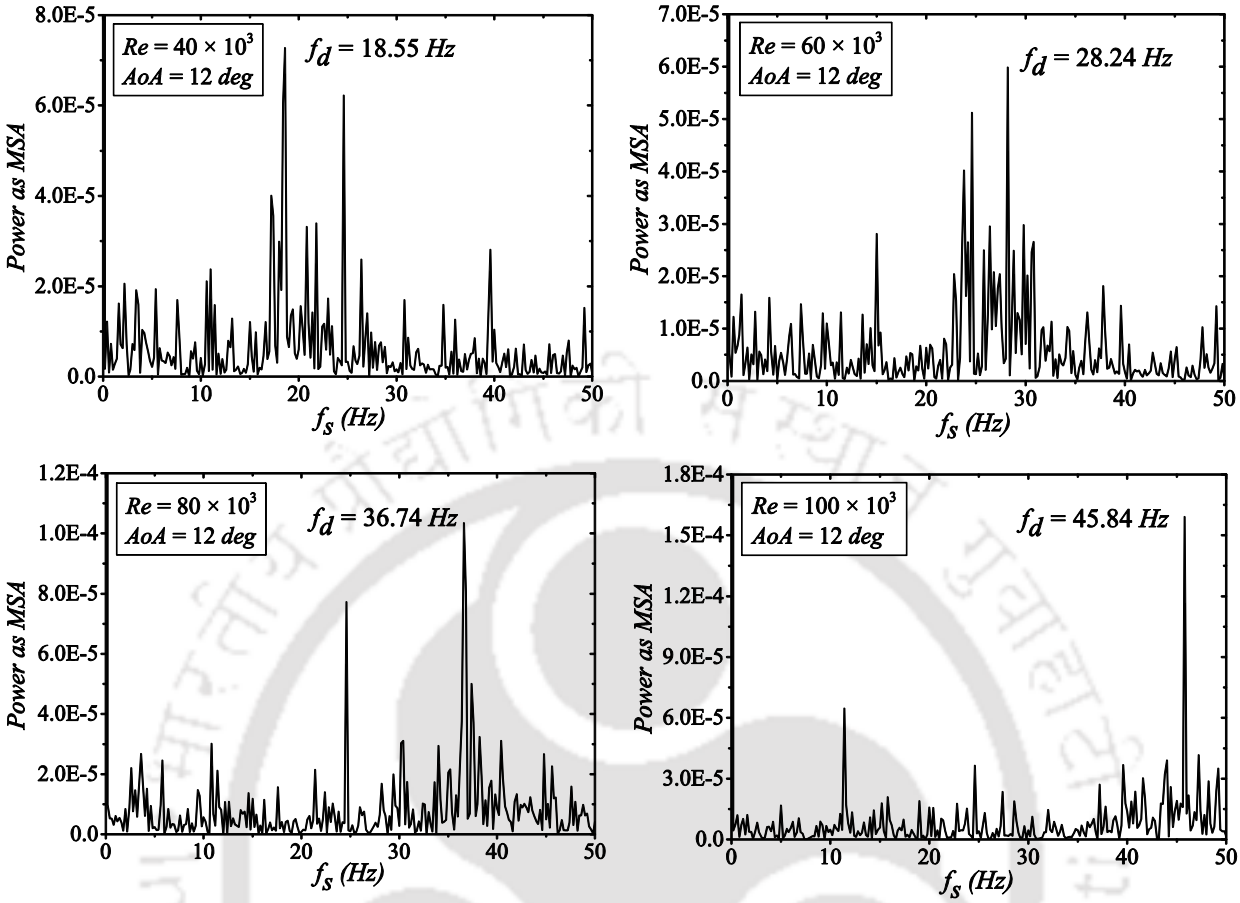

Fig. 4.8: Vortex shedding frequency response with various *Re* at *AoA* = 12°

These investigations are also extended to obtain the correlation between shedding frequency, *AoA* and *Re* for other *AoA* values (16°, 20°, 24°, 28°) and different *Re* range ($40 \times 10^3 \leq Re \leq 100 \times 10^3$), as presented in **Fig. 4.9a.** The analysis of the results shows that the magnitude of the spectral frequency increases linearly with *Re* at a given *AoA*, which is the same for all investigated *AoA* ranges. Despite different flow conditions and experimental parameters, similar linear dependency in the form of $f_s \sim Re$ is observed in the case of symmetric airfoils (NACA0012, NACA0018) and circular cylinders in low *Re* flow regime [Huang and Lin, (1995); Roshko, (1954b); Yarusevych and Boutilier, (2011)]. For a given *Re*, results indicate that shedding frequency decreases with increasing pitch angle, which is consistent for current *Re* ranges. Similar to current findings ($f_s \sim 1/AoA$), Huang and Lin had obtained the same correlation between *AoA* and shedding frequency for NACA0012 airfoil in low *Re* flows [Huang and Lin, (1995)]. Further, the Strouhal number (St_s) corresponding to shedding frequency (f_s) is obtained for various *Re* and *AoA* of S5010 airfoil, as demonstrated in **Fig. 4.9b.** The results show that for a given *AoA*, as the *Re* increases, the shedding

frequency also increases but the value of Strouhal number remains almost constant. This can be understood from the fact that the relative change in St_s with respect to an increase in the free stream velocity remains the same, as per the relation, $St_s = f_s\, c/U$. While for a specific *Re*, the St_s decreases as the *AoA* increases. At *AoA* = 12°, the Strouhal number is found to be 0.68 for *Re* range from 40 × 10^3 to 100 × 10^3. But as the *AoA* increases to 28°, the magnitude of St_s reduces to 0.36 for the same *Re* range. For *AoA* > 25°, the variation of St_s with *AoA* shows an almost constant value of 0.36 for the present free stream conditions.

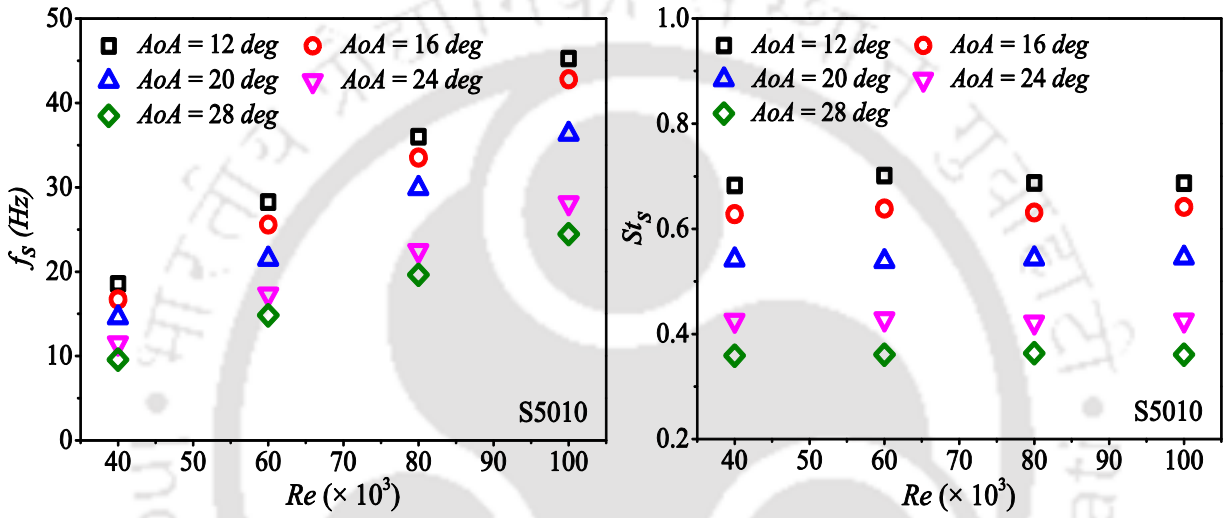

(a) Shedding frequency **(b)** Strouhal number

Fig. 4.9: Influence of *Re* on the wake shedding characteristics of S5010 airfoil at various *AoA*

As reported that, the shedding frequency in the wake region of a bluff body is closely related with wake width and separation angle [Chen and Fang, (1996)]. Since at a low *AoA*, the airfoil tends to have less divergent flow, thereby generating narrower width of wake with the shorter time period. Therefore, the vortex frequency and related Strouhal number are higher at a low *AoA*. In contrast, the flow gets more diverged at a high *AoA*, creating wider wake width, thereby obtaining lesser vortex frequency, and this also leads to relatively higher form drag. Thus, it can also be shown that the drag coefficient is directly proportional to wake width and inversely related to the shedding frequency of the airfoil wake. A similar variation of St_s as a function of *Re* and *AoA* was reported for NACA0012 airfoil in the regime of 20× $10^3 \leq Re \leq$ 100× 10^3 at *AoA* ≥ 15° [Huang and Lee, (2000); Huang and Lin, (1995)]. Similarly the Strouhal number in the wake of the circular cylinder was also found to be a as 0.21 for *Re* between 1 × 10^3 to 100 × 10^3 [Lienhard, (1966); Roshko, (1954a)]. The St_s for the S5010 airfoil shows a higher magnitude compared to cylinder

wake shedding, but as the *AoA* increases, the magnitude difference between them decreases. This result suggested that the wake structure of the airfoil at high *AoA* behaves as a bluff body wake. As anticipated, the bluff body diverges more flow in the wake as compared to the streamlined body; therefore, the shedding frequency and Strouhal number are higher for an airfoil than a bluff body.

4.3.3 Performance Analysis of E214 Airfoil

After studying the aerodynamic performance and wake periodicity for S5010 aerofoil section, similar experiments are performed for E214 aerofoil. The variation of a lift, drag, and pitching moment coefficients with *AoA* ($2° \leq AoA \leq 16°$) for E214 aerofoil section in the *Re* range of 40×10^3 to 100×10^3 is shown in **Fig. 4.10 – 4.11**. **Figure 4.10a** reveals that lift increases with rising *AoA* till 10°, after which it begins to fall significantly at $Re = 40 \times 10^3$. Whereas in the $Re = 60 \times 10^3 – 100 \times 10^3$, C_l continues to rise with a *AoA* up to 12°; thereafter, dropping trend is observed for all cases. Thus stall angle of the E214 airfoil is recorded as 10° at $Re = 40 \times 10^3$, while for others *Re*, it is noted as 12°. Further, the influence of *Re* on the C_l is less significant for the pre-stall angle ($AoA < 8°$), but it has a substantial effect at higher pitch angles. For $AoA > 8°$, It is observed that C_l has higher values for higher *Re*. Further, a 17% drop is noted in the maximum lift coefficient (C_{lmax}) when *Re* is decreased from 100×10^3 to 40×10^3. Winslow et al. found a 46% drop in C_{lmax} for NACA0012 when the *Re* was reduced from 100×10^3 to 10×10^3, and for Clark-Y airfoil, it was reduced by approximately 58% in the *Re* ranging from 20×10^3 to 1000×10^3 [Winslow et al., (2018)]. In comparison to these conventional airfoils, the peak lift coefficient of the E214 airfoil has lesser reduction with as *Re* below 100×10^3. When compared to the lift data of the S5010 profile, it is found that E214 has a higher value of C_{lmax} at a given *Re*. Moreover, a substantial effect of *Re* and *AoA* on the linearity of the lift curve is seen at low *AoA*. The lift curve reveals that C_l varies almost linearly with increasing *AoA* up to 6°, after which non-linear variation occurs for $Re = 40 \times 10^3$. While in the case of $Re = 100 \times 10^3$, the linear portion of the lift curve is extended up to *AoA* of 8°. As a result, high *Re* flows exhibit more linear variation of C_l with *AoA* in the lift curve for pre stall region than low *Re*. Further, the lift curve slope of the linear region ($2° \leq AoA \leq 6°$) is evaluated at $Re = 40 \times 10^3$ and found to be 0.11/*deg*, which is equivalent to the theoretical slope value predicted by thin airfoil theory. For $Re = 100 \times 10^3$, the linear lift slope is estimated as 0.11 / *deg* for the curve portion of $2° \leq AoA \leq 8°$, which is also similar to the theoretical

slope of 0.11 /*deg* or 2π /*rad*. As discussed above for S5010, the presence of non-linearity at higher *AoA* in the lift curve is due to the growth of separation bubbles on the upper surface of the airfoil at different *AoA*.

The drag coefficient data as a function of *AoA* ($2° \leq AoA \leq 16°$) for E214 airfoil at *Re* range from 40×10^3 to 100×10^3 is presented in **Fig. 4.10b**. As per the curve, drag force continues to rise with rising pitch angle, which is consistent for the present *Re* range. However, the magnitude of C_d is almost constant with increasing *AoA* up to 8°, but after this angle it increases rapidly with *AoA*. This may be due to variation of form drag with different *AoA*. It has been also found that, as the pitch angle exceeds 10°, the form drag increases rapidly. Consequently, the magnitude of C_d rises at a faster rate at high *AoA* ($AoA \geq 10°$). Furthermore, the effect of *Re* on the drag characteristics is less significant at low *AoA* ($AoA < 8°$) but becomes more effective for $AoA > 8°$. The profile drag of the airfoil decreases with increasing *Re* from 40×10^3 to 100×10^3, which is particularly observed for the *AoA* range from 8° to 16°. The evolution of the laminar separation bubble on the airfoil surface is expected to be early at low *Re* flows, causing higher form drag; therefore, the magnitude of total drag shows higher values at higher *AoA* and lower *Re*. When compared with the drag of S5010 section, the E214 airfoil exhibits a slightly higher drag value at a high *AoA* for $Re = 40 \times 10^3$, while for $Re = 60 \times 10^3$ - 100×10^3, no significant variation is observed in the drag statistics of these two airfoils even at high *AoA*.

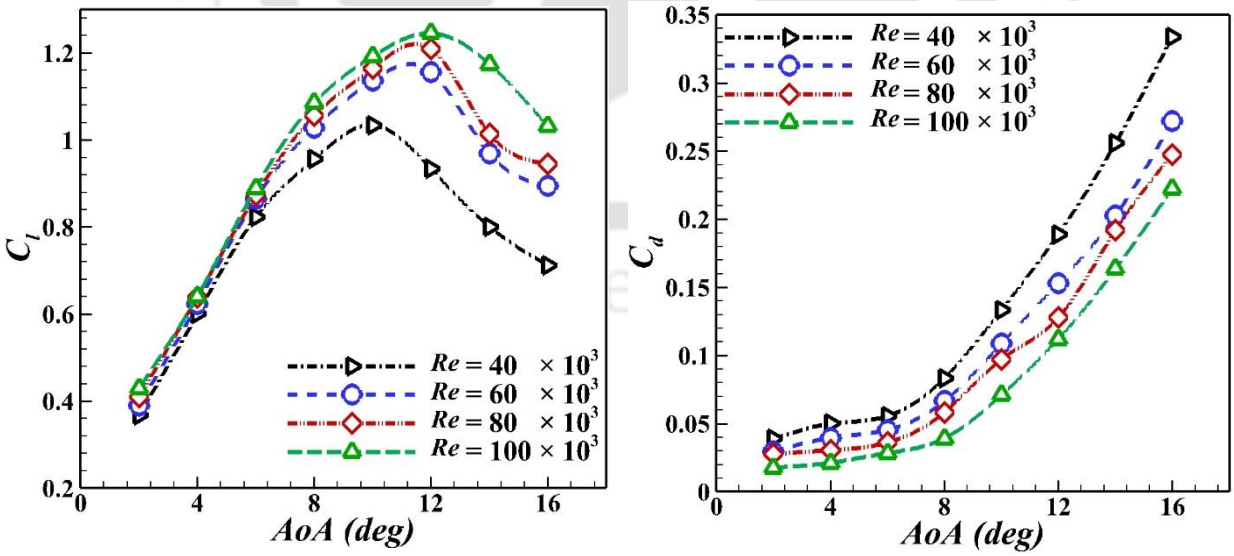

(a) Lift coefficient **(b)** Drag coefficient

Fig. 4.10: Lift and drag characteristics of E214 airfoil at various *Re*

Further, lift to drag ratio of the E214 airfoil is evaluated for various *AoA* ($2° \leq AoA \leq 16°$) and *Re* ($40 \times 10^3 \leq Re \leq 100 \times 10^3$) (**Fig. 4.11a**). The results show that C_l / C_d increases with rising *AoA* up to 6°, then declining trends are observed, that is same for all tested *Re*. The strong effect of *Re* on the lift-to-drag characteristics is observed, an increase of *Re* from 40×10^3 to 100×10^3, the magnitude of $(C_l / C_d)_{max}$ rises approximately from 15 to 31. When compared to the S5010 data, the E214 airfoil has a higher value of $(C_l / C_d)_{max}$ at a given *Re*. The pitching moment data variation with *AoA* for E214 at different *Re* is demonstrated in **Fig. 4.11b**. The magnitude of the moment reduces to a negative value with increasing angles up to 10° then it rises rapidly for $Re = 40 \times 10^3$. Similar to this, for $Re = 60 \times 10^3$ - 100×10^3, the moment curve decreases by an angle of 12°, after which an increasing trend is noticed. Rising moment values indicate that the static stability of the airfoil decreases near the stall angle or in the post-stall region. No significant effect of *Re* is seen on the moment coefficient for a pre-stall region. However, for the post-stall region, pitching moment data drops with increasing *Re* at a given *AoA*. Comparing two airfoil bodies, the moment characteristics of the E214 profile show slightly higher negative values with respect to *AoA* than those of the S5010 airfoil for a given *AoA* and *Re*. This reveals that the pitch-down propensity of E214 is higher than the S5010 section for defined flow conditions.

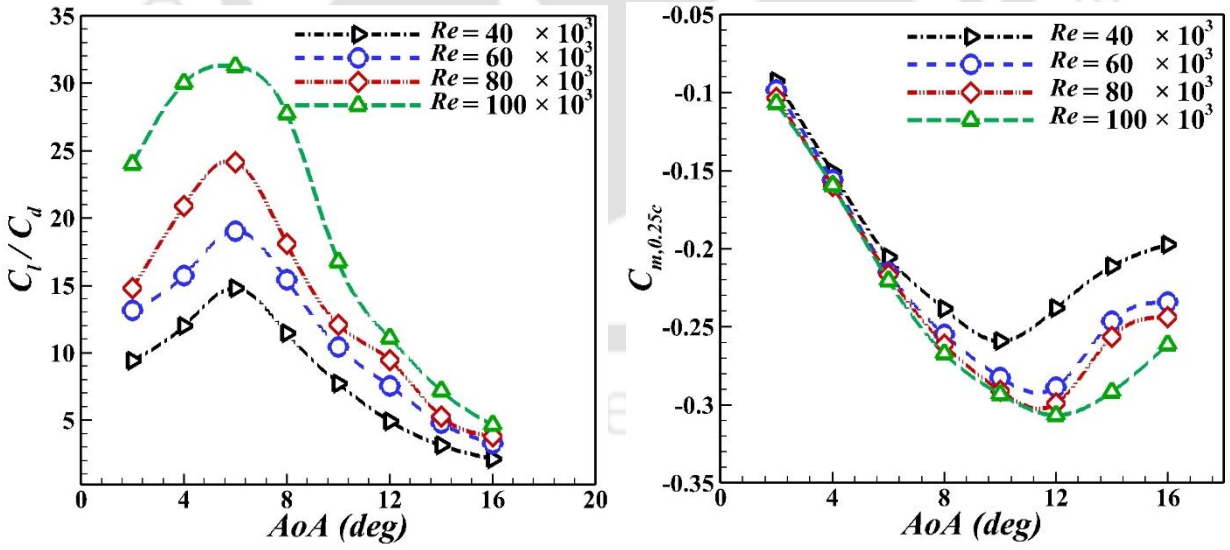

(a) Lift-to-drag ratio **(b)** Pitching moment coefficient

Fig. 4.11: Lift-to-drag ratio and pitching moment characteristics of E214 airfoil at various *Re*

4.3.4 Wake Vortex Shedding Analysis of E214 Airfoil

The frequency of shed vortices in the wake region of E214 airfoil for post-stall angle range of 12° ≤ *AoA* ≤ 30° in a flow regime of 40 × 10^3 ≤ *Re* ≤ 100 × 10^3 is measured and presented in **Fig. 4.12a**. In this analysis, the probe is moved in the wake in all directions, as stream wise (1.5 ≤ *z/c* ≤ 2.5), orthogonal to stream (-0.3 ≤ *y/c* ≤ 0.2), and span wise (1.0 ≤ *x/c* ≤ 2.0), in order to assess the frequency data. Analysis of the results shows that the shedding frequency remains almost constant with changes in the position of the probe within a marked set of coordinates in the downstream region and for a given *AoA* and *Re*. Further, the variation of sheading frequency with *AoA* and *Re* at a defined probe position of *z/c* = 1.8, *y/c* = 1.5, *x/c* = 1.2 behind the airfoil is shown in **Fig. 4.12a**. In the case of E214 airfoil, the magnitude of f_s decreases from 23.49 *Hz* to 14.39 *Hz* as *AoA* rises from 12° to 28° at *Re* = 60 × 10^3. Similar trends (f_s ~1/*AoA*) are observed for other *Re*, where the vortex frequency falls as the pitch angle increases, while for *AoA* ≥ 24°, this rate of this reduction decreases. In contrast, vortex shedding frequency increases with rising *Re* at a given *AoA*. The variation of Strouhal number as a function of *AoA* and *Re* in the wake region of E214 airfoil is as shown in **Fig. 4.12b**. As observed for S5010 airfoil, the same pattern is noted for E214 airfoil as well where, the St_s remains nearly constant with *Re* at a given *AoA* whereas it decreases with *AoA* for specific *Re*.

When comparing the wake periodicities for two airfoils, the St_s for E214 case reduces from 0.59 to 0.36 with an increase in *AoA* from 12° to 28° at *Re* = 60 × 10^3 and while in the case of S5010, it decreases from 0.68 to 0.36 for the same flow conditions (**Fig. 4.13b**). The shedding frequency and Strouhal number show a relatively higher magnitude for S5010 than E214 at all *AoA* ≤ 24° in the current freestream range. This is because of difference in thickness of the airfoils, where S5010 (*t/c* = 9.8%) is a thinner airfoil than E214 (*t/c* =11.1%). Thus S5010 airfoil diverges the flow less and creates a narrower wake in the downstream region compared to the E214 for *AoA* below 24°, therefore incurs a higher frequency periodic events. But for *AoA* > 24°, both airfoils exhibit almost identical values of frequency and Strouhal number in the measured *Re* range. For *AoA* > 24°, both the airfoil models behave as a bluff body, and the effect of airfoil thickness on the wake structure is diminished. The present finding is consistent with results reported for NACA0018 and NACA0025; thinner airfoils have a higher Strouhal number at a given *Re* and *AoA* [Yarusevych and Boutilier, (2011)].

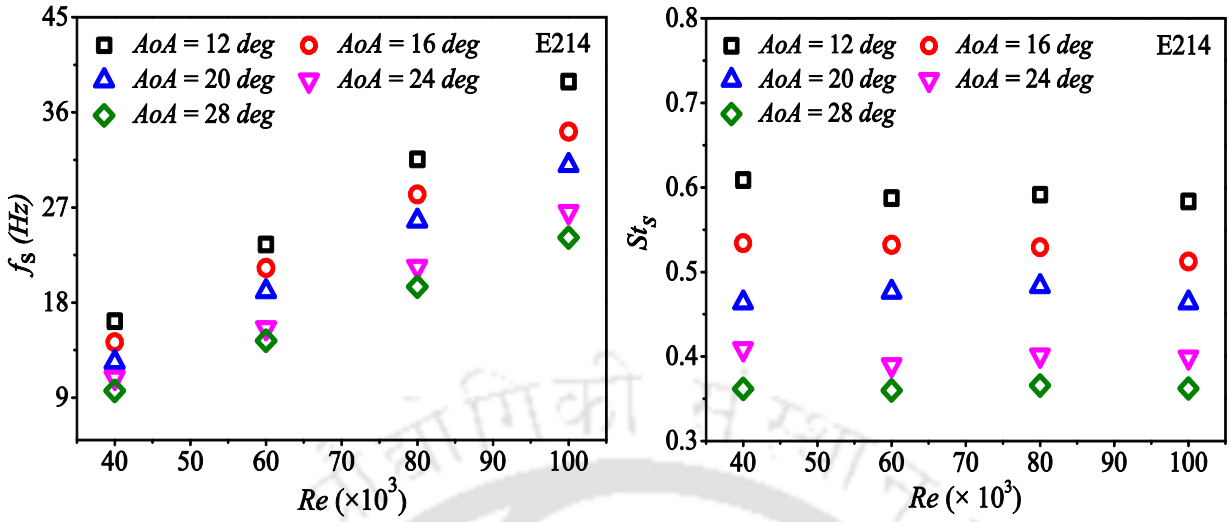

(a) Shedding frequency **(b)** Strouhal number

Fig. 4.12: Influence of *Re* on the wake shedding characteristics of E214 airfoil at various *AoA*

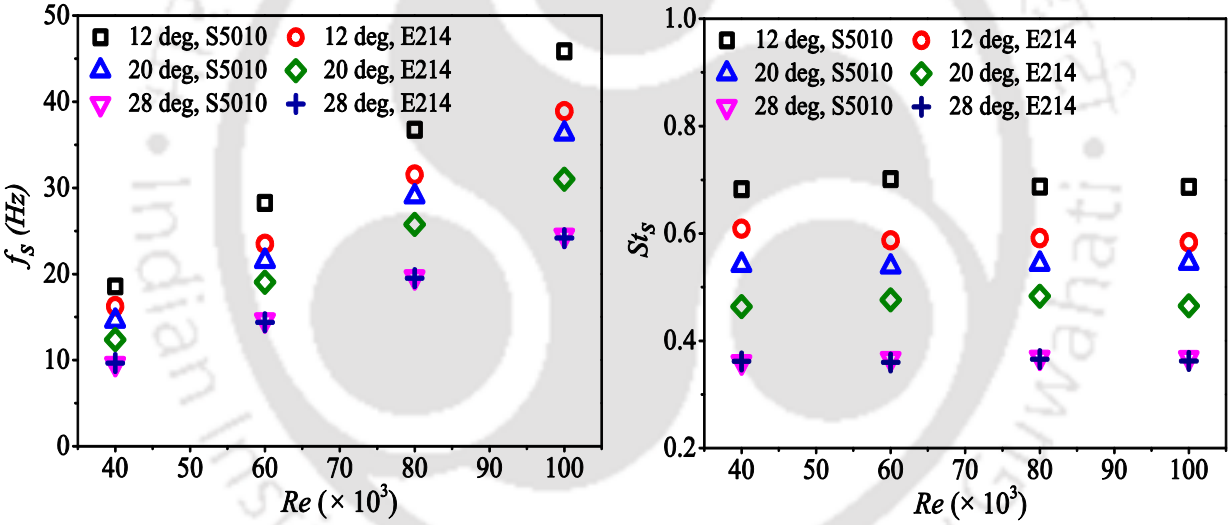

(a) Shedding frequency **(b)** Strouhal number

Fig. 4.13: Comparison of wake shedding characteristics of S5010 and E214 airfoils

4.3.5 Results for Aerodynamic Hysteresis Measurement of Airfoils

In order to observe hysteresis in the aerodynamic characteristics of S5010 and E214 airfoils, the wind tunnel investigations are conducted under steady-state or static conditions. For such an experiment, the wing's *AoA* is increased or decreased step by step with a defined interval of angle. In the present study, the *AoA* is set manually using a pitch controller unit (as provided in the balance apparatus) and measured using a digital spirit level. Once the angle was set, readings were

recorded for 20 seconds with the model fixed, and then the data were averaged over these readings. After data collection, it is varied to the next *AoA*. The experiments are repeated for a range of *AoA* from 2° to 16° with an interval of 1°. To study the possibility of hysteresis in the data within the tested range of *AoA*, measurements were carried out twice: during the increase of *AoA* (forward sweep) and during the decrease of this angle (reverse sweep). The static approach utilized in this study is a conventional method commonly employed by researchers to analyse hysteresis in aerodynamic studies [Hu et al., (2007); Yang et al., (2023)].

The lift and drag measurements of the S5010 airfoil with rising and lowering pitch angles in the range from 2° to 16° at two Reynolds numbers, $Re^a = 100 \times 10^3$ and $Re^b = 40 \times 10^3$ are plotted in **Figs. 4.14**. The analysis of these figures shows that the magnitude of C_l and C_d, with respect to *AoA* is almost similar with increasing *AoA* as that of decreasing angles for the respective *Re*. Moreover, similar experiments are carried out to examine the hysteresis effect in the force and moment measurement for E214 airfoil at the present *Re* regime. No hysteresis is observed in the aerodynamic data of either airfoil for the current *Re* and *AoA* range. The current finding of the hysteresis effect on the aerodynamic coefficients agrees with the reported observation by Ananda et al., (2012) and Torres and Mueller, (2004) for thin profile wings. In their experimental investigations of thin profile wings at low *Re*, they also did not observe any hysteresis in the data and claimed that the small thickness ratio of the wing helps to eliminate the hysteresis.

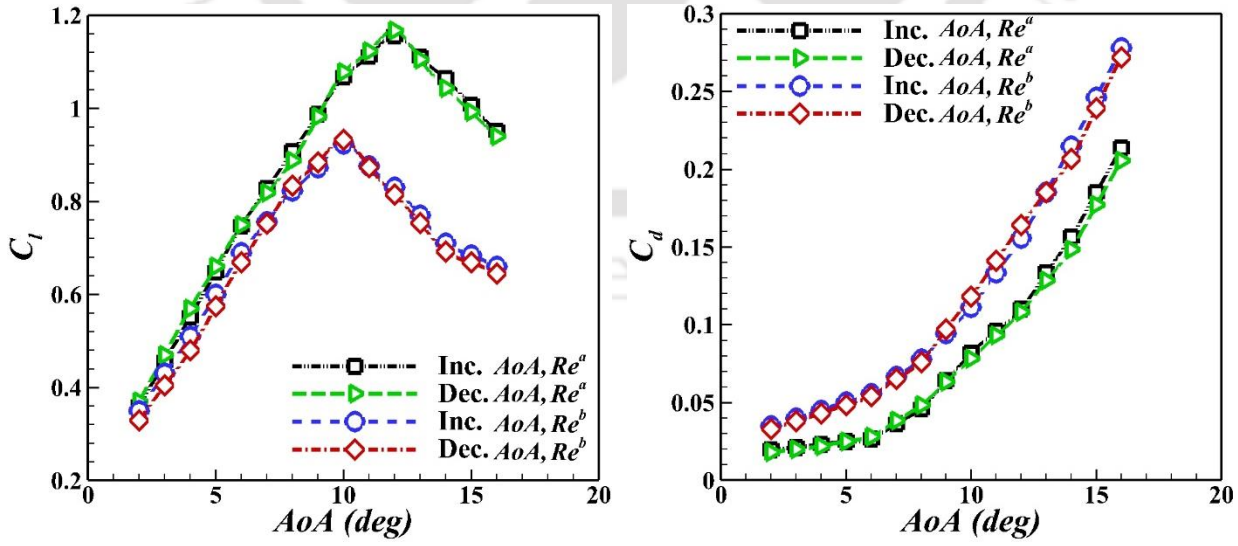

(a) Lift coefficient **(b)** Drag coefficient

Fig. 4.14: Hysteresis analysis in the measurement of C_l and C_d for S5010 airfoil

4.4 Summary

The present study aims to explore the aerodynamic behavior and wake region characteristics of airfoils for the *Re* range of MAV applications. Regarding this, wind tunnel experiments are successfully carried out on the two rectangular infinite wings of sections S5010 and E214 to obtain the aerodynamic coefficients and wake frequency data in the flow regime of $40 \times 10^3 \leq Re \leq 100 \times 10^3$. In this study, the influence of *Re* and *AoA* on different performance and flow parameters such as linearity of lift curve, lift-to-drag ratio, drag coefficient, pitching coefficient, vortex shedding frequency, and Strouhal number for both airfoils have been discussed. It is noticed that the lift curve depicts more linear variation in the pre-stall region, beyond which non-linear variation is observed. For S5010, the slope of lift curve, in the linear region, is found to increase by 14% as *Re* is increased to 100×10^3 for the same *AoA* range. Whereas in the case of E214, this increment is 11%. These findings demonstrate that the performance of the tested airfoil is less responsive to changes in *Re* below 100×10^3 than a conventional airfoil [Winslow et al., (2018)]. This reflects the stability of airfoil within a low flow regime with changing *Re*.

The drag magnitude is almost constant at low *AoA* ($AoA \leq 6°$), after which it increases rapidly, which is expected from the increase in form drag caused by the elongation separation bubble region. Moreover, the *Re* has little effect on the C_d at lower angles ($AoA < 6°$), whereas, for higher angles, the drag increases as the *Re* reduces. The strong influence of *Re* is noticed on the lift-to-drag ratio characteristics of both airfoils; it rises with an improvement of *Re*. For the same *Re*, the magnitude of $(C_l/C_d)_{max}$ is higher for the E214 airfoil compared to the S5010. Here, the pitching moment characteristics are seen to be depend on the lift values where the magnitude of $C_{m,0.25c}$ decreases towards a negative value (pitch-down) as lift increases with *AoA* up stall point; after that increasing trends are observed. The effect of *Re* on the $C_{m,0.25c}$ *is* less prominent for the pre-stall region. However, in the post-stall zone, moment data decreases as the *Re* number increases at a given *AoA*. This represents that the nose-down tendency of the wing is higher for high *Re* in the post-stall region. Comparing the moment data of the two airfoils reveals that E214 has a greater negative value than S5010, which indicates that E214 has a higher propensity to pitch down for the same *Re* and *AoA* range.

In order to investigate the behavior of unstable periodic coherent structures in the wake field of airfoils for post-stall angles, the vortex shedding frequency and associated Strouhal number are

experimentally estimated for *AoA* range of $12° \leq AoA \leq 30°$ and *Re* of $40 \times 10^3 \leq Re \leq 100 \times 10^3$. The analysis shows that the frequency of shed vortices remains constant with varying probe locations within a defined set of coordinate layouts in the wake domain. This signifies that the wake-shedding structure maintains the same coherency and periodicity within a certain defined region. The magnitude of the shedding frequency and corresponding Strouhal number lower as the *AoA* rises for a given *Re*. The flow gets more diverged at a high *AoA*, creating wider wake width, thereby obtaining lesser vortex frequency, and this also leads to relatively higher form drag. Further, shedding frequency rises linearly with the Reynolds number in the form of $f_s \sim Re$ at the given *AoA*. At the same time, the Strouhal number remains almost constant with the variation of *Re* for a particular *AoA*. The magnitude of Strouhal number for both the airfoils shows higher values as compared to bluff body wakes, but as the *AoA* increases, the magnitude difference between them decreases. This finding reveals that the wake structure of the airfoil at high *AoA* behaves as bluff body wakes. Comparing the Strouhal number of both sections, E214 has a lower magnitude than the S5010 below an *AoA* of 24°. Beyond this angle, both the airfoils show almost identical Strouhal numbers. This is a cause of the thickness of the airfoil; S5010 is thinner than the E214 airfoil. Consequently, the S5010 airfoil diverges the flow less and forms a narrower width of wake in the downstream region than the E214. But at high angles ($AoA > 24°$), both airfoil models behave as a bluff body, and therefore, the effect of airfoil thickness on the wake structure is diminished.

CHAPTER 5

Performance of Low Aspect Ratio Wings of Different Cross-sectional Configurations

Overview

An experimental investigation is performed to study the effect of aspect ratio (AR) and Reynolds number (Re) on the wing performance in the low Re range. Force measurement experiments are carried out in the subsonic wind tunnel for the low AR wings composed of S5010 and E214. The AR in each case was varied in the range of 0.5 to 2.0, whereas the Re was varied in the range of 60×10^3 to 150×10^3. The effect of Re on the lift is found to be more prominent in the post-stall region for all ARs except 0.5. This study also indicates that with a decrease in AR, the impact of Re on performance becomes less pronounced. As the AR reduces, the maximum lift coefficient and the lift-to-drag ratio of the wings drop significantly. Similarly, the slope of the lift curve also decreases with a decrease in AR. In contrast, the stall angle shows an improvement with the reduction of AR, and it is more prominent for the wing of the E214 airfoil. The pitching moment values become more negative with an increase in AR, indicating the pitch-down tendency of the wing to rise with AR. Further, no hysteresis is seen in the aerodynamic data of all the wing models of any sections in the present Re limit.

5.1 Introduction

Understanding the characteristics of low aspect ratio (*AR*) wings in a low Reynolds number (*Re*) regime is essential for the design of a low-speed unmanned aircraft. Usually, the *AR* below 2.0 (*AR* ≤ 2.0) comes to the category of a low *AR* of a wing [Torres and Mueller, (2004)]. The aerodynamics associated with these wings, in the *Re* range of 70×10^3 to 200×10^3, are crucial for the efficient design of micro air vehicles (MAVs). The combination of these low *AR* wings and *Re* range has some special aerodynamic characteristics, such as a higher stall angle and nonlinear variation of lift with angle of attack (*AoA*), as compared to a high *AR* wing. In fact, the aerodynamic characteristics of a finite wing (3D) are different from that of an infinite wing (2D) [Zhi-Yong et al., (2018)]. Hence, a finite wing being a three-dimensional object, has a considerable effect on the flow characteristics in the span-wise direction. The classical aerodynamic theory has the potential to analyse such flows like the flow over a full-scale aircraft model, but it has the limitations in predicting the aerodynamic behavior of low *AR* wings in the said range of *Re*. In view of this, various investigations were performed in this flow regime ($70 \times 10^3 \leq Re \leq 200 \times 10^3$) for low *AR* wings to analyse their aerodynamic characteristics and hence the aerodynamic performances [Torres and Mueller, (2001); Weinig, (1947)]. As an outcome of those studies, the lift generation mechanisms of low *AR* wings are divided into two main types of additive lift sources: linear and nonlinear. A linear lift source can be characterized by the presence of a circulation which is the common justification for having lift in high *AR* wings. Whereas, a nonlinear lift is attributed to the presence of large wingtip vortices, which create high cross-flow velocities on the wing's suction side surface [Ruifeng, (2015)].

Numerous theoretical and analytical studies have been reported to model the nonlinear lift variation of the low *AR* wings [Bera and Suresh, (1989); Polhamus, (1966); Weinig, (1947)]. Furthermore, the established Prandtl's lifting-line theory can successfully forecast the pressure distribution of the high *AR* wings, however, it fails to predict the forces of a low *AR* wing accurately. The modified version of Prantl's lifting-line theory for low *AR* was suggested by Boley and Beloterkowski, which predicted properly the pressure distribution and formation of counter-rotating vortical structures at the wing tip [Belotserkovskii, (1968); Bollay, (1939)]. In addition, numerous experimental studies were conducted to investigate the aerodynamic performance of flat plate wings with varied *AR*s and *Re*s. The aerodynamic characteristics of flat plate wings with *AR*

= 0.5 - 2.0 of various planforms (rectangle, Zimmermann, inverse Zimmermann, elliptical) were determined for $Re = 70 \times 10^3$ - 140×10^3 by Torres and Mueller [Torres and Mueller, (2001)]. As per their results, the lift curve becomes progressively nonlinear and the stall angle also rises with a reduction of *AR*. Further, the rectangle and Zimmerman planforms of $AR \leq 1.0$ showed improved performances than other profiles at $Re = 100 \times 10^3$. A similar experiment was also performed for the flat plate (AR = 0.5 - 2.0) at $Re = 70 \times 10^3$ - 200×10^3, which revealed that the transition between nonlinear to linear lift generation mechanism occurs near $AR = 1.25$ [Torres and Mueller, (2004)]. Moreover, Okamoto and Azuma tested various wing planforms (elliptical, rectangular, triangular) with varying *AR* in the range of 0.5 - 8.0 at $Re = 100 \times 10^3$ [Okamoto and Azuma, (2011)]. The stall angle was found to increase significantly for the wing with $AR \leq 1.0$, and the aerodynamic characteristics of rectangular wings were seen to be very similar for $AR \geq 2.0$. Further, the effect of *AR* on the wing performance was noted to be absent at the *AoA* higher than 60°. The slope of the lift curve also needs attention for any finite wing design, which indicates how quickly the wing changes the lift coefficient (C_L) as the *AoA* changes [Gudmundsson, (2014b)]. This slope is generally obtained from the C_L - *AoA* curve, in the region of linear variation of C_L. The lift slope depends on various factors such as *Re*, *AR* [Pelletier and Mueller, (2000); Torres and Mueller, (2004)], turbulence intensity [Mueller et al., (1983)], airfoil geometry (thickness, camber, edge shape, surface roughness) [Sunada et al., (1997)], and others. However, Gutierrez-Castillo proposed a correlation for linear lift-curve slope based on the flat plate experiments ($1.0 \leq AR \leq 8.0$, $40 \times 10^3 \leq Re \leq 200 \times 10^3$) [Gutierrez-Castillo et al., (2021)]. This slope correlation is a function of both *Re* and *AR*. The relation incorporated the concept of Prantl's finite wing theory and extends it to any *Re*.

In the case of a finite wing, the total drag is equal to the sum of form drag, skin friction drag, and induced drag [Anderson, (2011); Sunada et al., (1997)]. The first two contributions are the result of viscous effects, which are also present for the airfoil section and are referred as profile drag. But the induced drag is caused mainly due to the wingtip vortices. It has been seen that, the pressure drag dominates the induced drag for a high *AR* rectangular wings [Okamoto and Azuma, (2011)]. Because of the significant form drag, the drag coefficient (C_D) of high *AR* wings is higher than that of low *AR* wings at smaller *AoA*. However, at a higher *AoA*, the induced drag becomes prominent for low *AR*; and hence, it leads to a higher total drag of the low *AR* wings than that of the high *AR* wing. In the case of low *AR* wing, the increment of drag force is dominated by 3D flow through

the tip over the span induced by wingtip vortices. But, the flow through the wing tip can be controlled by attaching some passive flow control devices like end plates, winglets and others at the wing tips [Beves and Barber, (2017); Miklosovic, (2008); Villeneuve et al., (2019); Yen and Fei, (2011)].

In earlier studies, the aerodynamic hysteresis was commonly seen in the measured data, and usually, it occurs around the stall region and eventually affects the stall conditions [Marchman et al., (1987), (1985); Mizoguchi et al., (2014)]. In such a situation, the aerodynamic coefficient becomes multiple-valued with respect to the *AoA*. The effect of hysteresis during stall has been noticed in lift data for thick and high *AR* wings at low *Re* [Marchman et al., (1987); Marchman and Abtahi, (1985); Schmitz, (1967)]. Contrarily, Ananda et al., (2012) observed the absence of stall hysteresis for the thin wing of low to moderate *AR* range ($2.0 \leq AR \leq 5.0$) in the range of $70 \times 10^3 \leq Re \leq 200 \times 10^3$. Similarly, Torres and Mueller, (2004) also indicated that there was no hysteresis in their experiments ($0.5 \leq AR \leq 2.0$, $70 \times 10^3 \leq Re \leq 200 \times 10^3$). Here, the hysteresis loop gets affected by a variety of parameters such as *AR*, *Re*, turbulence intensity, thickness ratio of wing, and others. [Marchman et al., (1998), (1985); Mizoguchi et al., (2014)]. In case of thicker wings, it has been observed that the hysteresis becomes more noticeable during stall. It is mainly due to the fact that, the wing *AR* and thickness increase and this can be eliminated by reducing the *AR* towards unity. Further, an increased turbulence level in the freestream flow can greatly diminish the size of hysteresis loop [Hoffmann, (1991); Marchman et al., (1987)]. In terms of *Re*, Mueller observed that increasing the *Re* reduces the chance of hysteresis in the lift curve and eliminates its possibilities for Lissaman 7769 and Miley M06-12-128 airfoils [Mueller, (1985a)]. In contrast, for the airfoils S1210 and FX 63-137, the size of hysteresis loop was found to be increased with increasing *Re* [Selig et al., (1996a)]. These findings indicate that the geometry of an airfoil has a major effect on the hysteresis characteristics at low *Re*.

A thorough literature survey showed that, most of the studies have focused on the low *AR* wings of thick symmetric aerofoils or cambered and un-cambered flat plate at low *Re*. Typically, the flat plate and symmetric profiled wings produce lower aerodynamic performance compared to cambered or thin airfoil-based wings in the low *Re* regime [Roy et al., (2020); Soylak, (2016); Winslow et al., (2018)]. But the use of a cambered low-speed (low *Re*) aerofoil in the design of low *AR* wings is still unattained. These airfoils are expected to deliver higher aerodynamic

performance at lower *AoA*. Although an earlier numerical study [Cosyn and Vierendeels, (2006)] addressed the dynamics of flow for the flat plate and S5010 profiled wings at $Re = 100 \times 10^3$, the study mainly compared the flow fields and aerodynamic performance between a flat plate and S5010-wing models of various *AR*s. The study did not address the effect of *Re* and *AR* on the wing performance. Thus it becomes necessary to explore the impact of *Re* and *AR* on the wing performance, especially concerning the use of low-speed airfoils in the design of low *AR* wings with the intention of achieving an improved aerodynamic performance. In view of this, an attempt has been made to generate aerodynamic data of unsymmetrical aerofoil-based low *AR* wings at low *Re* so as to improve the existing design of MAV. These experiments are carried out for rectangular planform wings composed of S5010 and E214 airfoils. The *AR* in each case was varied in the range of 0.5 to 2.0, whereas the *Re* was varied in the range of 60×10^3 to 150×10^3. Experiments are also extended to analyse the hysteresis of the low *AR* wings. Details of the test models, results, and analysis are given in the following sections.

5.2 Wing Models

Different low *AR* wing models, having S5010 and E214 aerofoil sections and rectangular planform, are fabricated for present studies. An *AR* of these low *AR* wings vary from 0.5 to 2.0. These wing models are made out of PLA material using a 3D printing machine. For the same *AR*, the wing dimensions of both the profiles are same, and the dimension of wing details are presented in **Table 5.1**. Here, the model is mounted on top of the balance, which is at the centre of the test section, as can be seen in **Fig. 5.1.** Further, the blockage ratio is one of the important parameters which needs to be considered in the current study. The blockage factor lies between 0.34% and 2.19% when the wing of *AR* = 0.5 is tested in the range of *AoA* = 4^o - 26^o. While it lies between 0.55% and 2.47% for the wing of *AR* = 2.0 in the range of *AoA* = 4° - 18°. As suggested in the literature, it is not necessary to include the blockage correction for the blockage factor values lesser than 5% [Chen and Liou, (2011); Jeong et al., (2018)]. For the error estimation in aerodynamic coefficients measurement, the standard deviation of the samples and subsequent standard error of the mean is estimated. The maximum standard errors of the mean are found to be less than ±3.0 % for lift and moment measurements, while for drag, it is less than ±2.0 %. These estimated errors are represented by the error bars in the lift and drag curves for S5010 wing configurations of *AR* = 2.0 at two different *Re*, as shown in **Fig. 5.2**.

Table 5.1: Wing dimensions

AR	Chord *c (m)*	Span *b (m)*	S5010 t_{max} *(m)*	E214 t_{max} *(m)*	Area $A\ (m^2)$
0.5	0.19	0.095	0.0186	0.0211	0.01805
1.0	0.17	0.17	0.0167	0.0189	0.0289
1.5	0.15	0.225	0.0147	0.0166	0.03375
2.0	0.12	0.24	0.0118	0.0133	0.0288

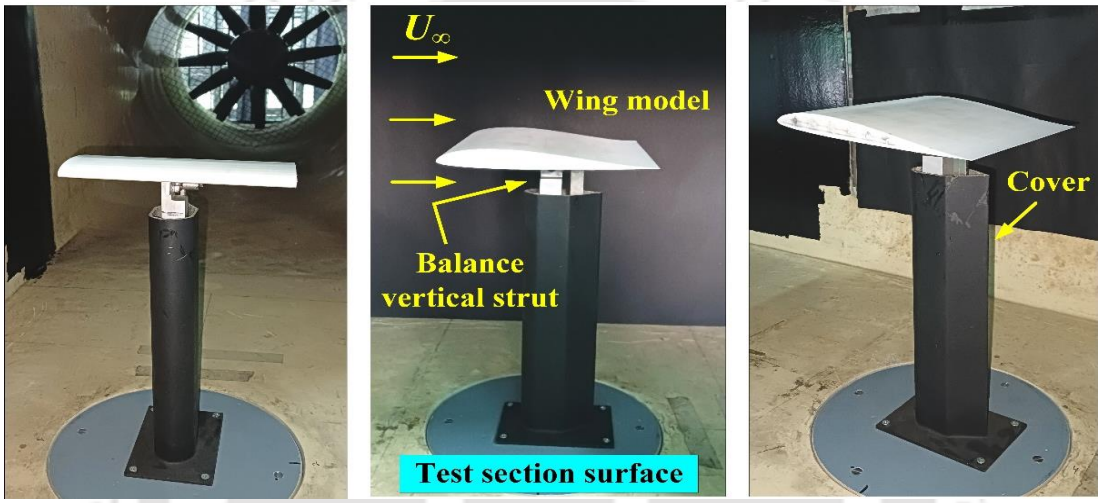

Fig. 5.1: Different views of mounting the test model on the force balance inside the test section

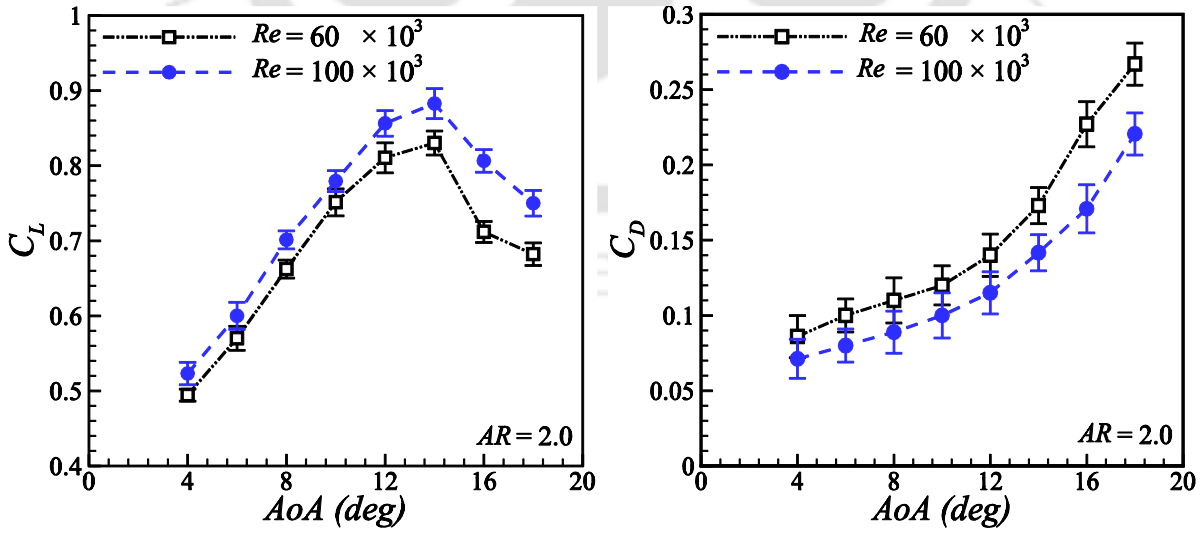

(a) Lift coefficient **(b)** Drag coefficient

Fig. 5.2: Error analysis in the lift and drag measurement

5.3 Results and Discussion

The experimental investigations have been carried out to reveal the aerodynamic forces and moment for the wing models composed of S5010 and E214 airfoils. The *AR* of the models were in the range of 0.5 to 2.0 and they were tested in the range of *Re* from 60×10^3 to 150×10^3. The results of present experiments are discussed in two different sections. The first part of the discussion exhibits the analysis of performance characteristics for S5010 profile-based wing models. While the second part discusses the aerodynamic performance of the low *AR* wing of section E214. It is known that for thick airfoils, the aerodynamic hysteresis is commonly observed in force and moment data at high *AoA* or near stall for low *Re* flow [Mueller, (1985a), (1985b); Selig et al., (1996a)]. Therefore, experiments are also conducted to evaluate the aerodynamic forces and moment data for the test models for both rising and lowering angles of attack to access the hysteresis and the same is also discussed separately.

5.3.1 Results for S5010 Profile-based Wing Models

The performance characteristics of the wing with section S5010 are discussed below in the following sub sections. This discussion includes the effect of *AoA*, *Re* and *AR* on the lift, drag and pitching moment of low *AR* wings.

5.3.1.1 Lift Characteristics

The experimental results of lift characteristics as a function of *AoA* for the S5010 wing model ($0.5 \leq AR \leq 2.0$) with *Re* range ($60 \times 10^3 \leq Re \leq 150 \times 10^3$) are presented in **Fig. 5.3. Figure 5.3a** demonstrates the lift coefficient variation for a wing of $AR = 2.0$ at $60 \times 10^3 \leq Re \leq 100 \times 10^3$. The results indicate that C_L increases with an increased *AoA* up to 14°; after that, it starts to decline rapidly for the present *Re* range. Thus the stall point is detected as 14°, which is consistent with the existing *Re* range, although, the maximum lift coefficient (C_{Lmax}) does differ considerably with *Re*. Also, changing the *Re* has little effect on the C_L for the pre-stall region but has some effect on the lift values in the post-stall region. Further, **Figs. 5.3b and c** show the lift characteristics of the wings of *AR*s = 1.5 and 1.0, respectively. In the case of $AR = 1.5$, the C_L advances near to 16°, and even in the case of $AR = 1.0$, it increases up to 20°. After that, decreasing C_L trend is observed in both cases. The lift coefficients data as a function of *AoA* ($4° \leq AoA \leq 26°$) for the wing of $AR = 0.5$ at the *Re* range ($100 \times 10^3 \leq Re \leq 150 \times 10^3$) is presented in **Fig. 5.3d**. The result indicates that

C_L increases continuously with an increase in *AoA*, with no stall point up to an angle of 26°. In this case, the influence of *Re* on the C_L is minimal till *AoA* ≤ 20°; however, above this angle, the influence of *Re* becomes significant. Further, the influence of the *Re* on the C_L of *AR*s = 1.5 and 1.0 is demonstrated to be small at low *AoA*, when it is in the range of $80 \times 10^3 \leq Re \leq 120 \times 10^3$. But at high angles, the *Re* shows a substantial effect on the C_L.

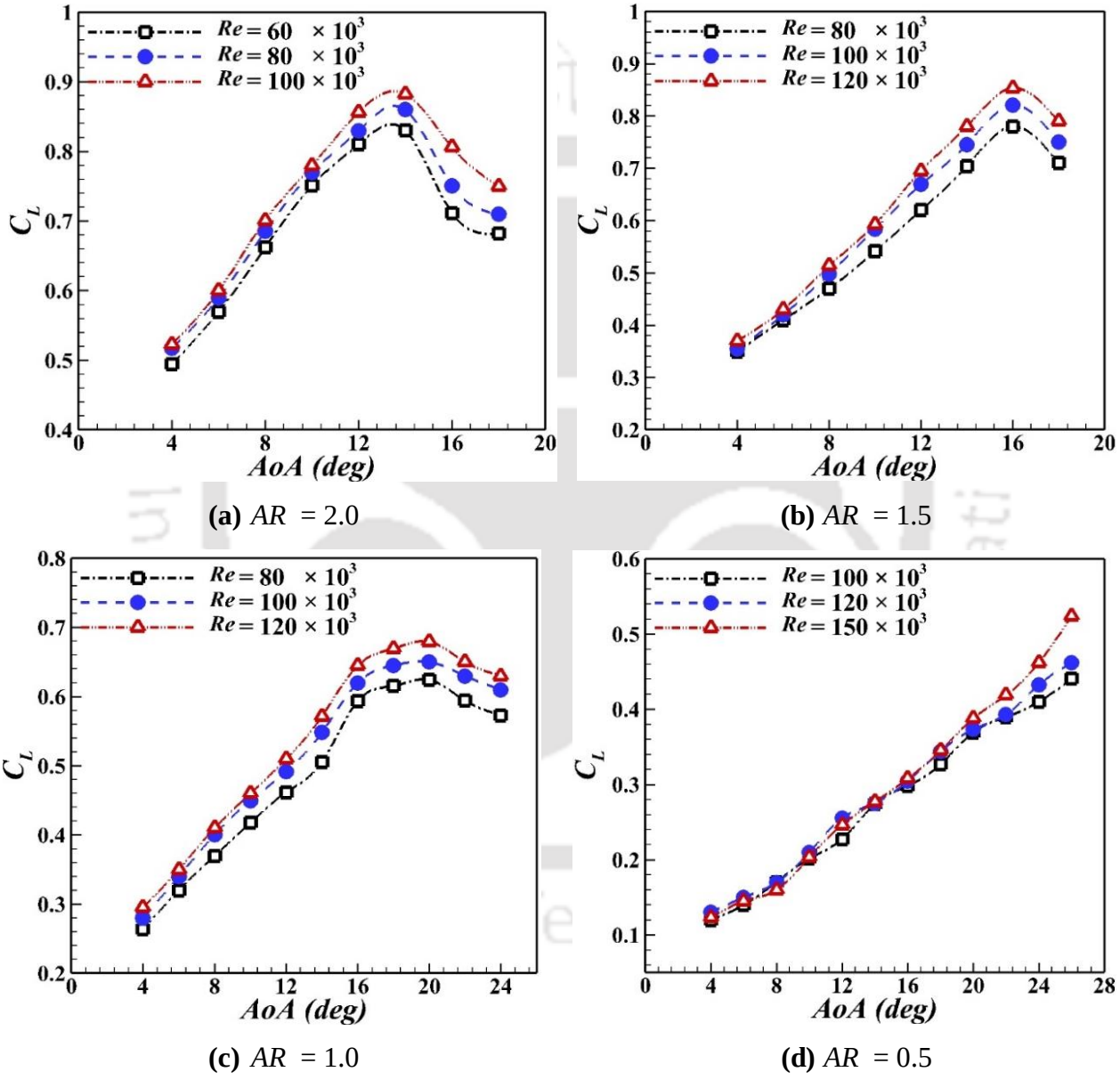

(a) *AR* = 2.0 **(b)** *AR* = 1.5

(c) *AR* = 1.0 **(d)** *AR* = 0.5

Fig. 5.3: Lift characteristics of S5010 wing model at various *AR* and *Re*

For the wing with *AR* = 2.0 - 1.0, the C_{Lmax} increases as the *Re* increases, as shown in **Fig. 5.4**. Similar behavior of C_{Lmax} as a function of *Re* is seen for the cambered plate wings (0.5 ≤ *AR* ≤

3.0) at *Re* range from 50 × 10^3 to 200 × 10^3 [Pelletier and Mueller, (2000)]. The present study reveals that a small change in the *AR* leads to a substantial change in the lift characteristics. A wing of *AR* = 2.0 shows a higher lift value than the wing of *AR* = 0.5 for the current set of *AoA* and *Re* limit. Further, the stall angle also increases with a decrease of *AR*. This can be justified by the classical theory. As per the conventional theories for the prediction of aerodynamic lift for low *AR* wings, the lift generation has two sources: linear and nonlinear [Hoerner and Borst, (1985)]. Linear lift is described by the potential theory where lift is associated with circulation around a wing, while the nonlinear lift component appears from the presence of wing tip vortices. When the wing *AR* is reduced, the potential theory-based lift reduces because of the strong downwash caused by the tip vortices [Mizoguchi and Itoh, (2013)]. Thus, with a decreasing wing *AR*, the total lift decreases. In present studies as well, with a decrease of wing *AR* from 2.0 to 1.0, the C_{Lmax} decreases close to 25% at *Re* = 100 × 10^3, although the corresponding stall angle increases from 14° to 20°. Hence, the C_{Lmax} of the wing decreases with a decrease of *AR*. These C_{Lmax} characteristics agree with the results of thin cambered-plate wings (4% camber, 0.5 ≤ *AR* ≤ 3.0) [Pelletier and Mueller, (2000)]. In contrast, for flat plate wings with 0% camber and *AR* ≤ 3.0, it has been observed that C_{Lmax} rises as *AR* falls [Mizoguchi et al., (2016); Shields and Mohseni, (2012); Torres and Mueller, (2004)]. This demonstrates that the geometry of the wing section influences the C_{Lmax} characteristics associated with *AR*.

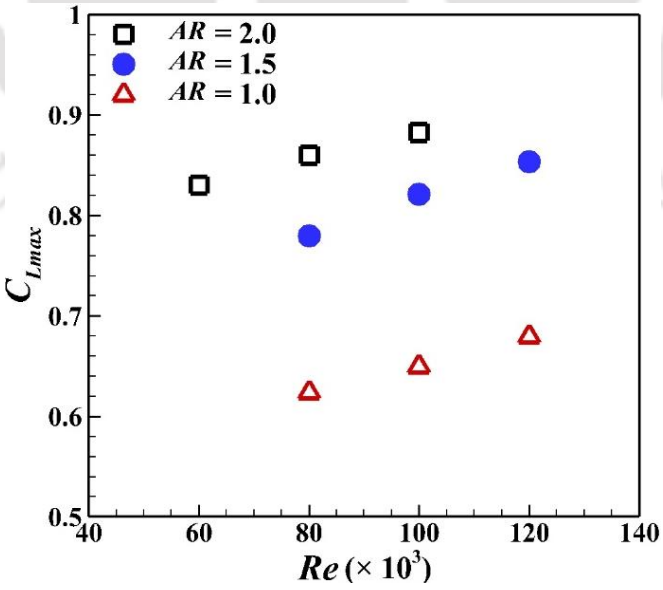

Fig. 5.4: Maximum lift coefficient as a function of *Re* for S5010 wings

Also, the linear characteristics of the lift curve below the stall point is found to be highly influenced by *AR*. Further, a significant change in the lift slope is observed in the C_L - *AoA* curve with the change of *AR*. The high *AR* wings show a linear variation of lift with *AoA*. Therefore, the lift slope is easy to estimate. On the other hand, the low *AR* wings have nonlinear characteristics that makes it difficult to determine the lift-curve slope. Thus, instead of assuming it as linear, the same can be expressed by a polynomial fit. The series of data points are fitted to a second-degree polynomial having R^2 close to unity that shows the best fit to the data for the C_L - *AoA* curve for the pre-stall region. Here, the lift curve slope indicates how quickly the wing changes the lift as the *AoA* changes [Gudmundsson, (2014b)]. The lift slope values are obtained by the first derivative of this polynomial equation with respect to *AoA*. A similar methodology was adopted by Torres and Mueller to obtain C_L slope values for various wing planforms with an *AR* range from 0.5 to 2.0 [Torres and Mueller, (2004)]. Results indicate that the lift slope $(C_{L\alpha})$ of the C_L - *AoA* curve decreases from 0.044 /*deg* to 0.015 /*deg*; when the *AR* changes from 2.0 to 0.5. These slope values are estimated at $Re = 100 \times 10^3$ and are compared with the theoretical predictions of lift-curve slope for thin wings of various *AR*s. The theoretical values of $C_{L\alpha}$ are estimated for the low *AR* wing by using **Eq. 5.1,** which is based on Prandtl's lifting line theory [Anderson, (2011)].

$$C_{L\alpha} = \frac{C_{l\alpha}}{1+\left(\frac{57.3C_{l\alpha}}{\pi AR}\right)(1+\tau)} \quad \left(\frac{1}{deg}\right) \tag{5.1}$$

Here τ is the lift efficiency factor, and the values of τ were calculated by Glauert, which vary between 0.05 and 0.25. The $C_{l\alpha}$ is the slope of the C_l - *AoA* curve for an infinite wing. The conventional value of $C_{l\alpha}$ is 2π /*rad* or 0.1 /*deg*, which is approximated by the thin airfoil theory. In the present study, separate experiments have been carried out on the S5010 infinite wing at $Re = 100 \times 10^3$ to estimate the value of $C_{l\alpha}$. The value of $C_{l\alpha}$ is found to be 0.087 /*deg*. This slope value is determined for a pre-stall region of the C_l - *AoA* curve of the infinite wing. The lower and upper limits of the theoretical values of lift slope are plotted using $\tau = 0.05$ and $\tau = 0.25$ in the *AR* range of $0.25 \leq AR \leq 2.25$ (**Fig. 5.5**). This figure shows the comparison between experimental and theoretical predictions of the C_L - curve slope of the low *AR* wing. The experimental values of $C_{L\alpha}$ for the *AR* of 0.5 to 2.0 show good agreement with the theoretically predicted slope values at $\tau = 0.25$. Also, it reveals that the lift slope decreases when the wing *AR* is reduced. A similar trend of the C_L slope as a function of *AR* was also reported for the flat plate wing [Mizoguchi and Itoh,

(2013); Okamoto and Azuma, (2011)]. This decrease in lift slope with *AR* reflects the lack of a linear region in the C_L - curve. It is observed that when the *AR* reduces from 2.0 to 0.5, the linear area of the C_L - curve becomes smaller. For *AR* = 2.0 model, the C_L-curve shows almost linear variation up to *AoA* ≤ 12°, beyond which nonlinearity is evident. This is because, most of the lift induced by the wing at low *AoA* comes in the form of circulation-based lift, as observed in the high *AR* wings [Bera and Suresh, (1989); Weinig, (1947)]. Thus, the low *AR* wing exhibits a linear lift variation in the C_L - curve at a low *AoA*. When the *AoA* increases, the wingtip vortex increases in size, as a result, the rate of contribution of nonlinear lift to the total lift increases, which in turn, leads to a nonlinear variation in the C_L - curve at large *AoA* [Mizoguchi and Itoh, (2013)].

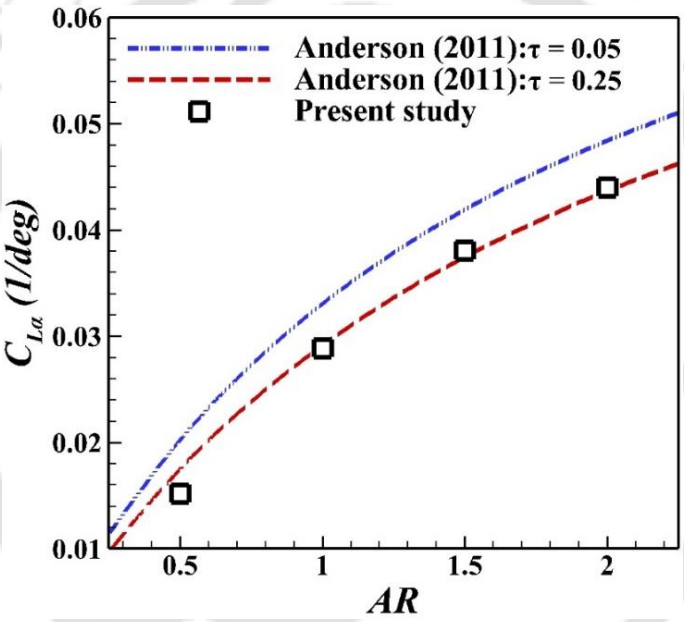

Fig. 5.5: Comparison of experimental and theoretical lift slope values of S5010 wing models at $Re = 100 \times 10^3$

Moreover, the stall characteristics of the wing is found to be more sensitive to the *AR*. For a wing with an *AR* = 2.0, the stall angle is noticed at 14°, whereas no stall angle is detected up to 26° for the model of *AR* = 0.5. Thus, the stall *AoA* rises as the *AR* of the wing diminishes. Identical characteristics of stall angle with *AR* was noted for the low *AR* flat/cambered plate wing in past studies [Mizoguchi et al., (2016); Torres and Mueller, (2004)]. Previously reported results suggested that the strength of the tip vortices increases on the suction surface of the wing with decreasing *AR* [Karasu et al., (2018); Mizoguchi and Itoh, (2013); Montes Gomez and Sumner, (2022)]. The flow induced by these tip vortices is able to re-energize the slower-moving boundary

layer on the suction surface of the wing and thereby delay the flow separation in the downstream direction. These dynamics ultimately increases the stall angle for the lower *AR* wings.

5.3.1.2 Drag Characteristics

Variation of the C_D with *AoA* for the S5010 wing models ($0.5 \leq AR \leq 2.0$) in the *Re* range of $60 \times 10^3 \leq Re \leq 150 \times 10^3$ is illustrated in **Fig. 5.6**. Here, the C_D corresponds to the total drag force of a finite wing, which is the sum of parasite or profile drag and induced drag. Basically, the parasitic drag is a combination of two drags: skin friction (depending on the body surface) and form drag (due to flow separation) [Anderson, (2011)]. Further, the induced drag $(C_{Di} = C_L^{\,2}/\pi AR)$ is created by the presence of downwash, which is due to wing tip vortices in the case of finite wings, and is also called drag due to lift. It has been noticed that the profile drag coefficient of a finite wing is the same as that of the profile drag coefficient of its airfoil sections for a low to moderate *AoA* [Mizoguchi and Itoh, (2013)]. In the present study, the C_D continues to increase with increasing *AoA*, which is the same for all *AR*s of the wing. The value of C_D increases very gradually in the range of lower *AoA* ($AoA \leq 12°$), whereas above 12°, the rate of increase of drag force is higher. This may be due to the variation of surface pressure and induced drag. Because, at a low *AoA*, the flow is completely attached to the wing surface, resulting in lower form drag. But as the angle increases up to stall, the flow begins to separate from the surface and as a result of which both the pressure and the induced drag increase. Beyond the stall point, the flow is completely detached from the suction surface, resulting in a very high-form drag, while the induced drag reduces due to a drop in C_L. Hence at a higher *AoA*, the rate of increase of total drag is higher.

The influence of *Re* on the drag characteristics of the wing is less significant at lower angles but substantial at higher angles ($AoA \leq 14°$). For $AR = 2.0$ and 1.5, a small reduction in the C_D is observed in the post-stall region when the *Re* is increased from 60×10^3 to 120×10^3, which can be seen in **Figs. 5.6a** and **b**. Moreover, no significant effect of *Re* on the drag value is marked for $AR = 1.0$ and 0.5 even at a higher *AoA* (**Figs. 5.6c-d**). Thus, the drag characteristics of wings with $AR \leq 1.0$ is not sensitive to the effect of *Re* in the range of 80×10^3 to 150×10^3. The same drag trend as a function *Re* was also observed for the flat plate in the range of *Re* from 10×10^3 to 100×10^3 [Mizoguchi and Itoh, (2013)]. To study the influence of *AR* on the drag characteristics, the drag data of the *AR* from 0.5 to 2.0 of the wings is compared at $Re = 100 \times 10^3$. This comparison

indicates that the C_D does not change substantially until AoA = 12°, when the AR is lowered from 2.0 to 0.5. However, for $AoA \geq 12°$, an unpredictable behavior of the drag characteristics is observed as the AR of the wing is decreased.

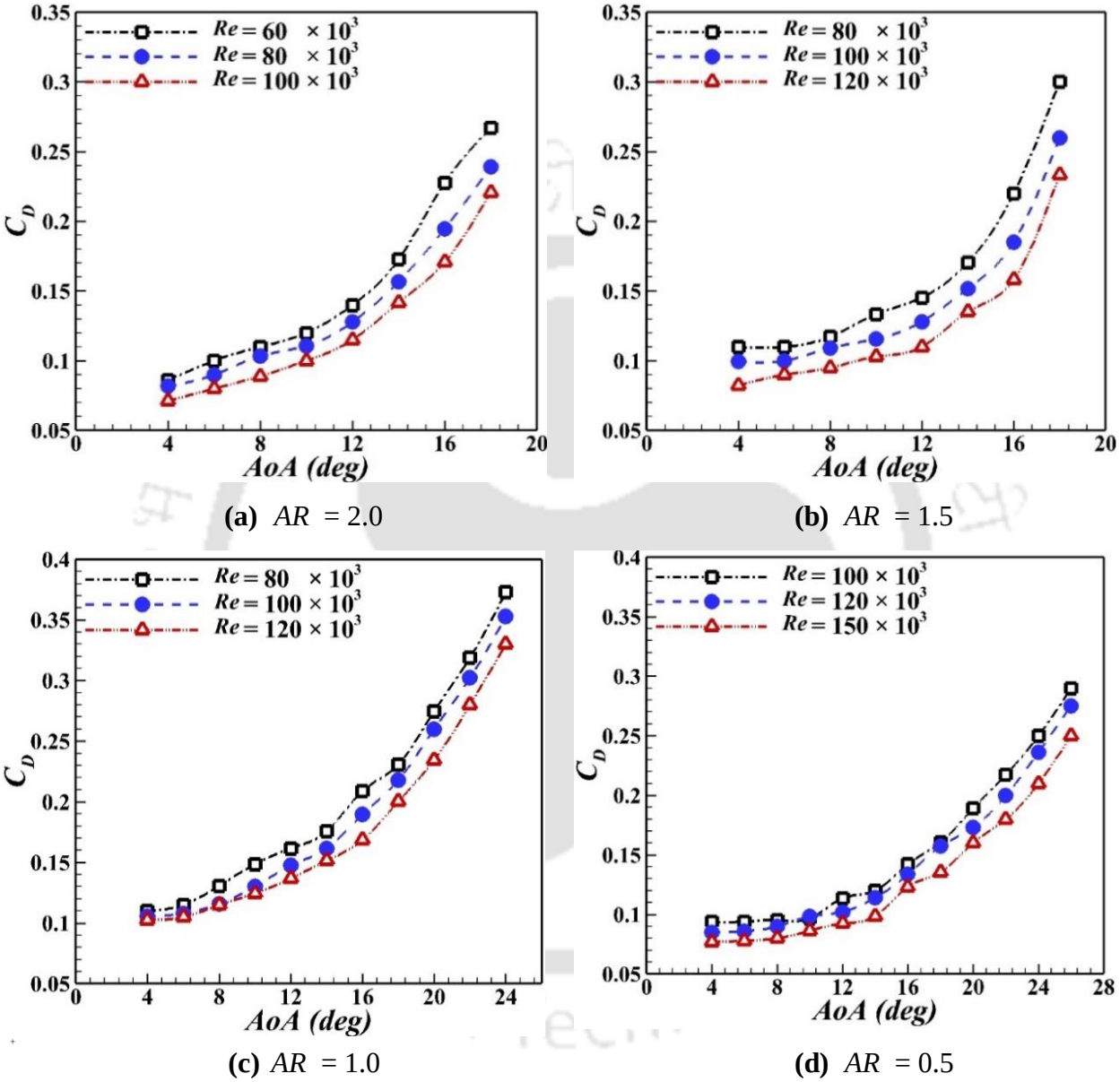

(a) AR = 2.0 **(b)** AR = 1.5

(c) AR = 1.0 **(d)** AR = 0.5

Fig. 5.6: Drag characteristics of S5010 wing model at various AR and Re

Further, the behavior of maximum lift force over drag force ratio as a function of Re, for S5010 wing of various ARs, is presented in **Fig. 5.7**. Usually, the $(L/D)_{max}$ ratio indicates the maximum range for a propeller-based aircraft. In this investigation, the $(L/D)_{max}$ ratio increases significantly when Re is increased from 60×10^3 to 100×10^3 for AR = 2.0. A similar effect of Re on the $(L/D)_{max}$

has been observed for the wing with AR = 1.5 and 1.0 in the Re range of 80 × 10^3 to 120 × 10^3. The same $(L/D)_{max}$ characteristics as a function of Re is noticed by Ananda et al. for the flat plate wing ($2.0 \leq AR \leq 5.0$) at $50 \times 10^3 \leq Re \leq 150 \times 10^3$ [Ananda et al., (2015)]. In addition, when the AR of the wing changes, a significant change in the lift-to-drag ratio is observed. The value of $(L/D)_{max}$ decreases from 8.4 to 3.45 when the wing's AR is reduced from 2.0 to 1.0. This is due to the fact that the C_L is highly dependent on the AR, whereas the C_D is less sensitive. Thus, the $(L/D)_{max}$ ratio reduces with a reduction in AR of the wing. The same behavior of $(L/D)_{max}$ as a function of AR and Re is reported for the flat / cambered plate wings [Mizoguchi et al., (2016); Pelletier and Mueller, (2000)].

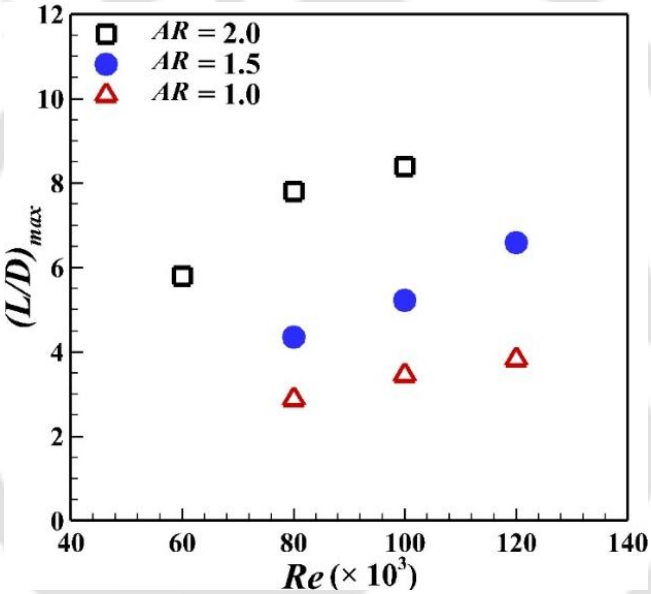

Fig. 5.7: Maximum lift-to-drag ratio as a function of *Re* for S5010 wing models

5.3.1.3 Pitching Moment Characteristics

Figure 5.7 demonstrates the pitching moment about the quarter chord ($C_{M,0.25c}$) as a function of *AoA* for various *AR*s and in the given *Re*s range. The moment coefficient decreases with an increase in *AoA* up to 14°; beyond which, an increasing trend is observed for AR = 2 (**Fig. 5.8a**). Similarly, the value of $C_{M,0.25c}$ drops with the rise of angle up to 16° for AR = 1.5, whereas, for AR = 1.0, it decreases to an angle of 18° (**Figs. 5.8b-c**). Beyond stall, the values of $C_{M,0.25c}$ increase with *AoA* for AR = 1.5 and 1.0. Although, the pitching moment is the consequence of lift and drag forces acting on the model, the rise in the moment curve after a certain *AoA* is related to the reduction of

lift. This because the moment curve changes its behavior close to the stall angle for all wings of *AR* = 2.0, 1.5, and 1.0. But, at *AR* = 0.5 (**Fig. 5.8d**), the $C_{M,0.25c}$ continues to decrease to negative values for the tested *AoA* range ($4° \leq AoA \leq 26°$). For *AR* = 0.5, it is observed that the C_L also increases with an angle of up to 26°. Therefore, it can be concluded that the pitching moment behavior depends more on the lift characteristics of the wing.

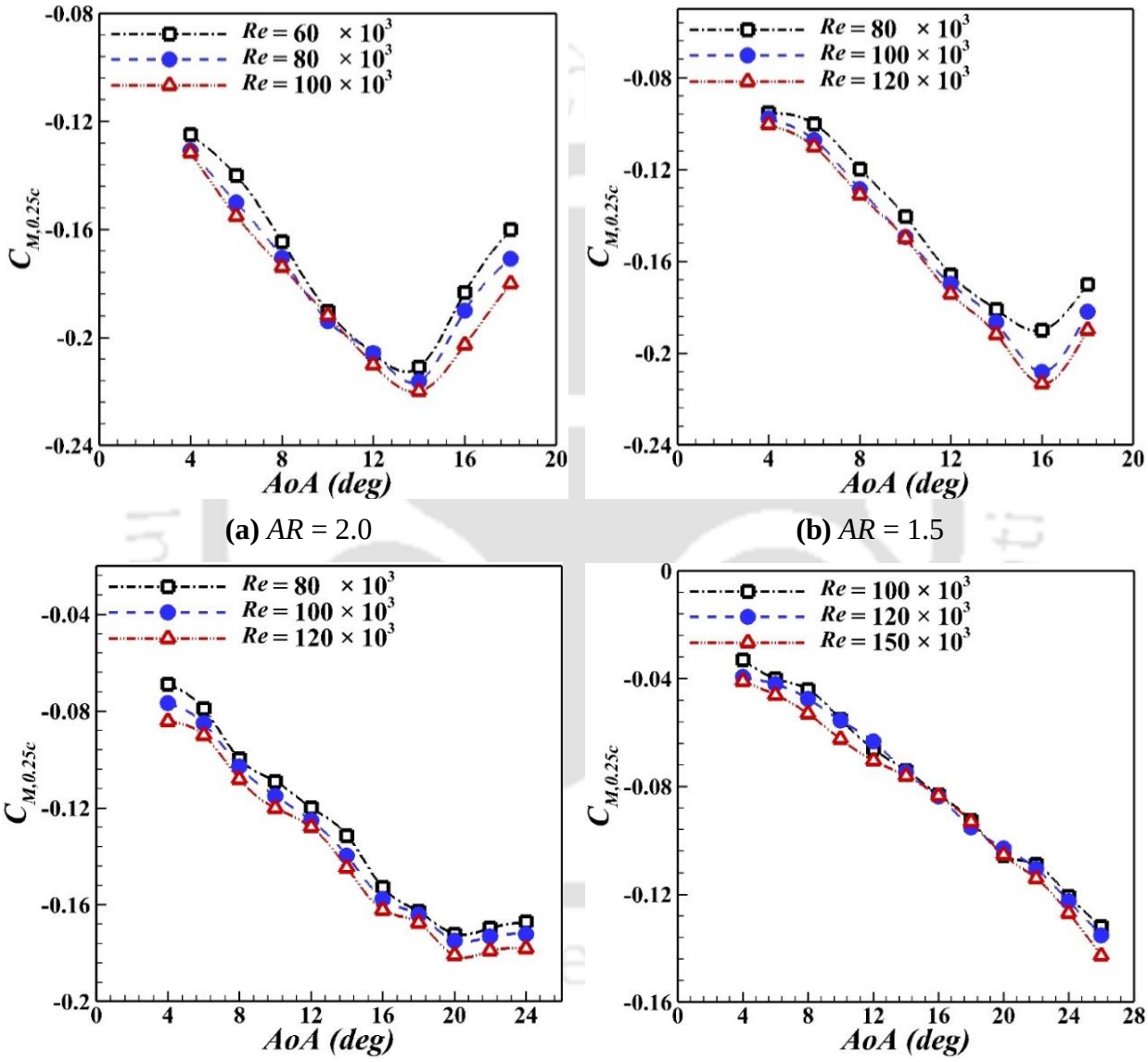

(a) *AR* = 2.0 **(b)** *AR* = 1.5

(c) *AR* = 1.0 **(d)** *AR* = 0.5

Fig. 5.8: Pitching moment characteristics of S5010 wing model at various *AR* and *Re*

In this case, the negative pitching moment indicates that when the *AoA* rises, it tends to rotate the wing towards its equilibrium position to counteract the disturbances induced by the *AoA*. Further,

Mizoguchi and Itoh, (2013) stated that if the low-pressure region advances towards the trailing edge on the suction surface, the pitching moment reduces to negative values. Consequently, the cause of the pitching moment reducing to negative values before the stall angle is assumed to be the spread of the separation bubble over the suction surface. Also, a significant effect of the *AR* has been seen on the moment coefficient. The value of $C_{M,0.25c,}$ changes very rapidly with pitch angles for wings with *AR* = 2.0 and 1.5, whereas for *AR* = 1.0 and 0.5, it changes very gradually. These changes are related to the different lift values for the wing with different *AR*s. Similar moment behavior with flat plate wings of various *AR*s has been noted by Okamoto and Azuma, (2011). In addition, no measurable difference is observed in the pitching moment values of the tested wings due to the change of respective *Re* range. The same effect of *Re* on the pitching moment behaviour is noticed for the flat plate in the range of 10×10^3 to 100×10^3 [Mizoguchi and Itoh, (2013)]. However, the strong influence of *AR* on the moment characteristics is noticed for the tested *AR* range and at $Re = 100 \times 10^3$. The moment values become more negative for the same *AoA* when the *AR* increases from 0.5 to 2.0. Hence, the moment slope in the $C_{M,0.25c}$ - *AoA* curve reduces when the *AR* changes from 0.5 to 2.0. This signifies that the pitching-down tendency of the wing increases with the increase of *AR* for the same flow conditions.

5.3.2 Results for E214 Profile-based Wing Models

The aerodynamic performance of the low *AR* wings composed of E214 airfoil is discussed to find the effect of *AoA*, *Re*, and *AR* on the lift, drag, and pitching moment.

5.3.2.1 Lift Characteristics

The results of C_L of the wing with *AR* = 2.0 are presented in **Fig. 5.9a**. The value of C_L increases with an angle up to 14°, and then decreasing trend is marked at $Re = 60 \times 10^3$. While for $Re = 80 \times 10^3$ and 100×10^3, the C_L increases up to 16°, and thereafter, it begins to decrease rapidly. At two different *Re*, two distinct stall angles have been recorded for the same airfoil (*AR* = 2.0). In the case of *AR* = 1.5, the C_L rises to an angle of 18°, after which it declines rapidly with an increase in *AoA* for the tested *Re* range (**Fig. 5.9b**). Moreover, the C_L grows very gradually with *AoA* for *AR* = 1.0 and 0.5. For *AR* = 1.0, the stall point is recorded as close to 22° (**Fig. 5.9c**). While no stall has been detected for *AR* = 0.5 till the angle of 26° (**Fig. 5.9d**). The strong influence of the *AR* is seen on the stall characteristics as well as the C_{Lmax} of the E214 wing. When the *AR* changes

from 2.0 to 1.0, the C_{Lmax} is reduced by about 38% at $Re = 100 \times 10^3$. A similar increase in C_{Lmax} with *AR* was also noticed for the cambered plate wings [Pelletier and Mueller, (2000)]. However, the corresponding stall angle increases from 16° to 22° as *AR* is varied from 2.0 to 1.0. Hence, the influence of the *AR* on the lift curve slope is also noticed for the E214 wing models.

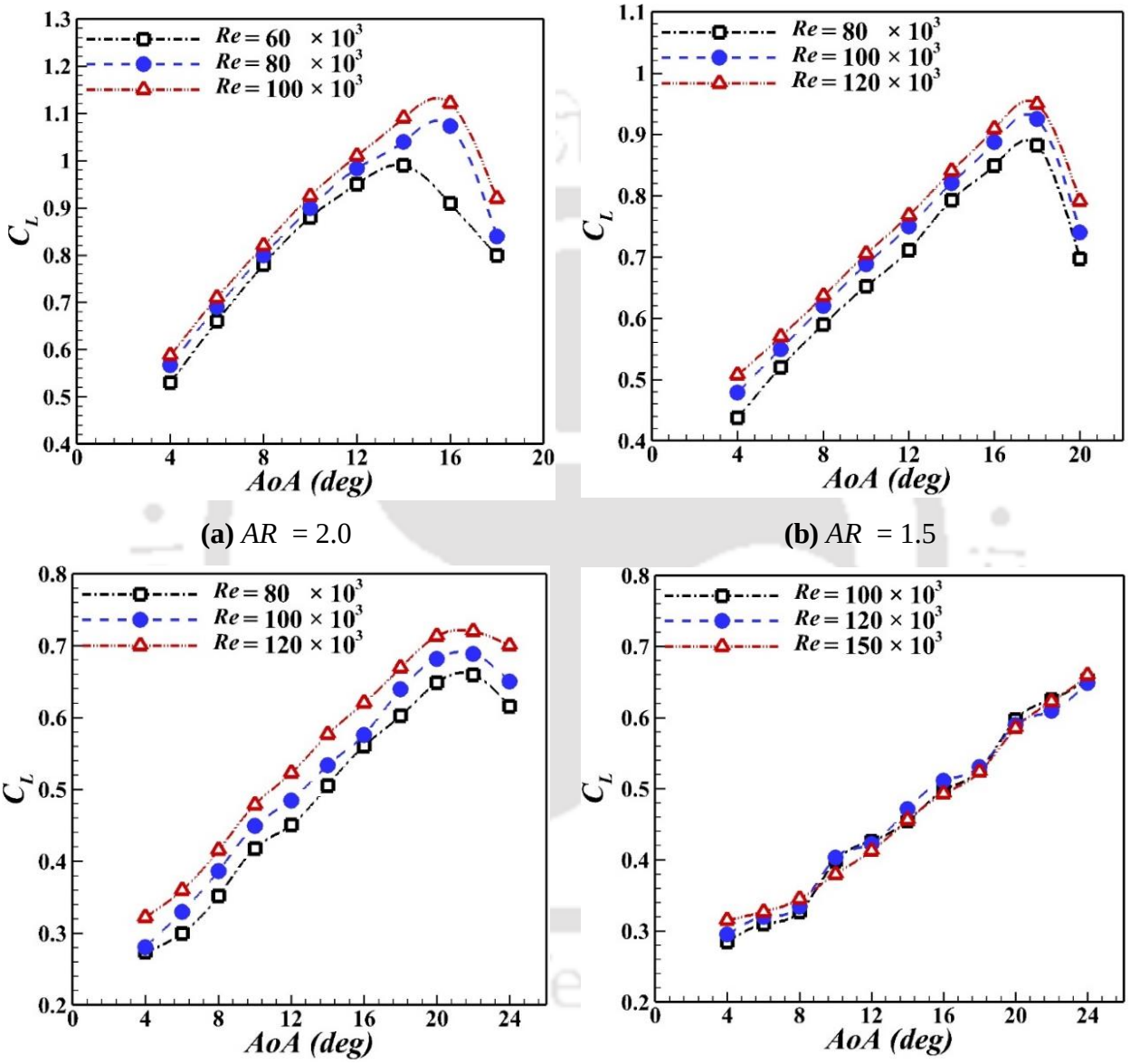

(a) *AR* = 2.0 **(b)** *AR* = 1.5

(c) *AR* = 1.0 **(d)** *AR* = 0.5

Fig. 5.9: Lift characteristics of E214 wing model at various *AR* and *Re*

Similar to the S5010 case, the lift slope values are also calculated by taking the first derivative of the second-degree polynomial equation with respect to the *AoA*. This polynomial equation is obtained from the C_L - *AoA* curve by the curve fitting process. According to the estimates for the

slope of the C_L - *AoA* curve, the value of $C_{L\alpha}$ declines from 0.053 /*deg* to 0.026 /*deg* when the *AR* reduces from 2.0 to 1.0 for $Re = 100 \times 10^3$. The present behavior of the lift slope associated with *AR* is supported by reported experimental studies of flat plate wings [Mizoguchi and Itoh, (2013); Okamoto and Azuma, (2011)]. Furthermore, the influence of *Re* is less significant on the lift characteristics before stall region for wing with an *AR* range of $1.0 \leq AR \leq 2.0$ at $60 \times 10^3 \leq Re \leq 120 \times 10^3$. However, for the post-stall region in the C_L - *AoA* curve, a small improvement in the lift is observed due to a change in the *Re* from 60×10^3 to 120×10^3. For $AR = 2$, the C_{Lmax} increases by 13% when the *Re* changes from 60×10^3 to 100×10^3. For $AR = 1.5$ and 1.0, the value of C_{Lmax} increases close to 10% when *Re* changed from 80×10^3 to 120×10^3. The effect of *Re* on the C_{Lmax} characteristics is supported by the past studies of the flat plate wing [Murphy and Hu, (2010); Pelletier and Mueller, (2000)]. For $AR = 0.5$, changing the *Re* does not appear to have a substantial effect on lift characteristics in the *Re* range from 100×10^3 to 150×10^3.

5.3.2.2 Drag Characteristics

The variation of drag for various wing models ($0.5 \leq AR \leq 2.0$) in the tested *Re* range is illustrated in **Fig. 5.10**. The C_D increases with increasing *AoA* for all the wing models. However, the value of C_D rises gradually with an angle for $AoA \leq 12°$, while at higher angles, the drag force rises rapidly with the *AoA*. It has been reported for the streamlined bodies that at lower angles, the values of form drag and induced drag are low, and so most of the drag force is due to the contribution of skin friction drag [Anderson, (2011)]. This theory helps to explain the lower rate of rising C_D for lower *AoA*. However, as the *AoA* increases, the flow begins to separate from the suction surface of the wing. As a result, form drag begins to increase due to flow separation, and hence the C_D increases rapidly at high *AoA*. The effect of the *Re* on the drag characteristics of the wing models is less substantial for lower *AoA* but is more significant at higher *AoA* for $AR = 2.0$ and 1.5 (**Fig. 5.10a-b**). When the *Re* drops from 100×10^3 to 60×10^3, a considerable increase of drag is noticed at $AR = 2.0$ for $AoA \geq 15°$. Whereas $AR = 1.5$, the *Re* effect on the C_D is seen after an angle of 18°. With changing *Re* from 80×10^3 to 150×10^3, no significant improvement in the drag curve is found even at higher *AoA* for $AR = 1.0$ and 0.5. Hence, it may be concluded that for $AR \leq 1.0$, the drag characteristics of the wing shows minimal variation with the changing *Re*. In addition, the drag characteristics of the wing does not change substantially when the *AR* is varied between 2.0 and 1.0 for $AoA \leq 14°$ and $Re = 100 \times 10^3$. Moreover, the drag characteristics of $AR = 0.5$ appears

almost identical to other *AR*s for *AoA* ≤ 10°, but above this angle, higher drag values are observed compared to others.

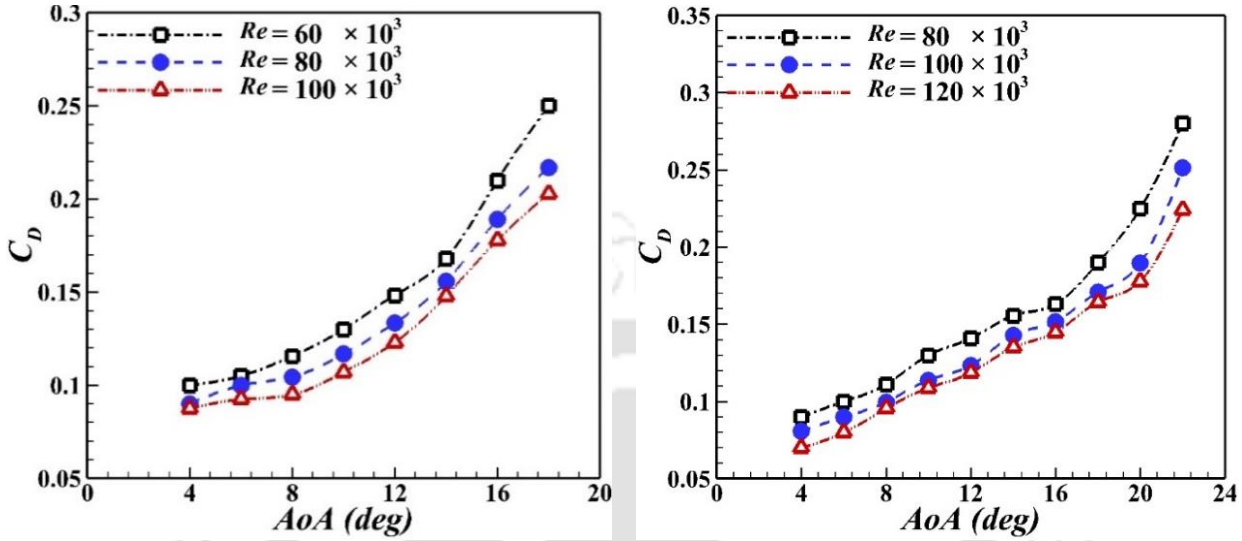

(a) *AR* = 2.0

(b) *AR* = 1.5

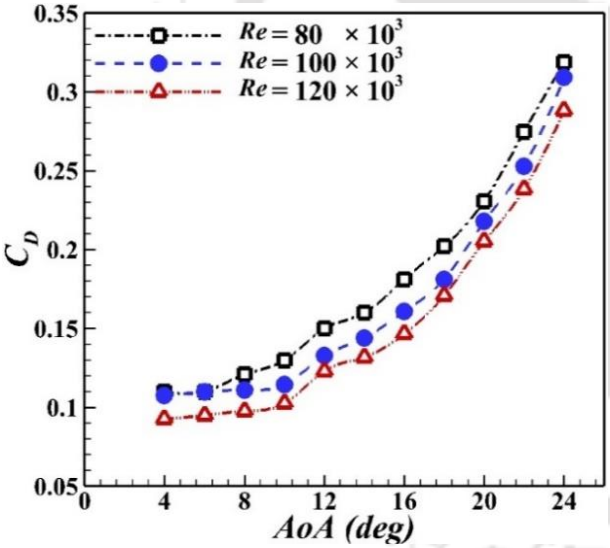

(c) *AR* = 1.0

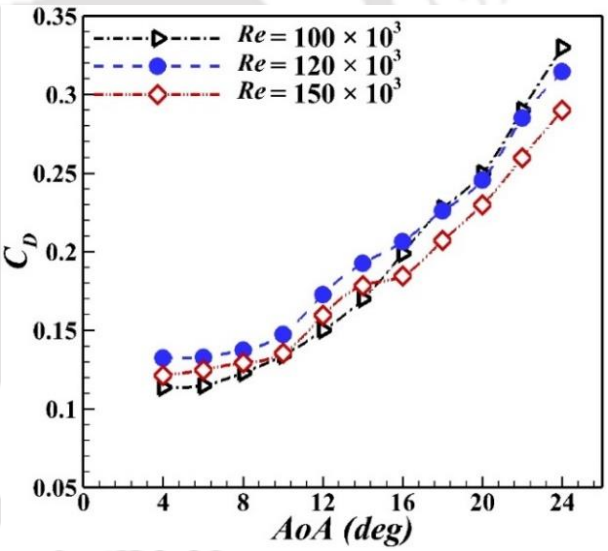

(d) *AR* = 0.5

Fig. 5.10: Drag characteristics of E214 wing model at various *AR* and *Re*

5.3.2.3 Pitching Moment Characteristics

Similar to the S5010 wing model, here also, the pitching moment data for all E214 models is obtained at about a quarter chord of the wing ($C_{M,0.25c}$). It is then plotted as the $C_{M,0.25c}$ - *AoA* curve for various *Re* ranges, as shown in **Fig. 5.11**. The moment coefficient reduces to negative values

with increasing *AoA* up to 14°, beyond which, there is an increasing trend for *AR* = 2.0 at *Re* = 60 × 10^3. For the same *AR*, the pitching moment curve decreases to 16° at *Re* of 80 × 10^3 and 100 × 10^3, and then an increasing trend with *AoA* is noticed (**Fig. 5.11a**). The rise in moment curve after a certain *AoA* is related to the reduction of lift [Okamoto and Azuma, (2011)]. Since it is observed that the lift curve changes its behavior closer to the stall angle, a similar pattern is observed for the moment curve as well. It also changes its behavior near the stall point.

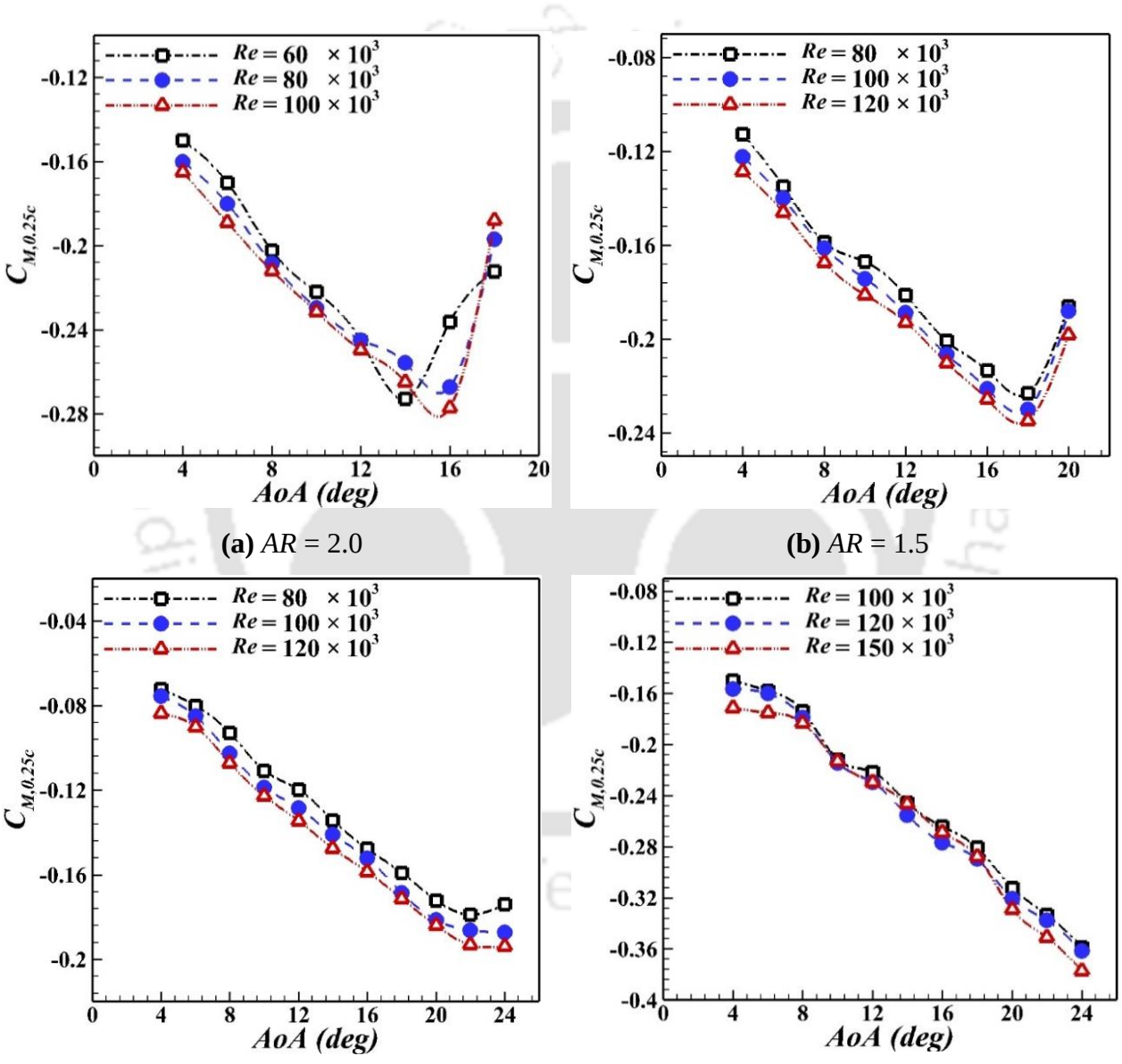

(a) *AR* = 2.0 **(b)** *AR* = 1.5

(c) *AR* = 1.0 **(d)** *AR* = 0.5

Fig. 5.11: Pitching moment characteristics of E214 wing model at various *AR* and *Re*

Similar trends of $C_{M,0.25c}$ - *AoA* are observed for *AR* = 1.5 and 1.0. The value of $C_{M,0.25c}$ declines towards negative values and then rises beyond *AoA* = 18° in the case of *AR* = 1.5, while for *AR* = 1.0, it decreases to 22° (**Figs. 5.11b-c**). Thus, the moment curve of the model with *AR* of 1.0 - 2.0 continues to decrease until the stall angle of respective wings, and increasing trends are observed thereafter. Therefore, it can be said that the pitching moment characteristics depend on the lift behavior of this wing. The same behaviour of the moment curve with lift has also been observed for the S5010 wing case. For wing of *AR* = 0.5, the moment coefficient continues to increase its negative value in the tested range of *AoA* (4° ≤ *AoA* ≤ 26°) (**Fig. 5.11d**). Furthermore, the value of $C_{M,0.25c,}$ changes very significantly with *AoA* at *AR* = 2.0 and 1.5, whereas it changes relatively slowly for wings at *AR* = 1.0 and 0.5. These changes are related to the different lift slope values for a wing with different *AR*s. As seen in the case of S5010 wings, here also *AR* substantially impacts the moment values of the pre-stall region. When the wing's *AR* varies from 0.5 to 2.0, the moment value becomes more negative for the same *AoA* (for pre-stall region), which is estimated at *Re* = 100 × 10^3. Moreover, there is no effect of *Re* on the moment characteristics of all the test models in the present respective *Re* range. Similar behavior of pitching moment associated with *Re* is reported for the flat plate wing [Mizoguchi and Itoh, (2013)].

5.3.3 Comparative Analysis of S5010 and E214 Wing Models

Analysis of results revealed that S5010 and E214 wing models show different aerodynamic characteristics in the same *AR* and *Re* range. This difference may be due to different profile geometries and maximum thickness-to-chord ratios (*t/c* = 9.8%, S5010, *t/c* = 11.1%, E214) at different locations of the wing sections. However, the *Re* and *AR* have shown similar effects on the performance curves of the respective wings for both airfoils. In the case of E214 wing models, the stall angle increases from 16° to 22° when the *AR* decreases from 2.0 to 1.0. However, for the S5010 model, it changes from 14° to 20°. Thus, the E214 profile wing shows a higher stall angle as compared to the S5010 profile at the same *AR* and *Re*. Moreover, the C_{Lmax} data are presented for wing models of both airfoils at various *AR* and at *Re* = 100 × 10^3 (**Fig. 5.12**). The results indicate that the E214 wing has a higher C_{Lmax} value than the S5010 model for *AR* = 2.0 and 1.5. But, for *AR*= 1.0, the C_{Lmax} is almost similar for the two airfoils, however, it is found at a higher *AoA* in the case of the E214 airfoil than the S5010 airfoil. Further, the $(L/D)_{max}$ ratio characteristics as a function of *Re* for both airfoils at *AR* = 2.0 and 1.0 are presented in **Fig. 5.13**. For wings with

an *AR* range from 1.0 to 2.0, the E214 models show a better $(L/D)_{max}$ value than S5010 at a given *Re* range. Also, for a given *AR* and *Re*, no significant difference has been observed in the drag characteristics of the two models at low to moderate *AoA* for the *AR* range ($1.0 \leq AR \leq 2.0$). However, for *AR* = 0.5, E214 wings show a higher drag value than S5010 airfoil for $100 \times 10^3 \leq Re \leq 150 \times 10^3$. The moment characteristics for the E214 model offer more negative values with respect to the *AoA* than the S5010 wings for a given *AR* and *Re*. This observation suggests that the E214 model has a more pronounced tendency to pitch-down than the wing based on S5010 airfoil.

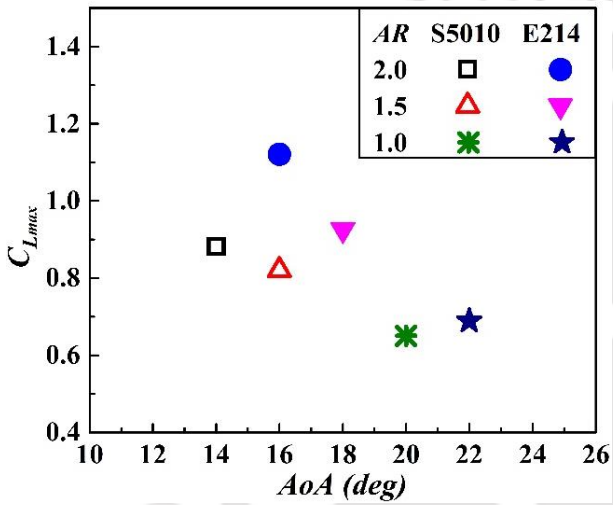

Fig. 5.12: Maximum lift coefficient for S5010 and E214 wings for various *AR*

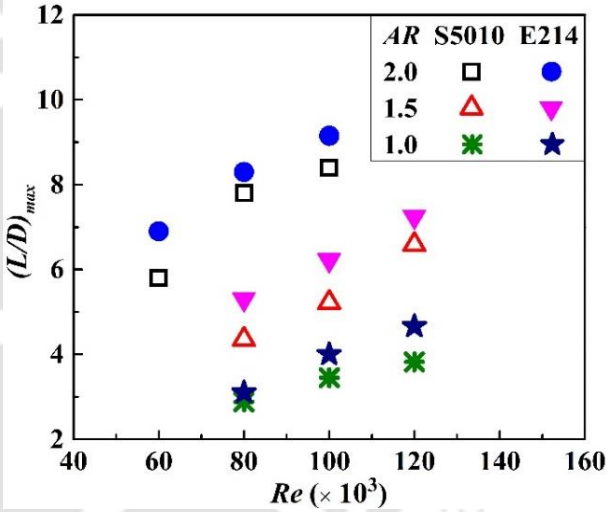

Fig. 5.13: Maximum *L/D* ratio as a function of *Re* for S5010 and E214 wings

5.3.4 Results for Hysteresis Measurements

To investigate the hysteresis behavior in the C_L, $C_{D,}$ and C_M data, experiments are performed to evaluate the aerodynamic forces and moment of the models at both increasing and decreasing *AoA*. The results of C_L and C_D for the S5010 wing of *AR* = 2.0 in the *AoA* range of 4° to 18° at two different *Re*, $Re^a = 100 \times 10^3$ and $Re^b = 60 \times 10^3$, are presented in **Fig. 5.14.** The analysis reveals that the values of C_L and C_D for increasing *AoA* are the same as those for decreasing *AoA* between angles 4° and 18°. Consequently, no hysteresis is observed in the aerodynamic behavior of the S5010 wing within the tested *AoA* range and *Re*. Similar experiments are also carried out to assess hysteresis for other wing models with various *AR* at different *Re*. Resulting in no appreciable aerodynamic hysteresis has been seen in the data for the tested wing models and *Re* range. Similarly, Ananda et al., (2012) and Torres and Mueller, (2004) also found no stall hysteresis for

different ranges of low *AR* flat plate wings over the low *Re* range. They presumed that hysteresis does not exist for thin and low to moderate *AR* wings at a low *Re*, and it can be eliminated with the use of a small thickness of wings. The present study agrees with the reported observations because both sections (S5010 and E214) of a wing belong to the category of a thin airfoil, and no hysteresis is observed in the data even at high *AoA* of the tested range of *AR* and *Re*.

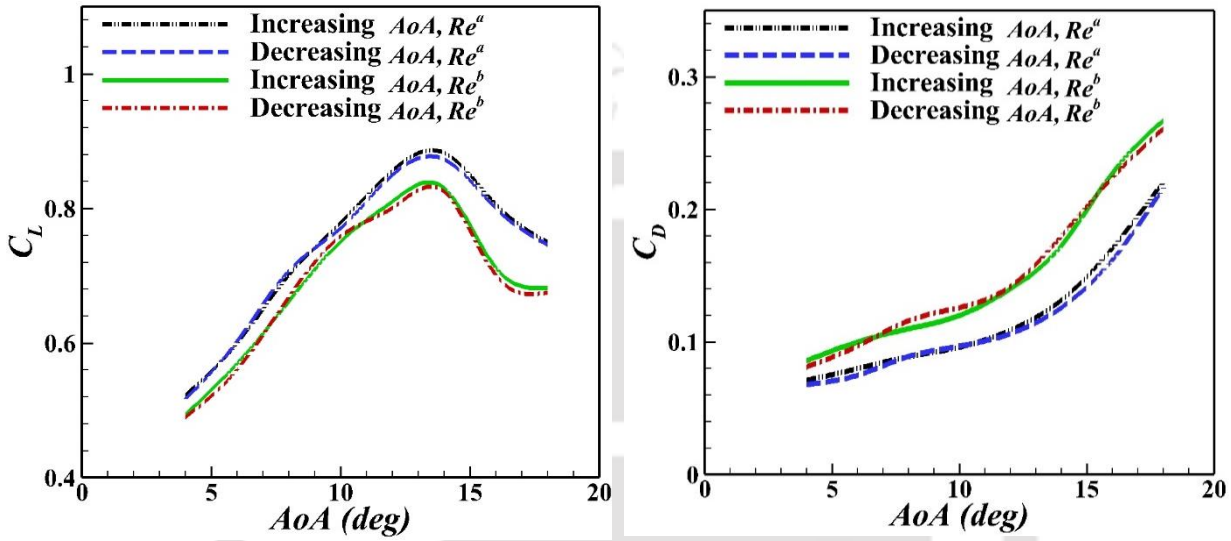

(a) Lift coefficient **(b)** Drag coefficient

Fig. 5.14: Hysteresis analysis in C_L and C_D measurements for S5010 wing of *AR* = 2.0

5.4 Summary

Wind tunnel tests are conducted with two different sections of a rectangular wing with various *AR*s in the *Re* range of 60×10^3 - 150×10^3. The effect of *Re* and *AR* on the aerodynamic performance is explored successfully for the wings of the S5010 and E214 sections. For a wing of *AR* in the range of 2.0 to 1.0, the effect of the *Re* is less significant on the lift characteristics before the stall region. While, for post-stall-region, C_L increases with increasing *Re*. Additionally, the C_{Lmax} and $(L/D)_{max}$ parameters of the wing improve with rising *Re*. In contrast, the stall characteristics of the wing are less affected by the *Re*. For *AR* = 2.0 and 1.5, the effect of the *Re* on the C_D of the wing is less significant at lower *AoA* but it is more substantial at higher angles. The C_D of the wing for the stall zone considerably reduces as the *Re* increases. Moreover, no significant effect of *Re* on drag value is noted for *AR* = 1.0 and 0.5 even at a higher *AoA*. It is concluded that when the *AR* ≤ 1.0, the drag values of the wing show minimal variation with changing *Re*. Thus, it is believed

that, as the *AR* of a wing reduces, the effect of the *Re* on wing performance diminishes. In addition, no measurable difference is observed in the pitching moment values in the tested *AR* due to the change in the respective *Re* range.

The effect of *AR* on wing performance is a more influencing factor than the *Re*. A wing of *AR* 2.0 shows a higher lift value than an *AR* of 0.5 for the same *AoA* and *Re*. When the *AR* changes between 2 and 0.5, the C_{Lmax} and $(L/D)_{max}$ for the S5010 and E214 wing configurations dropped significantly. In addition, the stall characteristics of the wing improves with a decrease of *AR*. The lift slope value of the C_L - *AoA* curve drops with decreasing *AR*. This decrement in slope value with *AR* indicates a reduction in the linear region of the C_L - *AoA* curve. For the S5010 wing, the C_D does not alter significantly until *AoA* = 12°, with a varying *AR* from 2.0 to 0.5. In case of E214 wing, similar drag characteristics as a function of *AR* are found for *AoA* ≤ 14° and *AR* range of 2.0 to 1.0. Further, the C_D of *AR* = 0.5 is almost identical to other *AR* for *AoA* ≤ 10°, but above this angle, this wing shows higher drag values than others. It is also found that the pitching moment values of the wing become more negative with increasing *AR*. Hence, the pitch-down tendency of the wing rises with increasing *AR*. From the above discussion, it concluded that the *AR* effect on the wing performance increases at lower *AR*. Further, no hysteresis is seen in the aerodynamic forces and moment data of all the wing models of any sections in the tested *Re* range. A comparison of results of two wing configurations (S5010, E214) shows that E214 wings offer better aerodynamic characteristics than S5010 wings in the tested range of *AR* and *Re*. Overall, the aerodynamic results obtained for a low *AR* wing based on low-speed airfoils in the low *Re* regime provide valuable insights for the aerodynamics of MAVs. These findings emphasize the critical role of *AR* in shaping wing performance under low-speed aerodynamic conditions, contributing to the optimization and advancement of MAV technologies.

CHAPTER 6

Self-Adjustable Flaps on Low Aspect Ratio Wings

Overview

The self-adjusting flexible flap is a biomimetic passive flow control device, which is evolved by emulating the covert feathers on the upper wing of a bird. The effectiveness of such a flap was explored mostly for infinite or high AR wings from low to high Re in prior studies. However, the aerodynamic characteristics of a high AR wing are completely different from the lower one due to wingtip vortices. Therefore, in the present work, this flap is tested on the S5010 profiled wing of two different low ARs, such as 2.0 and 1.0, in the Re range of 60 × 10^3 to 100 × 10^3. Three flap chord length setups, 0.12c, 0.15c, and 0.20c, are investigated at various chord-wise locations between 0.3c and 0.8c. Results show that the best performance enhancement is achieved when flaps cover 80% of the wingspan for an AR = 2.0 and 70% in the case of an AR = 1.0. The flap does not affect the wing performance for pre-stall angles. While all the flapped configurations reveal improvement in the post-stall lift, drag, and stall characteristics over the clean wing in most cases. In case of a pitching moment, flaps do not change the longitudinal stability of the wing for pre-stall angles but increase the pitch-down tendency of the wing in the post-stall region. The optimal chord-wise position of the flap for better performance enhancement is near the mid-chord for both models.

6.1 Introduction

Flow separation is a common phenomenon for any wing operating at *Re* below 100×10^3, which is directly associated with loss of lift, increased pressure drag, and generation of aerodynamic noise. Therefore, controlling flow separation becomes very important for the effective design of low-speed vehicles, such as MAVs. Aerodynamicists all over the globe are contributing to addressing these issues through modifications in the wing configuration or by adopting flow control approaches. The flow control techniques are broadly categorized into active and passive strategies [Gad-el-Hak and Pollard, (1998)]. Synthetic jets, blowing, suction, plasma actuators, etc., are some active techniques that were used to improve the aerodynamic performance of the airfoil/wing [Baljit et al., (2017); Kim et al., (2007); Rizzetta and Visbal, (2012), (2008)]. Additionally, several passive techniques were also employed to enhance the performance of airfoils or wings, including the implementation of a gurney flap, self-actuating flap, creation of a cavity on the suction surface, etc. [Cravero, (2017); Lam and Leung, (2018); Meyer et al., (2007)].

The active approaches require power unit to operate, while passive ones require no power source. Consequently, the implementation of an active strategy in the small-scaled aircraft creates difficulty for the designer due to constraints of wing size, power unit as well as weight. Therefore, current study explores the self-actuating flap as a passive flow separation control approach. This method is completely inspired by a bird's flight. Because of their morphological system, birds have the ability to fly at incredibly low speeds and with extremely high angles of attack (*AoA*) [Azuma, (1992); Bechert et al., (1997)]. This potential not only helps them to execute their preferred trajectories with effortlessness, but it also lets them land softly in congested places and take off quickly from the small nest. In addition, birds have ability to naturally deal with flow separation using the upper wing surface of the covert feathers. An example of this is shown in **Fig. 6.1**. It has been noticed that the wing coverts tend to pop-up naturally during their landing approach or in other situations, such as flight at high *AoA* or while passing through gusty wind situations. In contrast, the same coverts are then instantly returned to their usual location by reducing the wing's *AoA*. This type of wing action is retained sinusoidally during low-speed flying.

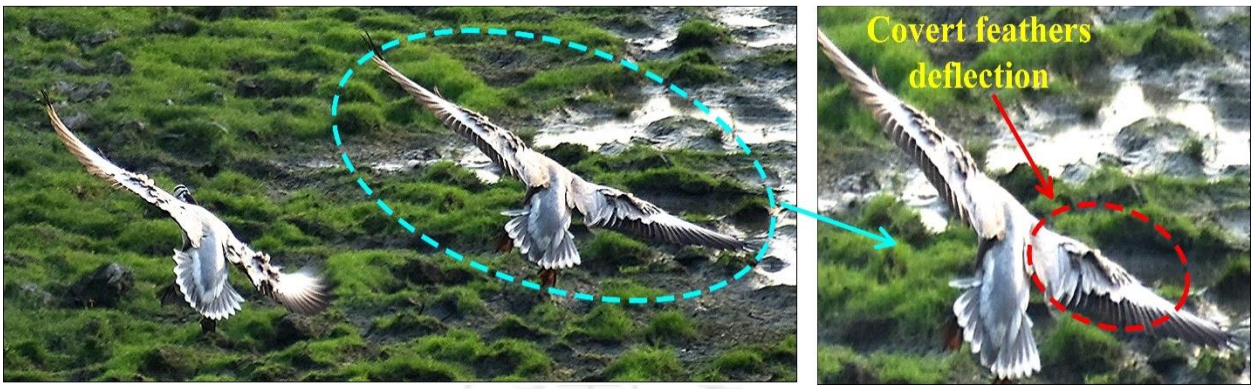

Fig. 6.1: A Bar-headed goose's wing with deflection of covert feathers to prevent the propagation of flow separation (*Captured by the author*)

These passive pop-up covert feathers are theorized to control flow separation and allow higher lift at low speeds, as well as to improve the bird's flight performance at high *AoA*. Liebe explained the behavior of a bird's feather as a biological high-lift device and suggested that it acts as a brake to prevent the propagation of the separation bubble towards the leading edge [Bechert et al., (1997)]. On Liebe's suggestions, this concept was initially tested in flight experiments on the fighter aircraft Messerschmitt Me-109 in early 1938. In this experiment, a thin leather sheet (known as self-adjustable flap / self-movable flap / lift enhancing effectors) was placed spanwise on the upper surface of the aircraft's wing to imitate a bird's covert feathers function. The results showed that the flying behavior of the aircraft with this attachment was satisfactory at a low *AoA*. However, for flying at a higher *AoA*, it was difficult to handle the aircraft, primarily due to the aerodynamic asymmetry of the wing. Much later in this event, various experimental investigations were conducted by putting lightweight, thin sheets on the upper surface of the wing to replicate the motion of the bird's wing coverts [Arivoli and Singh, (2016); Bramesfeld and Maughmer, (2002); Hao et al., (2022); Kernstine et al., (2008); Schatz et al., (2004); Wang and Schlüter, (2012)]. Those studies concluded satisfactory effect of this self-movable passive flap on the performance of the airfoil/wing for post-stall *AoA* at low to high *Re*. Initially, the flap remains attached to the surface of the wing, but when the flow begins to separate, the flap gradually rises due to the momentum of reverse flow and continuously adjusts itself to an equilibrium position that obstructs the progression of the separation bubble. These lift-enhancing effectors act as pressure dams that reduce the adverse pressure effect of separation on the pressure distribution of attached flow upstream of the flap location, resulting in lower pressure upstream of the upper surface than downstream of the flap [Bramesfeld and Maughmer, (2002)].

Bechert et al. explored how these effectors functioned and proved the feasibility of thin flaps as lift enhancement effectors in the high *Re* range of 1000×10^3 to 2000×10^3. Similarly, Meyer et al. found an improvement in the lift at higher *AoA* for a wing section using passive flaps closer to the trailing edge for the same *Re* [Meyer et al., (2007)]. Further, this study was extended to a low *Re* regime to examine the flap effectiveness up to $Re = 30 \times 10^3 - 40 \times 10^3$ [Schlüter, (2010)]. Moreover, the aerodynamic characteristics of the wing resulting from installing the flap depend on various factors such as flap size and its material (weight, stiffness, and flexibility), installation location on the wing surface, and hinge configuration for its easy rotation. Kernstine et al., (2008) explored with the flap material selection and suggested that the flap should be made of a material that is thin, lightweight, flexible, and should have adequate strength to prevent tearing. These properties allow the flap to follow the curvature of the airfoil, which avoids loss of lift at low *AoA* and to prevent tearing against aerodynamic forces at high *AoA*. Other parameters that influence flap performance are flap width, hinge arrangement, and its location on the wing surface.

Most of the earlier studies accounted flap widths between 10% and 40% of the chord length and found a favourable effect on the lift of the airfoil in the post-stall region [Kernstine et al., (2008); Meyer et al., (2007); Schlüter, (2010); Wang and Schlüter, (2012)]. The flap size below 10% of the chord was found to be inadequate to obstruct the reverse flow during the stall. While flap lengths, more than 40% of the chord demonstrated lift loss at lower *AoA* due to premature flap deployment caused by a reduction in surface pressure across the flap. Further, any flap position was not found universally effective for all flap lengths and wing sections but it was noted to be dependent on the pressure distribution and boundary layer separation characteristics of the wing surface [Altman and Allemand, (2016); Meyer et al., (2007)]. For example, Arivoli et al. noticed a considerable lift enhancement for the rectangular flat plate planform, when the flap was placed close to the trailing edge ($0.8x/c$) [Arivoli et al., (2020); Arivoli and Singh, (2016)]. While in the case of the Zimmerman planform, the flapping effect was more significant when it was fixed at the maximum span location ($0.4\ x/c$) of the wing for the same flap length and flow conditions. It was revealed that, for a wing with leading edge stall behavior, placing the flap near the trailing edge may not be useful since the reverse flow has already spread on the wing surface before reaching the trailing edge of the flap. Similarly, a flap does not create a favourable effect for a wing with trailing edge stall characteristics when it is positioned in an upstream location on the wing.

Previous studies have demonstrated that self-deployed flaps are a feasible technique for improving the lift and stall characteristics of an infinite wing or airfoil under various *Re* regimes. Most investigations have focused on the effect of parametric variation in flaps on the performance of conventional airfoils or large *AR* wings. However, there is a lack of information and understanding available regarding the application of this passive flap in low-aspect-ratio wings. In fact, the aerodynamic characteristics of a low aspect ratio wing are entirely different from those of a similar wing with a high *AR* or its airfoil section [Karasu et al., (2018); Mizoguchi and Itoh, (2013)]. This is mainly caused by wingtip vortices, which induce downwash on the upper wing surface. As an effect of this downwash, pressure distribution over the surface changes consequently affecting the performance of the wing. Further, as the wing *AR* reduces, the wingtip vortices become more significant. Hence, it is interesting to explore flap effectiveness for low *AR* wings, which would be beneficial for fixed-wing MAV applications. Although Allemand investigated the influence of flap on the finite wing's performance, but the studies were unable to predict flap effectiveness based on an *AR* below 3.0 [Altman and Allemand, (2016)]. As it was reported that the performance of the wing was found to be relatively similar with *AR* of 3.0 and above, whereas, for *AR* below 3.0, a significant effect of *AR* on the wing characteristics was observed [Mizoguchi and Itoh, (2013)]. As a result, the preceding investigation is insufficient to quantify the effectiveness of passive flaps for the wings with an *AR* below 3.0. Therefore, the present studies are planned to explore the impact of self-actuating flaps on the performance of wings with *ARs* below 2.0, specifically within the *Re* range relevant to MAVs. The primary objective commences with a detailed investigation into flap dynamics, concentrating on the analysis of parametric variations in flap span lengths to determine the optimal span size for enhanced performance. The details of the wing models and aerodynamic measurements are explained in the following sections.

6.2 Test Models

The S5010 airfoil section is chosen for fabricating the wing models of different aspect ratios 2.0 and 1.0. The geometrical characteristics of wing models are presented in **Table 6.1**. In this study, the self-movable flap is made of a thin Mylar sheet of thickness 0.12 mm and is considered for mounting at various chord-wise locations ranging between 0.3*c* and 0.8*c* on the suction side of the wing surface. The flap width sizes are chosen from 0.12*c* to 0.20*c*, and the leading edge of the flap is attached to the wing surface using Polypropylene adhesive tape of thickness 30 µm. This

configuration allows the flap to rotate freely about its leading edge at a fixed location. The tensile test is performed using a universal testing machine [**Model:** Acumen 12, **Make:** MTS systems corporation] for the Mylar sheet to estimate Young's modulus (E) for the calculation of flexural stiffness. For testing, a Mylar sheet with dimensions of 85 mm length, 18 mm width, and 0.12 mm thickness is used. The Young's modulus of the flap material is measured as 6.357 kN/mm^2 for the tested sample size. The flexural stiffness (EI) of this thin film is obtained as 16.477 N-mm^2 by adopting procedure as described by Combes and Daniel, (2003). The representation of flap span, chord size, and their position details on the wing surface are shown by a sketch in **Fig. 6.2**. In the initial phase of the flap experiments, four different flap span lengths are tested to study the three-dimensional effect on the flap dynamics for both the wing models. In the first arrangement, the flap span is extended over the entire span of the wing ($S = 1.0b$). For other configurations, the flap span is chosen as $0.9b$, $0.8b$, and $0.7b$, and placed on the wing surface in such a way that symmetry is maintained. Single and multiple flapped wing configurations are mounted on the force balance, as shown in **Fig. 6.3**.

Table 6.1: Clean wing dimensions

AR	*c (m)*	*b (m)*	t_{max} *(m)*	*A (m^2)*
1.0	0.170	0.170	0.0167	0.0289
2.0	0.120	0.240	0.0118	0.0288

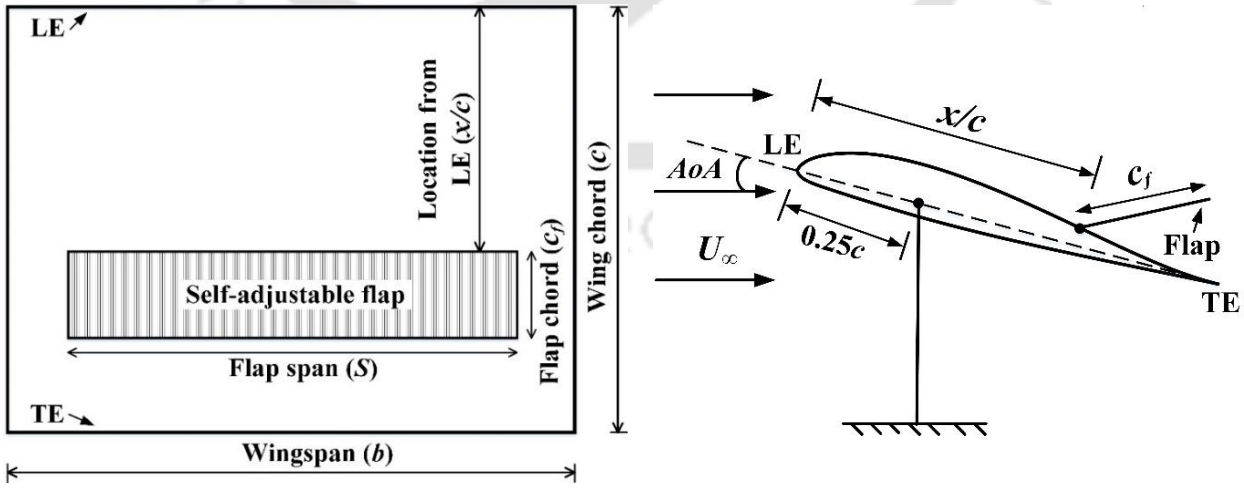

(a) Top view **(b)** Side view

Fig. 6.2: Schematic representation of flap geometry details and its placement on the wing surface

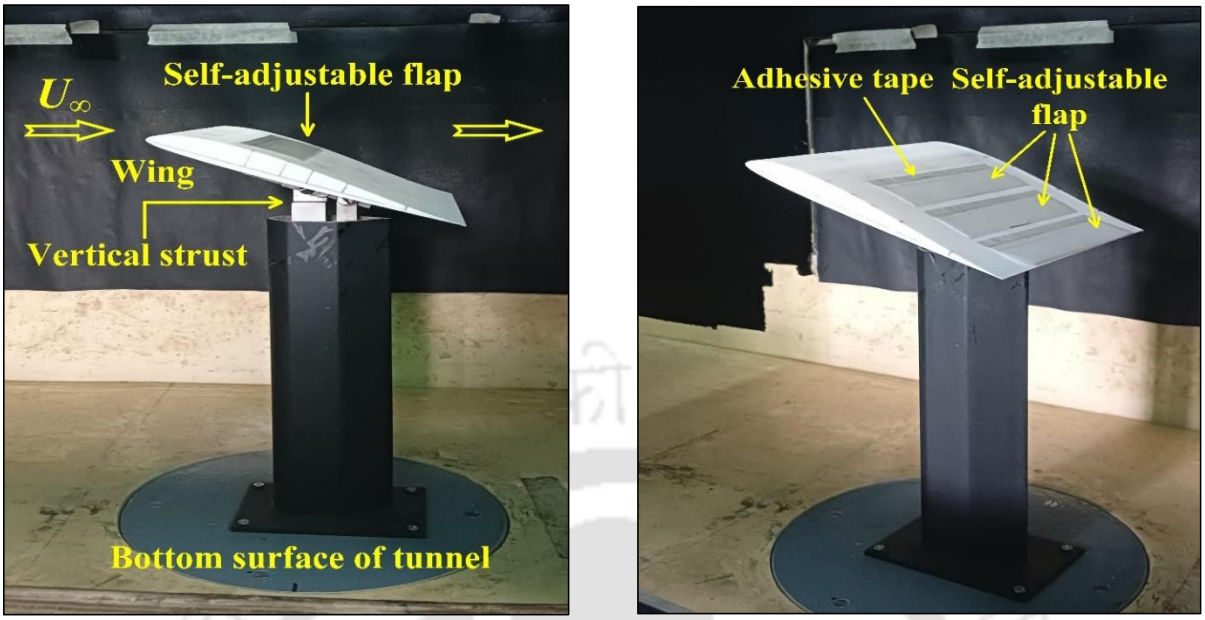

(a) Single flap configuration **(b)** Multiple flaps configuration

Fig. 6.3: Mounting of a wing with attached flap on the force balance inside the test section

In the current work, uncertainty is found to be less than ±3.0 % for lift and moment measurement, while for drag, it is less than ±1.5 %. These estimated errors are represented by the error bars in the lift and drag curve for various flapped wing configurations of AR = 2.0 at Re = 100 × 10^3, as shown in **Fig. 6.4**.

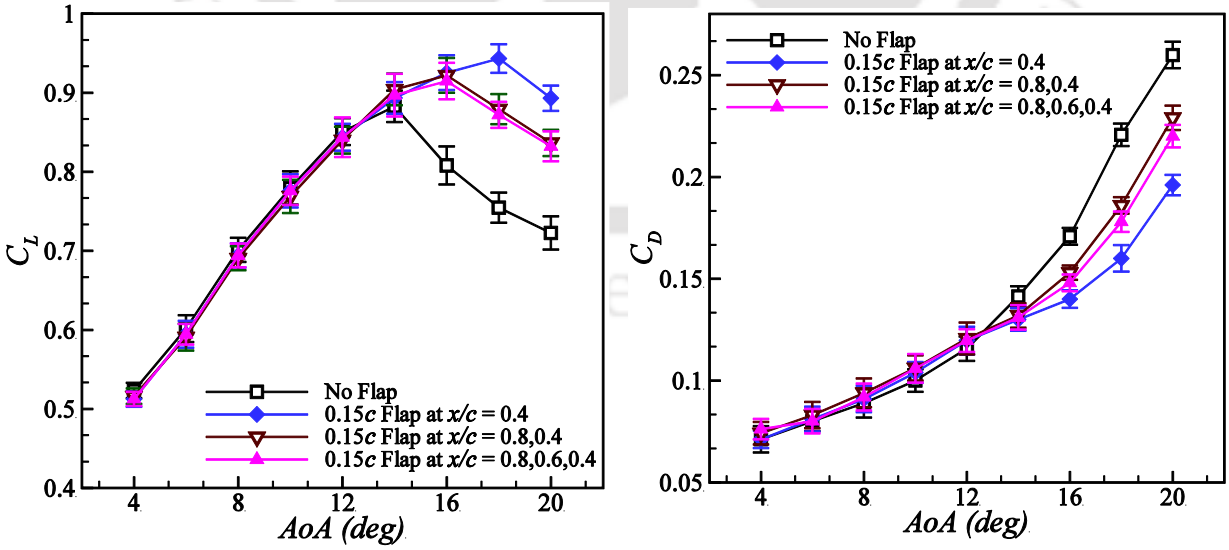

(a) Lift coefficient **(b)** Drag coefficient

Fig. 6.4: Uncertainty analysis in C_L and C_D for various flap configurations

6.3 Results and Discussion

Experimental studies are conducted to explore the effectiveness of passive flap for the S5010 profiled wing of two different aspect ratios (*AR* = 2.0, 1.0) in the *Re* range of 60 × 10^3 to 100 × 10^3. The results of the investigation are discussed in different sub-sections. The first sub-section discusses flap dynamics and analysis of parametric variation of flap span lengths to estimate the optimal flap span size. The next sub-section covers the discussion about the effect of different flap chord lengths and their chord-wise placement on the wing performance. Finally, the influence of aspect ratio and Reynolds number on the flap effectiveness is addressed in the last sub-section.

6.3.1 Understanding of Flap Dynamics and Flap Span Effects

Initial wind tunnel experiments are carried out to obtain an overview of the fundamental behavior and set of possible flap designs for the existing wing configurations. In this phase, a thin Mylar sheet, emulating the covert feathers of the bird, is installed on the suction surface of the wing near the trailing edge. When the flapped wing is tested at a lower angle of attack (*AoA*), it is observed that the flap remains attached to the surface and has no influence on the wing's aerodynamics. This observation is illustrated in the schematic shown in **Fig. 6.5a**. However, as the *AoA* is raised, the flap begins to rise and adjusts itself to an equilibrium position which eventually controls the flow separation (**Fig. 6.5b**). This is the reason due to which such flaps are called as self-adjusting flaps. This flap does not require an actuation device to actuate however the opening and closing actions of the flap are controlled by the flow surrounding the wing. Once the flow starts to separate from the trailing edge, reverse flow is bound to occur in this separation regime. Under these flow conditions, the flap begins to deploy passively as the recirculation bubble moves upstream for an increased *AoA*. Thus it acts as a brake since it prevents the spreading of separation bubble region towards the leading edge. Consequently, static pressure distribution on the suction surface upstream of the flap gets lowered than that of the rear part of the flap. This decrease of pressure on the suction surface upstream of the flap is beneficial to increase the lift at a higher *AoA*. As the present study deals with the finite wings, it is obvious that wingtip vortices will be present, as shown in **Fig. 6.6**. These wingtip vortices would alter the pressure distribution over the wing surface and flow over the flap. Therefore, it would be interesting to explore how the flapped wing's performance would change with decreasing flap span length along the wingspan.

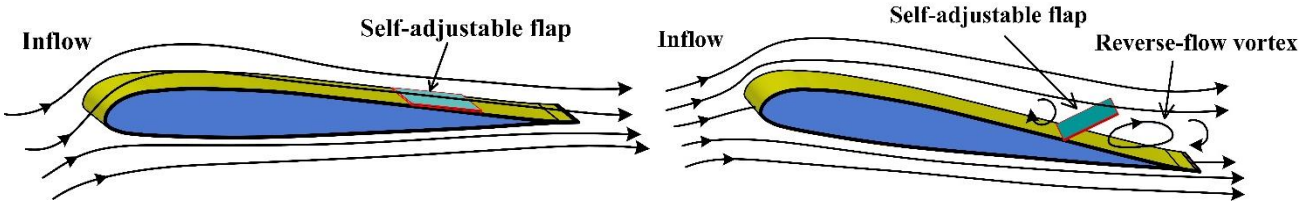

(a) Low *AoA* **(b)** High *AoA*

Fig. 6.5: Schematic representation of self-adjusting movable flap behavior for **(a)** pre-stall and **(b)** post-stall zones

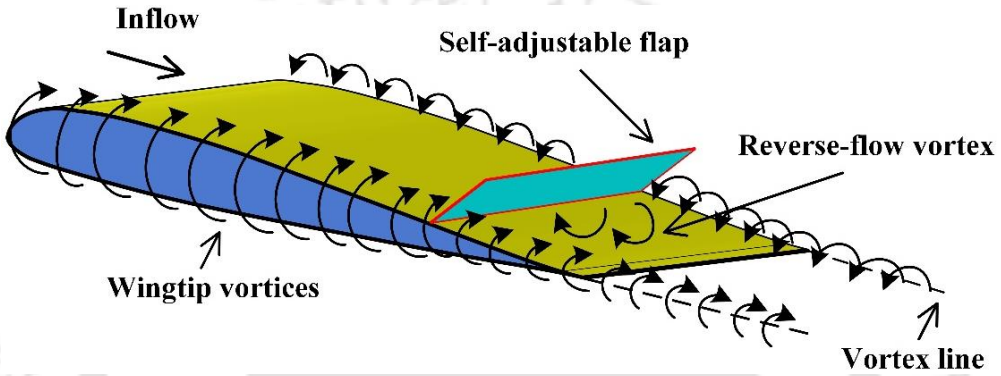

Fig. 6.6: Influence of wingtip vortices over flapped wing configuration

In this regard, experiments are carried out on the wing of AR = 2.0 and 1.0 with a flapped configuration of reducing flap span sizes from 1.0b to 0.7b along the wing spanwise. The study is accomplished for flap width between 0.12c and 0.2c and its various chord-wise locations between 0.3c and 0.8c at the Reynolds number of 100×10^3. The lift coefficient corresponding to different flap span lengths for a flap chord of 0.15c at a location of 0.4c is presented in **Fig. 6.7**. For the clean wing of AR = 2.0, C_L increases with increasing AoA up to 14°; beyond that, it begins to decline (**Fig. 6.7a**). So, the stall angle is recorded close to 14° and corresponding C_L is found as 0.88. In the instance of AR = 1.0, the stall point is noted as 20°, and associated C_L is 0.65 at Re = 100×10^3 (**Fig. 6.7b**). Further, all flapped wing configurations exhibit the same lift characteristics as respective clean wings in the pre-stall region irrespective of any flap spanning size. Beyond the stall angle of the wing, all the flap configurations show a significant effect on the lift characteristics except the flap span of 1.0b. The flap spanning 100% of wingspan (S = 1.0b) does not show any lift improvement, even in the post-stall region for any position and width of the flap.

In the case of full-span flap configuration, the flap movement is obstructed by the downwash, induced by wingtip vortices. So the flap remains attached to the upper wing surface at low to high

angles of attack; hence does not affect the aerodynamic performance of the wing. In contrast, this downwash effect is not significant for an infinite or high aspect ratio wing, so full-span flaps work effectively and have been proven to be a performance enhancement effector [Bramesfeld and Maughmer, (2002); Liu et al., (2010)]. Further, results reveal that as the span of the flap decreases, significant improvement in the lift and stall characteristics is observed for the configurations. When the flap span is 90% of the wingspan, the stall point increases to near 14% for AR = 2.0, and no improvement is seen for AR = 1.0 wings. As reported, the effect of downwash on the suction surface increases with the decrease in the wing aspect ratio [Mizoguchi and Itoh, (2013)]. Therefore, the effect of wingtip vortices is more pronounced on the flap motion of AR = 1.0 model. For a flap span of 80 to 70 % of wingspan, stall angle increases up to 28% and 20%, respectively, in the case of AR = 2.0 and 1.0. These experimental results indicate that by reducing the flap span, it is possible to minimize the effect of downwash acting on the flap dynamics, thereby contributing to higher lift generation. On the other side, greatly reducing the span of the flaps also reduces the contribution to lift generation for the post-stall region. In the current study, the optimal flap span length is found as 80% of wingspan (S = 0.8b) for AR = 2.0 and 70% of wingspan (S = 0.7b) for AR = 1.0, which is the same for all the flap chord sizes and their locations.

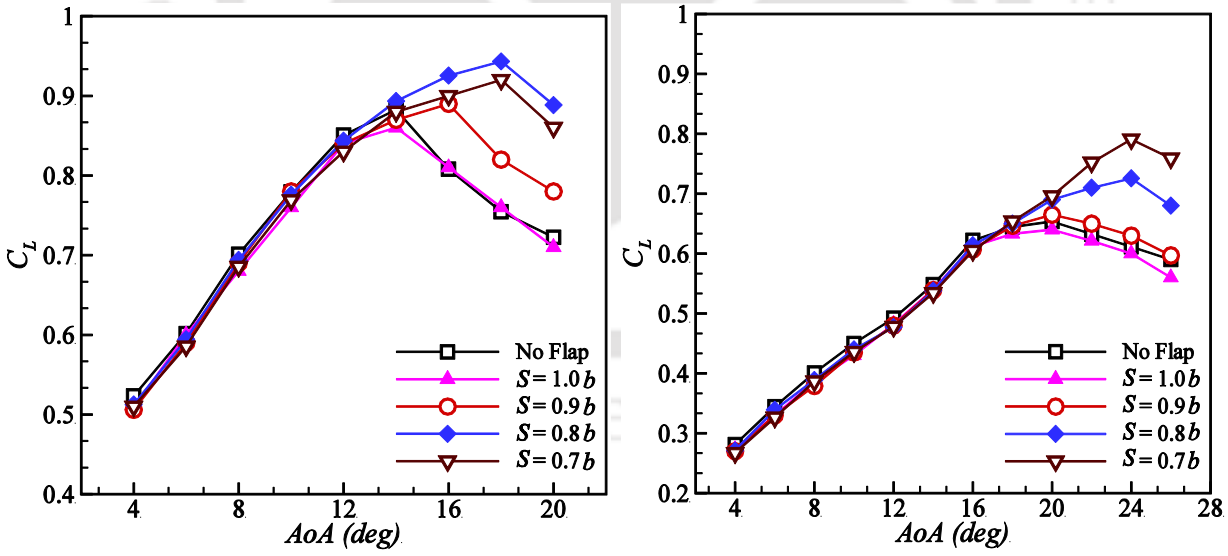

(a) AR = 2.0 **(b)** AR = 1.0

Fig. 6.7: Lift characteristics corresponding to different flap span lengths for chord flap chord of 0.15c at location 0.4c for Re = 100 × 10^3

6.3.2 Analysis of flap chord-sizes and positions

Since self-adjusting flaps are raised by reverse flow, the flap must be light in weight and positioned optimally on the wing so that it can respond properly to the reverse flow. Essentially, the weight is affected by two factors, namely, the flap material and its size. Here, the flap material and its thickness are not changed during testing. Therefore, to figure out the optimal flap size and position for the current models, experiments are carried out for different flap chord lengths ranging from 0.12*c* to 0.2*c* at Reynolds number of 100×10^3. These flap sizes are examined for different chord-wise flap positions starting from near the trailing edge at 0.8*c* and progressing upstream to 0.3*c*. The effect of these locations and flap dimensions are discussed in this section.

6.3.2.1 Lift Characteristics

The measured lift coefficients corresponding to various flap chord lengths (0.12*c*, 0.15*c*, 0.2*c*) and their positions (*x/c* = 0.8, 0.6, 0.4) for *AR* = 2.0 wing are presented in **Fig. 6.8**. The analysis of results show that the lift curve remains the same in the pre-stall zone for both clean and flapped models of any given flap chord length and its location. While, for the post-stall region, all the flapped wings reveal improvement in the lift and stall characteristics than the clean model. In the case of configuration with attached flap length of 0.12*c* at *x/c* = 0.8, 0.6, 0.4; the stall angle has been noticed to be increased by 14% (**Fig. 6.8a**). Further, the lift coefficient increases by 15% at *AoA* = 16°. Changing the flap location upstream does not provide any advantages in terms of lift or stall for this configuration. When the chord is 0.15*c*, flapped wing shows smooth stall characteristics, and the stall angle rises by 22% for flap locations at *x/c* = 0.6, 0.4 (**Fig. 6.8b**). For the same locations, C_L improves by approximately 27% at *AoA* = 18°. The flap mounting at *x/c* = 0.6, 0.4 has better lift and stall characteristics than the flap attached close to the trailing edge at *x/c* = 0.8. A similar test has been performed with a chord length of 0.2*c*, and the results show that the stall angle increases by 22% at *x/c* = 0.6 and by 14% at other places (**Fig. 6.8c**). An increase in flap chord length from 0.12*c* to 0.15*c* has shown a substantial improvement in both lift and stall angle. Further, increasing the flap chord from 0.15*c* to 0.2*c* resulted in an almost identical increase in lift on the wing. For *AR* = 2.0 wing, a flap chord size of 0.12*c* is less effective for obstructing the reverse flow, while sizes larger than 0.2*c* have difficulty in self-adjusting against the reverse flow conditions due to their self-weight. In addition, flap positions show a substantial effect on lift and stall behaviours. Configurations with attached flap at *x/c* = 0.6 or 0.4 provide a higher value of lift or stall angle than other locations, irrespective of any flap chord sizes.

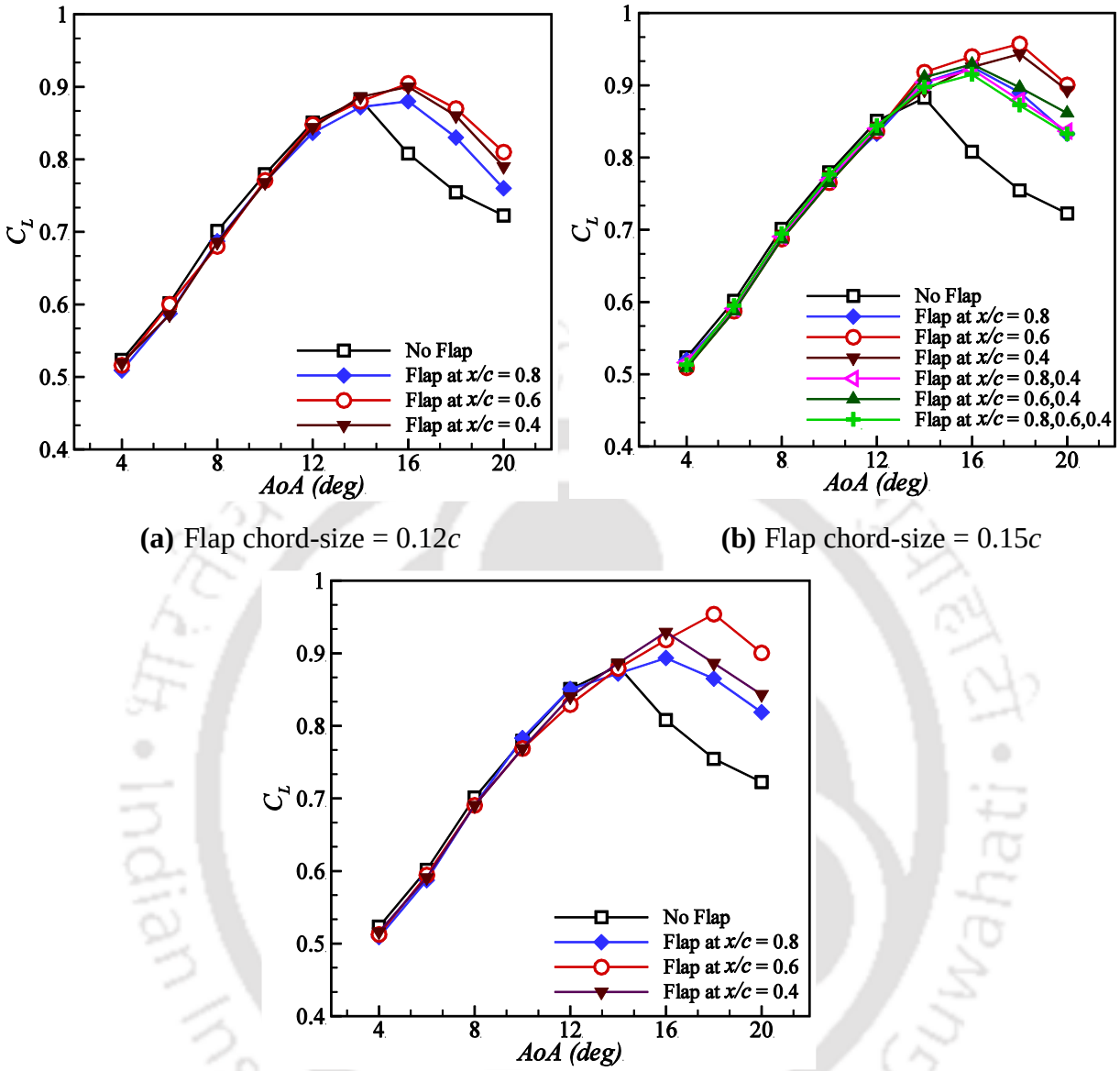

(a) Flap chord-size = 0.12*c* **(b)** Flap chord-size = 0.15*c*

(c) Flap chord-size = 0.2*c*

Fig. 6.8: Lift characteristics of an *AR* = 2.0 wing with various flap chord sizes and positions at *Re* = 100 × 10^3

Moreover, this experiment is also extended to study the effect of multiple flaps on the wing performance for the current Reynolds number. For this, three sets of flap configurations are explored. The first configuration has two flaps, one closer to the mid-chord (0.4*c*) and the other near the trailing edge (0.8*c*). In the second arrangement, both flaps are located around the midpoint of the chord (*x*/*c* = 0.4, 0.6), and in the final arrangement, the three flaps are placed at *x*/*c* = 0.8, 0.6, 0.4. The results of *AR* = 2.0 wing with arrangements of double and triple flaps of size 0.15c

are presented in **Fig. 6.8b**. It is observed that all multiple flap configurations exhibit higher post-stall lift and increase in stall angle than the clean wing. Here, the stall angle increases by 14%, and lift rises by 15% at *AoA* = 16°, which is the same for both double and triple flap setups. However, this gain in lift and stall is lower when compared to the increase obtained by the single-flapped wing for a location of 0.4*c* or 0.6*c*. Further, the same experiments have also been performed on other flap chord sizes like 0.12*c* and 0.2*c* for the same wing and similar results are obtained as that of 0.15*c* case. Thus single-flapped configurations show better lift and stall enhancements over double or triple-flapped arrangements for all flap chord sizes. Similar lift and stall behavior reductions were observed by employing double self-adaptive flaps compared to a single flap for the same rectangular flat plate wing [Arivoli and Singh, (2016)].

A similar flap experiment is also carried out for a wing of *AR* = 1.0 to study the effect of flap chord size and its locations on aerodynamic performance. In these tests, the flap is initially considered at a downstream location of *x/c* = 0.8 and then moved to other upstream locations such as 0.6, 0.5, 0.4, and 0.3. **Figure 6.9** shows lift coefficient variation attributed to different flap chord sizes (0.12*c*, 0.15*c*, 0.2*c*) and their placement at $Re = 100 \times 10^3$. The lift curve shows that stall occurs at 20° for the clean wing. Similar to the *AR* = 2.0 flap model, all flapped configurations have approximately the same lift as the clean wing in the pre-stall region. The flaps at locations *x/c* = 0.8 and 0.6 do not provide significant improvements in the lift and stall angle for *AR* = 1.0 wing. For a flap of 0.12*c* size at upstream positions *x/c* = 0.5, 0.4, 0.3, the stall point increases by 10% over the clean model (**Fig. 6.9a**). When the flap size increases from 0.12*c* to 0.15*c*, the stall angle increases by 20% at *x/c* = 0.4 (**Fig. 6.9b**). Further increase in flap size does not provide any benefit for improving lift and stall than the flap of 0.15*c* (**Fig. 6.9c**). Moreover, moving the flap positions on the model from the trailing edge towards upstream shows a beneficial effect on the post-stall lift characteristics. For the *AR* = 1.0 model, a configuration with a flap of 0.15*c* at *x/c* = 0.4 on the model demonstrates better lift or stall behavior compared to other flap sizes and locations. The experiments are also performed for multiple flaps on the wing to evaluate the performance enhancement capacity in the case of a low aspect ratio wing (*AR* = 1.0). Similar to the *AR* = 2.0 model, all double or triple flap configurations show higher post-stall lift values and stall angles than the baseline case. However, this increase in the lift is lower when compared to the lift obtained by the single-flapped arrangement. Thus in the case of *AR* = 1 also single flap is found beneficial.

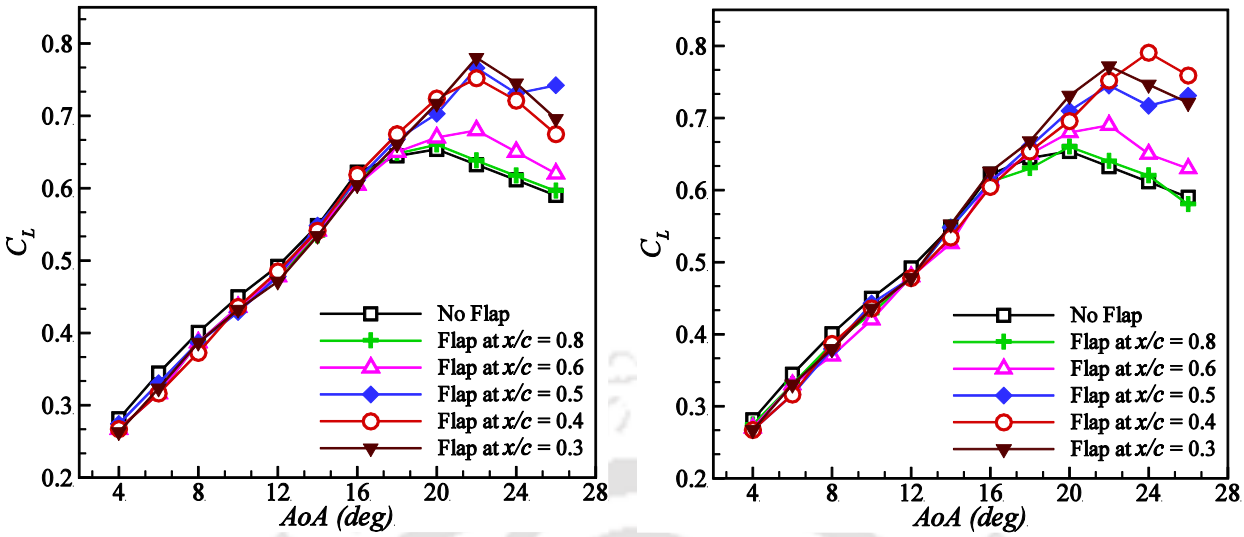

(a) Flap chord-size = 0.12*c* **(b)** Flap chord-size = 0.15*c*

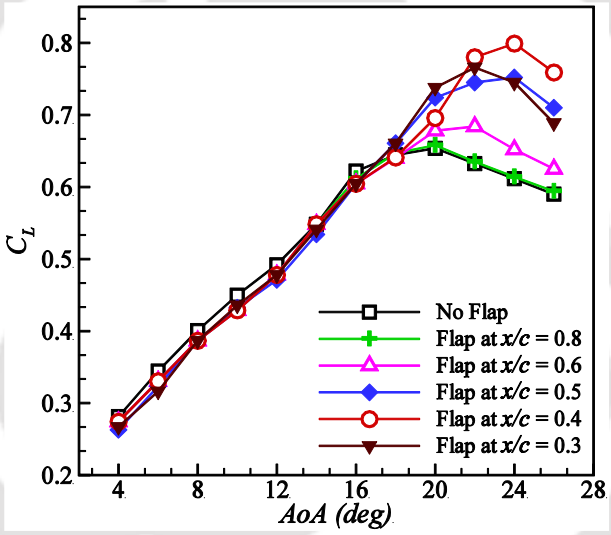

(c) Flap chord-size = 0.2*c*

Fig. 6.9: Lift characteristics of an *AR* = 1.0 wing with various flap chord sizes and positions at *Re* = 100 × 10^3

The present analysis demonstrates that variations in wing aspect ratio result in significant changes in lift and stall behaviours. For the clean wing, with a decrease in the aspect ratio from 2.0 to 1.0, the maximum lift coefficient (C_{Lmax}) decreases by close to 26% at *Re* = 100 × 10^3, while the associated stall angle increases from 14° to 20°. Hence, the C_{Lmax} of the wing decreases with a decrease in aspect ratio. Similar behavior of C_{Lmax} as a function of aspect ratio was also observed for the flat plate wings ($1.0 \leq AR \leq 3.0$; $60\times 10^3 \leq Re \leq 200\times 10^3$) [Pelletier and Mueller, (2000)]. In the case of flap configurations, also *AR* shows a substantial effect on the flap effectiveness.

Reducing the aspect ratio of the wing reduces flap span size to work effectively by eliminating the effect of wing tip vortices. Further, the optimal flap location also varies with the aspect ratio. For AR = 2.0, the positioning of the flap between the mid-chord and trailing edge locations has a favourable influence on lift and stall characteristics for all flap chord sizes. While in the case of AR = 1.0, the positive effect of the flap is noticed only for the upstream location of the mid-wing. However, Allemand observed for high aspect ratio wings that changing the AR from 7.0 to 4.0 had no major effect on flap effectiveness [Altman and Allemand, (2016)]. In terms of lift coefficient, the AR = 2.0 wing appears to be more sensitive to parametric variations in flap chord lengths and its positions for a given Reynolds number than AR = 1.0.

6.3.2.2 Drag Characteristics

The influence of single or multiple flap arrangements on the drag characteristics of the wing is estimated at $Re = 100 \times 10^3$, as presented in **Fig. 6.10**. **Figure 6.10a** shows the variation of C_D as a function of AoA for AR = 2.0 wing with different flap positions of chord size 0.15c. The drag value continues to increase with an increasing AoA, which is the same for both clean and flapped configurations. However, the value of C_D rises gently with an angle for a lower AoA ($AoA \leq 12°$), while at higher angles, the drag force rises rapidly. Here, the plotted drag data is the total drag acting on the wing, which is a combination of profile drag (skin friction and form drag; arising due to viscous effect) and induced drag (resulting from wingtip vortices). It has been noted that, for streamlined bodies at lower angles, the values of form drag and induced drag are small, which means that the majority of the drag force is due to skin friction drag [Anderson, (2011)]. This concept helps to explain the lower rate of rising C_D for lower AoA. However, as the AoA increases, the flow begins to separate from the upper surface of the wing. As a result, form drag begins to increase due to flow separation, and hence the C_D increases rapidly at high AoA.

The influence of flap arrangement on the drag force is less significant for the pre-stall region but more significant for the post-stall angles. All the flapped configurations show significantly low values of drag against the baseline case, except for the flap location of 0.8c. The drag curve for a flap position near the trailing edge (x/c = 0.8) is similar to that of a clean wing. Further, double (0.4c and 0.8c, 0.4c and 0.6c), and triple (0.4c, 0.6c, 0.8c) flapped configurations exhibit relatively higher drag coefficients as compared to the flap location of 0.4c (**Fig. 6.10a**). Flap chord size also reveal significant effects on the post-stall drag behavior. As the flap chord is increased from 0.12c

to 0.15*c*, the magnitude of the drag coefficient for the post-stall zone decreases. Whereas with a further increase, i.e., from 0.15*c* to 0.2*c*, the drag force does not change significantly. A similar experiment is also carried out for estimating the drag force for *AR* = 1.0 wing with different flap sizes and their arrangements; results are presented in **Fig**. **6.10b**. Drag coefficients for the pre-stall region are unaffected by the presence of flap, which is the same for all flaps configurations. For post-stall angles, flap placement between the leading edge to the mid-wing chord has shown a lower drag value than the un-flapped one. Similar drag reduction was observed for the NACA0012 airfoil attached to the passively flexible thin fin close to the leading edge (*x/c* = 0.1, 0.2) in the post-stall zone [Liu et al., (2010)]. In contrast, the configuration with flap placement downstream of the mid-wing exhibits a drag curve similar to that of a clean wing, even in the post-stall region. Similar to *AR* = 2.0, here also, the double and triple flap arrangement models show higher drag than the single flap at *x/c* = 0.4. Further, a flap of 0.12*c* chord length reveals a higher drag value than a chord of 0.15*c* and 0.2*c* for all the locations. Compared to *AR* = 2.0 flap configurations, changing flap parameters such as cord, location, and flap numbering have less effect on the drag characteristics for *AR* = 1.0.

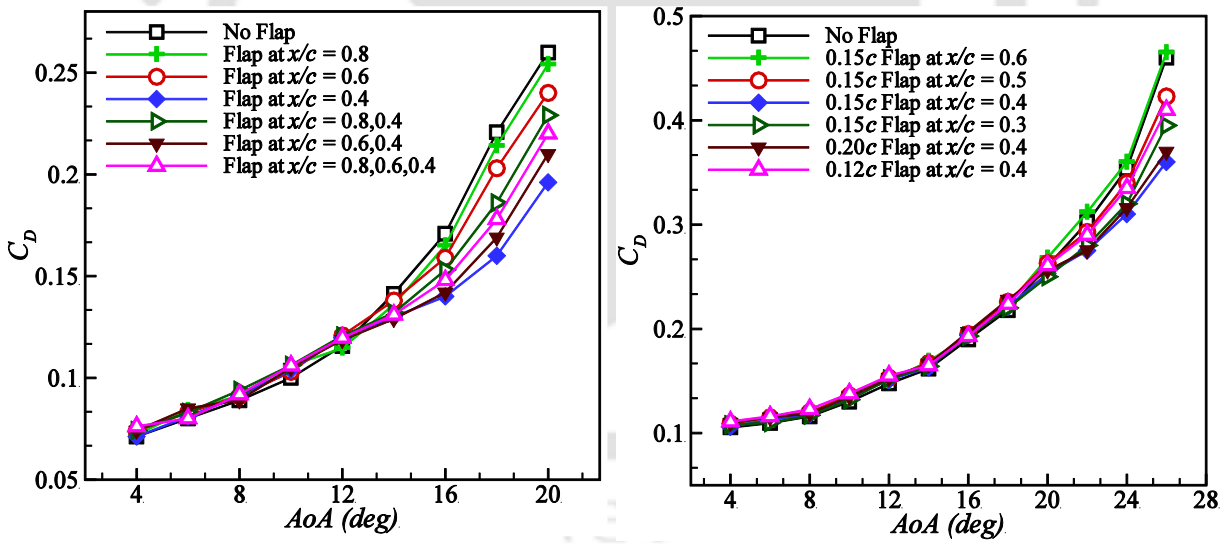

(a) *AR* = 2.0 **(b)** *AR* = 1.0

Fig. 6.10: Drag characteristics of different flapped wing configurations at *Re* = 100 × 10^3

6.3.2.3 Moment Characteristics

The pitching moment data is obtained at about a quarter chord (*0.25c*) of the wing for all the flap configurations at *Re* = 100 × 10^3. Here, the moment coefficients as a function of *AoA* for *AR* = 2.0

and 1.0 wing with different flap chord sizes and their positions are presented in **Fig. 6.11**. For the clean wing, the magnitude of $C_{M,0.25c}$ decreases to negative values with increasing angle up to 14°, and after this angle, an increasing trend is seen for *AR* = 2.0 (**Fig. 6.11a**). Also, in case *AR* = 1.0, the pitching moment curve decreases till 20°, then an increasing trend is noticed (**Fig. 6.11b**). The rise in the moment curve following a specific angle is related to the reduction in lift. As it has been noted that the behavior of the lift curve alters as it gets near the stall angle, a similar trend has also been noted for the moment curve. It also changes its behavior near the stall point. Similar moment behavior associated with lift characteristics was observed for flat plate wings of various planforms [Okamoto and Azuma, (2011)]. The significance of the negative pitching moment refers to the fact that when the *AoA* rises, it tends to rotate the wing towards its equilibrium position to offset the disturbance caused by the *AoA*. Also, it was emphasized that the slope of the moment curve must be negative for the static longitudinal stability of aircraft [Nelson, (1998)]. In this study, the moment slope is estimated from the linear region of the curve and is found in negative values as -0.0104 /*deg* and -0.0072/*deg* for the base wing of *AR* = 2.0 and 1.0, respectively.

Further, the moment characteristics in the pre-stall region are unchanged by using this passive flap, irrespective of its size and position for both models. In contrast, the flap affects the moment behavior significantly after the stall point. All the flap configurations show more negative pitching values for the post-stall angles than the baseline. This indicates that the pitch-down tendency of the flapped wing is higher than the un-flapped one in the post-stall zone. A flap at locations of *x/c* = 0.6 or 0.4 exhibits a more negative magnitude of $C_{M,0.25c,}$ than other flap arrangements for *AR* = 2.0 (**Fig. 6.11a**). Moreover, single-flap configurations show more pitch-down tendencies as compared to the double or triple-flapped wings. When the flap chord length increases from 0.12*c* to 0.15*c*, the post-stall moment rises in the negative magnitude. In contrast, a further increase in chord size, such as from 0.15*c* to 0.2*c*, does not affect the moment coefficient. For *AR* = 1.0 models, the moment curve is unaffected by the flap position close to the trailing edge (*x/c* = 0.8) but is affected by the upstream or mid-wing position of the flaps (**Fig. 6.11b**). Configuration with flap at *x/c* = 0.4 shows more pitch-down tendency as compared with other flap locations at high *AoA*. Similar to *AR* = 2.0, double or triple flap arrangement exhibits a lower negative value of $C_{M,0.25c,}$ than single. Moreover, increasing the flap size from 0.12*c* to 0.15*c* improves the more negative magnitude of the moment, while expanding the size above 0.15*c* does not affect the moment behavior. Similar to lift and drag behavior, the moment characteristics of the *AR* = 2.0 flap

configurations are more sensitive to changing flap parameters than those of a low aspect ratio wing.

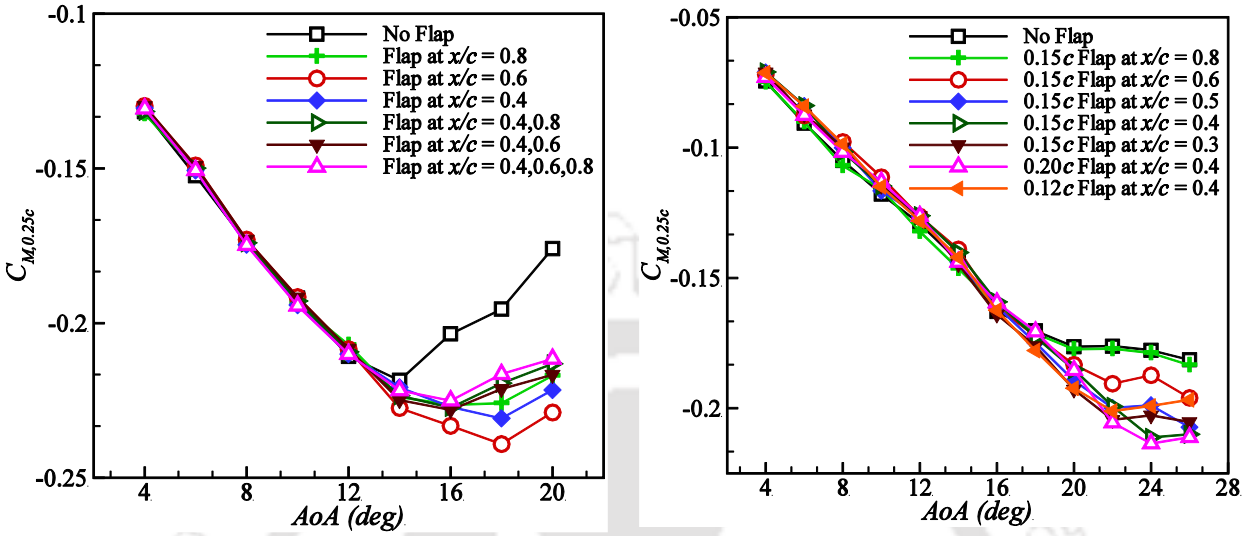

(a) *AR* = 2.0 **(b)** *AR* = 1.0

Fig. 6.11: Pitching moment characteristics of different flapped wing configurations at *Re* = 100 × 10^3

6.3.3 Effect of Aspect Ratio and Reynolds number on Flap Effectiveness

The present analysis demonstrates that variations in wing aspect ratio result in significant changes in lift and stall behaviors. For the clean wing, with a decrease in the aspect ratio from 2.0 to 1.0, C_{Lmax} decreases by close to 26% at *Re* = 100 × 10^3, while the associated stall angle increases from 14° to 20°. Hence, the maximum lift coefficient of the wing decreases with a decrease in *AR*. Moreover, C_{Lmax} increases with increasing Reynolds number for both the aspect ratio, as shown in **Fig. 6.12**. Similar behavior of C_{Lmax} as a function of *AR* and *Re* was also observed for the flat plate wings ($1.0 \leq AR \leq 3.0$; $60\times 10^3 \leq Re \leq 200\times 10^3$) [Pelletier and Mueller, (2000)]. In the case of flap configurations, also *AR* shows a substantial effect on the flap effectiveness. Reducing the *AR* of the wing reduces flap span size to work effectively by eliminating the effect of wing tip vortices. Further, the optimal flap location also varies with the aspect ratio. For *AR* = 2.0, the positioning of the flap between the mid-chord and trailing edge locations has a favourable influence on lift and stall characteristics for all flap chord sizes. While in the case of *AR* = 1.0, the positive effect of the flap is noticed only for the upstream location of the mid-wing. However, Altman and Allemand, (2016) observed for high aspect ratio wings that changing the *AR* from 7.0 to 4.0 had no major

effect on flap effectiveness. In terms of performance (lift, drag, moment), the *AR* = 2.0 wing appears to be more sensitive to parametric variations in flap chord lengths and its positions for the same *Re* than *AR* = 1.0.

Moreover, no significant effect of *Re* on the flap dynamics is observed in the pre-stall region. Therefore, lift, drag, and moment coefficient for pre-stall angles remain unchanged with varying *Re* from 60×10^3 to 100×10^3. But, this self-adjustable flap responds differently at various *Re* for particular flap size and their position for post-stall angles, as presented in **Fig. 6.12**. For *AR* = 2.0 flap configurations, the C_{Lmax} increases with increasing *Re* from 60×10^3 to 80×10^3 for all the cases (**Fig. 6.12a**). However, for *Re* between 80×10^3 and 100×10^3, the magnitude of C_{Lmax} is either almost constant or decreases with *Re*. With an increase in *Re*, the reverse flow momentum increases, which creates higher flap displacement and more lift to be produced. However, after a certain *Re* limit, the same flap is unable to resist these additional forces arising from increased velocity in the recirculation zone at some locations, causing the effect of a flap on the contribution of lift generation to be reduced. In the case of the *AR* = 1.0 model, the positive effect of *Re* is observed on the C_{Lmax} for the all the flapped configurations in the tested *Re* range (**Fig. 6.12b**). As *Re* increases from 6×10^4 to 1×10^5, the C_{Lmax} exhibits improvement for both chord lengths, 0.15*c* and 0.2*c*.

Based on the above observation, the behavior of C_{Lmax} as a function of *Re* shows a difference for both *AR* configurations, even while keeping the same flap chords and their placement. Thus, in order to obtain a positive response from the flap under different *Re*, flap size, position, and material will need to be changed. Similar behavior of flap with varying *Re* was reported by Kernstine et al., (2008). In the case of drag coefficients, when the *Re* is increased from 60×10^3 to $100 \times 10^{3,}$ post-stall drag data reduces for all flap configurations of *AR* = 2.0. While, for *AR* = 1.0 configurations, no significant effect of varying *Re* from 80×10^3 to 120×10^3 is noticed on the drag curve. For the pitching moment, it is found that the pitching moment values of the flapped wing of *AR* = 2.0 become more negative with increasing *Re*. Hence, the pitch-down tendency of the flapped wing rises with increasing *Re* in the post-stall region. At the same time, no significant effect of *Re* on moment characteristics is noted for the flapped *AR* = 1.0 model, even at a higher *AoA*. Therefore, it is evident that the impact of varying *Re* on flap effectiveness reduces as the wing aspect ratio decreases.

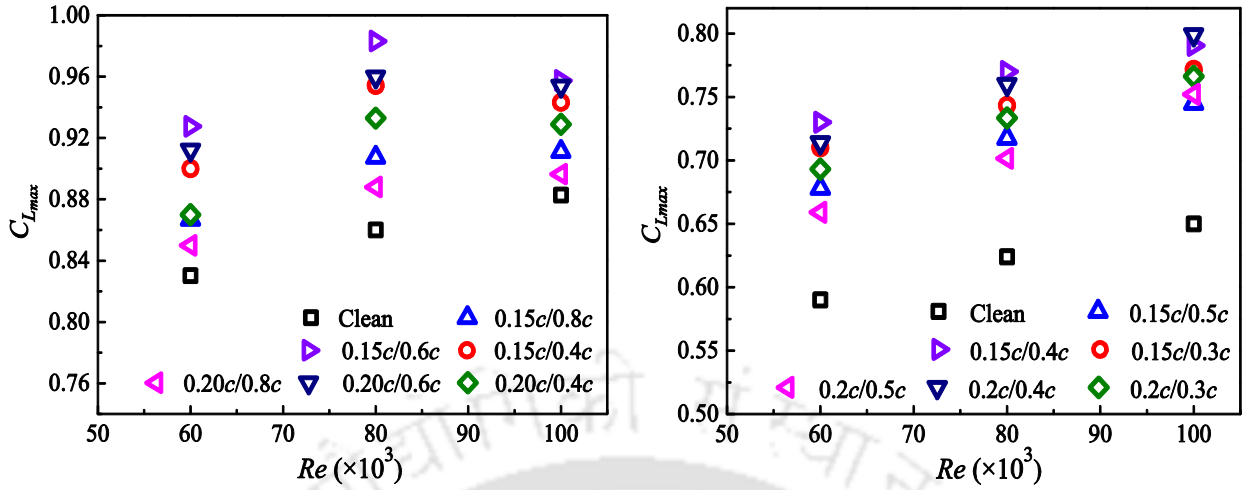

(a) AR = 2.0 **(b)** AR = 1.0

Fig. 6.12: Maximum lift characteristics of different flapped wing configurations at various *Re*

6.4 Summary

This study is focused on investigating the feasibility of a self-adaptive movable flap for low aspect ratio wings and exploring flap effectiveness in various aspects, including flap span, chord length, and chord-wise placement. In this regard, the experiments are conducted with a S5010 profiled wing of two different aspect ratios, such as 2.0 and 1.0, in the presence of a flap for the *Re* range of 60 × 10^3 to 120 × 10^3. Three different flap chord length setups, such as 0.12c, 0.15c, and 0.2c, have been tested for various chord-wise positions between 0.8c and 0.3c. Moreover, flap span size is also varied from 1.0b to 0.7b to study the effect of tip vortices on the flap effectiveness. The studies show that all flap configurations exhibit lift, drag, and moment curves similar to a clean wing for the pre-stall region at a given Reynolds number. The flap spanning 100% of wingspan does not provide any beneficial effect on the wing performance, even at a high *AoA*. When the flap span shrinks from both sides towards the wing centre line, the influence of downwash on the flap motion is reduced, contributing more to lift generation. The best performance improvement is obtained when the flap covers 80% of wingspan for AR = 2.0, and it is around 70% of span in the case of AR = 1.0.

The flapped wing configurations reveal higher stall angle and post-stall lift coefficients than baseline in most cases. Initially, when the flap chord size increases from 0.12c to 0.15c enhances the lift and stall characteristics for both models. Further increases in flap size, such as 0.15c to 0.20c, do not provide any improvement in performance for all locations. The optimal location of

this self-adjustable flap also varies with the aspect ratio of the wing. For AR = 2.0, the flap locations between 0.6c and 0.4c exhibit better performance in terms of lift, drag, and pitching moment than the other locations. Meanwhile, for AR = 1.0, better enhancement is observed for a flap location of x/c = 0.4, and no significant effect of the flap is noticed for a flap position downstream of a mid-wing chord. Multiple flap configurations have a relatively lower lift-enhancing capability as compared to single-flapped models at some locations. Further, in most cases, post-stall drag reduction is observed for flapped wings than a clean model, which is the same for both aspect ratios. However, double or triple-flapped configurations show a lower drag value than baseline but higher than single flap in the post-stall region. When the flap chord is increased from 0.12c to 0.15c, the drag and moment characteristics improve, but an increase above 0.15c provides no beneficial effect. In the case of the pitching moment, flaps do not change the longitudinal stability of the wing for pre-stall angles while increasing the pitch-down tendency of the wing in the post-stall region. Furthermore, the aerodynamic performance parameters (lift, drag, pitching moment) of a flapped wing of AR = 2.0 appear to be more sensitive to parametric variations in flap chord length and its positions for the same Reynold number than AR = 1.0. Overall, these experiments identify the appropriate size and place of attachment of a flexible flap on a low aspect ratio wing to delay the stall and, improve the lift, and reduce the drag and pitching moment compared to a wing without a covert flap. Therefore, this passive flap can be a valuable device for improving the flying performance and maneuverability of fixed-wing MAVs.

CHAPTER 7

Slotted Winglet Configurations for Low Aspect Ratio Wings

Overview

This investigation presents a comparative analysis of the effectiveness of various slotted winglet configurations on the performance of low AR wings. The inspiration for the slotted wingtip is drawn from the structural feature of primary feathers at the tips of bird wings. This bio-inspired approach aims to replicate the aerodynamic benefits observed in bird flight for enhanced wing performance. In this regard, the experiments are conducted with the S5010 profiled wing of two different ARs such as 1.0 and 0.5, in the presence of various attachment devices on the wingtip for the Re range from 80 × 10^3 to 150 × 10^3. For this study, two wingtip attachment shapes, tapered and conical, are selected and incorporated in a planar manner at the wingtips, forming slotted winglet configurations. The results are analysed in terms of lift, drag, induced drag, lift-to-drag ratio, and pitching moment. In every case, the tapered winglet arrangements showcase improvements in performance parameters compared to their corresponding base wings. Furthermore, the higher number of attachments at the wingtips leads to a more pronounced decrease in the induced drag and minimizes the tendency for upward pitching. It has also been observed that with an increase in Re, the performance of winglet configurations improves significantly.

7.1 Introduction

The wing design of low-speed vehicles, such as MAVs, relies heavily on the use of low *AR* wings (*AR* < 2.0) [Torres and Mueller, (2004)]. These wings face a significant challenge of producing lower lift values at low angles of attack (*AoA*) due to the presence of strong wingtip vortices. Additionally, at higher *AoA*, low *AR* wings experience higher levels of induced drag. As a result, the wing design of low-speed vehicles still encounters challenges while implementing low *AR* wings without any modifications to their geometry. These challenges underscore the need for innovative approaches and modifications to optimize the aerodynamic performance of low *AR* wings and overcome the limitations associated with their use in MAV applications. In this regard, an effective solution is the use of slotted wingtip arrangements on wings to reduce the adverse effects of wingtip vortices on wing performance [Lynch et al., (2018); Sachs and Moelyadi, (2006); Tucker, (1993)]. The concept of the slotted wingtip was inspired by the structural features observed in primary feathers at the tips of bird's wings, as illustrated in **Fig. 7.1**. This image was captured during the flight of a Black kite, where the bird separated its primary feathers to generate wingtip slots.

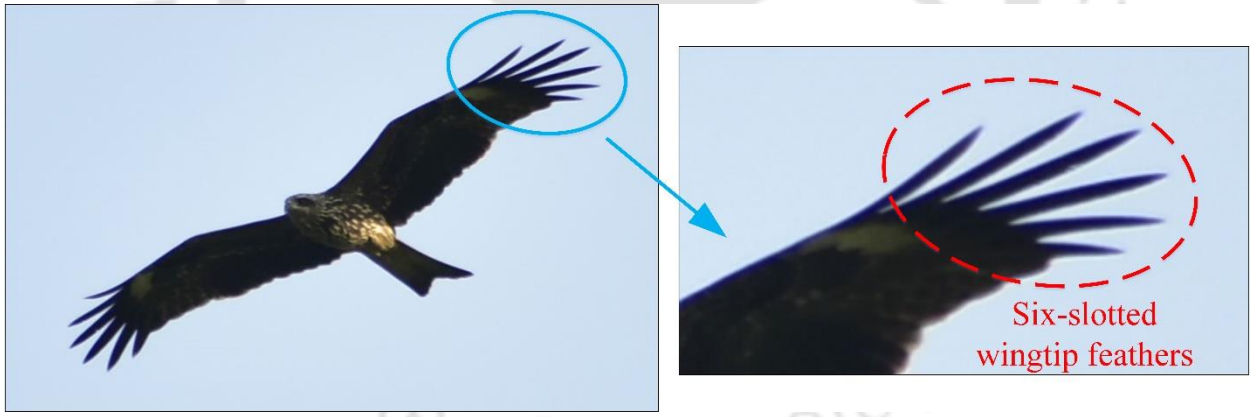

Fig. 7.1: Slots generated by separating primary feathers at the wingtips on the Black Kite's wing (*Captured by the author*)

The wing of birds showcases various feather systems that birds employ to enhance their flight capabilities and adaptability. These feather systems encompass the primaries, secondaries, coverts, and alula feathers, each serving a distinct function in relation to flight. Among these feathers, the primary feathers were observed to play a significant role in reducing induced drag [Tucker, (1995)]. In the wing structure of soaring birds (e.g., eagles, hawks, vultures and others), a

distinctive feature is the presence of wingtip gaps, formed due to primary feather emargination**.** The concept of spread-tip feathers and slotted wingtips observed in birds has been applied to experimental aircraft designs by integrating multiple winglets that imitate feather-like structures. The slotted wingtip design, characterized by both horizontal and vertical spreading of the primary feathers, allows for the individual aerodynamic action of each feather. This configuration effectively disrupts and disperses wingtip vortices, which is considered to be a notable advancement in flight performance following the evolution of birds. In order to investigate the impact of wingtip gaps on bird flight characteristics, Tucker conducted a series of wind tunnel experiments using a Harris Hawk wing [Tucker, (1995), (1993)]. They found lower induced drag values for wings whose tips were slotted with a non-planar configuration. The inclusion of tip slots in the wings can effectively reduce induced drag by horizontally spreading vorticity along the wing and by functioning as winglets. Winglets are commonly employed on aircraft to create non-planar wing configurations and vertically distribute vorticity. Similarly, in birds, the presence of tip slots serves a similar purpose, contributing to the reduction of induced drag by dispersing vorticity both horizontally and vertically. When a wing is non-planar, it exhibits vertical bending from the root to the tip. This means that the trailing edge, when projected onto a vertical plane, forms a curved shape. On the other hand, a planar wing remains straight from tip to tip, with its trailing edge sweeping out a flat plane. Both non-planar and planar wings experience two types of drag: induced drag and profile drag. However, a non-planar wing may have lower induced drag compared to a planar wing with the same lift, span, and flow conditions. This reduction in induced drag is attributed to the spreading of vertical vortices caused by the non-planar wing shape. These vortices are more effectively distributed vertically, resulting in a decrease in induced drag.

Based on the concept of slotted wingtips and spread feather of a bird, the effectiveness of multi-slotted wingtips was tested on profiled NACA0012 semi-span wing in the *Re* range of 161×10^3 to 300×10^3 [Smith et al., (2001)]. The construction of winglets involved the utilization of a flat plate section as part of slots. The wing with straight-slotted tips was found to exhibit a higher lift curve slope compared to the baseline. However, the slotted wing with appropriate dihedral and twist angle was found to be most efficient in improving the aerodynamic efficiency of the wing. Cerón-Muñoz investigated the potential application of adaptive wingtip sails on $NACA65_3$-018 wing for achieving a reduction in induced drag by varying the cant and incidence angle of the winglets [Céron-Muñoz et al., (2013); Cerón-Muñoz and Catalano, (2006)]. They selected 55

configurations, each with different cant angles, and conducted experiments in a wind tunnel. Through their analysis, the most effective layout of the wingtip sail was identified which demonstrated optimal aerodynamic characteristics for each specific flight condition. A similar study was also reported to optimize the performance of slotted winglets by varying the cant angle, tip twist angle, dihedral angle, and the number of slots on the tip [Fluck and Crawford, (2014)]. The findings suggested that the inclusion of multiple vertically spread tip slots, along with sufficient dihedral to create a non-planar wing configuration, had a favourable effect on the overall aerodynamic performance. When the twist angle was varied for each tip slot, some instances showed a slight increase in the $(C_L/C_D)_{max}$ ratio. However, the study also highlighted that twist might offer additional advantages when combined with dihedral.

Furthermore, Sachs and Moelyadi, (2006) analysed the application of a sweep wingtip to the slotted wing. They demonstrated that wingtip slots with sweep yielded a stabilizing yawing moment of significant magnitude, which substantially grew with the lift coefficient. The demonstration was key to understand the importance of the sweep at the slotted wingtip in generating the stabilizing yawing moments. Single and multiple-slotted winglet arrangements were also investigated on elliptical wing planform, and a higher Oswald efficiency factor was obtained for the configured wing compared to the clean wing [Coiro et al., (2008)]. In comparing single and multiple winglets, the single configuration was found to be more efficient in enhancing the performance of the elliptical wing planform. Furthermore, Lynch et al. conducted a study to compute the wingtip gap size for both planar and non-planar wing configurations [Lynch et al., (2018)]. The planar winglets with a gap size of 20% of the chord showed a 7.25% increase in pre-stall lift behavior and a 5.6% increase in C_{Lmax} when compared to wings without slot gaps. The non-planar configuration produced a lower lift value in the pre-stall region, but the reduction in induced drag was greater than that of a planar wing. Two different types of winglets, flexible and rigid, with flat or curved wingtip devices were also tested for flat plate wings at *Re* of 300×10^3 [Siddiqui et al., (2018)]. The rigid flat winglets configuration showed higher lift slope, C_{Lmax}, and induced drag when compared to the other winglet arrangement. Despite having a larger C_{Lmax}, the rigid flat wingtip exhibited a relatively small C_L/C_D ratio. In contrast, the rigid curved wingtip shape demonstrated the highest C_L/C_D ratio among all the configurations tested.

Previous studies have shown that provision of slotted winglets is a viable technique for enhancing the lift and reducing the induced drag of the wing across various *Re* regimes. Most investigations

have focused on the influence of parametric variation in slotted winglets on the performance of high *AR* wings (*AR* > 3.0) for *Re* higher than 100 × 10^3 [Catalano and Ceron-Muñoz, (2005); Céron-Muñoz et al., (2013); Siddiqui et al., (2018); Smith et al., (2001)]. There is a lack of information and understanding available regarding the application of this slotted winglets concept in low *AR* wings (*AR* < 2.0). However, understanding the aerodynamics of *AR* below 2.0 within the *Re* range of 70 × 10^3 to 200 × 10^3 is crucial for the design of MAVs [Torres and Mueller, (2004)]. In reality, the aerodynamic behavior of a low *AR* wing is totally different from that of a similar wing with a high *AR* [Karasu et al., (2018); Mizoguchi and Itoh, (2013)]. The primary reason for this difference is thought to be the presence of wingtip vortices, which induce downwash flow on the upper wing surface. These vortices lead to alterations in the pressure distribution over the wing surface, consequently affecting the wing's performance. Further, as the wing *AR* decreases, the influence of wingtip vortices becomes more prominent. Hence, it is interesting to explore the implementation of slotted winglets for low *AR* wings, which would be beneficial for fixed-wing MAV applications. In this regard, the current studies are planned to investigate the effectiveness of various slotted winglet configurations for improving the performance of low *AR* wings (*AR* ≤ 1.0), within the *Re* range of 80 × 10^3 to 100 × 10^3. The details of the winglet configurations and aerodynamic measurements are explained in the following sections.

7.2 Wing Model Configurations

The S5010 profiled rectangular wing planform of two different *ARs*, 1.0 and 0.5, are chosen for the experiment. Both the models are made from PLA material using a 3D printing machine and have six holes of diameter 4.90 mm on each surface of the wingtip, as shown in **Fig. 7.2**. The purpose of these holes is to allow attachment devices to be installed on the wingtips, making it possible to create a slotted winglet arrangement. However, the aerodynamic measurement for the base wing is conducted by filling these holes with wax. This study involves testing two different shapes of attachment devices, specifically tapered (trapezoidal) and conical. The cross-sectional dimensions of these wingtip attachments are demonstrated in **Fig. 7.3**. The choice of these two shapes aims to study the impact of streamlined and blunt body effects on the effectiveness of winglet configurations. The tapered attachment is designed with a flat plate profile of thickness 2 mm, featuring rounded leading and trailing edges, thereby classifying it as streamlined. The root-chord length of the tapered attachment is 10 mm, while the tip-chord length is 5 mm, which is the same for both 65 mm and 37.5 mm. On the other hand, the conical attachment has a circular cross-

section, with a root diameter of 10 mm and a tip diameter of 5 mm, categorizing it as a blunt body. Each of these shapes is tested with two different lengths, 65 mm and 37.5 mm. The taper ratio of all attachment devices remains constant at 0.5. All the wingtip attachment devices are fabricated from PLA material using a 3D printing machine. The geometrical details of wingtip devices are shown in **Fig. 7.4**.

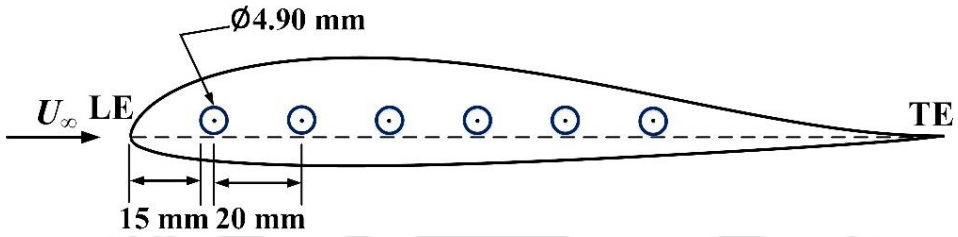

Fig. 7.2: Schematic of base wing with holes

(a) Tapered section view **(b)** Conical section view

Fig. 7.3: Cross-sectional dimension of the wingtip attachments at the tip

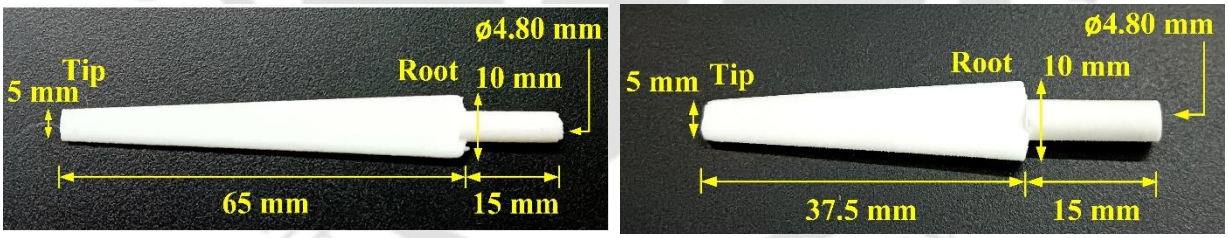

(a) Tapered wingtip devices

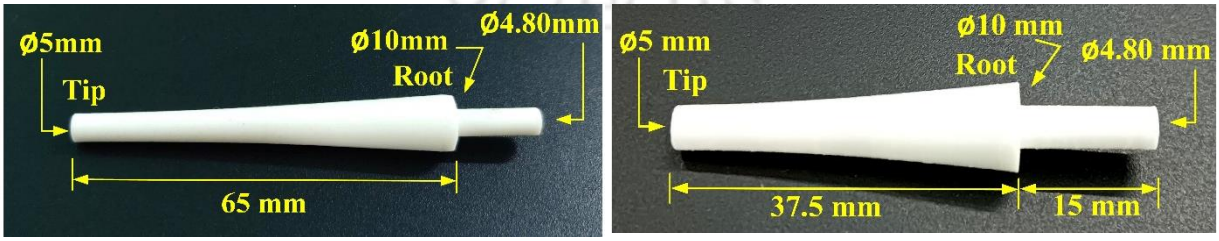

(b) Conical wingtip devices

Fig. 7.4: Geometrical details of wingtip attachment devices

These attachment devices are added in a planar manner to the wingtips to create tapered or conical slotted winglet configurations. In this study, four distinct winglet configurations of each attachment shape are designed for both *AR* wings. The first wing configuration consists of six tapered attachments on each side of the wingtip, while the second arrangement involves three attachments on either side. These arrangements of tapered devices on the wingtip are represented by 6T and 3T, respectively, and they transform the wing into slotted winglet configurations. Based on the attachment type and geometry, this winglet configuration is named 6T:65 and 3T:65, where "6T" or "3T" signifies the number of tapered attachments on the wingtips, and "65" represents the attachment length in mm. The schematic representation of 6T and 3T configuration for *AR* = 1.0 is shown in **Fig. 7.5.** In this study, the inspiration for designing six-slotted winglet configurations for the wing is drawn from the structural features observed in the separated primary feathers at the wingtips of Black Kite's wings, as displayed in **Fig. 7.1**. Similarly, for the other two configurations, the conical attachments are also held at the wingtip in the same number as in the tapered case. These slotted winglet configurations are represented by 6C:65 and 3C:65, where "6C" or "3C" denotes the number of conical attachments on the wingtips, and "65" indicates attachment length in mm. The spacing between the two wingtip attachments on the surface is 10 mm in the six-slotted winglets arrangement, whereas, for the three attachments, it is 30 mm (**Fig. 7.5b**). This spacing remains consistent for both *AR*s (*AR* = 1.0 or 0.5) of respective attachments. All the devices are added in a planar arrangement to the wingtips of *AR* = 1.0 and 0.5. Six and three slotted winglet configurations of *AR* = 1.0 and 0.5 models are mounted on the force balance, as shown in **Fig. 7.6.**

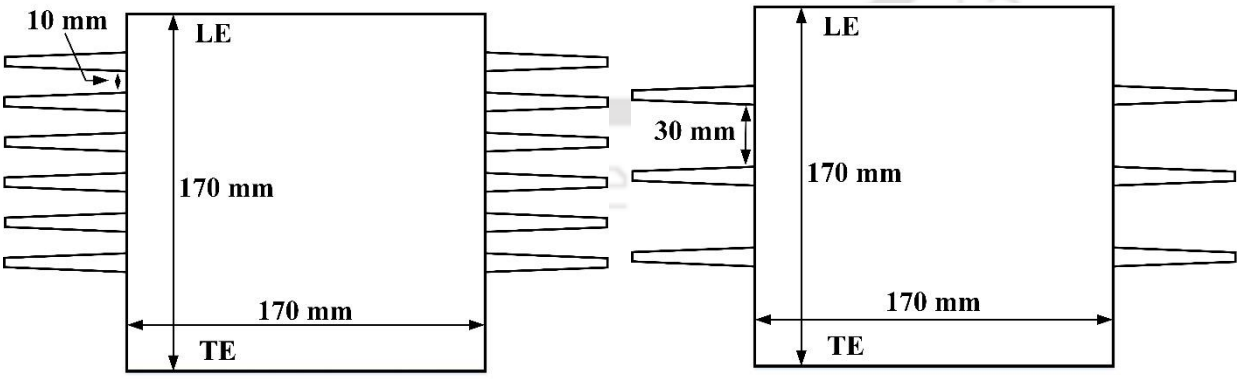

(a) 6T slotted winglets **(b)** 3T slotted winglets

Fig. 7.5: Representation of wing with slotted winglet configurations for *AR* = 1.0 model

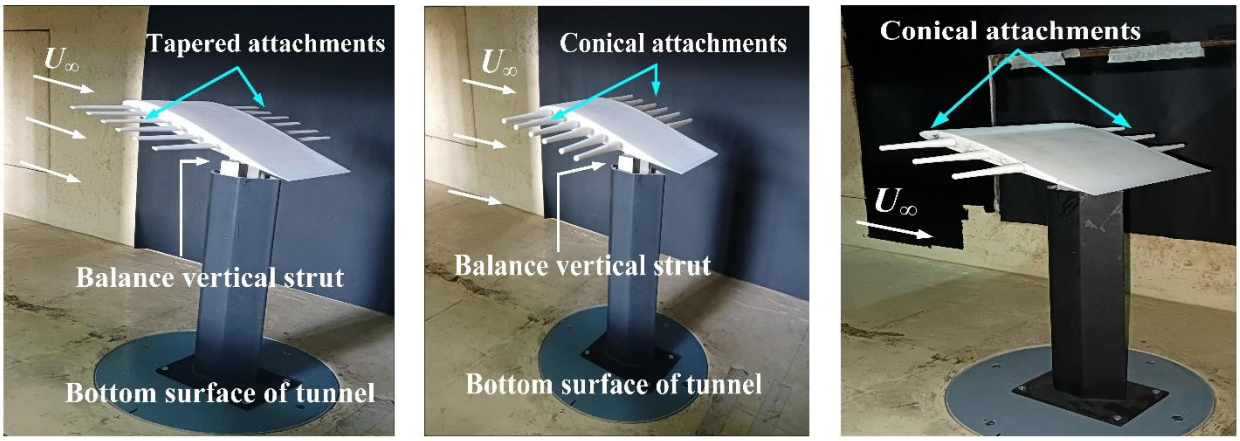

(a) 6T configuration of $AR = 0.5$ **(b)** 6C configuration of $AR = 0.5$ **(c)** 3C configuration of $AR = 1.0$

Fig. 7.6: Experimental setup for different wings with various slotted winglet configurations

In this study, the blockage ratio varies between 0.67% and 3.92% within the *AoA* range of 4° to 24° for the 6T:65 configurations of $AR = 1.0$. The reported studies suggest that, when the blockage factor is below 5%, there is no significant need for blockage corrections. For error estimation in aerodynamic coefficients measurement, the standard deviation of the samples and subsequent standard error of the mean is estimated. The maximum standard errors of the mean are found to be less than ±3% for lift and moment measurements, while for drag, it is less than ±1.5%. These estimated errors are represented by the error bars in the lift and drag curves for various winglet configurations of $AR = 1.0$ at *Re* of 100×10^3, as shown in **Fig. 7.7**.

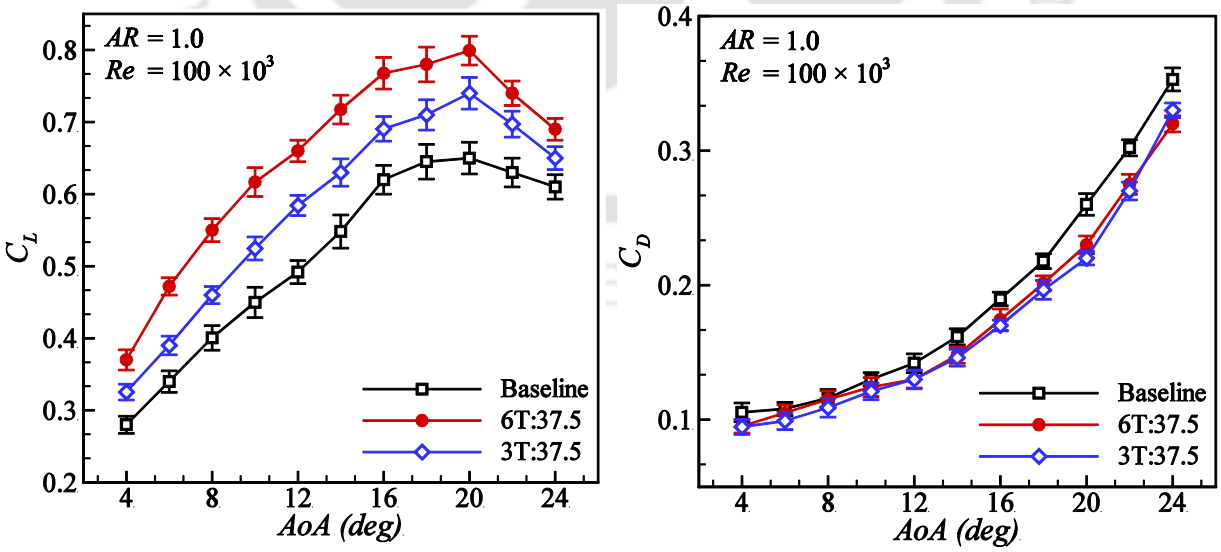

(a) Lift coefficient **(b)** Drag coefficient

Fig. 7.7: Error analysis in C_L and C_D for various winglet configurations

7.3 Results and Discussion

Experimental investigations are carried out to explore the effect of different attachment devices on the wingtip of low *AR* wings (*AR* = 1.0, 0.5) in the *Re* range of 80×10^3 to 150×10^3. The results of these investigations are organized into five distinct sub-sections. The initial part of the discussion includes the effect of parametric variation in the arrangements of slotted winglets on the lift characteristics of *AR* 1.0 and 0.5 wing models. These parameters cover various aspects, including wingtip attachment shape (tapered, conical), length (65 mm, 37.5 mm), and quantity (6, 3). The subsequent sub-sections cover the discussion about the drag, lift-to-drag ratio, and moment characteristics for various slotted winglet configurations with *AR* of 1.0 and 0.5. Finally, the section concludes with an analysis of the influence of *Re* on the performance of different winglet models.

7.3.1 Lift Characteristics of Various Wing Configurations

7.3.1.1 Wing Configurations of *AR* = 1.0

The variation of C_L with *AoA* for an *AR* = 1.0 wing with different slotted winglet arrangements is presented in **Fig. 7.8**. **Figure 7.8a** shows the comparison of C_L for different tapered slotted winglet configurations at *Re* of 100×10^3. The analysis of these results reveals that all winglet configurations exhibit higher C_L values than the baseline wing, both before and after the stall point, irrespective of any attachment length and number. These wingtip attachment devices do not alter the stall characteristics of the base wing, which is found to be the same at 20° for all cases. However, the C_{Lmax} of the tapered winglets arrangement is observed to be higher than that of the base wing. While comparing various winglet configurations, both 6T:65 and 6T:37.5 exhibit higher C_L and C_{Lmax} than the other 3T configurations for the entire range of tested *AoA*. For 6T winglet arrangements, the C_{Lmax} increases by 26% and 23% compared to the baseline for attachment lengths of 65 mm and 37.5 mm, respectively. Whereas, for the 3T arrangements, C_{Lmax} improves by 17% and 14% compared to baseline for lengths of 65 mm and 37.5 mm, respectively. This observation indicates that both pre-stall C_L values and C_{Lmax} are substantially improved by increasing the number of attachments on the wingtips. Conversely, an increase in attachment length does not significantly alter the lift values for the given winglet configurations. The observed higher lift generation in the slotted winglets configuration is expected due to reduction in the

wingtip vortices. The primary idea behind incorporating an attachment device at the wingtip is to establish a barrier that intercepts the flow of vorticity at the tips and to effectively divert them away from the wing's surface. As expected, adding attachment in the wingtip lowers the intensity of tip vortices and generates weaker vortices at the tips. Consequently, this diminishes their influence on the pressure distribution over the suction surface, leading to increased lift generation and reduction in the induced drag component. Further, while considering the geometric characteristics of the tapered devices, they are designed as thin flat plates with rounded leading and trailing edge profiles. This particular design feature may also contribute in enhancing the lift generation phenomenon.

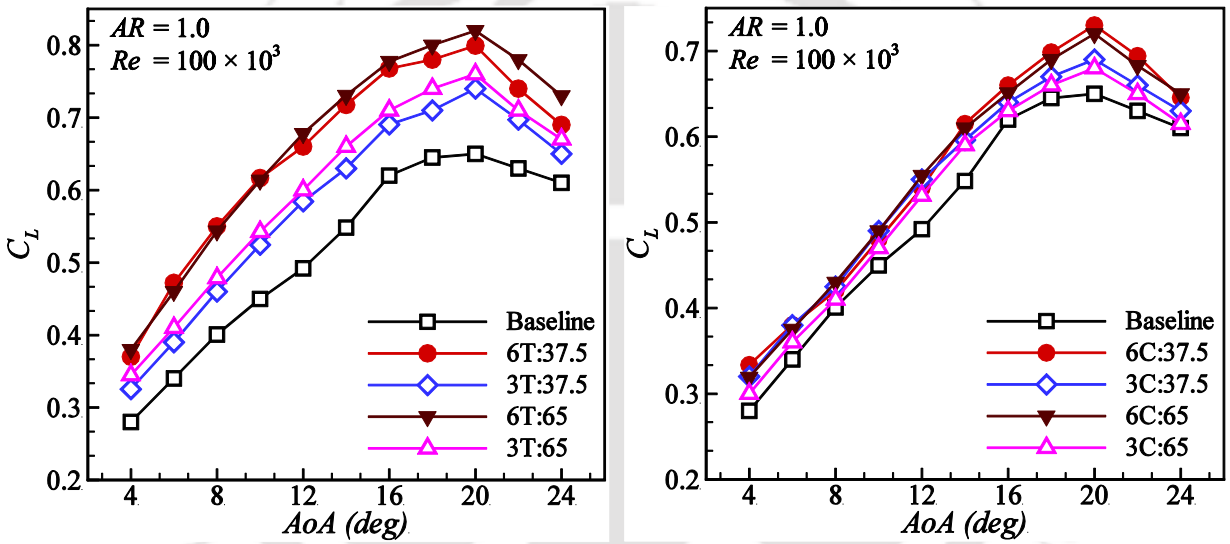

(a) Tapered slotted winglets **(b)** Conical slotted winglets

Fig. 7.8: Lift characteristics of various slotted winglet configurations of *AR* = 1.0

These slotted winglet arrangements also affect the linearity of the lift curve in the pre-stall region. The lift slope value is estimated in the linear region of the C_L-*AoA* curve, employing techniques similar to those utilized by Torres and Mueller to compute the lift slope for flat plate wings [Torres and Mueller, (2004)]. For the base wing, it is obtained as 0.0267 /*deg* within the pre-stall *AoA* range from 4° to 12° at *Re* of 100 × 10^3. However, all the winglet configurations with tapered devices exhibit a higher lift slope value than those without winglets. Specifically, the 6T:65 arrangements improve the lift slope by 40%, while 3T:65 enhances the lift slope by up to 21% than the baseline wing for the same *AoA* range. Similarly, the lift slope improves by 35.5% and 22% for 6T:37.5 and 3T:37.5 configurations, respectively. In the context of low *AR* wings, the

generation of nonlinear lift is attributed to the dominant wingtip vortices, which create substantial cross-flow velocity on the suction surface [Torres and Mueller, (2004)]. The resulting pressure reduction is considered as primary factor behind the occurrence of nonlinear lift in low *AR* wings when operating within the range of moderate to high *AoA*. This theory helps to explain the occurrence of non-linearity in the C_L-curve of the base wing. As anticipated, attachment at the wingtips establishes a barrier that effectively diverts the flow by passing through the tips. This helps to minimize the downwash effect on the pressure distribution and consequently reduces the influence of non-linear lift components within the overall lift generation process. Here, the 6T:65 and 6T:37.5 configurations exhibit an increase in lift slope by 16% and 11% for an *AoA* range of 4° to 12° than 3T:65 and 3T:37.5, respectively. As the number of wingtip attachments increases, the flow through the wingtip can be more obstructed. Consequently, its impact on the flow over the suction surface diminishes. Therefore, increasing the number of attachments at the wingtip results in a more linear variation in C_L with *AoA* in the lift curve. In contrast, no significant effect of changing attachment length on the lift slope is noticed for the currently chosen winglet configurations.

Further, the variation of C_L for various conical slotted wingtip configurations for the *AR* = 1.0 model at *Re* of 100×10^3 is shown in **Fig. 7.8b.** All conical slotted winglets do not provide any beneficial effect on the pre-stall lift compared to the reference wing. However, it improves C_L as *AoA* approaches close to the stall angle. The 6C:65 and 6C:37.5 configurations showcase an increase in C_{Lmax} of approximately 11% than the baseline. The other two winglet arrangements, 3C:65 and 3C:37.5, show an enhancement in C_{Lmax} of around 6%. In the case of a conical device, it has a circular cross-section and is characterized as a non-lifting body, making it non-contributing to the overall lift generation of the wing. The main reason for this is that when air flows around a circular object, the entire flow field exhibits symmetrical characteristics with respect to both the horizontal and vertical axes passing through the center of the circle [Anderson, (2011)]. As a consequence of this symmetry, the pressure distribution on the suction surface of the object is perfectly balanced by the pressure distribution on the pressure side; thereby, no lift is generated. Therefore, the conical device does not contribute to generating lift as compared to the tapered attachment. However, an improvement in lift is observed for the 6C:65 and 6C:37.5 configuration, which is expected due to the obstruction of flow by wingtip attachment. The winglet configurations disrupt the formation and strength of wingtip vortices, which are known to exert a downward force

that hampers lift. This disruption leads to a more uniform pressure distribution over the suction surface, leading to an enhancement in lift. It has also been noted that the disruption of wingtip vortices by slotted winglets becomes more significant at higher *AoA*, leading to a more noticeable increase in lift compared to lower *AoA*.

7.3.1.2 Wing Configurations of $AR = 0.5$

Similar experiments are also conducted on a wing with an $AR = 0.5$, attaching tapered and conical wingtip devices at *Re* of 100×10^3. The variation of C_L as a function of *AoA* for different tapered-slotted winglet configurations is shown in **Fig. 7.9a**. The C_L-curve of the base wing does not exhibit stall up to 26°. All tapered winglet configurations consistently demonstrate higher C_L than the base wing for the tested *AoA* range. Similar to the tapered configuration of $AR = 1.0$, in this case as well, both the 6T:65 and 6T:37.5 arrangements demonstrate higher lift compared to the 3T attachment. Moreover, the lift slope in the linear region of the lift curve ($4° \leq AoA \leq 12°$) is also estimated to investigate the effect of wingtip attachments on the linearity of the lift curve for $AR = 0.5$. The lift curve slope of the base wing with an $AR = 0.5$ is obtained as 0.0138 */deg*, which is lower than the case of $AR = 1.0$ for the *AoA* range of $4° \leq AoA \leq 12°$. It is observed that as the *AR* of the wing decreases, the intensity of wingtip vortices on the flow distribution of the suction wing surface increases [Mizoguchi and Itoh, (2013)]. This creates a more complex cross-flow on this surface and, as a result, increases the contribution of the non-linear lift component to the overall lift production. Hence, as the *AR* of the wing decreases, the linear region or slope of the lift curve is found to decrease. However, similar to the tapered winglets case of $AR = 1.0$, all tapered winglets models exhibit a higher lift slope of the lift curve than the baseline wing. The lift slope values for the 6T:65 and 6T:37.5 arrangements are observed to be 1.68 and 1.55 times the lift slope value of the base wing's lift curve, respectively. Similarly, for 6T:65 and 3T:37.5 configurations, these slope values are 1.35 and 1.26 times the slope of the baseline curve, respectively. As the number of attachments in the wingtip increases, the lift slope of the C_L-curve increases, which is similar to the $AR = 1.0$ model. However, changing the attachment length has some effect on the lift slope but is less significant for the slotted winglet configurations.

The behavior of C_L for $AR = 0.5$ wing with different conical winglet configurations is presented in **Fig. 7.9b**. Similar to the conical winglets model of $AR = 1.0$, all the configurations do not produce any improvement in the C_L for $AoA < 20°$. While for $AoA > 20°$, both 6C:65 and 6C:37.5

arrangements improve the C_L. As reported in the study, a stationary circular object does not generate lift due to the symmetric distribution of the flow field, therefore, the improvement in C_L observed for the conical winglet arrangement can be attributed to the disturbance of wingtip vortices caused by the presence of the attachment devices. Additionally, it has also been noticed that the improvement in the C_L for winglet configurations is larger at higher *AoA* as compared to lower *AoA*. This observation signifies that the impact of the attachment device on disrupting wingtip vortices becomes more significant as the *AoA* increases, resulting in a more noticeable lift improvement than at lower *AoA*.

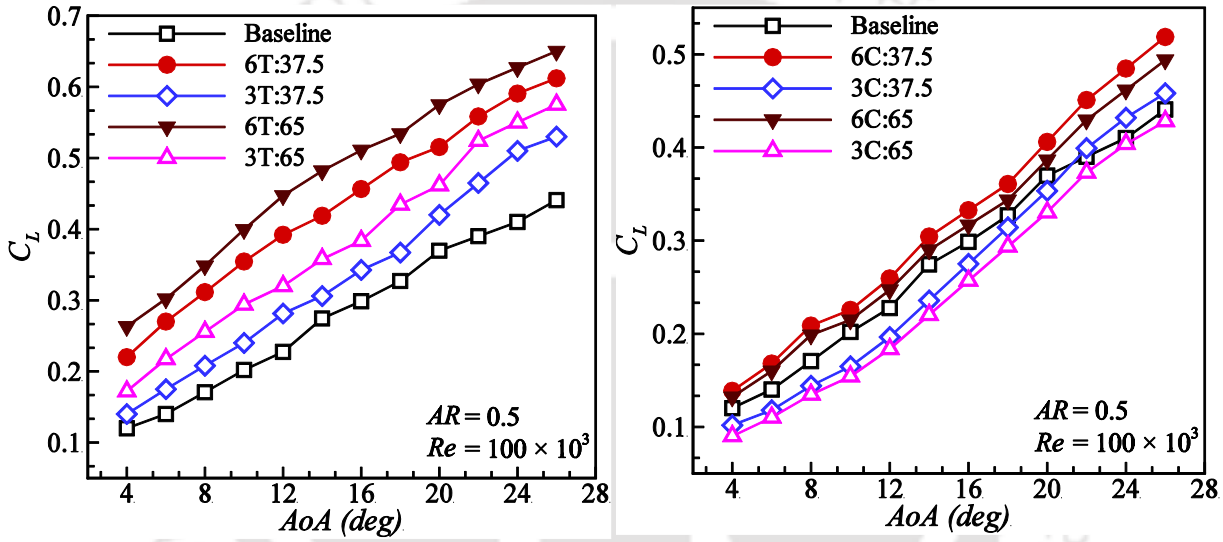

(a) Tapered slotted winglets **(b)** Conical slotted winglets

Fig. 7.9: Lift characteristics of various slotted winglet configurations of *AR* = 0.5

7.3.2 Drag Characteristics of Various Wing Configurations

7.3.2.1 Wing Configurations of *AR* = 1.0

The variation of C_D as a function of *AoA* for wings with different winglet configurations of the *AR* = 1.0 model at *Re* of 100×10^3 is shown in **Fig.7.10**. The results show that drag value continues to increase with an increase of *AoA*, which is same for both baseline wing and slotted winglet configurations. However, the rate of rise in C_D is observed to be slower in the pre-stall region (*AoA* < 12°) compared to the values seen in the vicinity of the stall or post-stall region. Here, the drag data shown on the plot represents the total drag experienced by the wing. This total drag is summation of profile drag and induced drag. Profile drag consists of skin friction drag and form

drag. The frictional drag remains relatively constant when the *AoA* is changed, while the form drag increases as the *AoA* increases. On the other hand, induced drag emerges as a consequence of lift generation and the creation of wingtip vortices. The effect of induced drag becomes more pronounced with an increase in *AoA*, which is due to the increasing effect of downwash. Hence, it has been concluded for streamlined bodies at lower angles, the values of form drag and induced drag are small, which means that the majority of the drag force is due to skin friction drag. This concept helps to explain the lower rate of rising C_D for lower *AoA*. However, as *AoA* increases, both form drag and induced drag increase; consequently, the total drag value increases rapidly.

The influence of tapered wingtip attachment does not exhibit any significant effect on the drag curve for *AoA* < 15°, which exhibits similarity of drag data with the baseline wing (**Fig. 7.10a**). In contrast, for *AoA* > 15°, most of the winglet arrangements reveal relatively lower drag values compared to the baseline case. However, it is expected that skin friction drag will be higher for the winglet configurations. Nevertheless, the reduction in the contribution of induced drag to the total drag may result in drag values equal to or even less than that of the base wing. The attachment length and their number also show a significant effect on the drag behavior for *AoA* > 15°. Most of the winglet configurations exhibit lower drag values than the reference wing. For example, the 6T:65 and 3T:65 configurations achieve a drag reduction of 8.33% and 13% compared to the baseline at *AoA* of 20°. Similarly, the 6T:37.5 arrangement leads to a 13% drag reduction at 20°, while the 3T:37.5 displays an even more notable decrease of 18%. Lowering the length from 65 mm to 37.5 mm and decreasing the number of attachments at the wingtip result in a more significant reduction in C_D compared to the base wing. As anticipated, increasing the number of attachments at the wingtip produces more pronounced obstructions to the flow of vortices along the wingtip. As a result, the strength of wingtip vortices can be reduced, leading to a reduction in induced drag. However, introducing more attachments at the wingtips has an adverse impact, leading to a significant increase in frictional drag. Thus, the total drag of configurations with fewer wingtip attachments is observed to be lower than those with a higher number.

Similar experiments are also carried out to estimate the drag performance for different conical slotted winglet configurations at *Re* of 100×10^3, as depicted in **Fig. 7.10b**. The results demonstrate that the drag behavior of conical winglets is totally different from tapered ones. All the winglet configurations exhibit higher C_D than the baseline wing for the tested range of *AoA*. As expected,

the wingtip attachments effectively hinder the primary flow vortices through the tip, which leads to control of the induced drag component. However, the conical device consists of a circular cross-section that comes into the category of a blunt body. Blunt bodies generate more pressure drag than streamlined objects due to the occurrence of flow separation [Anderson, (2011)]. As the flow passes over the circular object, the windward face of the body experiences higher pressure than the leeward, which is due to flow separation. This pressure difference leads to the creation of higher pressure drag for the circular object. This concept helps to explain why the conical winglet configuration exhibits more significant drag than the baseline wing, even at lower *AoA*. Moreover, when the number of attachments in the wingtip is reduced from 6C to 3C, the C_D value of the configuration reduces. Similarly, decreasing the attachment length from 65 mm to 37.5 mm also leads to a reduction in C_D. However, this effect is comparatively less pronounced than the impact observed from altering the number of attachments in the wingtip. When comparing the C_D of two different wingtip attachment devices, the conical winglet arrangements generate more drag than the tapered case. It is obvious because its profile is a flat plate with rounded leading and trailing edges. Whereas the geometry of a conical device is like a blunt object, and it always generates more drag than a streamlined body.

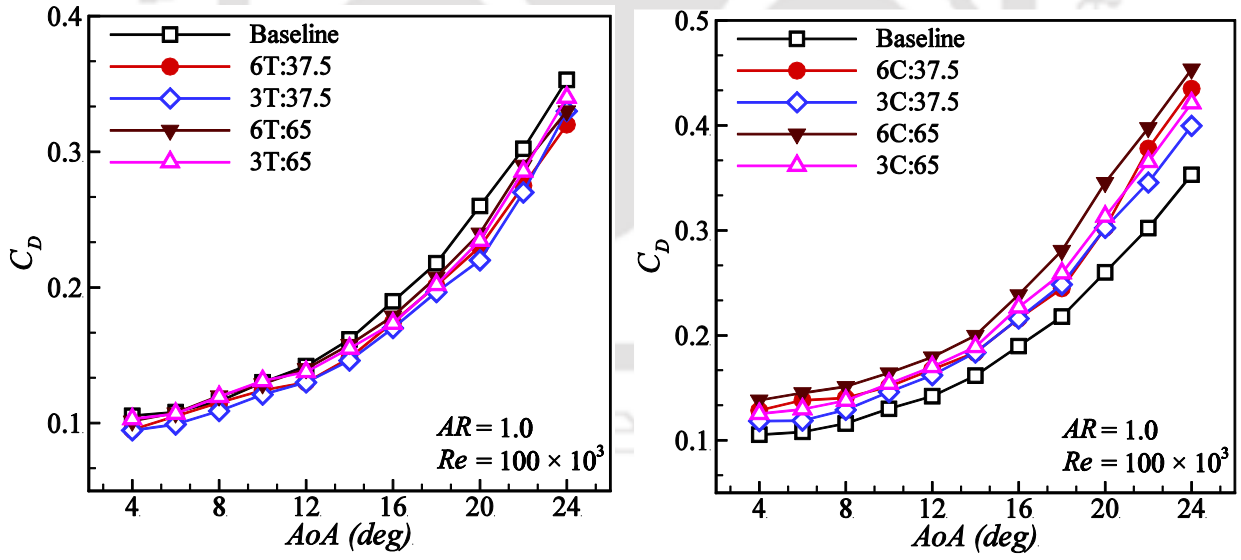

(a) Tapered slotted winglets **(b)** Conical slotted winglets

Fig. 7.10: Drag characteristics of various slotted winglet configurations of *AR* = 1.0

Furthermore, the influence of different wingtip attachments on the induced drag factor for the *AR* = 1.0 model is approximated by analyzing the slope of the linear portion of the C_D-C_L^2 curve.

According to **Eq. 7.1**, the slope (dC_D/dC_L^2) of the C_D-C_L^2 curve directly correlates to the induced drag factor $(k = 1/\pi eAR)$. This approach provides a simple way to measure the effect of different slotted winglet designs on induced drag, thereby facilitating comparison and optimization of aerodynamic performance. A steeper slope indicates a higher induced drag factor, while a shallower slope suggests a reduction in induced drag [Céron-Muñoz et al., (2013)]. In the present study, the slope of each tapered winglet configuration is obtained separately through a linear fit of the C_D versus C_L^2 curve, as shown in **Fig. 7.11.** The coefficient of determination (R^2) is found to be in the range between 0.9799 and 0.9938. This range validates the accuracy and reliability of the linear fit results, increasing confidence in interpreting the relationship between C_D and C_L^2 for the chosen wingtip configurations. For the base wing, the slope in the linear region ($4° \leq AoA \leq 14°$) of the C_D-C_L^2 curve is estimated to be 0.2713 at $Re = 100 \times 10^3$. This slope value reduces to 48% for the 6T:65 case, while it decreases by 38% in the case of 3T:65 configuration than the baseline for the same AoA range (**Fig. 7.11a**). This observation indicates that a higher number of attachments in the wingtips leads to a greater reduction in the drag factor. Moreover, in the case of 6T:37.5, the decrease in the slope value is observed to be 50%, which is very similar to the case of the 6T:65 arrangement. For 3T:37.5, the slope is reduced by 35% more than the baseline wing, which is close to the drag reduction observed in the 3T:65 case. This observation implies that increasing the attachment length from 37.5 mm to 65 mm has a similar effect in reducing induced drag compared to a shorter length within a given slotted winglet configuration.

$$C_D = C_d + \frac{C_L^2}{\pi eAR} \tag{7.1}$$

Similar to the tapered winglets scenario, the slope of C_D-C_L^2 curve is also estimated to understand the behavior of induced drag factor for the wing with different conical attachments at the wingtip (**Fig. 7.11b**). Herein, the R^2 values are obtained in the range from 0.9761 to 0.992, which indicate a good alignment between the plotted data and the linear fit. The 6C:65 and 6C:37.5 configurations exhibit a 17% reduction in the slope of C_D-C_L^2 curve compared to the baseline curve. In contrast, for the 3C:65 and 3C:37.5 arrangements, the slope values are found to be the same as observed in the baseline case. Similar to tapered wingtip attachment, the higher number of conical devices in the wingtip reduces the induced drag more, and changing its length does not alter the induced drag for the winglet configurations. However, tapered attachment in the wingtips reduces the slope of

the C_D-C_L^2 curve more prominently as compared to the conical case for the same arrangements. This signifies that the tapered wingtip attachment is more efficient in reducing the induced drag factor than the conical ones. Tapered attachments, characterized by their streamlined nature, are predicted to facilitate smoother airflow and enhanced vortex control at the wingtips. This can reduce the formation of turbulent flow and the intensity of wingtip vortices, which are primary contributors to the induced drag. Conversely, the conical attachments, while offering some obstruction to vortices, are anticipated to potentially trigger more flow separation and turbulence due to their blunt body configuration. As a result, the streamlined design of tapered attachments is anticipated to demonstrate greater effectiveness in addressing the root cause of induced drag, providing potentially more significant reductions in drag than conical devices.

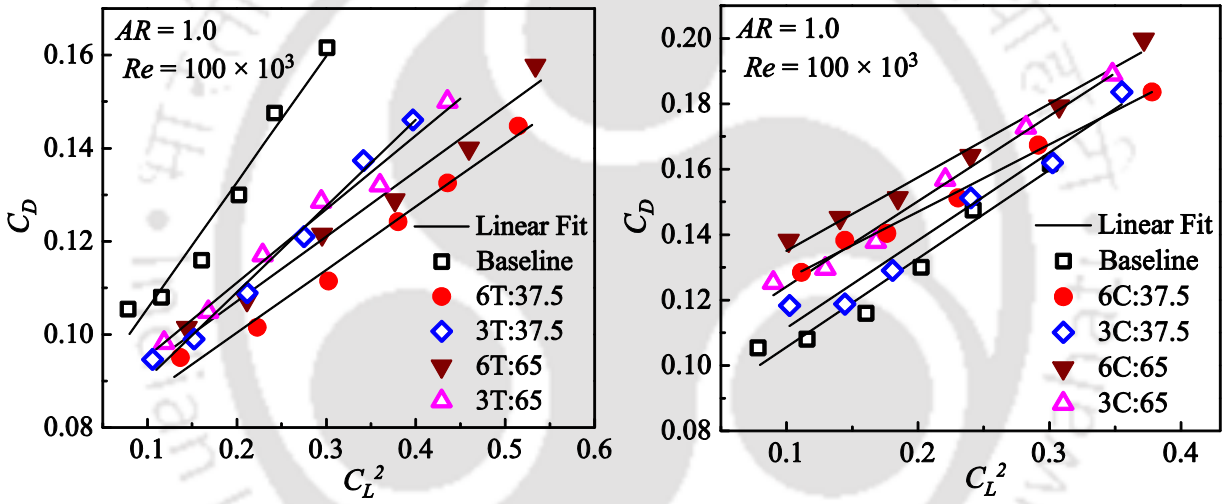

(a) Tapered slotted winglets **(b)** Conical slotted winglets

Fig. 7.11: Estimatiion of induced drag factor for various slotted winglet configurations

7.3.2.2 Wing Configurations of *AR* = 0.5

The variations in C_D for different taper and conical winglet configurations of a wing with an *AR* = 0.5 are depicted in **Fig. 7.12**. In the case of tapered attachment, all the wingtip configurations exhibit higher drag values than the baseline wing (**Fig. 7.12a**). However, this drag difference between the slotted wingtip configuration and the baseline become minimal for the lower number of attachments as 3T:37.5, which may be due to lower friction drag. Although all the configurations reduce induced drag, but due to high friction drag, the reduction in induced drag is unable to overcome the friction drag penalty. The reason for higher frictional drag for the winglet

configurations of *AR* = 0.5 can be attributed to larger contribution of the attachment area. For *AR* = 0.5, the attachment area of 6T:65 and 6T:37.5 arrangement is more significant to the contribution in total wing area, which generates more frictional drag value. Whereas, in the case of *AR* = 1.0, the contribution of attachment area is less significant in the total projected wing area. For example, 6T:65 and 6T:37.5 arrangements provide additional surface area as 32% and 19% of base wing area, respectively, in the case of *AR* = 0.5 winglet configurations. On the other hand, this area contributes up to 20% and 12% for the same attachments in the case of *AR* = 1.0. Based on these observations, it is noted that using same attachment device for *AR* = 1.0 is not advantageous for *AR* = 0.5. To achieve better drag improvement with an *AR* = 0.5, it is essential to decrease the attachment area. Similar experiments are also carried out with conical configurations of *AR* = 0.5, as presented in **Fig. 7.12b**. All the attached wingtip models exhibit higher drag values than the baseline, for the tested range of *AoA*, which is similar to *AR* = 1.0 with conical attachments. The conical device is classified as a blunt body, which typically generates more pressure drag. Therefore, higher drag is observed for conical winglet configurations. In the case of *AR* = 0.5, an increase in either attachment length or number results in higher drag values compared to configurations with fewer attachments. This trend remains consistent for both tapered and conical slotted winglet configurations.

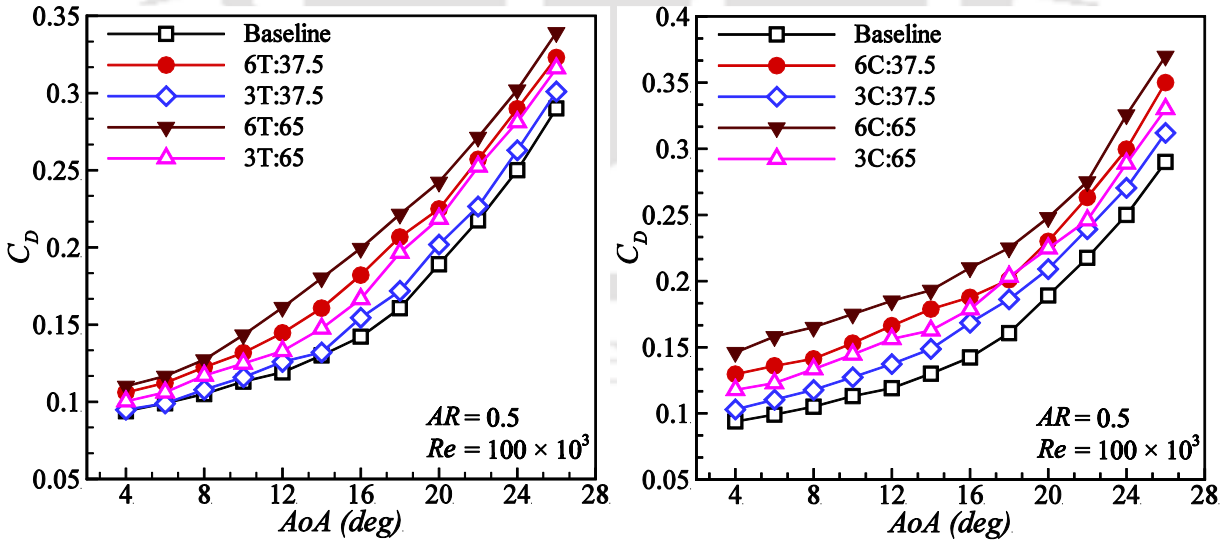

(a) Tapered slotted winglets **(b)** Conical slotted winglets

Fig. 7.12: Drag characteristics of various slotted winglet configurations of *AR* = 0.5

Similar to AR = 1.0 configurations, the term induced drag factor $(k = 1/\pi eAR)$ is also estimated by applying linear fit of the C_D-C_L^2 curve for each winglet configuration (**Fig. 7.13)**. As indicated by **Eq. 7.1**, the slope of the C_D-C_L^2 curve is directly related to the induced drag factor. For the selected C_L data, the value of R^2 is obtained in the range between 0.9737 and 0.9921, which is almost the same as for the AR = 1.0 case. The slope of C_D-C_L^2 curve for the baseline wing of AR = 0.5 is approximated to be 0.812 at Re of 100×10^3, which is higher in comparison to the AR = 1.0 case. This observation indicates that the impact of induced drag is more prominent for a wing AR = 0.5 than that of 1.0. Furthermore, all tapered wingtip attachments, regardless of length and number, exhibit lower induced drag factors than their baseline (**Fig. 7.13a**). The 6T:65 and 3T:65 arrangements reduce slope by 33% and 23%, respectively, compared to the baseline. Whereas, for 6T:37.5 and 3T:37.5 cases, this slope value reduces to 30% and 19%, respectively. Similar to AR = 1.0 with tapered wingtip attachments, this finding also implies that increasing the number of attachments at the wingtips results in a more substantial reduction in drag factor. Conversely, increasing the length from 37.5 mm to 65 mm has a similar effect in reducing the induced drag factor for the winglet configurations. Additionally, compared to the AR = 1.0 case, the same wingtip attachments for a wing of an AR = 0.5 demonstrate a lower reduction in induced drag relative to their respective baseline data. For instance, a 48% reduction in the induced drag factor is observed for the 6T:65 configuration in the AR = 1.0 case compared to its baseline. Similarly, for the same winglet configuration in case of AR = 0.5, the reduction is observed to be 33%. The observed difference can be attributed to the increasing significance of wingtip vortices as the AR decreases [Mizoguchi and Itoh, (2013)]. Therefore, using the same attachment size employed for higher AR wings may be inadequate to restrict airflow through the wingtip for lower AR wings. However, for better performance with a low AR case, modifications to the wingtip attachment design become necessary to efficiently control induced drag.

For conical slotted arrangement, the linear range of C_D versus C_L^2 data is also plotted to understand the behavior of induced drag factor for different conical attachments at the wingtips (**Fig. 7.13b**). In this case, the R^2 values are obtained in the range from 0.9892 to 0.9942, which indicate a good alignment between the plotted data and the linear fit. Analysis of results shows that the slope of C_D-C_L^2 curve decreases by 9% and 12% than the baseline curve for 6C:65 and 6C:37.5 configurations, respectively. In contrast, for the 3C:65 and 3C:37.5 arrangements, the slope values

are found to be almost the same as noticed in the baseline case. Similar to the tapered attachment, higher number of conical attachments at the wingtip lead to higher reduction in induced drag, and altering its length does not affect induced drag for the current configuration. For identical winglet configurations, the tapered attachment exhibits a more pronounced reduction in the slope of the C_D-C_L^2 curve as compared to the conical device, which is similar to the AR = 1.0 case.

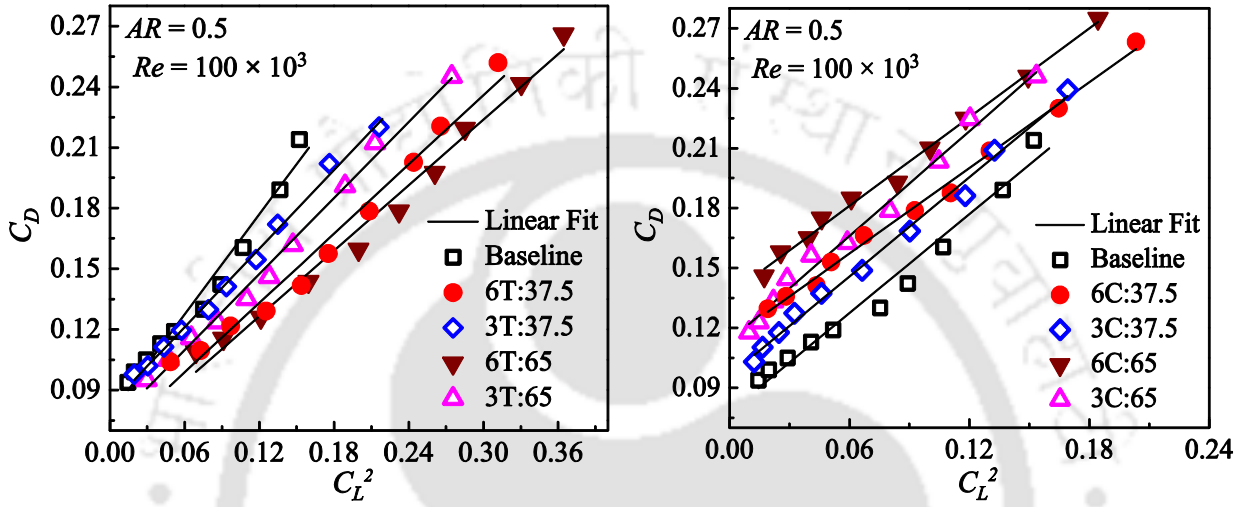

(a) Tapered slotted winglets **(b)** Conical slotted winglets

Fig. 7.13: Estimation of induced drag factor for various slotted winglet configurations

7.3.3 C_L/C_D ratio Characteristics of Various Wing Configurations

7.3.3.1 C_L/C_D for Wing Configurations of AR = 1.0

The effectiveness of wing with different winglet configurations is assessed by estimating the value of C_L/C_D ratio for different *AoA* mountings, as presented in **Fig. 7.14**. The results show that all the tapered slotted winglet arrangements provide better C_L/C_D than the reference wing in the range of tested *AoA* for AR = 1.0 (**Fig. 7.14a**). For the baseline wing of AR = 1.0, the value of $(C_L/C_D)_{max}$ is obtained as 3.46 at Re of 100 × 10^3. The 6T:65 configuration demonstrates an increase in the $(C_L/C_D)_{max}$ by 40% than the baseline. However, when the number of winglets attached decreases to 3T, the increase in the $(C_L/C_D)_{max}$ is still significant, but it reaches 26% compared to the baseline. In the case of 6T:37.5 and 3T:37.5, this value is found to be increased by 46% and 30%, respectively, as compared to the base wing. This observation shows that $(C_L/C_D)_{max}$ decreases significantly with the decrease in number of attachments at the wingtips. However, changing attachment length has a smaller impact on $(C_L/C_D)_{max}$ than varying the number of attachments at

the wingtips. For conical wingtip devices, all wing configurations exhibit lower C_L/C_D values than the baseline for the tested range of *AoA*, as shown in **Fig. 7.14b.** Conical devices have been identified as having a blunt body shape, it is expected that they generate more pressure drag and do not generate any significant lift. This imbalance leads to a scenario where the total drag increases more substantially than the lift, resulting in reduced aerodynamic efficiency. Moreover, for the tapered case, the lower drag is expected due to their thin flat plate design, which also contributes to lift generation. Hence, the C_L/C_D magnitude for wings with conical winglet configurations is typically observed to be lower compared to both the baseline and tapered winglet cases.

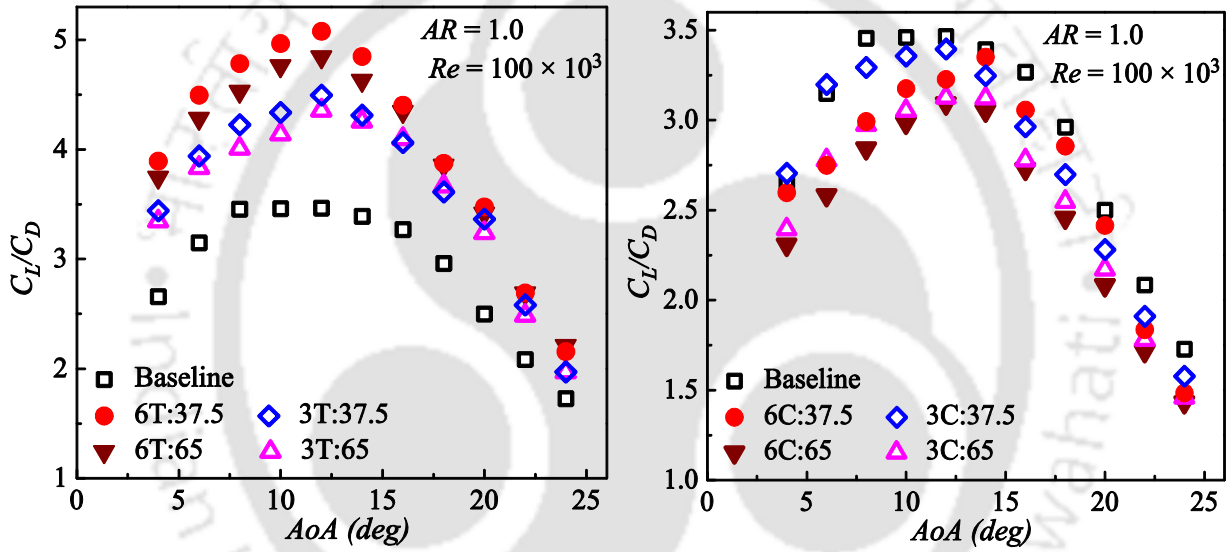

(a) Tapered slotted winglets **(b)** Conical slotted winglets

Fig. 7.14: Comparison of C_L/C_D behavior for various slotted winglet configurations of *AR* = 1.0

7.3.3.2 C_L/C_D for Wing Configurations of *AR* = 0.5

The C_L/C_D ratio for *AR* = 0.5 wing with tapered and conical winglet arrangements is obtained for various *AoA* ranges, as exhibited in **Fig. 7.15**. All the configurations with tapered winglets indicate higher C_L/C_D values than the baseline for all tested *AoA* ranges. The 6T:65 and 3T:65 arrangements improved their $(C_L/C_D)_{max}$ value by 32% and 15% than the baseline (**Fig. 7.15a**). Similarly, for 6T:37.5 and 3T:37.5 configurations, there is an improvement of 28% and 9%, respectively, in their $(C_L/C_D)_{max}$ values. Furthermore, the impact of altering the winglet length from 65 mm to 37.5 mm is less significant on the $(C_L/C_D)_{max}$ values compared to changing the number of winglets. It is

observed that for the same tapered winglet configurations, improvement in respective $(C_L/C_D)_{max}$ is greater for AR = 1.0 as compared to 0.5. For example, the 6T:37.5 arrangement enhances the $(C_L/C_D)_{max}$ by 46% than their baseline for AR = 1.0. Similarly, this value is found to be enhanced up to 28% in the case of AR = 0.5 for the same winglets configuration. The difference in improvement can be attributed to the changing influence of wingtip vortices with AR. As the AR decreases, wingtip vortices become more dominant. [Mizoguchi and Itoh, (2013)]. This means that the use of the same wingtip attachment employed on higher AR wings is insufficient to effectively control airflow around the wingtip for lower AR. Thus, it becomes clear that the effectiveness of winglet configurations proven for high AR wings may not translate into similar benefits for low AR cases. Moreover, similar to the tapered winglets arrangement of AR = 0.5, the value of C_L/C_D for various AoA is also estimated for conical wingtip attachment (**Fig. 7.15b**). The results indicate that no improvement in C_L/C_D is observed for the wing equipped with conical winglets compared to its base wing. This finding is consistent with the performance of AR = 1.0 conical winglets configuration.

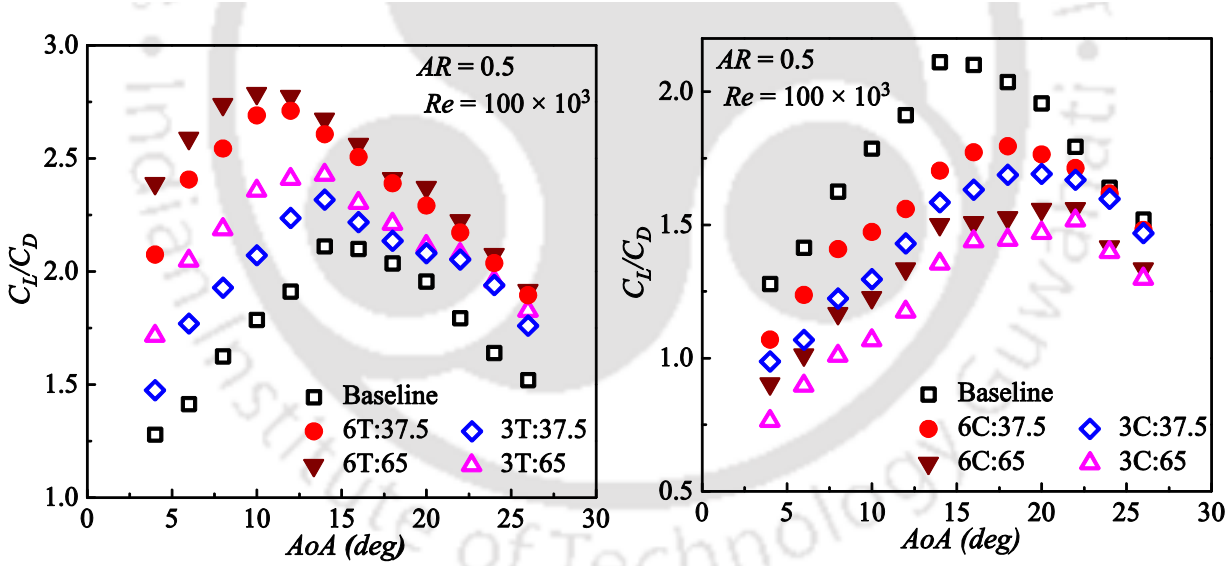

(a) Tapered slotted winglets **(b)** Conical slotted winglets

Fig. 7.15: Comparison of C_L/C_D behavior for various slotted winglet configurations of AR = 0.5

7.3.4 Pitching Moment Characteristics of Various Wing Configurations

7.3.4.1 Wing Configurations of AR = 1.0

The pitching moment has a substantial impact on the longitudinal stability of the wing. Here, the pitching moment data is obtained at about quarter chord location (*0.25c*) of the wing for all

winglets configurations at $Re = 100 \times 10^3$. The variation of pitching moment coefficient $(C_{M,0.25c})$ as a function of *AoA* for an *AR* = 1.0 model with different slotted winglet arrangements is presented in **Fig. 7.16.** For all the configurations, the magnitude of $C_{M,0.25c}$ decreases to negative values with increasing *AoA* up to 20°, and after this angle, an increasing trend is observed. The rise in the moment curve after reaching a particular *AoA* is associated with a decrease in lift. As it has been noted that the behavior of the lift curve alters as it gets near the stall angle, a similar trend has also been noted for the moment curve. The importance of the negative pitching moment refers to the fact that when *AoA* increases, it rotates the wing towards its equilibrium position to overcome the disturbance caused by *AoA*. Additionally, as reported for the static longitudinal stability of an aircraft, it is important for the slope of the moment curve to remain negative [Nelson, (1998)]. In the current study, the moment slope is obtained from the linear region of the moment curve and is found as –0.0071/*deg* and –0.0042/*deg* for the base wing of *AR* = 1.0 and 0.5, respectively.

Furthermore, the strong influence of different wingtip attachments on the moment characteristics is noticed for both *AR*s wings. All winglet configurations of *AR* = 1.0 exhibit more negative pitching values for both pre-stall and post-stall angles compared to the baseline wing (**Fig. 7.16**). This observation suggests that the wing with equipped winglets has a greater pitch-down tendency than the clean wing. In the case of tapered wingtip attachment for *AR* = 1.0, both the 6T:65 and 6T:37.5 configurations exhibit more negative pitching values than the 3T arrangement of both lengths (**Fig. 7.16a**). For example, arrangements like 6T:65 and 6T:37.5 reduce the magnitude of $C_{M,0.25c}$ by 22% and 20%, respectively, than clean wing at *AoA* = 16°.Similarly, the pitching moment has been observed to decrease by up to 12% and 9% only with the configurations 3T:37.5 and 3T:37.5, respectively, when compared to the baseline at the same *AoA*. This suggests that incorporating more attachments at the wingtip enhances stability and diminishes the tendency for upward pitching. However, the influence of variations in winglet length on the pitching moment is relatively minor compared to the effect of altering the number of winglets. A similar result of varying the parameters of multi-tip winglets on pitching moment behavior was observed by Narayan and John [Narayan and John, (2016)]. In the case of conical winglets arrangement, variations in the parameters of winglets have negligible impact on the pre-stall pitching moment coefficient has influence it in the post-stall region (**Fig. 7.16b**). For post-stall *AoA*, the downward pitching tendency of the wing with winglets configuration is reduced with the reduction in the attachment devices on the wingtip. No significant effect of changing the attachment length on post-

stall pitching moment values is observed for the conical winglets. When comparing the $C_{M,0.25c}$ of both winglet configurations, the tapered winglet configuration results in a greater reduction in the negative pitching moment value than the conical case.

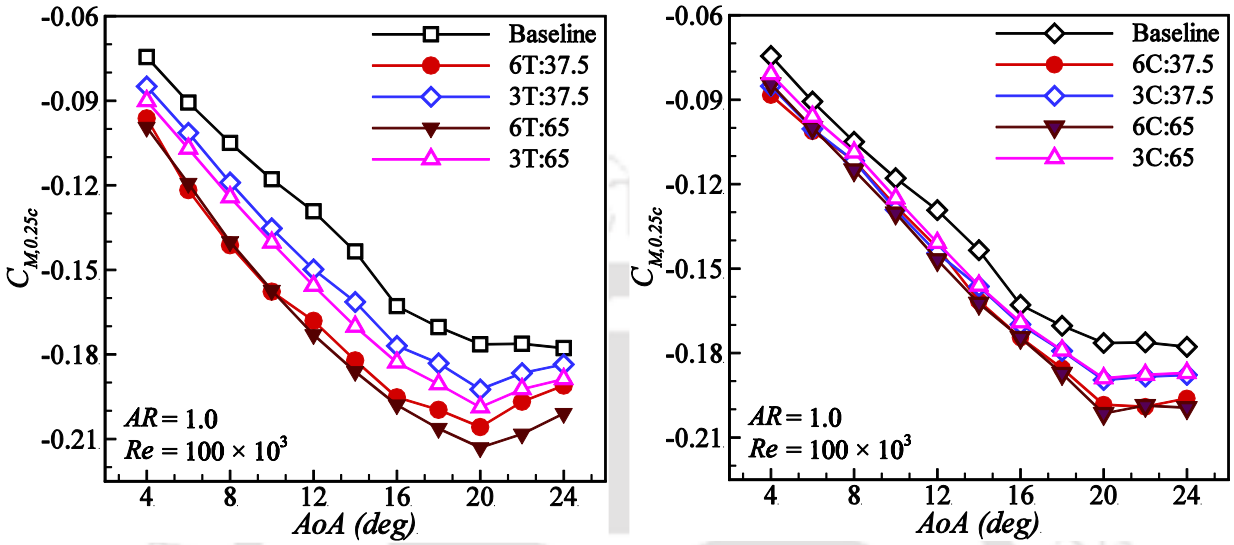

(a) Tapered slotted winglets **(b)** Conical slotted winglets

Fig. 7.16: Pitching moment characteristics of various slotted winglet configurations of *AR* = 1.0

7.3.4.2 Wing Configurations of *AR* = 0.5

Similar to the *AR* = 1 .0 model, the pitching moment data for different slotted winglet configurations of *AR* = 0.5 is also obtained for various *AoA* ranges, as illustrated in **Fig. 7.17**. In this case, as well, all wing configurations, incorporating tapered slotted winglets, exhibit a more negative magnitude of $C_{M,0.25c}$ than clean wing (**Fig. 7.17a**). Both the attachment number and its length have an impact on the pitching moment characteristics of the *AR* = 0.5 wing configuration. When either the number of attachments increases from 3T to 6T or the length increases from 37.5 mm to 65 mm, the $C_{M,0.25c}$ value becomes more negative. This implies an increase in the pitch-down tendency or longitudinal stability of the wing configurations. However, the impact of altering the number of attachments at the wingtips has a more significant effect on the pitching moment compared to variations in length. For instance, configurations like 6T:65 and 3T:65 reduce the magnitude of $C_{M,0.25c}$ by 66% and 26%, respectively, compared to the original wing at an *AoA* = 16°. While, the 6T:37.5 and 3T:37.5 arrangements have shown a magnitude reduction of $C_{M,0.25c}$ by 49% and 14% respectively for the same *AoA*. This emphasizes that the values of the pitching moment are more significantly affected by changes in the number of attachments at the wingtips

than by changes in the length of the attachments. In the context of conical slotted winglets, only the 6T:65 and 6T:37.5 configurations show a slightly favorable effect on the pitching moment compared to the baseline (**Fig. 7.17b**). Conversely, the other two configurations offer pitching moment characteristics similar to the base wing. Similar to the *AR* = 1.0 case, all arrangements featuring tapered slotted winglets show a more pronounced improvement in pitching moment compared to the conical device. In summary, incorporating different wingtip attachments resulted in notable changes in the pitching moment characteristics for both *AR*s wings. This analysis highlights the direct correlation between pitching moment behavior and the effectiveness of winglet designs in mitigating flow vortices at the wingtips.

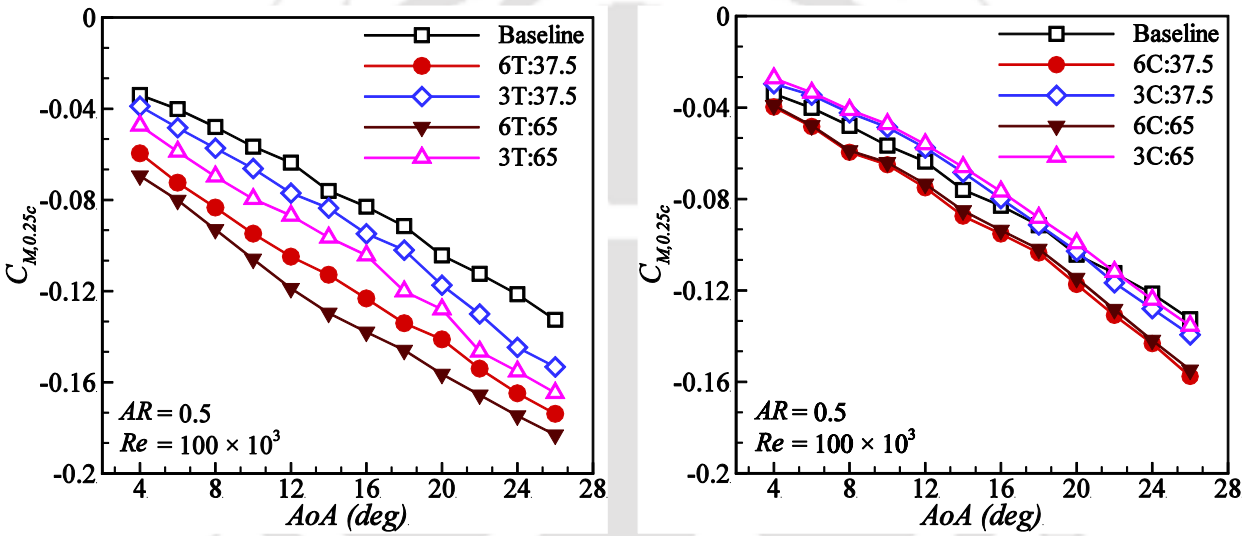

(a) Tapered slotted winglets **(b)** Conical slotted winglets

Fig. 7.17: Pitching moment characteristics of various slotted winglets configurations of *AR* = 0.5

7.3.5 Effect of *Re* on the Performance of Various Wing Configurations

The present study is also extended to investigate the impact of varying *Re* on the performance of different types of slotted winglet arrangements. The wingtip configurations of *AR* = 1.0 are tested in the *Re* between 80 × 10^3 and 120 × 10^3, while *AR* = 0.5 configurations are examined in the *Re* range of 100 × 10^3 to 150 × 10^3. This analysis demonstrates that variations in *Re* lead to significant alteration in the performance metrics, specifically C_{Lmax} and $(C_L/C_D)_{max}$, for wing models of both *AR*s. The variation of C_{Lmax} as a function of *Re* for different tapered and conical slotted winglet arrangements of *AR* = 1.0 is shown in **Fig. 7.18**. For the base wing of *AR* = 1.0, when the *Re* increases from 80 × 10^3 to 120 × 10^3, the C_{Lmax} increases by 9% while no change is observed in

the stall point of the wing. Similarly, all the slotted winglet configurations also show improvement in the C_{Lmax} with increasing *Re*, but no improvement in the stall angle is noticed in any case. For example, within the current *Re* range, tapered configurations such as 6T:65 and 3T:65 show an increase in C_{Lmax} of approximately 12.5% and 12.7%, respectively (**Fig. 7.18a**). Similarly, in the case of conical attachments, this improvement is observed to be around 13% and 11% for 6C:65 and 3C:65, respectively (**Fig. 7.18b**). In the examined *Re* flow regime, the configuration with a higher number of attachments at wingtips, regardless of their length or shape, consistently demonstrate a higher C_{Lmax} than those with fewer attachments.

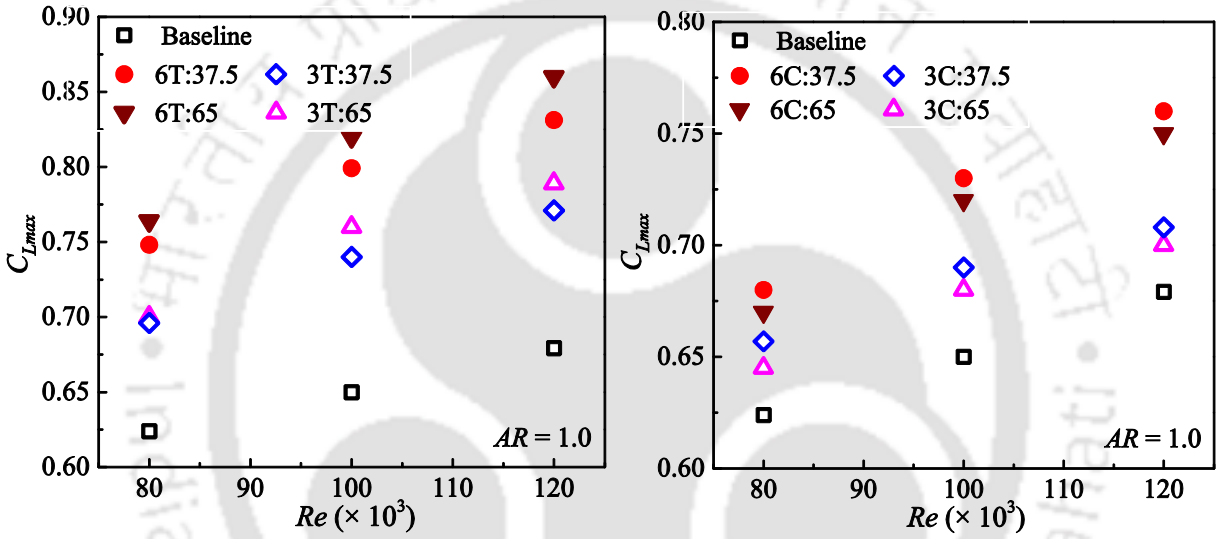

(a) Tapered slotted winglets **(b)** Conical slotted winglets

Fig. 7.18: Variation of C_{Lmax} with *Re* for various slotted winglet configurations

Furthermore, the C_L/C_D ratio for various wingtip configurations of *AR* = 1.0 and 0.5 are also estimated at different *Re*. These investigations reveal that the C_L/C_D values, in both the pre and post-stall regions, exhibit enhancement with an increase in *Re*, and this trend is consistent across all wingtip models. However, the results are presented only for the maximum C_L/C_D ratio of various tapered slotted winglets configurations of both *AR*s, as illustrated in **Fig. 7.19**. This data also highlights a substantial rise in the maximum C_L/C_D ratio as *Re* increases. For instance, when *Re* increased from 80×10^3 to 120×10^3, the $(C_L/C_D)_{max}$ for 6T:65 and 3T:65 arrangement of *AR* = 1.0 increased by 23% and 21%, respectively (**Fig. 7.19a**). Similarly, this improvement is observed as 26% and 23% for the same winglets configurations of *AR* = 0.5 as *Re* is varied from 100×10^3 to 150×10^3 (**Fig. 7.19b**). **Figure 7.19** also indicates that within the tested *Re* range, wing models

with a greater number of wingtip attachments exhibit higher $(C_L/C_D)_{max}$ values than models with fewer attachments. No significant effect of attachment length on the $(C_L/C_D)_{max}$ is observed in the current flow regime. Moreover, for better clarity and ease of understanding, **Table 7.1** presents a tabular overview of the $(C_L/C_D)_{max}$ values for the base wing and the corresponding improvements achieved through different winglet configurations at various *Re*. The table clearly demonstrates that, for the same winglet configurations and *Re*, the improvement in $(C_L/C_D)_{max}$ ratio is more significant in the case of higher *AR* compared to lower ones.

Table 7.1: Comparison of $(C_L/C_D)_{max}$ for various winglet configurations at different *Re*

***AR* = 1.0**				***AR* = 0.5**			
Re **($\times 10^3$)**	**Baseline $(C_L/C_D)_{max}$**	**% improvement in $(C_L/C_D)_{max}$ over baseline**		***Re*** **($\times 10^3$)**	**Baseline $(C_L/C_D)_{max}$**	**% improvement in $(C_L/C_D)_{max}$ over baseline**	
		6T:65	**3T:65**			**6T:65**	**3T:65**
80	2.88	47.56	33.82	100	2.11	32.08	15.06
100	3.46	39.79	25.77	120	2.50	24.00	9.20
120	3.82	37.43	22.25	150	2.81	25.26	8.89

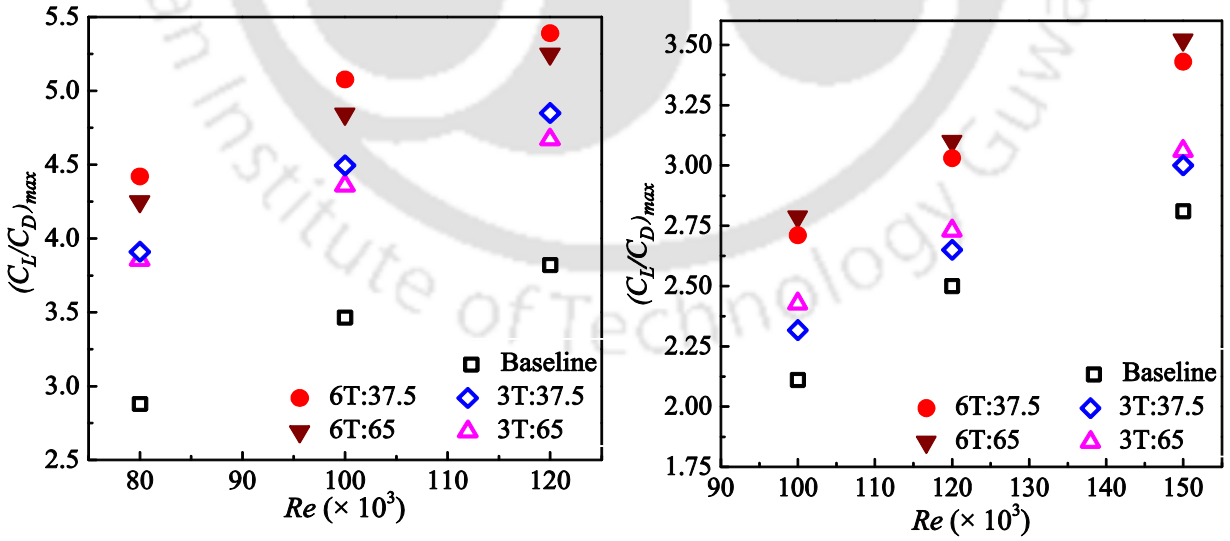

(a) *AR* = 1.0 **(b)** *AR* = 0.5

Fig. 7.19: Variation of $(C_L/C_D)_{max}$ with *Re* for various tapered winglet configurations of both *AR*s

7.4 Summary

An experimental investigation is carried out to examine the effectiveness of different bionic slotted winglet configurations for improving the performance of low *AR* wings within the *Re* range of MAVs applications. This study is conducted with the S5010 profiled wing of two different *AR*s such as 1.0 and 0.5, in the presence of various attachment devices on the wingtip for the *Re* range of 80×10^3 to 150×10^3. Two different wingtip attachment shapes, tapered and conical, have been chosen for this study and added in a planar manner to the wingtips to create tapered or conical slotted winglet configurations. In this study, four distinct winglet configurations of each shape have been tested for both the *AR* wings. For the base wings, findings indicate that the stall angle is 20° for *AR* = 1.0, and no stall point is observed up to an *AoA* of 26° for *AR* = 0.5 wing. In all cases, the tapered slotted-winglet configurations have demonstrated improvements in C_L, lift slope, C_L/C_D, induced drag factor, and $C_{M,0.25c,}$ compared to their respective base wings. These wingtip attachments do not modify the stall characteristics of the base wing; nevertheless, they exhibit a higher C_{Lmax} value than the baseline of *AR* = 1.0. On the other hand, all conical winglet configurations do not provide any beneficial effect on the C_L/C_D values than the baseline within the tested range of *AoA*. However, they exhibit an improvement in the C_L as the *AoA* approaches close to the stall angle for *AR* = 1.0. Regarding drag characteristics, the total drag of winglet configurations exhibits higher values than their respective baseline in most cases. This drag difference increases as the number or length of attachment on the wingtips increases. Despite the higher drag values, the C_L/C_D ratio still shows higher values in both regions before and after the stall point than the baseline for the tapered winglet configurations of both *AR*s.

The variation in winglet parameters also has a significant effect on the performance characteristics of wing configurations. When the number of attachments at the wingtip is increased, there is a more pronounced improvement in lift slope, $C_{Lmax,}$ and C_L/C_D compared to configurations with fewer attachments. Further, the configuration with the higher number of attachments leads to a greater reduction in the induced drag factor and diminishes the tendency for upward pitching. In contrast, changing the attachment length does not significantly affect these performance parameters. For the same winglet configurations and *Re*, the improvement in performance metrics is more significant in the case of *AR* = 1.0 compared to lower ones. This finding suggests that for a wing with low *AR*, modifications to the wingtip attachment design may be necessary to efficiently

restrict airflow through the wingtip. The performance of winglet configurations is significantly influenced by *Re*, and as the *Re* increases, their performance also improves. While comparing the effectiveness of these two wingtip devices, the tapered attachments have been found to be more efficient in improving the performance characteristics of both *AR* wings than the conical one. This observation suggests that the shape of the attachment device needs to be streamlined to enhance the efficiency of slotted winglet arrangements. Overall, the incorporation of bio-inspired tapered slotted winglets have been proven to be beneficial for enhancing the performance of low *AR* wings. This approach can be implemented to improve the flight performance of low-speed vehicles such as MAVs. These vehicles often face significant weight constraints, and the addition of slotted winglets do not significantly alter their weight. The design modification is expected to enhance lift characteristics, reduce induced drag, and improve the lift-to-drag ratio, making MAVs more efficient and effective in various applications.

CHAPTER 8

Conclusions and Scope of Future Work

8.1 Conclusions

Special forms of unmanned aircraft, such as MAVs, are evolving rapidly each year due to their extensive applications in both civil and military sectors. For the efficient design and development of MAVs, various factors must be considered: aerodynamics, maneuverability, propulsion system, power unit, and various accessories (cameras, sensors, etc.). Among these, the major area of serious concern is the aerodynamic efficiency of the wing because such vehicles have limited wing dimensions ($AR \leq 2.0$) and power input, due to which they operate under a low *Re* range (10×10^3 -100×10^3). Within this *Re* range, the selection of airfoils is also a major issue, because conventional airfoils experience a significant decline in performance as the *Re* decreases below 100×10^3. Apart from this, the wing design of such vehicles relies majorly on the use of wings with an $AR < 2.0$. These wings face a significant challenge of producing lower lift values at low *AoA* due to the presence of strong wingtip vortices. However, at high *AoA*, wings experience higher levels of induced drag. As a result, the wing design of low-speed vehicles still faces challenges when implementing wings of $AR < 2.0$ without any modifications to their geometry.

In view of this, detailed experimental investigations have been conducted to explore the aerodynamic behaviours of wings with an $AR \leq 2.0$, both in the presence and absence of bio-inspired passive flow control devices. Regarding this, two low-speed airfoils, S5010 and E214, have been chosen to fabricate a rectangular wing model. In the initial phase of the study, the aerodynamic performance and wake field characteristics of these airfoil models are investigated within the *Re* range of $40 \times 10^3 \leq Re \leq 100 \times 10^3$. Subsequently, the effect of *Re* and *AR* on the performance of wings, associated with S5010 and E214 sections, has been presented in the next phase of the investigation. For this study, the *AR* and *Re* have been chosen in the range of $2.0 \leq AR \leq 1.0$ and $60 \times 10^3 \leq Re \leq 150 \times 10^3$, respectively. The analysis exhibited that wings based on the E214 airfoil showed better aerodynamic performance than the S5010 airfoil for the tested *Re* and *AR* ranges. Consequently, in an effort to enhance the performance of the S5010 wing, bio-inspired passively acting devices have been implemented on the wing and are discussed in the

subsequent phase of the study. These flow control devices have been tested, targeting two different flow modes, specifically flow separation over the surface and vorticity at the wingtip. In the first case, the self-actuating flaps, developed by imitating the covert feathers on a bird's upper wing, have been examined on wings of AR = 2.0 and 1.0 to control flow separation over the surface. This work has focus on exploring flap effectiveness in various aspects, including flap span, chord length, and chord-wise placement within a Re range of 60×10^3 to 120×10^3. Finally, various bionic wingtip devices have been successfully tested to reduce the effect of wingtip vortices for the S5010 wing of AR = 1.0 and 0.5 in the Re range from 80×10^3 to 150×10^3. The inspiration for the slotted wingtip concept came from the structural features observed in the primary feathers found at the tips of bird wings. In this regard, two different wingtip attachment shapes, tapered and conical, have been selected and added in a planar manner to the wingtips to create tapered or conical slotted winglet configurations. Overall, the present study is mainly concerned with the analysis of the key parameters that affect the aerodynamics of MAVs. All the objectives of the present study have been successfully achieved during the investigation, and the key outcomes drawn from the research are listed as follows:

- For S5010 airfoil, the $(C_l / C_d)_{max}$ increases from 12 to 28 as Re is varied from 40×10^3 to $100 \times 10^{3,}$ and in the case of E214 airfoil within the same Re range, it rises from 15 to 31. Compared to the S5010 data, the E214 airfoil has a higher value of $C_l / C_d)_{max}$ at a given Re. There is no observed hysteresis in the aerodynamic data of either airfoil within the current Re and AoA range.
- The Re has a minor effect on the C_d at lower AoA. However, for higher angles, the drag increases as the Re reduces. The effect of Re on the $C_{m,0.25c}$ is less significant in the pre-stall region, but in the post-stall zone, moment data decreases as the Re increases at a given AoA. This observation represents that the nose-down tendency of the wing is higher for high Re in the post-stall region.
- In the wake field analysis, the frequency of shed vortices reduces with rising AoA at a given Re, and it rises with the Re at a particular AoA. At the same time, the Strouhal number almost remains constant with varying Re at a fixed AoA. For the S5010, the Strouhal number varies in the range of 0.68 to 0.36 for AoA between 12° and 28° in the existing flow regime. In case of E214, this range is 0.58 to 0.36. The airfoils show a higher Strouhal number than the bluff body wakes up to specific AoA, but as the angle increases, the

magnitude difference between them decreases. This finding reveals that the wake structure of the airfoil at a high post-stall angle behaves as bluff body wake.

- For wings within an *AR* range of 2.0 to 1.0, the effect of the *Re* is less significant on the C_L and C_D before the stall point. However, C_L increases, and C_D decreases with increasing *Re* after the stall point. The parameters such as C_{Lmax} and $(C_L/C_D)_{\max}$ of the wing improve with rising *Re*. In contrast, the stall characteristics of the wing are not affected by the *Re*. It has also been noticed that as the *AR* of a wing reduces, the effect of the *Re* on wing performance diminishes. Further, no measurable difference is observed in the pitching moment values of all *AR* wings due to change in the respective *Re* range.
- Compared to *Re*, the influence of *AR* on the wing performance is found to be more significant. When the *AR* changes between 2 and 0.5, the C_{Lmax} and $(C_L/C_D)_{\max}$ for the S5010 and E214 wing configurations are found to drop significantly. Conversely, the stall point of the wing improves as the *AR* decreases. The lift slope of the $C_L - AoA$ curve drops with decreasing *AR*. It is also noted that the pitch-down tendency of the wing rises with increasing *AR*. Further, no hysteresis is seen in the aerodynamic forces and moment data of all the wing models of any sections in the present *Re* range.
- In case of the bionic flap study, the best performance improvement is obtained when the flap covers 80% of the wingspan for *AR* = 2.0, and it is around 70% of the span in the case of *AR* = 1.0. All the flapped wing configurations exhibit performance curves similar to a clean wing for the pre-stall region at a given *Re*. For the post-stall, most of the flapped configurations reveal performance improvement.
- For a flap chord size of 0.15*c* at 0.4*c*, the stall angle is observed to increase by 22% and 20% for *AR* = 2.0 and 1.0, respectively, compared to their respective baseline wings. The optimal chord-wise position of the flap for better performance enhancement is found near the mid-chord for both models. This flap does not change the longitudinal stability of the wing for pre-stall angles while increasing the pitch-down tendency of the wing in the post-stall region.
- The aerodynamic behaviour of the flapped wing of *AR* = 2.0 appears to be more sensitive to parametric variations in flap chord length and its positions than for *AR* = 1.0. It has also been observed that the effectiveness of this flap does not vary significantly with changes in the *Re* range of 60×10^3 to 150×10^3.

- In the scenario of slotted winglet investigations, all tapered slotted winglet configurations have presented improvements in C_L, lift slope, C_L/C_D, induced drag factor, and $C_{M,0.25c}$, compared to their respective reference wings. These wingtip attachments do not modify the stall characteristics of the base wing; nevertheless, they exhibit a higher C_{Lmax}. On the other hand, all conical winglet configurations do not provide any beneficial effect on the C_L/C_D values than the baseline within the tested range of *AoA*.
- The variation in winglet parameters also significantly affects the performance parameters of wing configurations. When the number of wingtip attachments are increased, there is more pronounced improvement in lift slope, C_{Lmax}, and C_L/C_D compared to configurations with fewer attachments. At the same time, the higher number of attachments also leads to a more significant reduction in the induced drag factor and it diminishes the tendency for upward pitching. In contrast, changing the attachment length does not significantly affect these performance parameters.
- For the given winglet configurations and *Re*, the improvement in performance metrics is more significant in the case of *AR* = 1.0 than the lower *AR*s. The performance of the winglet configurations is significantly influenced by *Re*, and as *Re* increases, their performance also improves. When comparing the effectiveness of these two wingtip devices, the tapered attachment device has been found to be more efficient in improving the performance of both *AR* wings than the conical one. This observation suggests that the shape of attachment needs to be streamlined to enhance the efficiency of slotted winglet arrangements.

8.2 Future Work

The present experimental investigation encompasses the effect of *Re* and *AR* on the wing performance, considering the presence or absence of passive flow control devices for MAV applications. However, there is still scope for future improvements, and some proposals for further investigations are listed below:

- The current study is limited to the design and analysis of low *AR* models of rectangular wing planform. Hence, it can be expanded to encompass investigations of various planforms, including Zimmerman, Inverse Zimmerman, elliptical, and cropped delta, to provide a more comprehensive understanding of aerodynamic performance across different wing configurations.

- Examining the frequency of vortices in the wake region is crucial for characterizing the flow field, and in this investigation, the analysis was limited to airfoil models. Therefore, hot-wire experiments can be performed to measure the vortex shedding frequency of finite wing models for different *Re* and *AoA*. Determining vortex shedding frequency is essential for enhancing our understanding of aerodynamic performance, flow stability, and aeroelastic behavior in aircraft design.
- Flow field measurements over the wing surface or within the wake region can also be conducted using advanced techniques like Particle Image Velocimetry (PIV). This analysis will provide insights into the complex flow behavior arising from variations in aspects such as *AoA*, *Re*, and *AR*, thus facilitating a better understanding of the relationships between flow dynamics and wing performance.
- In the present study, two bio-inspired passive flow control techniques, self-actuating flaps, and slotted winglets, have been employed for wing performance enhancement. This research can be extended to investigate the potential of other passively functioning devices, including leading-edge serrations inspired by the morphology of humpback whales, flexible membrane wings, segmented or partially flexible airfoils, etc., for the current applications.
- Apart from passive devices, the scope of this investigation can also be broadened to examine the feasibility and benefits of implementing active flow control devices, including synthetic jets, blowing or suction devices, plasma actuators, etc., to enhance the aerodynamic performance of low *AR* wings.
- The computational analysis using the software ANSYS Fluent can be employed to estimate the aerodynamic data of existing wing models. Such research will focus on visualizing flow patterns over the wing surface, optimizing wing performance, and validating computational results against existing experimental data. This exploration will enhance our understanding of aerodynamic behavior and facilitate the cost-effective development of improved wing designs.

References

Altman, A., Allemand, G., (2016). Post-stall performance improvement through bio-inspired passive covert feathers, in: 54th AIAA Aerosp. Sci. Meet. California, USA. https://doi.org/10.2514/6.2016-2042

Ananda, G.K., Sukumar, P.P., Selig, M.S., (2015). Measured aerodynamic characteristics of wings at low Reynolds numbers. Aerosp. Sci. Technol. 42, 392–406. https://doi.org/10.1016/j.ast.2014.11.016

Ananda, G.K., Sukumar, P.P., Selig, M.S., (2012). Low-to-moderate aspect ratio wings tested at low Reynolds numbers, in: 30th AIAA Appl. Aerodyn. Conf. New Orleans, Louisiana. https://doi.org/10.2514/6.2012-3026

Anderson, J.D., (2011). Fundamentals of Aerodynamics, 5th ed. McGraw–Hill, New York.

Anyoji, M., Liu, T., Nonomura, T., Oyama, A., Fujii, K., (2013). Effect of wing planform on aerodynamic characteristics at low Reynolds numbers using a low density wind tunnel, in: 43rd AIAA Fluid Dyn. Conf. San Diego, CA. https://doi.org/10.2514/6.2013-3180

Arivoli, D., Singh, I., (2016). Self-adaptive flaps on low aspect ratio wings at low Reynolds numbers. Aerosp. Sci. Technol. 59, 78–93. https://doi.org/10.1016/j.ast.2016.10.006

Arivoli, D., Singh, I., Suriyanarayanan, P., (2020). Rudimentary emulation of covert feathers on low-AR wings for poststall lift enhancement. AIAA J. 58(2), 501–516. https://doi.org/10.2514/1.J058562

Azuma, A., (1992). The Biokinetics of Flying and Swimming. Springer Tokyo, Japan, Tokyo. https://doi.org/10.1007/978-4-431-68210-3

Bai, P., Li, F., Liu, Q., Zhan, H., (2016). Evolution of the non-linear and unsteady low Reynolds number laminar separation bubble around the airfoil with small angle of attack, in: 46th AIAA Fluid Dyn. Conf. Washington, D.C. https://doi.org/10.2514/6.2016-4337

Baljit, S.S., Saad, M.R., Nasib, A.Z., Sani, A., Rahman, M.R.A., Idris, A.C., (2017). Suction and blowing flow control on airfoil for drag reduction in subsonic flow. J. Phys. Conf. Ser. 914(1). https://doi.org/10.1088/1742-6596/914/1/012009

Barlow, J.B., Rae, W., Pope, J.A., (1999). Low-Speed Wind Tunnel Testing, 3rd ed., John Wiley & Sons, New York. https://doi.org/10.1063/1.3061735

Bechert, D.W., Bruse, M., Hage, W., Meyer, R., (1997). Biological surfaces and their technological application - Laboratory and flight experiments on drag reduction and separation control, in: 28th AIAA Fluid Dyn. Conf. Snowmass Village, CO, U.S.A. https://doi.org/10.2514/6.1997-1960

Belotserkovskii, S.M., (1968). Calculation of the flow around wings of arbitrary planform over a wide range of angles of attack. Fluid Dyn. 3(4), 20–27.

Bera, R.K., Suresh, G., (1989). Comments on the Lawrence equation for low-aspect-ratio wings. J. Aircr. 26(9), 883–885. https://doi.org/10.2514/3.45855

Bertin, J.J., Cummings, R.M., (2009). Aerodynamics for Engineers, 5th ed. Pearson Prentice Hall, USA.

Beves, C.C., Barber, T.J., (2017). The wingtip vortex of a dimpled wing with an endplate. J. Fluids Eng. Trans. ASME 139(2), 1–9. https://doi.org/10.1115/1.4034525

Bollay, W., (1939). A non-linear wing theory and its application to rectangular wings of small aspect ratio. Zeitschrift Fur Angew. Math. und Mech. 19, 21–35.

Bramesfeld, G., Maughmer, M.D., (2002). Experimental investigation of self-actuating, upper-surface, high-lift-enhancing effectors. J. Aircr. 39(1), 120–124. https://doi.org/10.2514/2.2905

Brendel, M., Mueller, T.J., (1988). Boundary-layer measurements on an airfoil at low Reynolds numbers. J. Aircr. 25(7), 612–617. https://doi.org/10.2514/3.45631

Bruun, H.H., (1995). Hot-Wire Anemometry: Principles and Signal Analysis. Oxford University Press Inc., New York.

Burgmann, S., Brücker, C., Schröder, W., (2006). Scanning PIV measurements of a laminar separation bubble. Exp. Fluids 41(2), 319–326. https://doi.org/10.1007/s00348-006-0153-6

Carmichael, B.H., (1981). Low Reynolds number airfoil survey Vol. 1. NASA Contractor Report 165803.

Catalano, F., Ceron-Muñoz, H., (2005). Experimental analysis of aerodynamics characteristics of adaptive multi-winglets, in: 43rd AIAA Aerosp. Sci. Meet. Exhib. Reno, Nevada. https://doi.org/10.2514/6.2005-1231

Cerón-Muñoz, H.D., Catalano, F.M., (2006). Experimental analysis of the aerodynamic characteristics adaptive of multi-winglets. Proc. Inst. Mech. Eng. Part G J. Aerosp. Eng. 220(3), 209–215. https://doi.org/10.1243/09544100JAERO22

Céron-Muñoz, H.D., Cosin, R., Coimbra, R.F.F., Correa, L.G.N., Catalano, F.M., (2013). Experimental investigation of wing-tip devices on the reduction of induced drag. J. Aircr. 50(2), 441–449. https://doi.org/10.2514/1.C031862

Chen, J.M., Fang, Y.C., (1996). Strouhal numbers of inclined flat plates. J. Wind Eng. Ind. Aerodyn. 61, 99–112. https://doi.org/10.1016/0167-6105(96)00044-X

Chen, T.Y., Liou, L.R., (2011). Blockage corrections in wind tunnel tests of small horizontal-axis wind turbines. Exp. Therm. Fluid Sci. 35(3), 565–569. https://doi.org/10.1016/j.expthermflusci.2010.12.005

Coiro, D.P., Nicolosi, F., Scherillo, F., Maisto, U., (2008). Single versus multiple winglets: Numerical and experimental investigation. ICAS Secr. - 26th Congr. Int. Counc. Aeronaut. Sci. Anchorage, USA.

Combes, S.A., Daniel, T.L., (2003). Flexural stiffness in insect wings I. Scaling and the influence of wing venation. J. Exp. Biol. 206(17), 2979–2987. https://doi.org/10.1242/jeb.00523

Corda, S., (2017). Introduction to Aerospace Engineering with a Flight Test Perspective, 1st ed. John Wiley and Sons, United Kingdom.

Cosyn, P., Vierendeels, J., (2006). Numerical investigation of low-aspect-ratio wings at low Reynolds numbers. J. Aircr. 43(3), 713–722. https://doi.org/10.2514/1.16991

Cravero, C., (2017). Aerodynamic performance prediction of a profile in ground effect with and without a gurney flap. J. Fluids Eng. Trans. ASME 139(3), 1–15. https://doi.org/10.1115/1.4035137

CSIR-NAL, (2012). CSIR-NAL Technologies and Products Brochure.

Fluck, M., Crawford, C., (2014). A lifting line model to investigate the influence of tip feathers on wing performance. Bioinspiration and Biomimetics 9(4). https://doi.org/10.1088/1748-3182/9/4/046017

Gad-el-Hak, M., Pollard, A., (1998). Flow Control: Fundamentals and Practices, Lecture Notes in Physics. Springer Berlin Heidelberg, Heidelberg. https://doi.org/10.1007/3-540-69672-5

Gerakopulos, R., Boutilier, M.S.H., Yarusevych, S., (2010). Aerodynamic characterization of a NACA 0018 airfoil at low Reynolds numbers, in: 40th AIAA Fluid Dyn. Conf. Chicago, Illinois. https://doi.org/10.2514/6.2010-4629

Gerontakos, P., Lee, T., (2005). Near wake behind an airfoil with leading-edge flow control. J. Aircr. 42(2), 561–567. https://doi.org/10.2514/1.9778

Gudmundsson, S., (2014a). The Anatomy of the Airfoil, in: General Aviation Aircraft Design. pp. 235–297. https://doi.org/10.1016/b978-0-12-397308-5.00008-8

Gudmundsson, S., (2014b). The Anatomy of the Wing, in: General Aviation Aircraft Design, Chap. 9. Butterworth-Heinemann, pp. 299–399. https://doi.org/10.1016/C2011-0-06824-2

Gutierrez-Castillo, P., Aguilar-Cabello, J., Alcalde-Morales, S., Parras, L., del Pino, C., (2021). On the lift curve slope for rectangular flat plate wings at moderate Reynolds number. J. Wind Eng. Ind. Aerodyn. 208. https://doi.org/10.1016/j.jweia.2020.104459

Hao, L., Gao, Y., Wei, B., (2022). Experimental investigation of flow separation control over airfoil by upper surface flap with a gap. Int. J. Aeronaut. Sp. Sci. 23(5), 859–869. https://doi.org/10.1007/s42405-022-00488-x

Hassanalian, M., (2016). Wing shape design and kinematic optimization of bio-inspired nano air vehicles for hovering and forward flight purposes. New Mexico State University, USA.

Hassanalian, M., Abdelkefi, A., (2017). Design, manufacturing, and flight testing of a fixed wing micro air vehicle with Zimmerman planform. Meccanica 52(6), 1265–1282. https://doi.org/10.1007/s11012-016-0475-2

Hoerner, S.F., Borst, H. V., (1985). Characteristics of Small Aspect Ratio Wings, in: Fluid-Dynamics Lift, Chapter XVII. Hoerner Fluid Dynamics, pp. 17–1, 17–7.

Hoffmann, J.A., (1991). Effects of freestream turbulence on the performance characteristics of an airfoil. AIAA J. 29(9), 1353–1354. https://doi.org/10.2514/3.10745

Hu, H., Yang, Z., (2008). An experimental study of the laminar flow separation on a low-Reynolds-number airfoil. J. Fluids Eng. Trans. ASME 130(5), 0511011–05110111. https://doi.org/10.1115/1.2907416

Hu, H., Yang, Z., Igarashi, H. (2007). Aerodynamic hysteresis of a low-Reynolds-number airfoil. J. Aircr. 44(6), 2083-2086. https://doi.org/10.2514/1.32662

Huang, R.F., Lee, H.W., (2000). Turbulence effect on frequency characteristics of unsteady motions in wake of wing. AIAA J. 38(1), 87–94. https://doi.org/10.2514/3.14382

Huang, R.F., Lin, C.L., (1995). Vortex shedding and shear-layer instability of wing at low-Reynolds numbers. AIAA J. 33(8), 1398–1403. https://doi.org/10.2514/3.12561

Jeong, H., Lee, S., Kwon, S.D., (2018). Blockage corrections for wind tunnel tests conducted on a Darrieus wind turbine. J. Wind Eng. Ind. Aerodyn. 179, 229–239. https://doi.org/10.1016/j.jweia.2018.06.002

Karasu, I., Özden, M., Genç, M.S., (2018). Performance assessment of transition models for three-dimensional flow over NACA4412 wings at low Reynolds numbers. J. Fluids Eng. Trans. ASME 140(12), 1–15. https://doi.org/10.1115/1.4040228

Katopodes, N.D., (2019). Viscous Fluid Flow, in: Free-Surface Flow. Butterworth-Heinemann, pp. 324–426. https://doi.org/10.1016/b978-0-12-815489-2.00005-8

Kernstine, K.H., Moore, C.J., Cutler, A., Mittal, R., (2008). Initial characterization of self-activated movable flaps, "Pop-Up Feathers," in: 46th AIAA Aerosp. Sci. Meet. Exhib. Reno, Nevada. https://doi.org/10.2514/6.2008-369

Kim, S.H., Hong, W., Kim, C., (2007). Separation control mechanism of airfoil using synthetic jet. J. Mech. Sci. Technol. 21(9), 1367–1375. https://doi.org/10.1007/BF03177422

King, L. V., (1914). On the convection of heat from small cylinders in a stream of fluid: Determination of the convection constants of small platinum wires, with applications to hot-wire anemometry. Philos. Trans. R. Soc. London, 214(509-522), 373–432.

Laitone, E. V., (1997). Wind tunnel tests of wings at Reynolds numbers below 70 000. Exp. Fluids 23(5), 405–409. https://doi.org/10.1007/s003480050128

Lam, G.C.Y., Leung, R.C.K., (2018). Aeroacoustics of NACA 0018 airfoil with a cavity. AIAA J. 56(12), 4775–4786. https://doi.org/10.2514/1.J056389

Lee, S.P., Ken Kauh, S., (1997). A new approach to enhance the sensitivity of a hot-wire anemometer and static response analysis of a variable-temperature anemometer. Exp. Fluids 22(3), 212–219. https://doi.org/10.1007/s003480050039

Lienhard, J.H., (1966). Synopsis of lift, drag, and vortex frequency data for rigid circular cylinders. Bulletin 300. Tech. Ext. Service, Washington State University, Pullman, WA.

Lissaman, P.B.S., (1983). Low-Reynolds-number airfoils. Annu. Rev. Fluid Mech. 15(1), 223–239. https://doi.org/10.1146/annurev.fl.15.010183.001255

Liu, D., Song, B., Yang, W., Yang, X., Xue, D., Lang, X., (2021). A brief review on aerodynamic performance of wingtip slots and research prospect. J. Bionic Eng. 18(6), 1255–1279. https://doi.org/10.1007/s42235-021-00116-6

Liu, T., Montefort, J., Liou, W., Pantula, S., (2010). Effects of flexible fin on low-frequency oscillation in poststall flows. AIAA J. 48(6), 1235–1247. https://doi.org/10.2514/1.J050205

Lynch, M., Mandadzhiev, B., Wissa, A., (2018). Bioinspired wingtip devices: A pathway to improve aerodynamic performance during low Reynolds number flight. Bioinspiration and Biomimetics 13(3). https://doi.org/10.1088/1748-3190/aaac53

Lyon, C.A., Broeren, A.P., Gigu`ere, P., Gopalarathnam, A., Selig, M.S., (1997). Summary of low-speed airfoil data.Vol. 3, SoarTech Publications, Virginia Beach, Virginia.

Marchman, J.F., Abtahi, A.A., (1985). Aerodynamics of an aspect ratio 8 wing at low Reynolds numbers. J. Aircr. 22(7), 628–634. https://doi.org/10.2514/3.45176

Marchman, J.F., Abtahi, A.A., Sumantran, V., Sun, Z., (1985). Effects of aspect ratio on stall hysteresis for the Wortmann airfoil. 12th AIAA Atmos. Flight Mech. Conf. CO, U.S.A. 44–49. https://doi.org/10.2514/6.1985-1770

Marchman, J.F., Gunther, C.L., Gundlach, J.F., (1998). Semi-span testing at low Reynolds number. 36th AIAA Aerosp. Sci. Meet. Exhib. Reno, NV, U.S.A. https://doi.org/10.2514/6.1998-608

Marchman, J.F., Sumantran, V., Schaefer, C.G., (1987). Acoustic and turbulence influences on stall hysteresis. AIAA J. 25(1), 50–51. https://doi.org/10.2514/3.9578

McGhee, R.J., Walker, B.S., (1988). Experimental results for the Eppler 387 airfoil at low Reynolds numbers in the Langley low- turbulence pressure tunnel. NASA TM 4062.

McMasters, J.H., Henderson, M.L., (1979). Low speed single-element airfoil synthesis. Tech. Soar. 6(2), 1–21.

Meng, X., Hu, H., Yan, X., Liu, F., Luo, S., (2018). Lift improvements using duty-cycled plasma actuation at low Reynolds numbers. Aerosp. Sci. Technol. 72, 123–133. https://doi.org/10.1016/j.ast.2017.10.038

Meyer, R., Hage, W., Bechert, D.W., Schatz, M., Knacke, T., Thiele, F., (2007). Separation control by self-activated movable flaps. AIAA J. 45(1), 191–199. https://doi.org/10.2514/1.23507

Miklosovic, D.S., (2008). Analytic and experimental investigation of dihedral configurations of three-winglet planforms. J. Fluids Eng. Trans. ASME 130(7), 0711031–07110310. https://doi.org/10.1115/1.2948372

Mitchell, T.A., Jacob, J.D., (2013). Evaluation of bird-wing-inspired features on biomimetic UAVs, in: 51st AIAA Aerosp. Sci. Meet. New Horiz. Forum Aerosp. Expos. Grapevine, Texas. https://doi.org/10.2514/6.2013-89

Mizoguchi, M., Itoh, H., (2013). Effect of aspect ratio on aerodynamic characteristics at low Reynolds numbers. AIAA J. 51(7), 1631–1639. https://doi.org/10.2514/1.J051915

Mizoguchi, M., Kajikawa, Y., Itoh, H., (2016). Aerodynamic characteristics of low-aspect-ratio wings with various aspect ratios in low Reynolds number flows. Trans. Jpn. Soc. Aeronaut. Space Sci. 59(2), 56–63. https://doi.org/10.2322/tjsass.59.56

Mizoguchi, M., Kajikawa, Y., Itoh, H., (2014). Static stall hysteresis of low-aspect-ratio wings. 32nd AIAA Appl. Aerodyn. Conf. Atlanta, GA. https://doi.org/10.2514/6.2014-2014

Moffat, R.J., (1988). Describing the uncertainties in experimental results. Exp. Therm. Fluid Sci. 1, 3–17. https://doi.org/10.1016/0894-1777(88)90043-X

Montes Gomez, E., Sumner, D., (2022). The wake of a rectangular flat plate. Fluid Dyn. Res. 54(6). https://doi.org/10.1088/1873-7005/acabe3

Mueller, T.J., (1999). Aerodynamic measurements at low Reynolds numbers for fixed wing micro-air vehicles. RTO AVT/VKI Spec. Course Dev. Oper. UAVs Mil. Civ. Appl. Univ. Notre Dame.

Mueller, T.J., (1985a). The influence of laminar separation and transition on low Reynolds number airfoil hysteresis. J. Aircr. 22(9), 763–770. https://doi.org/10.2514/3.45199

Mueller, T. J., (1985b). Low Reynolds number vehicles. Advisory Group for Aerospace Research and Development, AGARD- AG-288.

Mueller, T.J., Batill, S.M., (1982). Experimental Studies of the laminar separation bubble on a two-dimensional airfoil at low Reynolds numbers. AIAA J. 20(4), 457–463. https://doi.org/10.2514/6.1980-1440

Mueller, T.J., Kellogg, J.C., Ifju, P.G., Shkarayev, S. V., (2007). Introduction to the Design of Fixed-Wing Micro Air Vehicles: Including Three Case Studies. American Institute of Aeronautics and Astronautics (AIAA), Reston ,VA. https://doi.org/10.2514/4.862106

Mueller, T.J., Pohlen, L.J., Conigliaro, P.E., Jansen, B.J., (1983). The influence of free-stream disturbances on low Reynolds number airfoil experiments. Exp. Fluids 1, 3–14. https://doi.org/10.1007/BF00282261

Murphy, J.T., Hu, H., (2010). An experimental study of a bio-inspired corrugated airfoil for micro air vehicle applications. Exp. Fluids 49, 531–546. https://doi.org/10.1007/s00348-010-0826-z

Narayan, G., John, B., (2016). Effect of winglets induced tip vortex structure on the performance of subsonic wings. Aerosp. Sci. Technol. 58, 328–340. https://doi.org/10.1016/j.ast.2016.08.031

Nelson, R.C., (1998). Flight Stability and Automatic Control. 2nd ed., Mc Graw Hill, New York.

O'Meara, M.M., Mueller, T.J., (1987). Laminar separation bubble characteristics on an airfoil at low Reynolds number. AIAA J. 25(8). https://doi.org/10.2514/6.1986-1065

Oertel, H., (1990). Wakes behind blunt bodies. Annu. Rev. Fluid Mech. 22, 539–564. https://doi.org/10.1146/annurev.fluid.22.1.539

Ojha, S.K., (1995). Aerodynamic Forces on Aircraft, in: Flight Performance of Aircraft. American Institute of Aeronautics and Astronautics (AIAA), Washington, DC, pp. 81–124. https://doi.org/10.2514/5.9781600868535.0081.0124

Okamoto, M., Azuma, A., (2011). Aerodynamic characteristics at low Reynolds numbers for wings of various planforms. AIAA J. 49(6), 1135–1150. https://doi.org/10.2514/1.J050071

Okamoto, M., Yasuda, K., Azuma, A., (1996). Aerodynamic characteristics of the wings and body of a dragonfly. J. Exp. Biol. 199(2), 281–294. https://doi.org/10.1242/jeb.199.2.281

Park, D., Shim, H., Lee, Y., (2020). PIV measurement of separation bubble on an airfoil at low Reynolds numbers. J. Aerosp. Eng. 33(1), 04019105: 1–17. https://doi.org/10.1061/(asce)as.1943-5525.0001099

Pelletier, A., Mueller, T.J., (2000). Low Reynolds number aerodynamics of low-aspect-ratio, thin/flat/cambered-plate wings. J. Aircr. 37(5), 825–832. https://doi.org/10.2514/2.2676

Polhamus, E.C., (1966). A concept of the vortex lift of sharp-edge delta wings based on a leading-edge-suction analogy, NASA Tech. Note, NASA TN D-3767.

Raymer, D., (2018). Aircraft Design: A Conceptual Approach, 6th ed. American Institute of Aeronautics and Astronautics (AIAA). Washington, DC. https://doi.org/10.2514/4.104909

Rizzetta, D.P., Visbal, M.R., (2012). Plasma control for a maneuvering low-aspect-ratio wing at low Reynolds number. J. Fluids Eng. Trans. ASME 134(12), 1–19. https://doi.org/10.1115/1.4007947

Rizzetta, D.P., Visbal, M.R., (2008). Plasma-based flow-control strategies for transitional highly loaded low-pressure turbines. J. Fluids Eng. Trans. ASME 130(4), 0411041–04110412. https://doi.org/10.1115/1.2903816

Roshko, A., (1954a). On the drag and shedding frequency of two-dimensional bluff bodies. NACA Technical Note 3169.

Roshko, A., (1954b). On the development of turbulent wakes from vortex streets. NACA TR 1191.

Roy, A., Vinoth Kumar, R., Mukherjee, R., (2020). Experimental validation of numerical decambering approach for flow past a rectangular wing. Proc. Inst. Mech. Eng. Part G J. Aerosp. Eng. 234(9), 1564–1582. https://doi.org/10.1177/0954410020916311

Ruifeng, H., (2015). Three-dimensional flow past rotating wing at low Reynolds number: A computational study. Fluid Dyn. Res. 47(4). https://doi.org/10.1088/0169-5983/47/4/045503

Russo, G.P., (2011). Hot wire anemometer, in: Aerodynamic Measurements. Elsevier, pp. 67–98. https://doi.org/10.1533/9780857093868.67

Sachs, G., Moelyadi, M.A., (2006). Effect of slotted wing tips on yawing moment characteristics. J. Theor. Biol. 239(1), 93–100. https://doi.org/10.1016/j.jtbi.2005.07.016

Sadraey, M.H., (2013). Aircraft Design: A System Engineering Approach, 1st ed. John Wiley & Sons, Ltd.

Schatz, M., Knacke, T., Thiele, F., Meyer, R., Hage, W., Bechert, D., (2004). Separation control by self-activated movable flaps, in: 42nd AIAA Aerosp. Sci. Meet. Exhib., Reno, Nevada. https://doi.org/10.2514/6.2004-1243

Schlüter, J.U., (2010). Lift enhancement at low Reynolds numbers using self-activated movable flaps. J. Aircr. 47(1), 348–351. https://doi.org/10.2514/1.46425

Schmitz, F.W., (1967). Aerodynamics of the model airplane. Part-1. Airfoil Measurements. RSIC-721-PT-1.

Selig, M.S., Donovan, J.F., Fraser, D.B., (1989). Airfoils at low speeds. Soartect 8, SoarTech Publications, 1504 North Horseshoe Circle Virginia Beach, Virginia.

Selig, M.S., Guglielmo, J.J., Broern, A.P., Giguere, P., (1996a). Experiments on airfoils at low Reynolds numbers, in: 34th Aerosp. Sci. Meet. Exhib. Reno, NV, U.S.A. https://doi.org/10.2514/6.1996-62

Selig, M.S., Lyon, C.A., Giguere, P., Ninham, C.P., Guglielmo, J.J., (1996b). Summary of low-speed airfoil data, Vol 2. SoarTech Publications, Virginia Beach.

Shields, M., Mohseni, K., (2012). Effects of sideslip on the aerodynamics of low-aspect-ratio low-Reynolds-number wings. AIAA J. 50(1), 85–99. https://doi.org/10.2514/1.J051151

Siddiqui, N., Aldeeb, M., Asrar, W., Sulaeman, E., (2018). Experimental investigation of a new spiral wingtip. Int. J. Aviat. Aeronaut. Aerosp. 5(2). https://doi.org/10.15394/ijaaa.2018.1213

Siram, O., Kumar, R., Saha, U.K., Sahoo, N., (2022). Wind tunnel probe into an array of small-scale horizontal-axis wind turbines operating at low tip speed ratio conditions. J. Energy Resour. Technol. Trans. ASME 144(9), 1–13. https://doi.org/10.1115/1.4053579

Smith, M., Komerath, N., Ames, R., Wong, O., Pearson, J., (2001). Performance analysis of a wing with multiple winglets, in: 19th AIAA Appl. Aerodyn. Conf. Anaheim, CA, U.S.A. https://doi.org/10.2514/6.2001-2407

Soylak, M., (2016). Experimental investigation of aerodynamic performance of oscillating wings at low Re numbers. Proc. Inst. Mech. Eng. Part G J. Aerosp. Eng. 230(10), 1882–1902.

Sunada, S., Sakaguchi, A., Kawachi, K., (1997). Airfoil section characteristics at a low Reynolds number. J. Fluids Eng. ASME 119(1), 129–135. https://doi.org/10.1115/1.2819098

Torres, G.E., Mueller, T.J., (2004). Low-aspect-ratio wing aerodynamics at low Reynolds numbers. AIAA J. 42(5), 865–873. https://doi.org/10.2514/1.439

Torres, G.E., Mueller, T.J., (2001). Aerodynamic Characteristics of Low Aspect Ratio Wings at Low Reynolds Numbers, Chap 7, in: Fixed and Flapping Wing Aerodynamics for Micro Air Vehicle Applications. pp. 115–141. https://doi.org/10.2514/5.9781600866654.0115.0141

Tucker, V.A., (1995). Drag reduction by wing tip slots in a gliding Harris' hawk, Parabuteo unicinctus. J. Exp. Biol. 198(3), 775–781. https://doi.org/10.1242/jeb.198.3.775

Tucker, V.A., (1993). Gliding birds: reduction of induced drag by wing tip slots between the primary feathers. J. Exp. Biol. 180(1), 285–310. https://doi.org/10.1242/jeb.180.1.285

Van Treuren, K.W., (2015). Small-scale wind turbine testing in wind tunnels under low Reynolds number conditions. J. Energy Resour. Technol. Trans. ASME 137(5), 1–11. https://doi.org/10.1115/1.4030617

Villeneuve, T., Boudreau, M., Dumas, G., (2019). Lift enhancement and drag reduction of lifting blades through the use of end-plates and detached end-plates. J. Wind Eng. Ind. Aerodyn. 184, 391–404. https://doi.org/10.1016/j.jweia.2018.12.006

Wagner, T.C., Kent, J.C., (1988). On the directional sensitivity of hot-wires: a new look at an old phenomenon. Exp. Fluids 6(8), 553–560. https://doi.org/10.1007/BF00196602

Wang, C.H.J., Schlüter, J., (2012). Stall control with feathers: Self-activated flaps on finite wings at low Reynolds numbers. Comptes Rendus - Mec. 340(1–2), 57–66. https://doi.org/10.1016/j.crme.2011.11.001

Wang, S., Zhou, Y., Alam, M.M., Yang, H., (2014). Turbulent intensity and Reynolds number effects on an airfoil at low Reynolds numbers. Phys. Fluids 26(11). https://doi.org/10.1063/1.4901969

Weinig, F., (1947). Lift and drag of wings with small span, NACA Tech. Memo. NACA TM 1151.

Winslow, J., Otsuka, H., Govindarajan, B., Chopra, I., (2018). Basic understanding of airfoil characteristics at low Reynolds numbers (10^4–10^5). J. Aircr. 55(3), 1050–1061. https://doi.org/10.2514/1.C034415

Xia, T., Dong, H., Yang, L., Liu, S., Jin, Z., (2021). Investigation on flow structure and aerodynamic characteristics over an airfoil at low Reynolds number—A review. AIP Adv. 11(5). https://doi.org/10.1063/5.0044717

Yan, M., Ebel, T., (2019). Titanium and titanium alloys in drones and other small flying objects, in: Titanium for Consumer Applications. Elsevier, pp. 91–113. https://doi.org/10.1016/B978-0-12-815820-3.00018-6

Yang, Y., Li, C., Pröbsting, S., Liu, X., Liu, Y., Arcondoulis, E. J. G. (2023). Hysteresis effect on airfoil stall noise and flow field. Phys. Fluids 35(9). https://doi.org/10.1063/5.0160288

Yarusevych, S., Boutilier, M.S.H., (2011). Vortex shedding of an airfoil at low Reynolds numbers. AIAA J. 49(10), 2221–2227. https://doi.org/10.2514/1.J051028

Yarusevych, S., Sullivan, P.E., Kawall, J.G., (2009). On vortex shedding from an airfoil in low-Reynolds-number flows. J. Fluid Mech. 632, 245–271. https://doi.org/10.1017/S0022112009007058

Yarusevych, S., Sullivan, P.E., Kawall, J.G., (2006). Coherent structures in an airfoil boundary layer and wake at low Reynolds numbers. Phys. Fluids 18(4). https://doi.org/10.1063/1.2187069

Yavuzkurt, S., (1984). A guide to uncertainty analysis of hot-wire data. J. Fluids Eng. Trans. ASME 106(2), 181–186. https://doi.org/10.1115/1.3243096

Yen, S.C., Fei, Y.F., (2011). Winglet dihedral effect on flow behavior and aerodynamic performance of NACA0012 wings. J. Fluids Eng. Trans. ASME 133(7). https://doi.org/10.1115/1.4004420

Zhi-Yong, Z., Wang-Long, Z., Zhi-Hua, C., Xiao-Hui, S., Chen-Chao, X., (2018). Suction control of flow separation of a low-aspect-ratio wing at a low Reynolds number. Fluid Dyn. Res. 50(6). https://doi.org/10.1088/1873-7005/aad903

List of Publications

Journal Publications (Peer-reviewed)

- **Verma A.** and Kulkarni V., "Monitoring the Wake of Low Reynolds Number Airfoils for Their Aerodynamic Loads Assessment" *Journal of Applied Fluid Mechanics*, 2024; 17(11), 2481-2498. https://doi.org/10.47176/jafm.17.11.2607

- **Verma A.,** Shinde S. and Kulkarni V., "Experimental Investigations of Self-Adjustable Bionic Flaps on Low Aspect Ratio Wings" *Journal of Applied Fluid Mechanics*, 2025; 18(4), 992-1006. https://doi.org/10.47176/jafm.18.4.2922

- **Verma A.** and Kulkarni V., "Exploration of Bio-inspired Wingtip Devices for Low Aspect Ratio Wing" *Engineering Research Express (IOP journal)*, 2024, 6(4), 045558. https://doi.org/10.1088/2631-8695/ad937d

- **Verma A.,** Borah B., Kulkarni V. and Saha U. K., "Wind Tunnel Investigation into the Bio-inspired Slotted Winglets for Micro Air Vehicles" *Part C: Journal of Mechanical Engineering Science,* 2024. https://doi.org/10.1177/09544062241308358

- Borah B., **Verma A.**, Kulkarni V. and Saha U. K., "Experimental Exploration of Bio-inspired Planar Wingtip Configurations in Low Reynolds Number Regime" *ASCE Journal of Aerospace Engineering*, 2024; 36(7), 04024075. https://doi.org/10.1061/JAEEEZ.ASENG-5359

Conference Publications (Peer-reviewed)

- **Verma A.** and Kulkarni V., "Computational Analysis of Performance and Flow Field of Airfoil in Low Reynolds Number Regime", In *Proceeding of the 67th Congress of the Indian Society of Theoretical and Applied Mechanics (ISTAM)*, IIT Mandi, Dec 14-16, 2022, Paper ID: ISTAM/2022/0281

- **Verma A.,** Borah B. and Kulkarni V., "Cavity for Flow Control and Performance Improvement of Airfoil", In *Proceeding of the ASME GT-India Conference* 2021. https://doi.org/10.1115/GTINDIA2021-76415

- **Verma A.** and Kulkarni V., "Effect of Self-Actuating Flap on the Aerodynamic Performance of Flat Plate Wing at Low Reynolds Number", In *Proceeding of the ASME IMECE conference* 2021. https://doi.org/10.1115/IMECE2021-70495

- Borah B., **Verma A.**, Kulkarni V. and Saha U. K., "Vortex Shedding Analysis in the Wake of a Flat Plate at Low Reynolds Number", In *Proceeding of the ASME GT-India Conference* 2021. https://doi.org/10.1115/GTINDIA2021-75959
- **Verma A.**, Barfa P. and Kulkarni V., "Self-actuating Flap for Fixed Wing Micro Air Vehicle", In *Proceeding of the 25th National and 3rd International ISHMT-ASTFE Heat and Mass Transfer Conference* 2019. https://doi.org/10.1615/IHMTC-2019.40
- **Verma A.** and Kulkarni V., "Experimental Study of Study-adjustable Flap for Fixed Wing MAV", In *Proceeding of the ASME GT-India Conference* 2019. https://doi.org/10.1115/GTINDIA2019-2512
- **Verma A.** and Kulkarni V., "Understanding Aerodynamics of Low Aspect Ratio Wings", In *Proceedings of the 7th International and 45th National Conference on Fluid Mechanics and Fluid Power* 2018.